

“Thermophysical properties of liquid Al-Ti alloys under the influence of oxygen”

Von der Fakultät für Georessourcen und Materialtechnik
der Rheinisch-Westfälischen Technischen Hochschule Aachen

zur Erlangung des akademischen Grades eines
Doktors der Naturwissenschaften

genehmigte Dissertation

vorgelegt von **M.Sc.**

Johanna Wessing

aus Bergisch Gladbach

Berichter: PD Dr. rer. nat. Jürgen Brillo
Univ.-Prof. Dr.-Ing. Andreas Bührig-Polaczek

Tag der mündlichen Prüfung: 30. Mai 2018

Diese Dissertation ist auf den Internetseiten der Universitätsbibliothek online
verfügbar

*'Nothing in life is to be feared,
it is only to be understood.
Now is the time to understand
more, so that we may fear less.'*

Marie Curie
(1867-1934)

Abstract

The central objective of this work was to study thermophysical properties of liquid Al, Ti, as well as the creation and completing of materials databases with systematically varied compositions in the binary Al-Ti system. Also, it has been found that thermophysical property data on the binary Al-Ti system are also a good starting point for investigations on multicomponent alloys and industrially used compounds, as well as the need for thermophysical data for materials processing. The overall method used for the measurements of this work was electromagnetic levitation (EML). As Al-Ti alloys are highly reactive and generally show high evaporation at elevated temperatures, conventional container-based techniques render vast difficulties. Therefore, contact-free electromagnetic levitation methods offer many advantages, enable to minimize error sources and measure with high accuracy. The measurements were performed at the German Aerospace Center (DLR), Institute of Materials Physics in Space in Cologne, Germany and at the Fukuyama lab at Tohoku University in Sendai, Japan.

High-temperature density, ρ , measurements as a function of temperature were performed over the whole Al-Ti composition range. The data were analyzed concerning the density at liquidus temperature, ρ_L , the molar volume, V , the density temperature coefficients, ρ_T , the thermal volume expansion coefficient, β , and the excess molar volume, V^E . For all Al-Ti compositions, the density, ρ , decreases linearly with increasing temperature. Additionally, ρ_L decreases gradually with increasing Al mole fraction from 4.12 gcm^{-3} to 2.30 gcm^{-3} for pure Ti and Al, respectively. It was found that Al-Ti exhibits significantly large negative values for the excess molar volume. It was suggested that shrunk Al radii upon mixing contribute to that mechanism.

The normal spectral emissivity, ε , of four compositions in the Al-Ti system was measured in dependence of the wavelength and temperature. It was found that all compositions show negligible temperature dependence. The emissivity results at a wavelength of 940 nm, amount to 0.30, 0.32, 0.40 and 0.37 for $\text{Al}_{70}\text{Ti}_{30}$, $\text{Al}_{50}\text{Ti}_{50}$, $\text{Al}_{20}\text{Ti}_{80}$ and Ti, respectively. The composition dependence of the emissivity results of the Al-Ti melts is in very good agreement with literature data of binary and multi-component Al-Ti-based alloys. The obtained values were used as input data for the isobaric heat capacity measurements, C_p , of this work, analogously conducted of the same four compositions of liquid Al-Ti melts as a function of temperature. For all compositions, the isobaric heat capacity shows negligible temperature dependence with average values of 57.59, 46.20, 54.61 and 48.50 $\text{JK}^{-1}\text{mol}^{-1}$ for $\text{Al}_{70}\text{Ti}_{30}$, $\text{Al}_{50}\text{Ti}_{50}$, $\text{Al}_{20}\text{Ti}_{80}$ and Ti, respectively. The composition dependence of the isobaric heat capacity results at constant pressure was compared to results by the Neumann-Kopp rule and literature. The deviation between the measured values and the Neumann-Kopp rule, the excess heat capacity, C_p^E , was evaluated, exhibiting positive values for all compositions.

High-temperature viscosity, η , of liquid $\text{Al}_{50}\text{Ti}_{50}$ was measured as a function of temperature during parabolic flight measured in the DLR μg -EML facility, TEMPUS. The results were fitted by an Arrhenius law with 2.23 mPas and $1.27 \cdot 10^4 \text{ Jmol}^{-1}$ corresponding to the Arrhenius fit parameters, η_∞ and E_A , respectively. The isothermal viscosity at 1750 K shows a positive deviation from the linear composition dependence of the pure elements. The Hirai model, the Kaptay model and the Kozlov model were calculated to predict the composition dependence of the viscosity in the Al-Ti system with the closest agreement of the experimental results found with the Kozlov model.

The surface tension, γ , of ten compositions in the Al-Ti system was measured as a function of temperature, including $\text{Al}_{50}\text{Ti}_{50}$ surface tension data obtained under microgravity conditions. For all compositions the surface tension decreases linearly with rising temperature yielding linear fit parameters; the surface tension at liquidus, γ_L , and the surface tension temperature coefficient, γ_T . In addition, within the measured composition range, the surface tension increases gradually with decreasing, X_{Al} at the respective liquidus temperatures. The isothermal surface tension at $T=1950 \text{ K}$ is in good agreement with predictions according to the Butler and the Chatain model for subregular nonideal solutions. A positive excess surface tension, γ^E , was evaluated over the whole composition range with a suppressed surface segregation of the surface-active component Al due to interatomic attractions.

Additionally, the influence of oxygen on Al and Ti melts was investigated with regards to the surface tension. Surface tension measurements were conducted as a function of time, the oxygen partial pressure in the surrounding gas and chemical addition of oxygen to Ti in the form of TiO_2 . For all composition, the surface tension results showed a negligible dependence on the oxygen partial pressure over the measured range. However, with increasing chemical addition of oxygen to Ti in the form of TiO_2 , the surface tension decreased gradually. All results for Ti-O were fitted by the Belton/Szyszkowski adsorption equation. Overall it was suggested in the case of liquid Ti, that the reduction of the surface tension of occurs at higher oxygen concentrations than assumed and covered ($P_{\text{O}_2} > 10 \text{ Pa}$). Concerning liquid Al, the maximum oxygen partial pressure boundaries in the chamber and the sample's vicinity for a "clean" surface were calculated. The Al surface tension results for 'clean conditions' are in very good agreement with corresponding literature results. It was suggested that these measurements relate to oxide free surfaces with either zero or minor adsorbed oxygen particles.

Finally, all thermophysical properties investigated in this work were compared with special regards to excess properties and the relations to the enthalpy of mixing, ΔH_{mix} , and the Gibbs free energy of formation, ΔG . Overall it was shown that liquid Al-Ti alloys generally exhibit highly nonideal behaviour for all investigated thermophysical and thermodynamic properties. Most of the properties are directly or indirectly interacting, however, no unified trend over all properties could be observed as the range of processes contributing are too wide-ranging.

Kurzfassung

Die primäre Zielsetzung dieser Arbeit war es, thermophysikalische Eigenschaften von Al, Ti und binären Al-Ti-Schmelzen zu untersuchen und damit Datenbanken zu diesem System zu vervollständigen. Zusätzlich hat sich gezeigt, dass sich das binäre System Al-Ti als geeigneter Ausgangspunkt für mehrkomponentige und industriell verwendete Al-Ti-Legierungen anbietet und damit einem Bedarf an thermophysikalischen Daten in der Materialverarbeitung entgegenkommt. Die Grundlage für alle Messungen dieser Arbeit war die elektromagnetische Levitation (EML). Da Al-Ti-Legierungen sehr reaktiv sind und bei erhöhten Temperaturen stark abdampfen, können herkömmliche, Behälter gestützte Verfahren zu Schwierigkeiten führen. Die EML Technik bietet den Vorteil des berührungsfreien Messens, wodurch Fehlerquellen minimiert werden und mit hoher Genauigkeit gemessen werden kann. Die Messungen dieser Arbeit wurden am Deutschen Zentrum für Luft- und Raumfahrt (DLR), am Institut für Materialphysik im Weltraum in Köln, Deutschland und am Fukuyama Lab an der Tohoku Universität in Sendai, Japan durchgeführt.

Dichtemessungen, ρ , in Abhängigkeit der Temperatur wurden über den gesamten Zusammensetzungsbereich von flüssigen binären Al-Ti-Legierungen realisiert. Die Dichte von allen Al-Ti-Legierungen nimmt mit zunehmender Temperatur linear ab und verringert sich mit steigendem Al-Molanteil. Im ganzen System stellt sich ein signifikant negatives molares Exzessvolumen ein. Dies kann dadurch begründet werden, dass sich während des Mischens die Atomradien zwischen den Al-Atomen verkleinern, was auf makroskopischer Ebene zu einem reduzierten molaren Volumen führt.

Die Emissivität, ε , von $\text{Al}_{70}\text{Ti}_{30}$, $\text{Al}_{50}\text{Ti}_{50}$, $\text{Al}_{20}\text{Ti}_{80}$ und Ti wurde in Abhängigkeit der Wellenlänge und der Temperatur gemessen. Bei allen Verbindungen zeigt sich eine vernachlässigbare Temperaturabhängigkeit. Die Ergebnisse in Abhängigkeit der Zusammensetzung stimmen sehr gut mit Literaturdaten zu binären und mehrkomponentigen Al-Ti-Legierungen überein. Die daraus gewonnenen Werte wurden als Eingangsparameter für isobare Wärmekapazitätsmessungen verwendet.

Entsprechend den Emissivitätsmessungen wurden Wärmekapazitätsmessungen an denselben flüssigen Al-Ti-Verbindungen durchgeführt. Hierbei zeigt sich ebenfalls eine vernachlässigbare Temperaturabhängigkeit. Die Wärmekapazitätsergebnisse in Abhängigkeit des Al-Molanteils wurden mit Literaturergebnissen und der Neumann-Kopp Regel verglichen. Die Abweichung zwischen den Messwerten und der Neumann-Kopp-Regel, die Exzesswärmekapazität, C_p^E , wurde ausgewertet und zeigt durchgehend positive Werte.

Die Viskosität, η , von flüssigem $\text{Al}_{50}\text{Ti}_{50}$ wurde als Funktion der Temperatur in reduzierter Schwerkraft in der DLR μg -EML Anlage, TEMPUS während eines Parabelfluges gemessen. Die Ergebnisse wurden mit einem Arrhenius Fit angepasst. Die isotherme Viskosität bei 1750 K zeigt eine positive Abweichung von der linearen

Viskositätsabhängigkeit zwischen den reinen Elementen. Zusätzlich wurden Viskositätsmodelle nach Hirai, Kaptay und Kozlov in Abhängigkeit der Zusammensetzung berechnet, wobei sich die engste Übereinstimmung der Messergebnisse mit dem Kozlov-Modell erkennen lässt.

Oberflächenspannungsmessungen, γ , wurden an zehn Al-Ti-Verbindungen in Abhängigkeit der Temperatur realisiert, einschließlich Messungen an $\text{Al}_{50}\text{Ti}_{50}$, die unter Mikrogravitationsbedingungen durchgeführt wurden. Bei allen Verbindungen sinkt die Oberflächenspannung linear mit steigender Temperatur ab und erhöht sich mit sinkendem Al-Molanteil. Die isotherme Oberflächenspannung bei 1950 K zeigt eine sehr gute Übereinstimmung mit den Modellen nach Butler und Chatain für subreguläre nicht-ideale Lösungen in Abhängigkeit der Zusammensetzung. Bei allen Legierungen ist eine positive Exzessoberflächenspannung, γ^E , erkennbar, zurückzuführen auf eine unterdrückte Oberflächensegregation der oberflächenaktiven Komponente Al durch interatomare Anziehungen.

Außerdem wurde der Einfluss von Sauerstoff auf die Oberflächenspannung von Al- und Ti-Schmelzen untersucht. Die entsprechenden Messungen wurden in Abhängigkeit der Zeit, des Sauerstoffpartialdrucks des umgebenden Gases und der chemischen Zugabe von Sauerstoff zu Ti in Form von TiO_2 durchgeführt. Bei allen Zusammensetzungen und über den gesamten gemessenen Bereich zeigen die Oberflächenspannungsdaten eine vernachlässigbare Abhängigkeit vom Sauerstoffpartialdruck. Allerdings nimmt die Oberflächenspannung mit zunehmender chemischer Zugabe von Sauerstoff im Ti-O-System logarithmisch ab, was sich mit der Belton/Szyszkowski Adsorptionsgleichung angepasst werden kann. Daraus lässt sich schließen, dass eine Reduktion der Oberflächenspannung von flüssigem Ti bei höheren Sauerstoffpartialdrücken stattfindet als angenommen und durch die Messungen abgedeckt ($P_{\text{O}_2} > 10 \text{ Pa}$). Im Fall von flüssigem Al wurden im Rahmen der Arbeit maximale Sauerstoffpartialdruckgrenzen für eine „saubere“ Oberfläche berechnet. Die Oberflächenspannungsmessergebnisse für „saubere“ Bedingungen zeigen eine sehr gute Übereinstimmung mit entsprechenden Literaturwerten. Daraus kann die Schlussfolgerung gezogen werden, dass diese Messungen auf oxidfreie Probenoberflächen mit keinem oder geringfügig absorbierten Sauerstoff hinweisen.

Abschließend wurden alle thermophysikalischen Eigenschaften, die in dieser Arbeit untersucht wurden, im Hinblick auf Exzesseigenschaften und den Zusammenhang mit der Mischungsenthalpie, ΔH_{mix} , und der Gibbs-Energie, ΔG , analysiert. Insgesamt konnte gezeigt werden, dass Al-Ti bei allen untersuchten Eigenschaften in der Regel ein sehr nicht-ideales Verhalten zeigt. Hierbei interagieren die meisten Eigenschaften direkt oder indirekt. Trotzdem konnte kein einheitlicher Trend beobachtet werden, da das Spektrum der beitragenden Prozesse zu umfangreich ist.

Table of contents

Introduction.....	1
1.1 New materials	1
1.2 Challenges	1
1.3 Strategy and procedure	3
1.4 Goals.....	4
2 Thermophysical properties of liquid metals	5
2.1 Density, molar volume, and thermal expansion	5
2.2 Normal spectral emissivity	8
2.3 Heat capacity	9
2.4 Surface Tension	10
2.4.1 Gibbs formalism	11
2.4.2 Butler Model.....	13
2.4.2.1 Ideal solution.....	13
2.4.2.2 Sub-regular solutions	14
2.4.3 Chatain model.....	15
2.4.4 Egry model	16
2.4.5 Empirical models.....	17
2.5 Shear viscosity.....	18
2.5.1 Temperature dependencies	18
2.5.2 Composition dependencies	19
2.6 Oxygen partial pressure	20
2.6.1 Adsorption of oxygen	21
2.6.2 Formation of oxides.....	23
2.7 Summary.....	25
3 Experimental methods	26
3.1 Conventional techniques.....	26
3.2 Electromagnetic levitation (EML).....	26
3.2.1 Electromagnetic levitation technique	27
3.2.2 Experimental setup	28
3.2.3 Temperature control	30
3.3 Electromagnetic levitation in microgravity (TEMPUS).....	32
3.4 Optical dilatometry	34
3.5 Static magnetic field	36
3.6 Normal spectral emissivity measurement.....	37
3.6.1 Calibration of the spectrometer	37

3.6.2	Experimental setup	38
3.7	Non-contact modulated laser calorimetry.....	39
3.8	Oscillating drop method	42
3.8.1	Oscillation modes	45
3.8.2	Oscillating drop method in microgravity (TEMPUS)	48
3.9	Viscosity measurement.....	48
3.10	Oxygen control and monitoring.....	49
3.10.1	Oxygen ion pump	49
3.10.2	Oxygen control system (OSC).....	50
3.10.3	Sublimation pumps	53
3.10.4	Oxygen equilibrium in buffer gas mixtures.....	53
3.11	Summary.....	54
4	Sample preparation, procedures, and analysis	55
4.1.1	Binary alloys Al-Ti	55
4.1.2	Binary alloys Ti-TiO ₂	57
4.2	Sample analysis	59
4.2.1	Scanning electron microscope (SEM)	59
4.2.2	Oxygen analysis.....	59
4.3	Summary.....	60
5	Results and discussion	61
5.1	High-temperature density	61
5.1.1	Results	61
5.1.2	Discussion.....	69
5.2	Normal spectral emissivity	72
5.2.1	Results	72
5.2.2	Discussion.....	75
5.3	Isobaric heat capacity	78
5.3.1	Results	79
5.3.2	Discussion.....	81
5.4	High-temperature viscosity under reduced gravity (μg).....	85
5.4.1	Results	85
5.4.2	Discussion.....	87
5.5	High-temperature surface tension.....	90
5.5.1	Results	90
5.5.2	Discussion.....	94
5.6	Influence of oxygen on the surface tension	103
5.6.1	Results	103
5.6.2	Discussion.....	107

5.6.2.1 Al-O system	107
5.6.2.2 Ti-O system.....	116
5.7 Summary.....	128
6 Inter-property relations	129
7 Summary	136
Appendix.....	140
Bibliography	149
Abbreviations	164
Method abbreviations	173
Acknowledgements	174
Curriculum Vitae	175

Introduction

The term metal comes from the Greek word μέταλλον, translating to ‘mine, quarry, metal’ [1]. A metal is commonly understood as a solid material, that looks shiny and opaque with good electrical and thermal conductivity. Metals can be defined according to their position in the periodic table, and respective subgroups exist, including alkali metals, alkaline earth metals, transition metals, and rare earth metals [2]. Humans have been fascinated by metals for centuries and have used them for tools, jewelry, in medicine and science, for weapons and various other industries. Some of the best-known metals include gold and silver which have been used by humans since the end of the Stone Age [2]. Much later at the end of the 18th century, aluminum and titanium were discovered which has added incredible value to the human species in many uses including science and engineering, such as components with automotive and aerospace applications.

1.1 New materials

There is a constant demand for high-end materials with specific properties designated for various applications and industries. Al-Ti binary and multi-component alloys have been extensively studied as potential solutions to fulfill those needs. Al-based alloys form the basis for most industrial lightweight casting alloys due to their low densities, low cost, good castability, good processability, excellent oxidation and corrosion resistance [3-6]. Especially Al-Ti based alloys additionally exhibit high melting points, low ductility, and high tensile strength even at elevated temperatures [7, 8].

These properties make Al-Ti intermetallic compounds particularly interesting for applications in the automotive and aerospace industries [9]. They are used as exhaust valves for car engines, turbocharger rotors, and aero-engine gas turbine blades, where the low density helps to reduce emissions [8-10]. Moreover, Ti-based alloys find medical applications as bone implants, because of their biocompatibility and corrosion resistance [7].

1.2 Challenges

As the vast majority of material components are produced from the melt directly, the properties of the liquid phase are crucial to know as input parameters for numerical simulations of casting processes [10]. Consequently, they play a key role, linking the experimental work and the modeling [11]. Among the properties relevant in this context,

density, surface tension, viscosity, emissivity, and heat capacity of the liquid phase are of pronounced importance [12].

Density and the thermal expansion coefficient of liquids are important for the discussion of thermodynamic properties and belong to the fundamental material properties. Their knowledge gives access to the compressibility, the thermal pressure coefficient and other microscopic parameters, such as the packing in the hard-sphere model and is crucial for casting processes [13]. Moreover, they are used as input data for the determination of other properties from the measured raw data, such as surface tension and emissivity. Surface tension plays a critical role for the castability of an alloy, as well as for the mold-filling capability, which is often problematic in Ti-based alloys. From a scientific point of view, density and surface tension provide insights into processes on the atomic scale [7]. Similar to density and surface tension, viscosity data are needed for the modeling of different casting processes in metal production, powder production by spray forming, and welding [14]. Emissivity and heat capacity are important input data for estimating the heat loss to ambient air and the contributions to the heat transfer in the liquid. Additionally, emissivity data are needed for the noncontact modulation laser calorimetry to estimate the laser absorptivity for accurate heat capacity measurements [15-19].

Despite the technical importance of the knowledge about these properties, corresponding data are sparse. The main reason for this is the high chemical reactivity of liquid Al-Ti alloys paired with a large solubility of oxygen. Thus, investigations with conventional container based techniques are challenging, and adequate inert substrate materials that show negligible interactions with the sample are rare [7, 20].

Nevertheless, there are container-based methods which have been used to investigate thermophysical properties of pure Al and Ti, as well as their binary and multicomponent alloys, such as the pendant and sessile drop method for density and surface tension measurements [21]. In the cases of emissivity and heat capacity, among the methods used are He-Ne laser ellipsometry, pulse heating and differential scanning microscopy (DSC) [22].

For each investigated property more information about used methods in literature is provided in the respective chapters, 5.1, 5.2, 5.3, 5.4 and 5.5. All methods and the method abbreviations are listed in the section *Method abbreviations*. For a more comprehensive review, a detailed study on high temperature measurements and methods has been published by Fukuyama et al. [22].

Oxygen may influence thermophysical properties, which is especially pronounced with regards to the surface tension [7]. Depending on the metal only a few ppm of oxygen can cause a decrease of the surface tension by several percents, and a reversal of the temperature

coefficient sign from negative to positive, as reported for Ag [23]. Previous studies have suggested that Ti melts might be sensitive to oxygen impurities due to the high oxygen solubility in liquid Ti [20, 24]. Studies on liquid Al, on the other hand, suggest that already very low oxygen partial pressures in the sample surrounding atmosphere may lead to oxide formation in the melt [25].

1.3 Strategy and procedure

To avoid pollution of the materials due to reactions with the container walls, levitation methods with a contact-free technique offer many advantages. Using these techniques, the negative effects of the high chemical reactivity of the material are minimized, and it is possible to measure over broad temperature ranges including deep undercooling of the melts far below their equilibrium melting temperature [7]. There are numerous different levitation techniques such as; acoustic, aerodynamic, electrostatic (ESL), and electromagnetic levitation (EML). The latter is used for the measurements of this work. Each technique has its advantages and disadvantages making them preferable for different materials and applications. For electrically conducting samples, EML is a very suitable and relatively simple technique compared to for example ESL, enabling a stable positioning of the material in a high-frequency magnetic field under inert gas atmosphere [4, 24].

In the case of viscosity and some materials, this is the only possible method to measure the viscosity of the melt. As in the case of Al-Ti, the use of ESL is highly challenging due to pronounced evaporation under vacuum conditions. However, to ensure that no magnetic damping and turbulent fluid flow occur, the use of EML to measure the viscosity is only possible in microgravity [26]. Conventional techniques, such as the oscillating cup viscometry [27] entail the difficulties for highly reactive systems.

Although electromagnetic levitation is a very ‘clean’ method with reduced error contributions due to the reasons mentioned above, surface oscillation and translational motions of the sample may engender uncertainties in temperature and radiance measurements. Moreover, melt convections such as buoyancy and Marangoni convection induced by non-uniform temperature distributions must be taken into account as they may significantly influence the caloric measurement results [19, 28]. Therefore, Kobatake and Fukuyama et al. developed a technique to suppress translational motions, surface oscillations, and melt convection in the materials, reported in references [16, 17]. The emissivity and heat capacity measurement data presented in this work were carried out using this method, combining electromagnetic levitation with the use of a static magnetic field.

Even though electromagnetic levitation avoids pollution of the materials due to reactions with the container walls, the interactions with residual gas components of the surrounding environment can still not be excluded [27, 29]. As mentioned before, particularly the role of oxygen needs to be considered, for example, monitoring the oxygen content which is discussed extensively in section 5.6.

1.4 Goals

The research of this work is focused on thermophysical properties of Al, Ti, the binary Al-Ti system, and the creation and completion of materials databases with systematically varied compositions in the binary Al-Ti system [30]. However, to understand multicomponent systems, their binary basis must first be understood [7]. Therefore, the binary system Al-Ti is also a good starting point for investigations on multicomponent alloys and industrially used compounds and their need for thermophysical data for materials processing.

Even though electromagnetic levitation techniques have been established for many years [31] and despite the technical relevance of Al-Ti alloys, even for the binary system Al-Ti, few data exist. Only in the case of emissivity, a study over the whole Al-Ti composition range has been performed before [32]. Therefore, the goal of the present work is to deliver accurate density (section 5.1), emissivity (section 5.2), heat capacity (section 5.3), viscosity (section 5.4) and surface tension (section 5.5) data on binary liquid Al-Ti alloys and additionally consider the influence of oxygen with regards to the surface tension (section 5.6).

2 Thermophysical properties of liquid metals

In this chapter, the theoretical background is explained to understand the mechanisms of thermophysical properties of liquid metals. Using thermodynamics and processes on atomic scales, it builds the foundation to interpret the experimental results presented in chapter 5. In chapter 3, the experimental methods for the measurements of the corresponding thermophysical properties are introduced.

To gain an understanding of the properties of unary and binary systems, it is crucial to take a closer look at the terms *ideal solution*, *non-ideal solution* and *excess properties*.

In the following sections 2.1, 2.2, 2.3, 2.4 and 2.5 the properties density, molar volume, emissivity, heat capacity, surface tension, and viscosity will be introduced, respectively, with one focus on the mixing behavior of binary alloys. Additionally, the influence of the gas phase being in equilibrium with the liquid metals will be looked at in section 2.6.

2.1 Density, molar volume, and thermal expansion

Concerning density and molar volume in this work, ideal and non-ideal solutions will be distinguished. Excess properties are parameters that characterize the non-ideal behavior of mixtures. An ideal solution defines solutions with no excess properties, e.g., excess free energy, ${}^E G = 0$. For non-ideal solutions, different definitions exist. Up to now, there is no definite rule if a system shows non-ideal behaviour and if the excess properties are negative or positive. But generally, alloy systems with atoms that are chemically similar tend to have excess volumes close to zero, while de-mixing systems often feature positive excess molar volumes and mixing systems typically show strong negative excess molar volumes [30].

The Gibbs free energy, G , is an important thermodynamic value related to density and molar volume. Upon mixing, the Gibbs free energy can be related to the volume, V , the pressure, P , the entropy, S , the temperature, T , the chemical potential of component i in the mixture, μ_i , and the number of moles of component i , n_i by [33]:

$$dG = VdP - SdT + \sum_i \mu_i dn_i \quad (2.1)$$

For mixtures with different components i with the mole fraction $X_i = n_i / \sum_i n_i$, G can be defined by the Gibbs free energy, G_i^0 , of the pure component i and the Gibbs free energy of formation, ΔG :

$$G = \sum_i X_i G_i^0 + \Delta G \quad (2.2)$$

The mixing free energy determines whether mixing at a constant temperature, T , and pressure, p , is a spontaneous process, combining two physical effects, the enthalpy of mixing, ΔH_{mix} , and the entropy of mixing, ΔS .

$$\Delta G = \Delta H_{\text{mix}} - T\Delta S \quad (2.3)$$

The enthalpy of mixing is the enthalpy liberated or absorbed from a substance upon mixing, and the entropy of mixing describes the change in the total entropy of the system due to the mixing process.

From the Gibbs free energy of formation, ΔG , and mixing free energy of the ideal solution, $\Delta G^{\text{ideal}} = RT \sum_i X_i \ln X_i$, the corresponding excess free energy, ${}^E G$, can be defined written in a Redlich-Kister form with binary non-vanishing interaction parameters, ${}^v L_{i,j}(T) (v = 0 \dots N_{i,j})$ [30, 34].

$${}^E G = \Delta G - \Delta G^{\text{ideal}} \quad (2.4)$$

$$\begin{aligned} &= \Delta G - RT \sum_i X_i \ln(X_i) \\ &= X_i X_j \sum_{v=0}^{N_{i,j}} {}^v L_{i,j}(T) (X_i - X_j)^v \end{aligned}$$

Here, ${}^v L_{i,j}(T) (v = 0 \dots N_{i,j})$ and the upper bound of summation, $N_{i,j}$, are material-specific parameters of mixing components i and j with $X_{i,j}$ defining the mole fraction of component i, j in a mixture. Based on Eqs. (2.1) and (2.4), the molar volume of the mixture, V , can be equally expressed as the molar volume, V_i , of the pure component i and by an additional molar excess volume, V^E , which is caused by interactions between the particles:

$$V = \sum_i X_i V_i + V^E \quad (2.5)$$

Generally, V^E depends on the temperature and the mole fraction. In compliance with ${}^E G$ in Eq. (2.4), V^E is given by the following Redlich-Kister-type approach for binary alloys with components i, j [30]:

$$V_{i,j}^E = X_i X_j \sum_{v=0}^{N_{i,j}} {}^v V_{i,j}(T) (X_i - X_j)^v \quad (2.6)$$

The fit parameters ${}^v V_{i,j}(T)$ ($v = 0 \dots N_{i,j}$) are material-specific and represent the interactions between the elements i and j in the alloy melt and can be approximated as a linear function of the temperature:

$${}^v V_{i,j}(T) = {}^v C_{i,j} + {}^v D_{i,j} T \quad (2.7)$$

Excess properties are zero for ideal solutions, hence ${}^E G, V^E = 0$. Applying this to Eq. (2.7), leads to

$$V^{\text{ideal}} = \sum_i X_i V_i + 0 \quad (2.8)$$

On the other hand, a mixture with zero excess properties is not necessarily ideal as the pressure dependence of ${}^E G$ of liquid alloys may not be sufficiently known. Consequently, a system exhibiting ${}^E G = 0$ at a certain pressure may still belong to the class of non-ideal solutions when its partial derivative with respect to the pressure, p , is not equal zero [30]. Eq. (2.8) is referred to as *ideal law* following *Vegards law* [35] originally describing the change of lattice constants in crystalline materials in dependence of the composition.

The density, ρ_i , of a pure component with atoms, i , can be defined as the molar mass, M_i , divided by the molar volume, V_i :

$$\rho_i = M_i / V_i \quad (2.9)$$

For mixtures, the density can be derived from Eq. (2.9) as

$$\rho = \frac{\sum_i X_i M_i}{\sum_i X_i \frac{M_i}{\rho_i} + V^E} \quad (2.10)$$

Within a limited temperature interval including the liquidus point, the density, $\rho(T)$ and the molar volume, $V(T)$ of a liquid metal can be considered as linear functions of the temperature, T :

$$\rho(T) = \rho_L + \rho_T (T - T_L) \quad (2.11)$$

$$V(T) = V_L(1 + \beta(T - T_L)) \quad (2.12)$$

In Eqs. (2.11) and (2.12), ρ_L and V_L are the density and molar volume at the liquidus temperature, T_L , respectively and ρ_T is the density temperature coefficient $\partial\rho/\partial T$. The thermal expansion coefficient, $\beta = V^{-1}\partial V/\partial T$, can be expressed by [7]:

$$\beta \approx -\frac{\rho_T}{\rho_L} \quad (2.13)$$

The experimental methods used in this work to measure the density and obtain the molar volume will be introduced in section 3.4, and the corresponding results will be presented in section 5.1.

2.2 Normal spectral emissivity

Another important thermophysical property is emissivity. The emissivity of liquid metals, as well as the heat capacity, is among the properties used as input data for numerical simulations. Furthermore, the emissivity is indispensable for the determination of the heat capacity and the thermal conductivity. The emissivity of the surface of a material can be described as the effectiveness in emitting energy as thermal radiation, which may include visible and infrared radiation. The normal spectral emissivity of a sample, $\varepsilon(\lambda, T)$, is defined as the ratio of the normal spectral radiance emitted from the sample, $R_S(\lambda, T)$, to the theoretical black-body radiance from Planck's law, $R_B(\lambda, T)$, at the same wavelength, λ , and temperature, T [28, 36]:

$$\varepsilon(\lambda, T) = \frac{R_S(\lambda, T)}{R_B(\lambda, T)} \quad (2.14)$$

The value of $R_B(\lambda, T)$ can be estimated using Planck's law of radiation, which is expressed as the following equation:

$$R_B(\lambda, T) = \frac{C_1}{\lambda^5(e^{C_2/\lambda T} - 1)} \quad (2.15)$$

In Eq. (2.15), $C_1 = 3.742 \cdot 10^{16}$ (W m²) and $C_2 = 1.439 \cdot 10^2$ (m K) are constants.

The experimental methods for the emissivity measurement are described in section 3.6 and the corresponding results presented in section 5.2.

2.3 Heat capacity

The heat capacity, C_p , is an extensive material property equal to the ratio of heat added to or removed from a material to the resulting temperature change. Concerning different definitions, the molar heat capacity refers to the heat capacity per unit mole and the specific heat capacity is the heat capacity per unit mass of a material.

Generally, heat capacity can be related to the enthalpy, H , for constant pressure as follows:

$$C_p = \left(\frac{\partial H}{\partial T} \right)_{P=\text{const}} \quad (2.16)$$

When a binary liquid alloy system with components, i and j , is considered, the heat capacity is expressed as:

$$C_p = \left(\frac{\partial H_{i,j}}{\partial T} \right) = X_i \left(\frac{\partial H_i}{\partial T} \right) + X_j \left(\frac{\partial H_j}{\partial T} \right) + \left(\frac{\partial \Delta H_{\text{mix}}}{\partial T} \right) \quad (2.17)$$

Where H_i denotes the enthalpy of the pure components and ΔH_{mix} the enthalpy of mixing. For a binary ideal solution, $\Delta H_{\text{mix}} = 0$, the following expression is obtained for the ideal heat capacity C_p^{ideal} :

$$C_p^{\text{ideal}} = X_i \left(\frac{\partial H_i}{\partial T} \right) + X_j \left(\frac{\partial H_j}{\partial T} \right) = X_i C_p^i + X_j C_p^j \quad (2.18)$$

Additionally to the case of an ideal solution with $\Delta H_{\text{mix}} = 0$, when the temperature dependence of the mixing enthalpy, $\Delta H_{\text{mix}} = \text{const.}$, consequently it leads to a vanishing mixing parameter, $\partial \Delta H_{\text{mix}} / \partial T = 0$. Therefore, the composition dependence in this case can be analogously expressed by Eq. (2.18), which is called Neumann-Kopp's rule.

The deviation of the heat capacity from the Neumann-Kopp relation indicates an excess heat capacity, C_p^E , resulting from a temperature dependence of the mixing enthalpy of the i, j -binary liquid alloy system:

$$C_p^E = C_p - (X_i C_p^i + X_j C_p^j) = \left(\frac{\partial \Delta H_{\text{mix}}}{\partial T} \right) \quad (2.19)$$

With this formalism, similar to the one for the excess molar volume (section 2.1), C_p^E may be fitted analogously with a Redlich-Kister polynomial:

$$C_{p_{i,j}}^E = X_i X_j \left(\sum_{v=0}^{N_{i,j}} {}^v c_{i,j} (X_i - X_j)^v \right) \quad (2.20)$$

With ${}^v c_{i,j}$ ($v = 0 \dots N_{i,j}$) being material-specific interaction parameters of v th order which can be determined by fitting Eq. (2.20).

The experimental methods for the heat capacity measurement are introduced in section 3.7 and the corresponding results discussed in section 5.3.

2.4 Surface Tension

Surface energy is a macroscopic property originating from interactions between interfaces of different thermodynamic phases. Regarding interactions between a liquid in contact with a gas phase, it is called surface tension and equals the energy per surface area, A [37]. Those interactions are based on microscopic processes which can be related to differences in pressure, ΔP [37, 38].

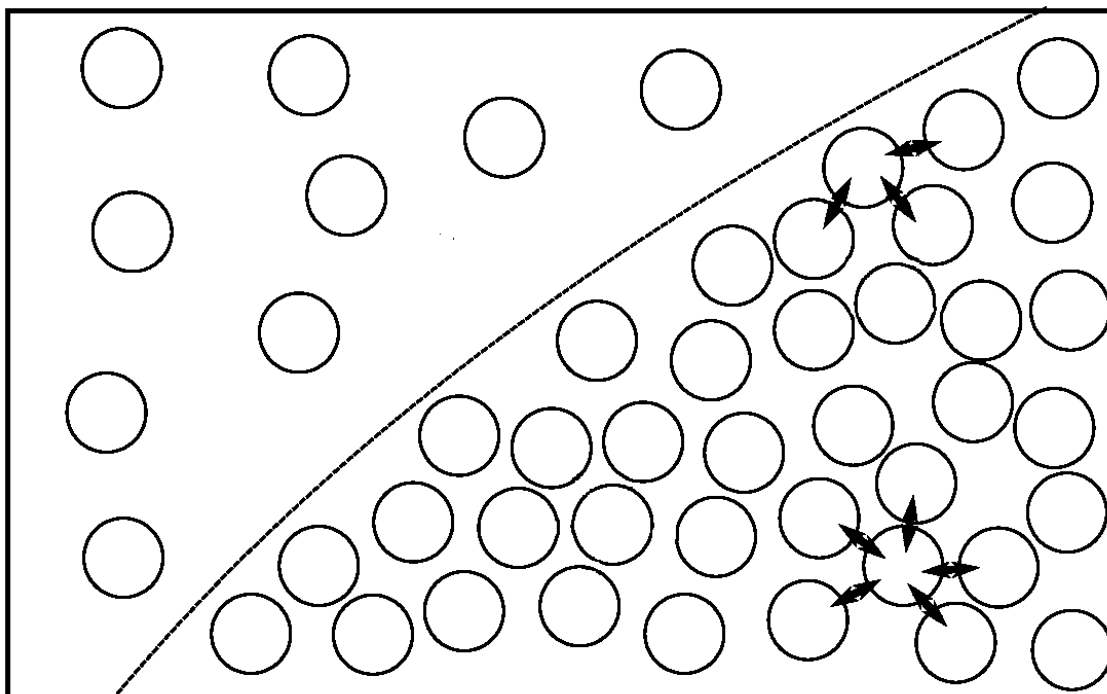


Figure 2.1: Schematic image of particles in a liquid droplet interacting with the surrounding particles in the gas phase. The arrows indicate the interactions between the particles.

Each phase consists of particles interacting with their neighboring atoms. This interaction is isotropic in the bulk phase. However, as there are comparatively fewer neighbors in the gas phase, the interactions of an atom on the surface with the gas phase are significantly lower than the interactions of the atom with the bulk. Therefore, atoms located on the surface are generally on a higher energy level. Consequently, there is a resulting force directed towards the liquid phase and atoms surging towards the surface must counteract with this force [38]. Thus creating a surface area, A , requires mechanical work, $dw =$

γdA , which can be expressed according to Gibbs as the change in the free energy, G , by the surface tension, γ [30, 39]:

$$\gamma = \left(\frac{\partial G}{\partial A} \right)_{P,V,T} \quad (2.21)$$

Where V denotes the volume and T the temperature. Eq. (2.21) provides a differential equation for evaluating the surface tension for any droplet form. There are different analytical thermodynamic approaches to calculate the surface tension of alloys, which primarily differ in the description of the surface [40]. In the following, some of those corresponding models will be introduced.

2.4.1 Gibbs formalism

The Gibbs formalism is commonly regarded as correct and a very basic description of surfaces processes. According to the Gibbs formalism, the surface (S) is considered as the plane between a bulk phase of a liquid phase (B) and the gas phase (G), schematically shown in Figure 2.2. Both phases are homogeneous with constant number densities, $\hat{\rho}_i^B$ and $\hat{\rho}_i^G$, of particles type, i . With V^B being the volume of the bulk and V^G the volume of the gas phase, the number of moles in the bulk phase, can be defined as $n_i^B = V^B \hat{\rho}_i^B$ and in the gas phase as $n_i^G = V^G \hat{\rho}_i^G$, respectively [30, 41]. The phases are separated by the so-called *Gibbs dividing plane* which denotes an abrupt change in the number density. However, realistically this change can be assumed to be more like a gradual transition within a limited zone, $\Delta\delta$, of a few atomic diameters. The total number of moles, n_{total} , in the entire system of Figure 2.2 is disturbed by this transitional area and a deviation or excess number of moles, Δn_i^S , is added to the sum of the number of moles in the two phases, $n_i^B + n_i^G$ [30]. Depending on the position of the dividing plane the excess number of moles, Δn_i^S , can be zero, negative or positive. The fundamental definition of the molar free energy of the surface, G^S for a mixture of N components, called the *Gibbs-Duhem relation for surfaces* is given by [30, 41]:

$$dG^S = -S^S dT + V dP - A_S d\gamma + \sum_i^N \mu_i dX_i^S \quad (2.22)$$

In Eq. (2.22), S^S is conform to the molar entropy, V is the molar volume, P is the pressure, A_S is the surface area of the surface phase and μ_i defines the chemical potential of component i . In relation to the surface tension the molar fraction X_i is differentiated into X_i^S and X_i^B , where the index ‘S’ and ‘B’ mark the amount of element i in the surface and bulk, respectively. In Eq. (2.22), $A_S d\gamma$ stands for the mechanical work needed to create

new surface of an area, A . Based on this equation different relations for surface processes can be derived.

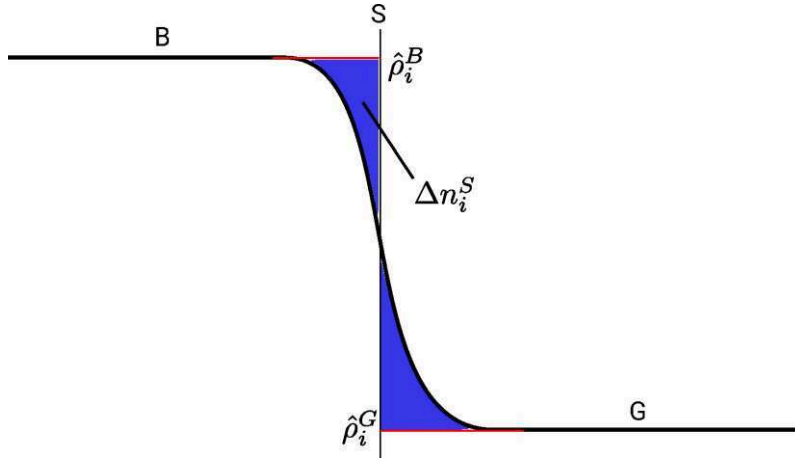


Figure 2.2: Schematic illustration of the number density change between the bulk liquid phase (B) and the gas phase (G), separated by a gradual transition zone describing the surface (S). Based on Fig. 4.1 by Brillo [30].

Correspondingly to the density, the surface tension, $\gamma(T)$, can be expressed as a linear function of temperature, provided that the temperature interval considered is sufficiently small [7]:

$$\gamma(T) = \gamma_L + \gamma_T(T - T_L) \quad (2.23)$$

In Eq. (2.23), γ_L , is the surface tension at the liquidus temperature, T_L , and γ_T is the corresponding constant temperature coefficient. The latter is related to the entropy difference, ΔS , between the surface and the bulk phase as follows [30]:

$$\gamma_T = -\frac{\Delta S}{A_S} \quad (2.24)$$

For a binary ideal solution, ${}^E G = 0$, the following expression is obtained for its ideal surface tension, γ^{ideal} [7, 42]:

$$\gamma^{\text{ideal}}(T) = X_i^S \gamma_i(T) + X_j^S \gamma_j(T) \quad (2.25)$$

The deviation from the ideal surface tension, γ^{ideal} , is called excess surface tension, γ^E as can be seen by the following equation:

$$\gamma = \gamma^{\text{ideal}} + \gamma^E \quad (2.26)$$

Analogously to the excess molar volume and the excess heat capacity in the sections 2.1 and 2.3, respectively, γ^E may be fitted by a Redlich-Kister polynomial:

$$\gamma_{i,j}^E = X_i^B X_j^B \left(\sum_{v=0}^{N_{i,j}} v u_{i,j}(T) (X_i^B - X_j^B)^v \right) \quad (2.27)$$

With $v u_{i,j}(T)$ ($v = 0 \dots N_{i,j}$) being temperature-dependent material-specific interaction parameters [7].

2.4.2 Butler Model

To quantitatively compare measured surface tension data, Butler introduced a model to estimate the surface tension of alloys by approximations [43]. Different to the Gibbs formalism, the Butler model neglects the gas phase and considers the surface as a separate thermodynamic phase. This phase is based on a monolayer of atoms in equilibrium with the bulk, illustrated in Figure 2.3 [30, 43].

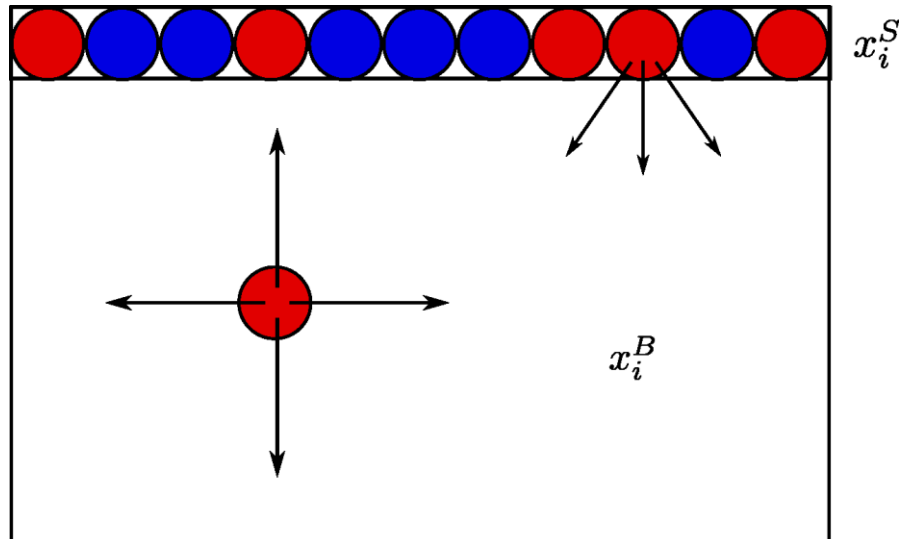


Figure 2.3: The Butler model: The surface of a liquid is considered as a separate thermodynamic phase consisting of a monolayer of atoms in equilibrium with the bulk with the molar fractions, X_i^S and X_i^B , of the component, i , relating to the surface and bulk, respectively. Based on Fig. 4.2 by Brillo [30].

2.4.2.1 Ideal solution

A special case of the Butler model is the ideal solution. With γ_i being the surface tension of the pure component, X_i^S and X_i^B the mole fractions of component i in the surface (S) and bulk (B) phase, respectively, A_i defining the area one mole of atoms of type, i , occupies, R the universal gas constant and T the absolute temperature, the surface tension of an ideal solution, γ^{ideal} , can be written as [30, 43]:

$$\gamma^{\text{ideal}} = \gamma_i + \frac{RT}{A_i} + \ln\left(\frac{X_i^S}{X_i^B}\right) \quad (2.28)$$

In the case of a binary alloy with components i, j Eq. (2.28) can be solved analytically assuming an approximation for the mole area $A_i \approx A_j \approx A$. Consequently, the surface concentration of components i and j relates as following:

$$X_i^S = \frac{X_i^B}{X_i^B + X_j^B S_e(T)} \quad (2.29)$$

$$X_j^S = \frac{X_j^B}{X_j^B + X_i^B / S_e(T)} \quad (2.30)$$

The segregation factor, $S_e(T)$, can be written as

$$S_e(T) = \exp\left(\frac{(\gamma_i - \gamma_j)A_s}{RT}\right) \quad (2.31)$$

Negative values for $\ln(S_e)$ indicate that $\gamma_A < \gamma_B$ and surface segregation takes place. In order to minimize the energy for the whole system and taking into account that creating surface area requires energy, the component with the smaller surface tension segregates to the surface layer, in this case, component i [30].

2.2.2.2 Sub-regular solutions

As for most systems the excess free energy, ${}^E G \neq 0$, the ideal solution does not model the surface tension correctly. In order to predict the surface tension of those sub-regular solutions the Butler model for ideal solutions can be extended by terms for the partial excess free energies, ${}^E G_i^S$ and ${}^E G_i^B$, of the surface and bulk, respectively [7, 30, 43]:

$$\begin{aligned} \gamma &= \gamma_i + \frac{RT}{A_{S,i}} + \ln\left(\frac{X_i^S}{X_i^B}\right) + \frac{1}{A_{S,i}} ({}^E G_i^S(T, X_i^S, X_j^S) - {}^E G_i^B(T, X_i^B, X_j^B)) \\ &= \gamma_j + \frac{RT}{A_{S,j}} + \ln\left(\frac{X_j^S}{X_j^B}\right) + \frac{1}{A_{S,j}} ({}^E G_j^S(T, X_i^S, X_j^S) - {}^E G_j^B(T, X_i^B, X_j^B)) \end{aligned} \quad (2.32)$$

Eq. (2.32) can be solved by equating both sides of the formula and substituting $X_j^S = 1 - X_i^S$. Solving Eq. (2.32), then, by minimization of the right-hand side yields the surface tension of the alloy and the concentration in the surface layer, X_i^S . The partial molar surface area, $A_{S,i}$, of the pure liquid component, i , can be approximated by the following

expression from the molar volumes of the pure elements, V_i , the Avogadro number, $N_A = 6.02214086 \cdot 10^{23} \text{ mol}^{-1}$, and the geometrical factor, f_{geo} :

$$A_{S,i} = f_{\text{geo}} V_i^{2/3} N_{\text{Av}}^{1/3} \quad (2.33)$$

Here, the value of f_{geo} corresponds to an assumed atomic arrangement in the surface similar to an *fcc* (111) plane with a coordination number in the bulk of $z = 12$. In this work the value of $f_{\text{geo}} = 1.0$ as proposed by Kaptay [44] is used. The main assumption of the Butler model is the approximation of the surface excess free energy by ${}^E G_i^S(T, {}^S X_i) = \xi {}^E G_i^B(T, {}^S X_i)$. Here, the factor ξ relates to the reduced coordination of atoms in the surface layer and corresponds to the ratio of the coordination numbers of atoms in the surface and the bulk, respectively. In this work, a value of 0.75 as suggested by Tanaka and Iida [45] is used to comply with the Chatain model which is also applied.

2.4.3 Chatain model

The Butler model may be criticized for its restriction to neglect concentration gradients perpendicular to the surface and, thus, consider the surface as a phase of a single monolayer. However, it has been shown recently [46] that this phase does not necessarily need to be a monolayer, as originally stated by Butler [7]. On the other hand, the Chatain model [47, 48] directly considers a concentration gradient with multiple layers, $n = 1 \dots k$, of different compositions, $X_i^{(n)}$, in each layer, n , as schematically shown in Figure 2.4.

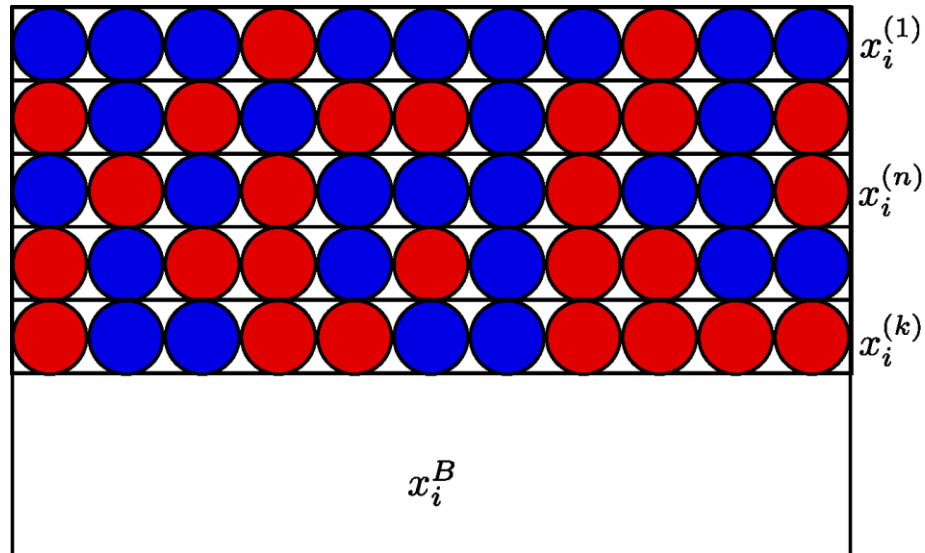


Figure 2.4: The Chatain model: Schematic illustration of the surface and bulk of a liquid with the surface displaying a concentration gradient with multiple layers, $n = 1 \dots k$, of different compositions, $X_i^{(n)}$, in each layer, n approximating the concentration of the bulk, X_i^S , with increasing n . Based on Fig. 4.4 by Brillo [30].

In the bulk phase, the atoms of the liquid are assumed to form a cubic lattice with a coordination number, $z = 12$, and a lateral coordination number, $z_l = 6$ [7]. The resulting number of neighboring atoms in the adjacent atom layer counts $z_v = 3$.

From these relations the surface free energy of a regular solution is expressed as [7, 46]:

$$\begin{aligned}
 A_S \gamma &= A_S \gamma_j X_j^{(1)} + A_S \gamma_i X_i^{(1)} & (2.34) \\
 &- z_v w (X_j^{(1)} - 2X_j^B X_j^{(1)} - (X_B^B)^2) \\
 &- z_v w \sum_{n=1}^k (X_j^{(n)} - X_j^B)(X_i^{(n)} - X_i^B) \\
 &- z_l w \sum_{n=1}^k (X_j^{(n)} - X_j^B)^2 \\
 &- RT \sum_{n=1}^k \left[X_j^{(n)} \ln \left(\frac{X_j^{(n)}}{X_j^B} \right) + X_i^{(n)} \ln \left(\frac{X_i^{(n)}}{X_i^B} \right) \right]
 \end{aligned}$$

With the regular solution constant, w , defined as following:

$$w = - \frac{T^2}{z \cdot X_i^B X_j^B} \frac{\partial}{\partial T} \left(\frac{{}^E G(T)}{T} \right) \approx \frac{{}^0 L(T=0)}{z} \quad (2.35)$$

Eq. (2.34) is solved by minimization of the right-hand side using a random sampling Monte Carlo algorithm. This procedure yields the surface tension of the alloy and the composition, $X_B^{(n)}$, in each layer and therefore, more detailed information about the surface composition than the Butler model. Furthermore, the Chatain model is in agreement with the Gibbs adsorption isotherm, as described in section 2.4.1. Besides the advantages of the Chatain model when investigating surface transitions, the model can be criticized for some mathematical inconsistencies. Additionally, only the first Redlich-Kister coefficient ${}^0 L(T=0)$ is considered, neglecting that for the accurate description of some systems a higher coefficient order is required with linear or logarithmic temperature dependence.

2.4.4 Egry model

To investigate the influence of compound formation in alloy systems, Egry [49] introduced a simple model that is based on the ideal solution approximation. The model is based on the assumption that compounds do not segregate to the surface. Therefore, in

the binary system with a potential compound composition Al_nTi_m , the segregation factor would then be enhanced by an additional contribution, as follows:

$$S_e(T) = \exp\left(\frac{(\gamma_j - \gamma_i)A_{S,i} - f_{se}(n+m)(X_i^B)^n(X_j^B)^m}{RT}\right) \quad (2.36)$$

The aforementioned parameter $A_{S,i}$, is defined in Eq. (2.33). Here, f_{se} is an adjustable fit parameter, related to the energy of a single bond in the compound, based on the assumption that the surface segregation factor is the ratio between the energy gained by surface segregation and the thermal energy, assuming that $\gamma_i < \gamma_j$. This leads to a definition of the surface tension [49]:

$$\gamma = \frac{\gamma_i X_i^B}{X_i^B + X_j^B \exp\left(-\frac{(\gamma_j - \gamma_i)A_{S,i} - f_{se}(n+m)(X_i^B)^n(X_j^B)^m}{RT}\right)} \quad (2.37)$$

$$+ \frac{\gamma_i X_i^B}{X_j^B + X_i^B \exp\left(\frac{(\gamma_j - \gamma_i)A_{S,i} - f_{se}(n+m)(X_i^B)^n(X_j^B)^m}{RT}\right)}$$

2.4.5 Empirical models

An empirical model has been introduced by Allen [50]:

$$\gamma_L = 3.6T_L \left(\frac{M}{\rho_L}\right)^{-\frac{2}{3}} \quad (2.38)$$

The surface tension at the liquidus temperature, γ_L , is related to the molar mass, M , and the density, ρ_L , at the respective liquidus temperature, T_L . The Allen model has been modified by Kaptay [51] in which the so-called cohesive energy is linked to the surface free energy and the liquidus temperature and two empirical parameters α_K and β_K .

$$\gamma_L(N_A)^{\frac{1}{3}}V_i^{\frac{2}{3}} \cong \alpha_K T_L + \beta_K T_L^2 \quad (2.39)$$

With V_i and N_A already defined in section 2.4.2, and the parameters $\alpha_K = 41 \pm 10$ and $\beta_K = (3,3 \pm 0.7) \cdot 10^{-3}$.

By differentiation of Eq. (2.39) Kaptay [51] also gives an estimation for the temperature coefficient, γ_T [30]:

$$\gamma_T \cdot A_{S,i} \cong (0.182 \pm 0.026)C_p - (1.2 \pm 2.3) - \frac{2}{3}\beta\gamma_L \cdot A_{S,i} \quad (2.40)$$

Here, C_p denotes the molar heat capacity and β the thermal volume expansion coefficient [30].

The experimental method used in this work for the surface tension measurement and the corresponding results are presented in the sections 3.8 and 5.5, respectively.

2.5 Shear viscosity

Shear viscosity is an important parameter in rheology used to describe the dynamic of fluids on a macroscopic scale. Commonly, it is associated with the ‘thicknesses of a liquid. It provides a measure for the internal friction of a fluid as the resistance of a liquid against shear flow [52, 53].

For the definition of the viscosity, a small volume of a liquid is considered, confined between two parallel plates with areas, A . If, as illustrated in Figure 2.5, one plate is sheared with force, F_x , in direction x , the plate moves in the same direction with a velocity, v_x . In the perpendicular direction, y , a velocity gradient, $\nabla_y v_x$, results from the inner friction of the liquid, proportional to the stress, $\sigma_{x,y}$. The coefficient, η , relating both parameters describes the shear viscosity [30]:

$$\sigma_{x,y} = \nabla_y v_x \cdot \eta \quad (2.41)$$

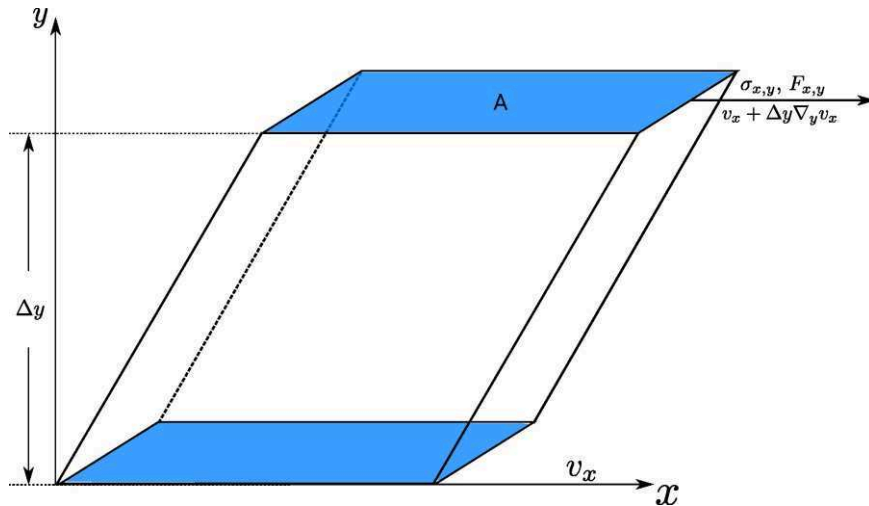


Figure 2.5: Schematic setup of a sheared liquid volume confined between two parallel plates with areas, A , with shear force, F_x , in direction x . Applying a shear stress, $\sigma_{x,y}$, in direction x induces a gradient, $\nabla_y v_x$, in the perpendicular direction, y . Based on Fig. 5.1 by Brillo [30].

2.5.1 Temperature dependencies

There are numerous and partly non-compliant approaches to relate the viscosity to temperature. Among the most frequently used ones are the Vogel-Fulcher-Tammann law

(VFT) for glass-forming systems and the Arrhenius law, used in this work. Using the Arrhenius law, the viscosity, η , can be expressed as a function of temperature, T , by a pre-exponential factor, η_∞ , the activation energy, E_A , and the molar gas constant, R , as following:

$$\eta(T) = \eta_\infty \exp\left(\frac{E_A}{RT}\right) \quad (2.42)$$

The Arrhenius law offers the advantage that a straight line is obtained if $\ln(\eta)$ is plotted against $1/T$ with a slope E_A/R . The pre-exponential factor, η_∞ , corresponds to an asymptotic viscosity for $\eta \rightarrow \infty$.

2.5.2 Composition dependencies

There are numerous models predicting the viscosity as a function of the alloy composition, e.g., relating it to the enthalpy of mixing, ΔH_{mix} , or the excess free energy, ${}^E G$ [54]. In this chapter, the models used in section 5.4 to predict the composition dependencies of viscosity in the binary Al-Ti system are introduced, counting models by Hirai [55], Kozlov/Romanov/Petrov [56] (in the following abbreviated Kozlov model) and Kaptay [57]. The Brillo/Schick model [30, 58] is not used in this work due to lack of available input data for the activation energy, E_A , and the pre-exponential factor, $\eta_{\infty,i}$, of the pure element Ti.

The semi-empirical model by Hirai [55] was originally derived to predict the viscosity of pure elements but has also been used in the case of alloys [30]. Here, the viscosity is defined by the liquidus temperature T_L , the molar mass, M , the density, ρ and the universal gas constant, $R = 8.314 \text{ JK}^{-1}\text{mol}^{-1}$.

$$\eta = 1.7 \cdot 10^{-7} \frac{\rho^{\frac{2}{3}} T_L^{\frac{1}{2}}}{M^{\frac{1}{6}}} \exp\left(\frac{2.65 T_L^{1.27}}{R} \cdot \left(\frac{1}{T} - \frac{1}{T_L}\right)\right) \quad (2.43)$$

The Kozlov model [56] is derived entirely from physical principles, giving a relation between the viscosity and the enthalpy of mixing, ΔH_{mix} , the mole fraction, $X_{i,j}$, and the viscosities, $\eta_{i,j}$, of the pure elements, i and j , as atomic vibration frequencies:

$$\ln(\eta) = X_i \ln(\eta_i) + X_j \ln(\eta_j) - \frac{\Delta H_{\text{mix}}}{3RT} \quad (2.44)$$

Kaptay [57] modified an approach by Seetharaman [30, 59] that used the activation energy, E_A , the excess free energy, ${}^E G$, and the molar volume, V , by adding a semi-

empirical parameter, $b = 0.155$, estimated from properties of pure metals and relating it to the enthalpy of mixing, ΔH_{mix} .

$$\eta = \frac{hN_A}{V} \exp\left(\frac{\sum_i^3 X_i G_i^* + b \cdot \Delta H_{\text{mix}}}{RT}\right) \quad (2.45)$$

Here, $h = 6.626 \cdot 10^{34}$ Js denotes the Planck's constant and $N_A = 6.023 \cdot 10^{23} \text{ mol}^{-1}$ the Avogadro number. The Gibbs energy of activation, G_i^* , for the viscous flow of the pure component i , is expressed by the molar volume, V_i , of the pure component i as

$$G_i^* = RT \ln\left(\frac{\eta_i V_i}{hN_A}\right) \quad (2.46)$$

The experimental methods for the viscosity measurement are introduced in section 3.9 and the corresponding results discussed in section 5.4.

2.6 Oxygen partial pressure

Oxygen is one of the most prominent surface-reactive elements in liquid metals, and it can drastically affect the thermophysical properties of melts. The effect can be especially pronounced with regards to the surface tension of metallic melts. Generally, it can be said that the interactions between the liquid metal interface and the oxygen molecules in the gas phase are very complex, which has been extensively described by Gasser [60]. As a first step, collisions of the gas molecules with the melt surface occur. Depending on the amount of energy lost, the gas molecule may still be able to leave the liquid interface with a lower velocity or be trapped and adsorbed on the surface. In the case of liquid surface adsorption, so-called chemisorption takes place, signified by a chemical bond between the gas molecule (adsorbate) and the metal surface (adsorbent) with an exchange of electrons. A typical value for the enthalpy of chemisorption amounts to about -400 kJ mol^{-1} [60]. In the following liquid and solid oxides may be formed between the adsorbate and adsorbent [60]. On the other hand, evaporation could set in, directly from the chemisorbed stage or with physisorption as a transitional state [60]. Which of these processes occur generally depends on the temperature and the oxygen concentration in the ambient gas, as will be discussed in the following sections 2.6.1 and 2.6.2. Additionally, the oxide on the surface and the bulk are in exchange, and the oxide may dissolve depending on the respective solubility limit of oxygen.

Figure 2.6 shows a metal in different states [61]. Figure 2.6 a) shows a metal with a 'clean' surface with no adsorbates or oxides which can only be achieved by very low ambient oxygen concentrations or high temperature, with metal-specific values. Figure 2.6 b)

displays an adsorption state, where individual oxygen molecules are adsorbed on the surface of the metal. In Figure 2.6 c) adsorbed oxygen molecules and formed oxides are exhibited on the metal's surface. Finally, Figure 2.6 d) indicates an oxidized state with a continuous oxide film covering the surface [25, 61].

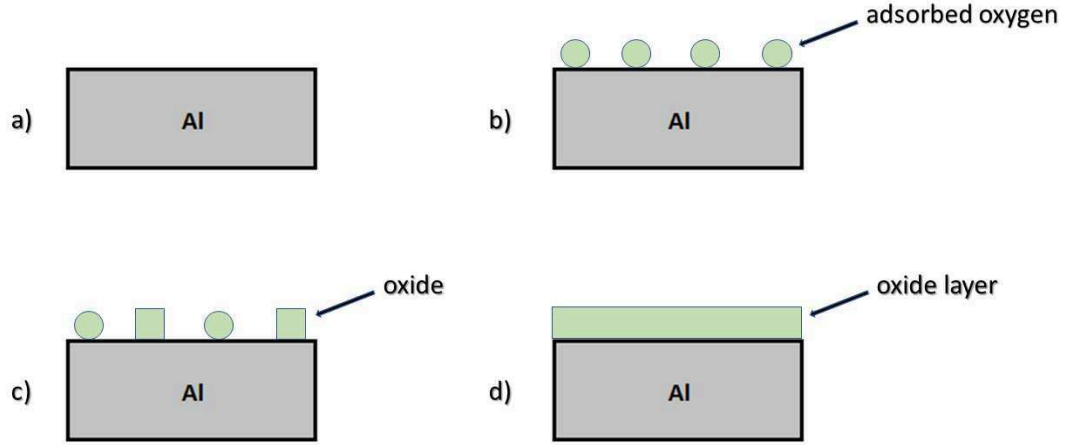


Figure 2.6: Metal's surface, as an example Al, with different states of oxygen adsorption and oxide cover: a) 'clean' surface b) individual oxygen molecules adsorbent c) oxygen molecules and formed oxides d) oxidized state with a continuous oxide film.

In the following respective sections 2.6.1 and 2.6.2, the adsorption of oxygen on the surface of a liquid metal and the formation of newly formed molecule species as oxides are described in more detail. The process of evaporation and the results obtained in this work will be discussed in section 5.6.

2.6.1 Adsorption of oxygen

Oxygen partial pressure or oxygen fugacity is a measure for the effective concentration of oxygen in the gas phase. To describe the influence of the oxygen partial pressure in the sample surrounding atmosphere on the adsorption of oxygen, different approaches have been made. Based on the *Gibbs-Duhem relation for surfaces* in Eq. (2.22), the *Gibbs isotherm* can be derived for constant temperature and pressure [30, 39]:

$$d\gamma + \sum_i^N \Gamma_i d\mu_i = 0 \quad (2.47)$$

Where $\Gamma_i = \Delta X_i^s / A$ (mol/cm²), describes the adsorption of component i , which can be interpreted as an excess surface density. In Eq. (2.47), μ_i stands for the chemical potential of a solution i , as a function of the chemical potential of the standard (bulk) state, μ_i^0 , the molar gas constant, R , the temperature, T , and the activity, α_i :

$$\mu_i = \mu_i^0 + RT \ln(\alpha_i) \quad (2.48)$$

Another isotherm, the *Langmuir isotherm*, is based on the assumption that the energy of adsorption of a species is independent of the atomic arrangement and coverage of this species on the surface. For a unary adsorbate system, constant temperature and single site occupancy, it can be denoted as [62]:

$$\frac{\theta_i}{1 - \theta_i} = K_{ad}\alpha_i \quad (2.49)$$

In this equation, θ_i symbolizes the fractional coverage of the adsorbate, i , with $\theta_i = \Gamma_i/\Gamma_i^0$, where Γ_i^0 is the saturated surface excess concentration of the surface-active component, i , for an adsorption at full coverage. The equilibrium constant of the oxygen adsorption is denoted by K_{ad} . The equivalent to the oxygen partial pressure (gas phase), is given in the liquid phase by the activity, α . Based on the Eqs. (2.47), (2.48) and (2.49) the Gibbs adsorption isotherm can be rewritten as [30, 41, 62]:

$$\frac{d\gamma}{d\ln(\alpha_i)} = - \sum_i^N RT\Gamma_i = - \sum_i^N RT\theta_i\Gamma_i^0 = - \sum_i^N RT\theta_i \frac{K_{ad}\alpha_i}{1 + K_{ad}\alpha_i} \quad (2.50)$$

On integration upon one integration limit as the pure adsorbent, the following, so-called Belton/Szyszkowski equation, for the surface tension of a liquid metal adsorbent, the influence of the oxygen adsorption on the surface tension can be derived from the surface tension of the pure adsorbent, γ^{pure} [62-64]:

$$\gamma = \gamma^{\text{pure}} - RT\Gamma_i^0 \ln(1 + K_{ad}\alpha_i) \quad (2.51)$$

In Eq. (2.51) the activity, α_i , of the surface-active component, i , is taken into account. To also include the adsorbate dissolution from the atmosphere into the melt in Eq. (2.51), the oxygen partial pressure, P_{O_2} , should be discussed, considering the oxygen molecules in the gas phase, $O_2(g)$, and the adsorbed oxygen in the melt, O_{ad} [23, 62].



The activity, α_i , can be expressed by the oxygen partial pressure, P_{O_2} :

$$\alpha_i = \sqrt{\frac{P_{O_2}(\text{Pa})}{P_{O_2}^0(\text{Pa})}} = \sqrt{P_{O_2}} \quad (2.53)$$

Where $P_{O_2}^0 = 10^{-5}(\text{Pa}) = 1 \text{ bar}$, is defined as the standard state of oxygen. Combining Eqs. (2.51) and (2.53) the following relation between the surface tension of a liquid metallic adsorbent and the oxygen adsorbate can be made under the condition that the oxygen partial pressure, $P_{O_2} \leq P_{O_2,\text{sat}}$, thus, lies below or equal to the saturated oxygen partial pressure, $P_{O_2,\text{sat}}$ [23]:

$$\gamma = \gamma^{\text{pure}} - RT\Gamma_i^0 \ln(1 + K_{\text{ad}}f_i P_{O_2}^{1/2}) \quad (2.54)$$

The activity coefficient, f_i , of oxygen in the liquid component, i , can be assumed to equal one for most metals, obeying *Henry's law*, for high oxygen solubilities [64]. Regarding the other parameters in Eq. (2.54), as described further in section 3.10, the surface tension, γ , can be measured as a function of the oxygen partial pressure, P_{O_2} . However the pure surface tension, γ^{pure} , the saturated surface excess concentration, Γ_i^0 , and the respective equilibrium constant, K_{ad} , may be given by literature or be unknown and thus, be evaluated as fit parameters (see section 5.6) [23].

2.6.2 Formation of oxides

New molecule species may be formed in the form of oxides either subsequent to the adsorption as liquids or solids on the liquid surface or in gaseous form inside the gas phase close to the interface. The oxides may undergo further processes such as further oxidation, condensation of gaseous oxides on the droplet's surface, evaporation from the surface to the gas phase and diffusion both in the liquid and in the gas phase. All these molecular events may influence the interface behavior and the thermophysical properties [65].

The formation of oxides can be predicted by thermodynamics, by calculating which products of a reaction are stable with regards to the temperature and the conditions in an equilibrium state. By these means, however, no prediction can be made concerning the speed needed for the respective reaction to take place [66].

A general oxidation reaction with A denoting the metal, B being the metal oxide and v_i being the stoichiometric coefficient of the respective component, i , can be given in the form of:



By the *law of mass action*, the equilibrium constant of the reaction, K , can be defined by the respective the activities, α_i , as:

$$K = \frac{\alpha_B^{v_B} \alpha_C^{v_C}}{\alpha_A^{v_A} P_{O_2}} \quad (2.56)$$

This equation yields the oxygen partial pressure, P_{O_2} . Activities of solid and pure liquid components can be approximated as one and, consequentially, be neglected in Eq. (2.56). The equilibrium constant can also be defined by the respective Gibbs free energy of formation, ΔG , the temperature, T , and the universal gas constant, R . In combination with Eq. (2.56) therefore, the oxygen partial pressure, P_{O_2} (bar), can, then be related as:

$$K = \exp\left(-\frac{\Delta G}{RT}\right) = \frac{1}{P_{O_2}} \quad (2.57)$$

Additionally, the equilibrium constant of the reaction can be calculated as the sum of the individual reactants' Gibbs energy of formation involved in the reaction:

$$\Delta G(T) = \sum_i v_i \Delta G_i(T) \quad (2.58)$$

With the Gibbs free energy of formation depending on the enthalpy of mixing, ΔH , the temperature, T , and the entropy of formation, ΔS , as $\Delta G = \Delta H - T\Delta S$, it can be derived that [66]:

$$\ln(P_{O_2}) = \frac{\Delta G}{RT} = \frac{\Delta H}{RT} - \frac{T\Delta S}{RT} \quad (2.59)$$

Plotting the values of ΔG against $1/T$ results in a straight line with ΔS being the slope and ΔH being the y-intercept, giving the so-called Ellingham-Richardson diagram as shown in Figure 2.7 [67]. The slope of the line changes when any of the materials involved experience a phase transition, e.g., melting or evaporation. Most metals are instable at high temperatures and oxides are formed from the reaction between a metal and oxygen above the corresponding critical oxygen partial pressure. Thus, the Gibbs free energy of formation is negative for most metal oxides [66, 68]. The scale on the right side of the diagram in Figure 2.7 denotes the oxygen partial pressure, P_{O_2} , and is used to determine the oxygen partial pressure in equilibrium with the metal and metal oxide at a given temperature. If the oxygen partial pressure is higher than the equilibrium value, the metal will be oxidized, if it is lower than the equilibrium value, the oxide will be reduced. The position of the line for a given reaction in the Ellingham diagram shows the stability of the oxide as a function of temperature [66]. The lower the position of the straight line in Figure 2.7, the more stable the oxide is and formed at lower oxygen partial pressures. As it can be seen among the most stable oxides, Al_2O_3 can be counted [68].

The experimental procedures related to an oxygen control and monitoring and the results obtained in this work will be discussed in the sections 3.10 and 5.6, respectively.

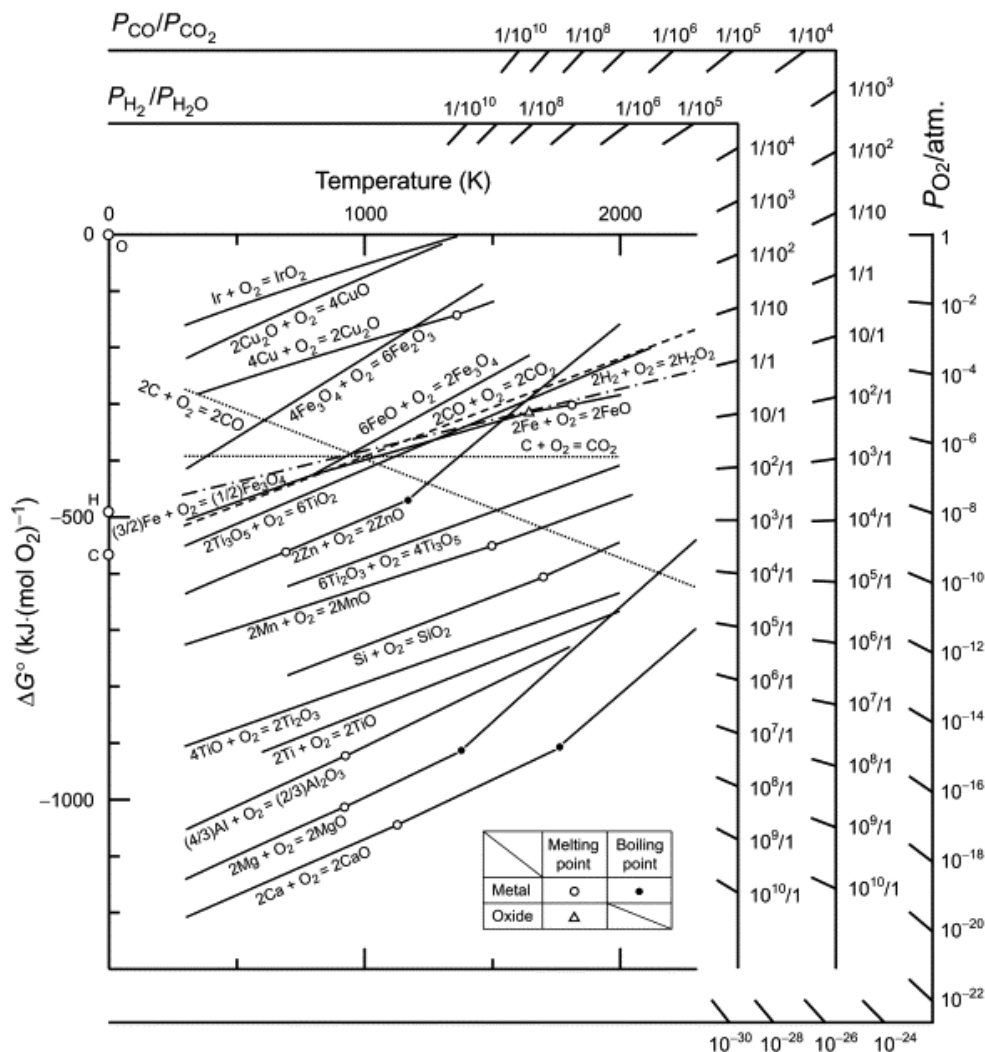


Figure 2.7: Ellingham diagram: Graph showing the temperature dependence of the stability of compounds generally used for the evaluation of the reduction of metal oxides and sulfides in dependence of the oxygen partial pressure. Taken from the work by Hasegawa [69] with Copyright granted by Springer Nature (License number 4264740668537).

2.7 Summary

In this chapter, the theoretical background concerning density and molar volume (section 2.1), normal spectral emissivity (section 2.2), heat capacity (section 2.3), surface tension (section 2.4), viscosity (section 2.5) and oxygen partial pressure (section 2.6) was established. In the subsequent chapter 3, the corresponding experimental method will be introduced.

3 Experimental methods

This chapter represents a conjunction chapter between the theoretical background introduced in chapter 2 and the experimental results presented in chapter 5. Its function is to create an understanding of how to measure and evaluate thermophysical properties of liquid metals.

In the following sections 3.1, 3.2, 3.3, 3.4, 3.5, 3.6, 3.6, 3.8, 3.9 and 3.10 the terms conventional techniques, electromagnetic levitation (EML), electromagnetic levitation in microgravity, optical dilatometry, static magnetic field, normal spectral emissivity measurement, non-contact modulated laser calorimetry, oscillating drop method, viscosity measurement and oxygen control and monitoring will be introduced, respectively.

3.1 Conventional techniques

Conventional techniques for the measurement of thermophysical properties of liquids are container-based which means that the liquid is in contact with a crucible, holder or substrate, as exemplarily described in section 1.2. Among those techniques, the bubble pressure method, the oscillating cup method and resistive pulse heating can be counted as acclaimed methods for the different property measurements. Another example is the sessile drop method, which can be used to evaluate the surface tension of a liquid droplet with regards to its contact angle on a substrate. In chapter 5, as part of a literature comparison with results of the present work, different techniques are listed for density, surface tension, emissivity and heat capacity measurements in the respective sections. A comprehensive overview of the methods has been given by Fukuyama and Waseda [22].

3.2 Electromagnetic levitation (EML)

Conventional techniques are based on contacts with containers and holders leading to disadvantages at high temperatures where the chemical reactivity of a melt may result in contamination with the container material. Especially, for materials with a high chemical reactivity, among them Al-Ti alloys, this can be very critical. For these materials, contact-free levitation techniques offer vast advantages. Among those advantages, the techniques make it possible to avoid heterogeneous nucleation on container walls and thus, undercool the melts far below their equilibrium melting temperature. Additionally, it allows access to high temperatures, broad temperature ranges, and processing of highly reactive

samples. There are many different levitation techniques, such as acoustic, aerodynamic, electrostatic (ESL), and electromagnetic levitation (EML), as shown in Figure 3.1. Each technique has its advantages and disadvantages making them preferable for different materials and applications. For electrically conducting samples, EML is a very suitable and easily applied technique compared to e.g., ESL, enabling a stable positioning of the material in a high-frequency magnetic field under inert gas atmosphere [4, 24, 43].

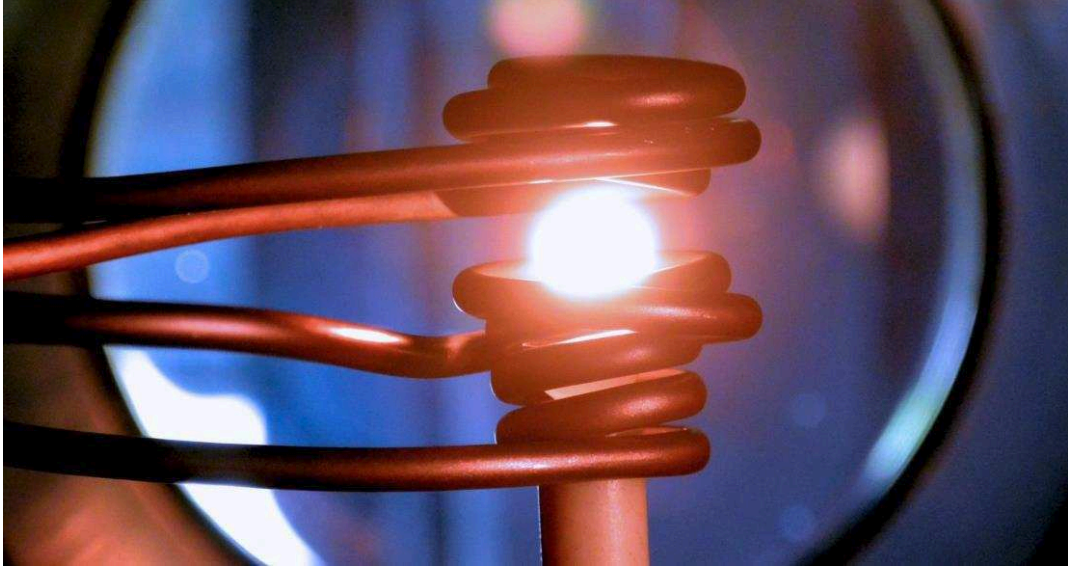


Figure 3.1: Photograph of an electromagnetically levitated liquid iron sample at a temperature of about 1873 K. Copyrights granted by C. Karrasch and taken from reference [70] Fig. 4.1.

3.2.1 Electromagnetic levitation technique

Electromagnetic levitation was first introduced by Westinghouse [71] who filed the technique for a patent in 1954. The EML principle is intrinsically stable and is based on the Lorentz force, \vec{F}_L , acting on an electrically conducting sample with a magnetic flux changing over time. A magnetic field, \vec{B} , is induced which is counter-directed to the primary field and the repulsive Lorentz force acts with $\vec{F}_L = \vec{\nabla}(\vec{m} \cdot \vec{B})$. Where \vec{m} describes the magnetic dipole moment induced in the sample [70, 72].

In more detail, the Lorentz force can also be expressed as a function of the magnetic permeability, μ_0 , the radius of an approximately spherical sample, R_d , a dimensionless quantity $q = R_d/\delta$, with $\delta = \sqrt{2\rho_e/\mu_0}$ being the skin depth of the field \vec{B} depending on the frequency, ω , an efficiency ratio, $Q(q)$ and the electrical resistivity, ρ_e [30, 73, 74]:

$$\vec{F}_L = -\frac{\nabla \vec{B}^2}{2\mu_0} \frac{4\pi}{3} R_d^3 Q(q) \quad (3.1)$$

In this equation the term $\frac{4\pi}{3}R_d^3$ equals the volume, V , of the sample and $Q(q)$ being defined as:

$$Q(q) = \frac{3}{4} \left(1 - \frac{3}{2q} \frac{\sinh(2q) - \sin(2q)}{\cosh(2q) - \cos(2q)} \right) \quad (3.2)$$

To steadily levitate the sample, the Lorentz force, \vec{F}_L , must equal the weight force, \vec{F}_G , of the sample, consequently:

$$\vec{F}_L = \vec{F}_G = g\rho V \quad (3.3)$$

Where g denotes the gravitational acceleration, V the sample's volume and ρ its density. From Eqs. (3.1) and (3.3) the following equation for a spherical sample can be derived.

$$\rho g = -\frac{\nabla \vec{B}^2}{2\mu_0} Q(q) \quad (3.4)$$

From Eq. (3.4) it becomes obvious that the density of the sample plays an important role in the levitation process. Here, small densities mean that only a small force has to act on the sample to levitate it [30, 73].

Different from other levitation techniques, such as ESL, for EML the positioning and inductive heating are not generally decoupled. This is due to the fact that the oscillating field induces eddy currents in the sample and for finite electrical conductivity the heating power, P_H , is absorbed through ohmic losses. Hence, P_H can be expressed as [30]:

$$P_H = \frac{\vec{B}^2 \omega}{2\mu_0} V H(q) \quad (3.5)$$

In this case, $H(q)$ expresses the efficiency ratio of the absorption of power [73]:

$$H(q) = \frac{9}{4q^2} \left(q \frac{3}{2q} \frac{\sinh(2q) + \sin(2q)}{\cosh(2q) - \cos(2q)} - 1 \right) \quad (3.6)$$

Therefore, in Eq. (3.5) P_H and the heating of the sample depend on the power density $\vec{B}^2 \omega / (2\mu_0)$ and the volume of the sample, V . For a perfect insulator, $q = 0$, consequentially Q and H equal zero and neither positioning nor heating takes place, respectively [30, 74].

3.2.2 Experimental setup

Figure 3.2 shows a schematic illustration of an electromagnetic levitation setup, which is explained in detail in reference [72]. The EML setups at the DLR-MP and the Fukuyama lab, consist of an inside vacuum chamber which can be evacuated by a rotary pump in

combination with a high molecular pump. At the Fukuyama lab, prior to evacuating to very low pressures, a cleaning phase precedes, comprising three times of purging with inert gases and subsequent evacuating down to about 10^{-2} mbar. In the following, the chamber is evacuated over 2-24 hours down to pressures of 10^{-7} mbar (DLR-MP facility) and 10^{-4} mbar (Fukuyama lab) to remove impurities, e.g., adsorbed water, oxygen, and CO.

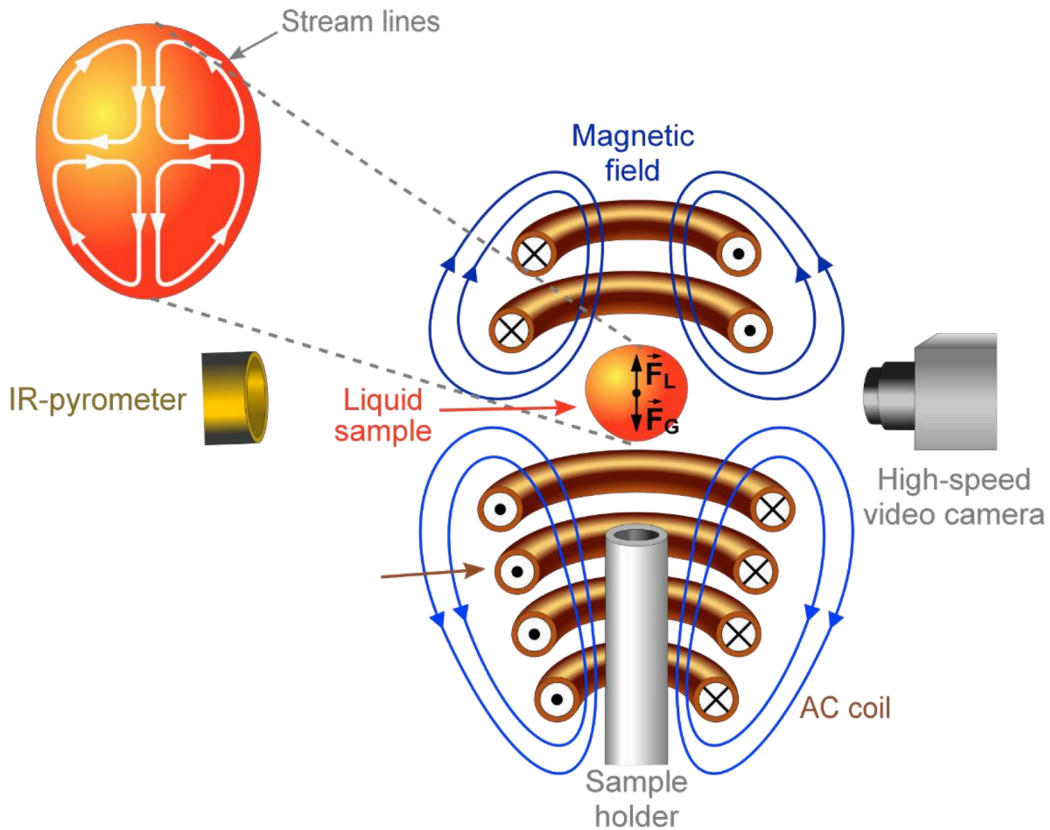


Figure 3.2: Schematic view of an electromagnetic levitation setup. The sample is processed under an inert gas atmosphere in a vacuum chamber and positioned in the minimum of an electromagnetic field produced by high-frequency alternating currents (ac) flowing through a water-cooled copper coil. Copyrights granted by C. Karrasch and taken from reference [70], Fig. 4.2.

Afterwards, the chamber is backfilled with high-purity inert gases. At the DLR-MP facility pure and mixtures of He and Ar gases are used with a purity of 99.9999 vol.-% [30]. At the Fukuyama lab also buffer gas mixtures containing Ar-5% H_2 gas are used to reduce oxide traces (explained more detailed in section 3.10.4) [28]. For each experiment, the sample is placed on the ceramic sample holder, positioned in the centre of the water-cooled induction coil (Figure 3.2). The induction coils consist of two parts. The upper part is a solenoid coil with two turns for stabilization of the sample, and the lower part is a tapered coil with five to six turns for lifting the sample [15]. Typically, the alloy samples have diameters of 3-10 mm and masses of approximately 0.5-1 g [7]. The alternating magnetic levitation field is produced by an alternating current (ac), I (≈ 300 -500 A) at

high frequencies (150-450 kHz) through the coil with a generated power of 5-10 kW [70]. The sample is repelled by the magnetic field and positioned in its potential minimum. Due to the cylindrical symmetry of the coil, the sample's geometry deviates from that of a perfect sphere, which has been described in references [75, 76]. Originating from an initially spherical sample shape, the forces acting on the levitated sample are high in the middle part and relatively low in the top and bottom part, the resulting shapes are flat at the top and elongated at the bottom. Since the electromagnetic force field enters the levitated specimen up to the skin depth, fluid flow occurs in the liquid state, which may be turbulent and needs to be taken into account. The effect may be homogenizing, e.g., concerning the temperature profile of the sample. On the other hand, it may also lead to disturbances, such as strong sample rotations [30, 77].

For emissivity and heat capacity measurements at the Fukuyama lab, a direct current (dc) magnetic field of 3-5 T, using a superconducting magnet was additionally imposed to suppress the fluid flow and the resulting surface oscillations and translations, as described in more detail in the sections 3.5, 3.6 and 3.7 [22].

3.2.3 Temperature control

Depending on the material and the available power, the samples can reach temperatures far above their melting point, restricted by evaporation. Overheating may be applied to get rid of pollutions and potential volatile oxide layers. Since, for EML, the positioning and heating are not generally decoupled, additional temperature control is provided by an adjustable cooling flow of inert gas, admitted to the samples via the sample holder which functions also as a nozzle [7].

After the completion of the melting process for all temperature dependent measurements (density, surface tension, emissivity and heat capacity), first, an initial temperature was set and afterwards step-wise decreased by increasing the gas cooling flow. Each measurement was then carried out at a certain temperature with a deviation to the previous temperature of about 5-20 K. For all measurements that were not dependent on the temperature, e.g., dependent on time or the oxygen partial pressure, as described in sections 3.8 and 3.10, respectively, the temperature was kept as stable as possible with respect to temperature fluctuations.

The sample temperature, T , is measured using an infrared pyrometer with a sampling rate of 100 Hz directed towards the specimen from the side. The pyrometer measures the radiation intensity from the sample using Wien's law to relate it to the sample's temperature, T . The accuracy of the pyrometer is approximately ± 3 K [7, 70]. As the spectral sample's emissivity is generally not known, the pyrometer signal, T_p , needs to be recalibrated with respect to the known liquidus temperature, T_L , and the apparent liquidus

pyrometer temperature, $T_{L,P}$. The apparent pyrometer liquidus temperature is identified during the measurement by an increase in the slope of $T_{L,P}$, as shown in Figure 3.3, which appears, when the melting process is completed, and the sample reaches its liquidus temperature, T_L [28]. The recalibration of T can be obtained using the following relation derived from Wien's law [78]:

$$\frac{1}{T} - \frac{1}{T_P} = \frac{1}{T_L} - \frac{1}{T_{L,P}} \quad (3.7)$$

Provided that the sample's emissivity at the operating wavelength remains constant over the investigated temperature interval, Eq. (3.7) gives a good approximation for the temperature of metallic melts [79]. For the pure elements and alloys, the values for the liquidus temperature, T_L , are shown, e.g., in Table 1 and Table 3 and taken from reference [34], [80], using the CALPHAD approach to evaluate thermodynamic data [28]. The data and the used model are taking recent experimental results into account [80]. Furthermore, the data have been used in the previous work by Wessing et al. [28]. The phase diagram of the binary system of Al-Ti is shown in Figure 4.1, respectively [28].

As an example, Figure 3.3 shows a typical temperature profile of a levitated sample during the cooling and solidification phase. As a first step, the electromagnetically levitated sample is heated up above its respective liquidus temperature by about 50-100 K to melt the sample. Additionally, this strategy enables further purification of the sample if volatile impurities, such as oxides are present on the sample's surface. In the following, the temperature is reduced step-wise using He gas flow admitted to the sample's surface. At each temperature step, the properties of the liquid phase are investigated, such as density and emissivity as explained in sections 3.4 and 3.6, respectively. Also, measurements at temperatures below the liquidus temperature in the undercooled region are carried out which is indicated in Figure 3.3. During the recalescence process, latent heat is released when the sample solidifies which is marked by a temperature increase up to the liquidus temperature which also signifies the end of each measurement.

At the Fukuyama lab, the setup also comprises a fiber-coupling type CW laser diode with a heating laser wavelength of 940 ± 3 nm, connected to a glass fiber holder. Preheating the sample by laser irradiation may be necessary to overcome critical instabilities at lower temperatures before inducing the electromagnetic field. Additional heating during the measurement may be needed if the provided field is not strong enough to reach the aimed temperature [22, 36].

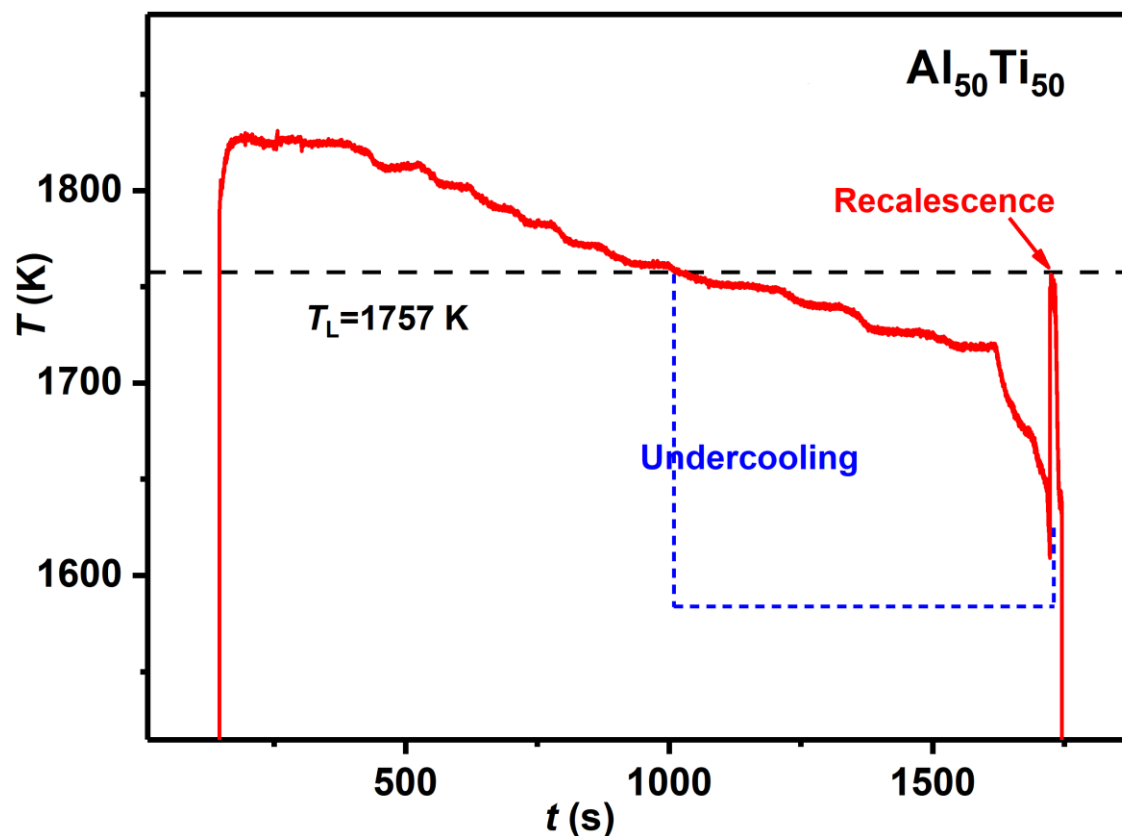


Figure 3.3: Temperature profile of a $\text{Al}_{50}\text{Ti}_{50}$ sample during levitation, including an undercooled region and the solidification (marked by the recalescence).

Electromagnetic levitation is the basis for all measurement techniques used in this work and will be discussed in more detail in the respective sections of this chapter with respect to the properties investigated.

3.3 Electromagnetic levitation in microgravity (TEMPUS)

Electromagnetic levitation under microgravity conditions allows measuring high-temperature surface tension and viscosity of melts, as described in the respective sections 3.8 and 3.9. The experimental setup in the μg -EML TEMPUS facility, as shown in Figure 3.4, is similar to the DLR-MP 1g-EML facilities. The main difference is that for experiments performed under microgravity conditions the positioning and heating can be decoupled. Thus, the weak quadrupole positioning field and the strong dipole heating field with frequencies of 150 kHz and 400 kHz, respectively, can be superpositioned or operated autonomously. Therefore, the electromagnetic field under microgravity conditions is about 100-1000 times weaker with respect to terrestrial conditions [81]. As a consequence, fluid flow can be reduced significantly and, potentially resulting disturbances are minimized [70].

The company NOVESPACE performs the parabolic flight campaigns in Bordeaux, France. To create microgravity conditions of about $10^{-3} g$, a specially converted aircraft flies parabolic maneuvers which are shown schematically in Figure 3.4. Initially, the airplane ascends on a parabolic trajectory with an angle up to 47° creating hyper-gravity conditions. At the injection point the aircraft transitions to a free-falling phase while establishing reduced gravity conditions for 22 seconds at each parabola. Eventually, at the recovery point, the pilots pull up the airplane's nose until a steady flight is regained after a secondary hyper-gravity phase of 20 seconds.

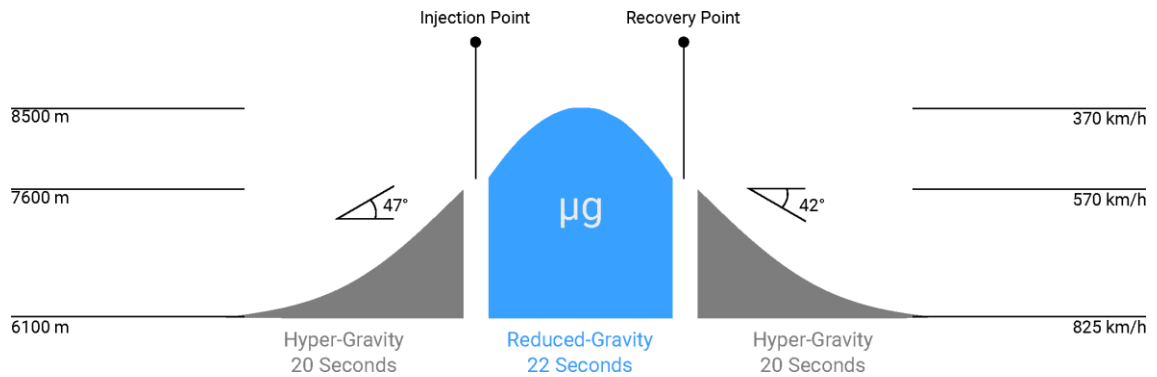


Figure 3.4: Schematic illustration of a parabolic flight maneuver.

In the TEMPUS facility, samples are processed in a specimen changing cup facility to not lose any samples in between parabolas. Analogously to the DLR-MP EML, the temperature is monitored with a single-color pyrometer, and the sample is monitored by cameras to record images for the analysis, using the in-house software TeVi [53].

Since 2014 an equivalent μg -EML is also installed on the *International Space Station* (ISS) when ESA astronaut Alexander Gerst implemented the setup during his first mission (Figure 3.5).



Figure 3.5: Left-hand side μg -EML TEMPUS facility and operators. Right-hand side Alexander Gerst is working on the μg -EML on the ISS. The picture is taken from reference [82] with copyrights granted by DLR/ESA.

3.4 Optical dilatometry

The optical dilatometry method, as described and further developed by Brillo et al. [72, 73, 83, 84], is used to study density, molar volume, and thermal expansion by measuring its volume. Although optical dilatometry can be combined with different levitation techniques, the following description of the procedure is the one used at the DLR-MP facilities in combination with EML experiments [30, 83]. The setup of the corresponding optical system is shown schematically in Figure 3.6.

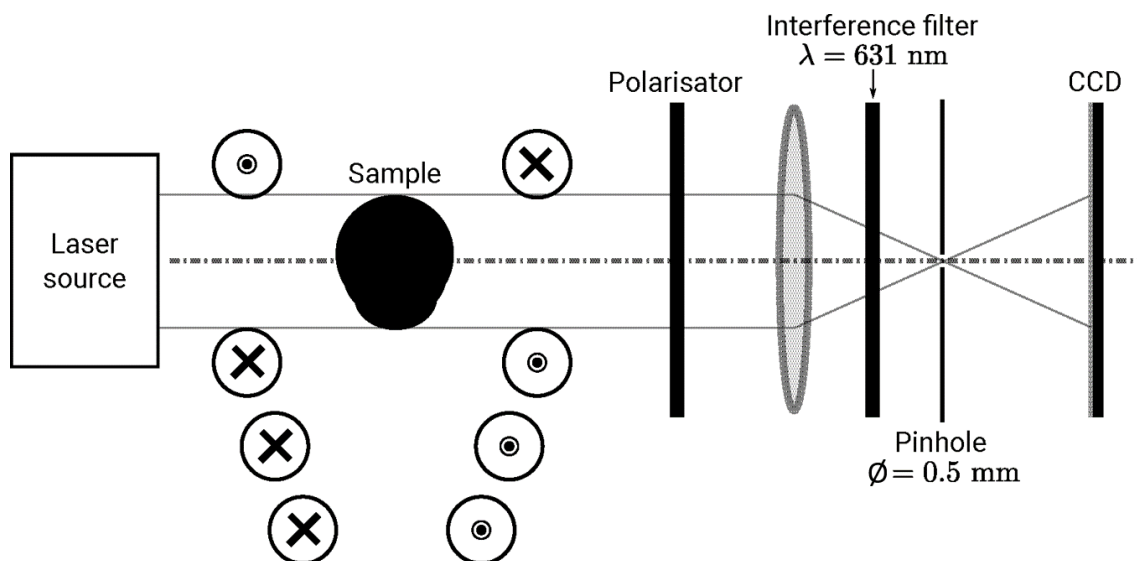


Figure 3.6: Schematic diagram of the optical setup used for the optical dilatometry method. Picture based on Fig. 2.6 by Brillo [30].

In this setup, a polarized laser beam is produced by a He/Ne-laser. A collimator redirects the laser beam so that a parallel beam of 25 mm diameter is produced which illuminates the sample from the rear. A polarization filter facilitates a variation of the light intensity [30]. Due to scattering and diffractions in the chamber, the laser beam is deflected, and non-parallel components may lead to interference, diffraction and noise patterns [30, 83]. To remove those error patterns an optical Fourier filter is attached, consisting of a lens (80 mm focal length) and a pinhole ($\varnothing = 0.5 \text{ mm}$). The interference filter together with the pinhole additionally removes contributions from the thermal radiation of the sample. This setup enables to obtain a sharp shadowgraph image on a uniform background with a contrast independently of the brightness of the sample [30, 83].

Figure 3.7 shows the laser beam directed from the left-hand side onto the sample creating lateral shadow images recorded by a digital charge-coupled device (CCD). The obtained shadowgraph images are analysed by an edge detection algorithm that determines the radius, R_d , in dependence to the drop centre (x_0, y_0) and the azimuthal angle φ [7, 30].

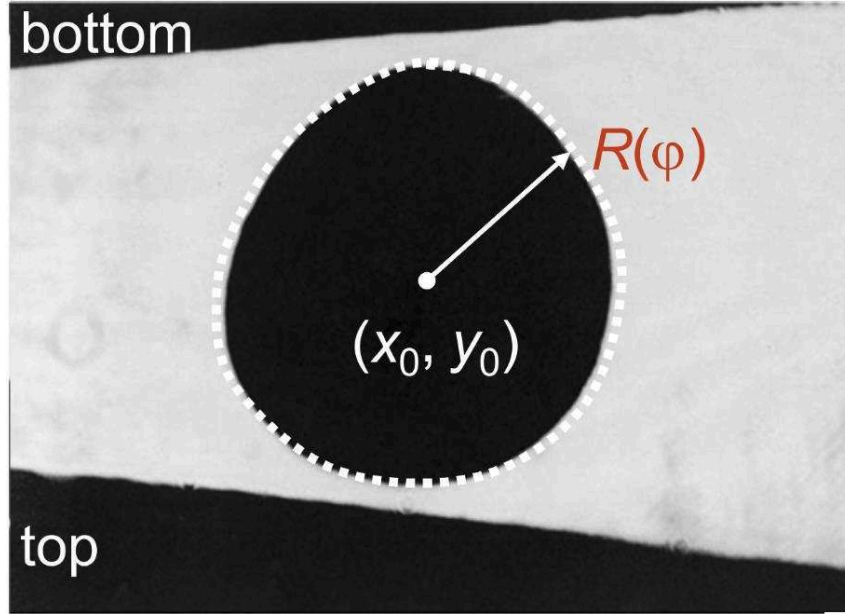


Figure 3.7: Shadowgraph image of an electromagnetically levitated sample displayed upside down due to the arrangement of the focusing lens. The sample's edge curve is marked, and the black regions at the top and bottom represent the shadows of the windings of the coil. The picture is taken from reference [30], Fig. 2.7 with copyrights by Walter de Gruyter GmbH & Co KG.

For the evaluation and to eliminate the influence of surface oscillations the obtained curve, $R_d(\varphi)$, is averaged over 1000 frames. Subsequently, a Legendre polynomials of order ≤ 6 , is fitted [7, 30, 83]:

$$\langle R_d(\varphi) \rangle = \sum_{l=0}^6 a_l P_l(\cos(\varphi)) \quad (3.8)$$

In Eq. (3.8), the brackets $\langle \dots \rangle$ denote averaging over time, P_l the l -th Legendre polynomial, and a_l are coefficients determined by the fit. Under the premise of the droplet's axial symmetry in mechanical equilibrium [84] the volume is calculated as following [7, 30]:

$$V_P = \frac{2}{3} \pi \int_0^\pi \langle R_d(\varphi) \rangle^3 \sin(\varphi) d\varphi \quad (3.9)$$

Here, V_P is the volume in pixel³ units with the real droplet volume, ${}^{\text{drop}}V$, being related to the pixel volume, V_P , by a scaling factor, q , with ${}^{\text{drop}}V = qV_P$. The scaling factor, q , can be obtained by a calibration procedure described in Ref. [83] using differently sized ball bearings. Finally, the density is calculated with respect to the sample mass, M , by $\rho = M/{}^{\text{drop}}V$.

Concerning the accuracy of the optical dilatometry method, it is necessary to consider the error sources. Among the sources of strong sample movements, mass loss due to

evaporation, errors in the temperature reading, and uncertainties in the calibration can be counted which are also inter-dependable [83]. The effect of mass loss can be severe because mass and density are directly proportional to each other and additionally, the mass loss might lead to changes in the chemical composition and thus, in density. To discard the effect of mass loss, measurements with critical mass loss have been neglected, as described in chapter 4. Strong sample movements might lead to a break of axial symmetry which is the pre-condition for Eq. (3.9). To eliminate a consequential error contribution, a critical form factor as a measure for the distortion of a sample in each measurement has been evaluated. Following the above-described procedure and provided that the error contributions mentioned are avoided, the obtained results are accurate within $\Delta\rho/\rho \leq \pm 1.0\%$ and $\Delta V/V \leq \pm 1.0\%$ for the density and molar volume, respectively, as derived in the *Appendix*.

Based on these experimental methods the density has been measured with the corresponding results presented in section 5.1.

3.5 Static magnetic field

For the measurements at the Fukuyama lab of the normal spectral emissivity, heat capacity and surface tension, analogously to the density investigations, electromagnetic levitation (EML) was used for the measurements. Moreover, melt convections such as buoyancy, magneto-hydrodynamic (MHD) and Marangoni convection induced by non-uniform temperature distributions and observed in electromagnetically levitated samples must be taken into account as they may significantly influence the caloric measurement results [16]. Kobatake and Fukuyama et al. developed a technique combining EML with non-contact modulated laser calorimetry with the use of a static magnetic field to suppress transitional motions, surface oscillations, and melt convection in the materials [19, 22, 85]. As can be seen in Figure 3.8, the setup comprises a coil that is fixed in the center of a superconducting magnet with a 220 mm bore (6T220-CSM; SHI, Japan). The superconducting magnet induces a dc magnetic field opposed to the convection in the liquid melt, thus suppressing surface oscillation and translational motions. Up to 5 T static magnetic field can be applied at the Fukuyama lab [19, 36].

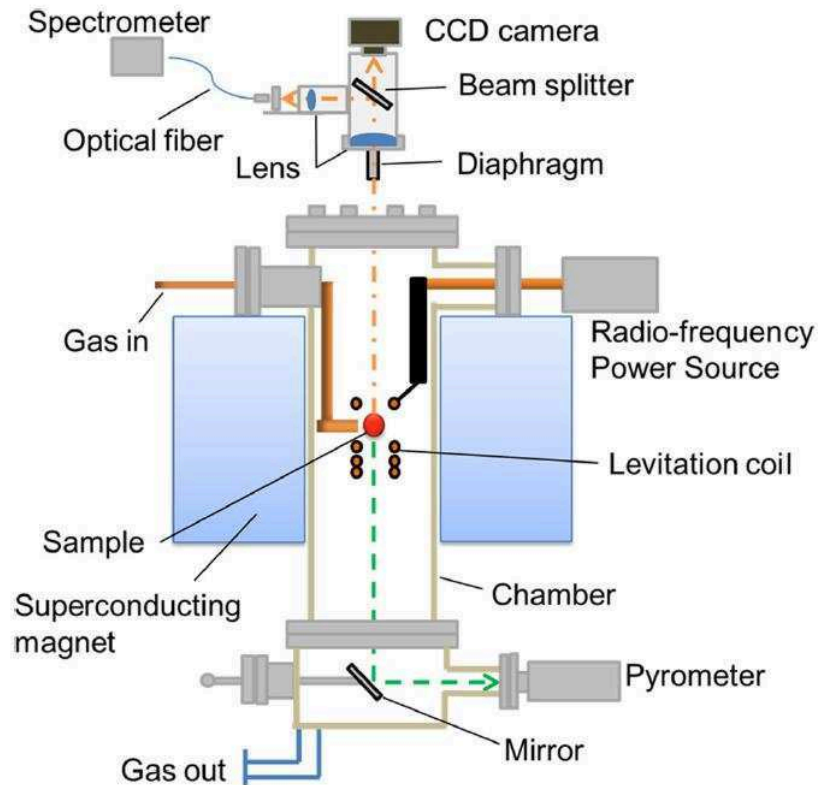


Figure 3.8: Schematic illustration of the experimental facility at the Fukuyama lab. The figure is taken from reference [86], Fig. 1 by Watanabe et al. with Copyrights granted by Springer Nature with the licence number 4265020121885.

3.6 Normal spectral emissivity measurement

As Kobatake et al. [15] have described in detail, the normal spectral emissivity can be obtained by directly measuring the radiance emitted from a molten droplet as a function of the wavelength and temperature using a spectrometer. For the radiance measurements, a multichannel spectrometer (USB2000; Ocean Optics Inc., FL) is used with a grating monochromator that provides a wavelength range of 530-1100 nm [15, 36]. The optical resolution lies within 4.0 nm. The optical system comprises a window, a collective lens, and a beam splitter. A carbon diaphragm of 2 mm diameter and 50 mm length is positioned 750 mm above a quasi-blackbody and is connected to the spectrometer through a glass fiber. For the temperature measurements, a single-color-optical pyrometer of 1350 nm wavelength with 1100-1500 nm bandwidths is used [15, 85].

3.6.1 Calibration of the spectrometer

The spectrometer can be calibrated with a quasi-blackbody using the relation between its spectral radiance and the corresponding output intensity of the pyrometer as given by Eq. (2.14). A schematic illustration of the quasi-blackbody made of graphite is shown in

Figure 3.9. The emissivity of graphite is higher than 0.9 and through the aspect ratio of the cavities an emissivity higher than 0.998 is provided [15, 28]. As can be seen in the figure there is one cavity at the top, used for the calibration of the spectrometer, and one at the bottom, used for the pyrometer, both of 5 mm width and 35 mm depths. Each cavity is surrounded by a copper metal bath to achieve a homogeneous temperature distribution and additionally enabling calibration of the pyrometer using a kink in the temperature signal during the melting process (see section 3.2.3). The quasi-blackbody is supported by a quartz glass tube of 10 mm diameter positioned in the center of a levitation coil and inductively heated [15, 22, 88]. Different to the actual levitation measurements a symmetric solenoidal coil was used to provide uniform heating of the quasi-blackbody [15].

3.6.2 Experimental setup

The experimental setup for the measurement, as can be seen in Figure 3.8, complies with the one of the calibration, but instead of the quasi-blackbody, a metallic sample is positioned in the center of the levitation coil. For emissivity measurements, EML is combined with a static magnetic field, as described in section 3.5, to suppress the translational and oscillation motions of the metallic droplet. As reported by Kobatake et al. [15], the static magnetic field of 1.5-3 T used for the measurements does not influence the measured values of the emissivity. In contrast, it is an effective means as it reduces the standard deviation of the temperature which is a sensitive factor for the emissivity measurements. Analogously to the temperature dependent density measurements, each measurement is carried out at a certain temperature (compare sections 3.2 and 3.4) [15, 36].

The uncertainty of the normal spectral emissivity, $\Delta\varepsilon$, is mainly caused by the uncertainties of the radiance, the wavelengths of the spectrometer and the temperature measurement, as discussed in detail in the *Appendix*.

The corresponding results for the emissivity measurements and experimental errors are presented in section 5.2.

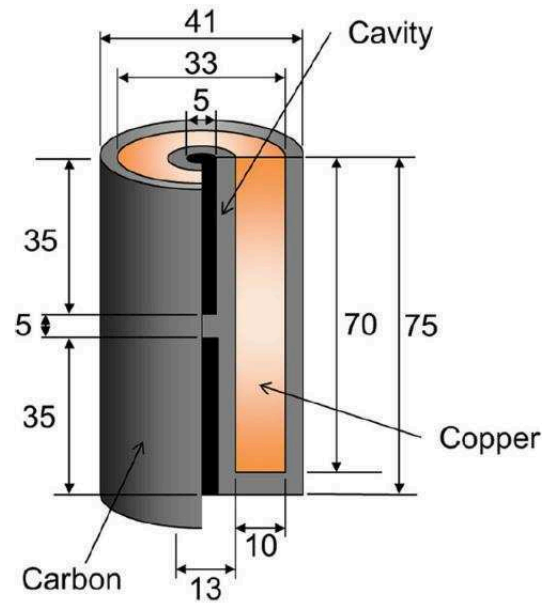


Figure 3.9: Schematic illustration of a quasi-blackbody. The figure is taken from reference [86] Fig. 2, by Watanabe et al. with Copyrights granted by Springer Nature with the licence number 4265020121885.

3.7 Non-contact modulated laser calorimetry

Fukuyama et al. [16] have described in detail how the heat capacity can be obtained using non-contact modulated laser calorimetry. The measurements have been carried out at the Fukuyama lab with means of EML (see section 3.2) in combination with a static magnetic field (section 3.5) with the same experimental setup as for the emissivity measurements (see section 3.6). For further experimental details, please refer to the corresponding chapters. A simplified heat flow model of non-contact modulation calorimetry in the present study is presented in Figure 3.10 [19, 22] resembling a model developed by Wunderlich and Fecht [87], illustrating the correlations between heat flow parameters as presented by the following equations.

The surface of the sample droplet's top is sinusoidally heated with an angular frequency, ω (rad s^{-1}), by a modulated laser (compare section 3.6.2 for the laser model and corresponding wavelength) with a laser power of $P_0(1 + \cos(\omega t))$ (Wm^{-2}) per unit area [18]. The temperature response is measured at the bottom of the droplet by a pyrometer. The modulation laser light is invisible to the pyrometer. The heat balances in this system include a laser-irradiated part and a laser non-irradiated part, as schematically illustrated in Figure 3.10 [17].

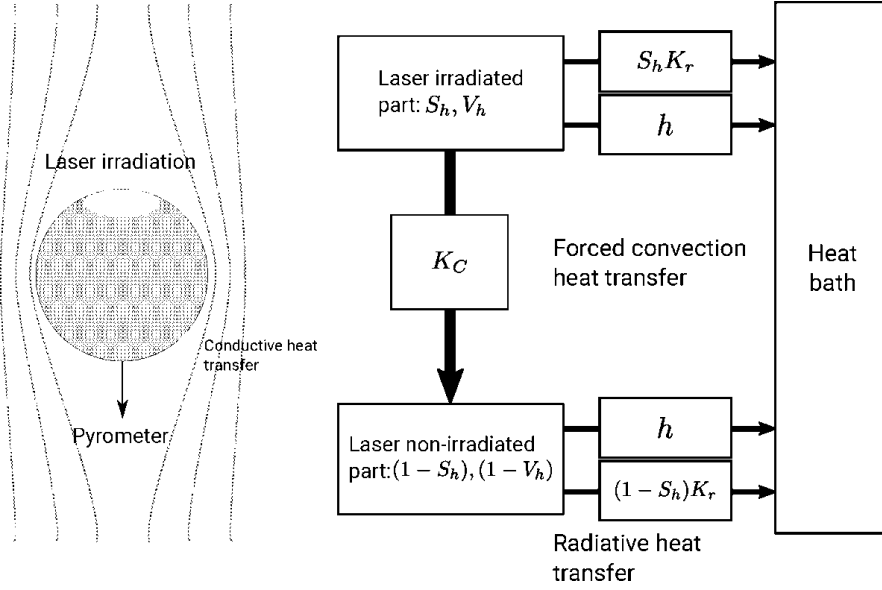


Figure 3.10: Heat flow model for the noncontact modulated laser calorimetry, illustrating the correlations between the heat flow parameters as presented in this section. The figure is based on figures in the works by Fukuyama et al. [16] and by Wunderlich and Fecht [87].

The heat balance at the laser-irradiated part is given by:

$$V_h C_p \frac{dT_h}{dt} = Q_h + \alpha S_h A P_0 (1 + \cos(\omega t)) - S_h A \left(\varepsilon \sigma (T_h^4 - T_\infty^4) + h_{\text{conv}} (T - T_\infty) \right) - K_c (T_h - T_l) \quad (3.10)$$

And for the laser-nonirradiated part:

$$(1 - V_h) C_p \frac{dT_l}{dt} = Q_l - (1 - S_h) A \left(\varepsilon \sigma (T_l^4 - T_\infty^4) + h_{\text{conv}} (T - T_\infty) \right) - K_c (T_h - T_l) \quad (3.11)$$

In these equations, S_h is the fraction of the irradiated surface area that is heated by the laser, V_h represents the volume fraction corresponding to S_h , C_p ($\text{JK}^{-1}\text{mol}^{-1}$) denotes the isobaric heat capacity, T (K) the absolute temperature, Q (W) the power input from the levitation coil, α is the absorptivity of the heating laser, A (m^2) gives the surface area of the droplet, h_{conv} ($\text{Wm}^{-2}\text{K}^{-1}$) is the forced convection heat transfer coefficient of a gas surrounding the sample droplet, K_c (WK^{-1}) is the thermal conductance for conductive heat transfer from the laser irradiated part to the non-irradiated part, K_r (WK^{-1}) is the thermal conductance for radiative heat transfer from the sample's surface to the heat reservoir in vacuum, ε is the hemispherical total emissivity and σ ($\text{Wm}^{-2}\text{K}^{-4}$) is the Stefan–Boltzmann

constant. The subscripts h and l relate to the laser-irradiated part and non-irradiated part, respectively [16]. The sample temperature is expressed by the sum of the initial temperature, T_0 , the average increase in temperature, ΔT_{dc} (dc component) and the modulation amplitude, $\Delta T_{ac} \cos(\omega t - \Phi)$ (ac component) [19, 22]:

$$T = T_0 + \Delta T_{dc} + \Delta T_{ac} \cos(\omega t - \Phi) \quad (3.12)$$

Assuming the internal thermal transfer derived from the thermal conductivity of the sample to be much higher than the external thermal loss caused by both radiation and buoyancy-driven convection heat transfer of the ambient gas, it can be followed that $K_r/K_c \leq 0.01$, with $K_r = A(4\varepsilon\sigma T_0^3 + h_{conv})$. Under this pre-condition and by solving Eqs. (3.11) and (3.12) the temperature amplitude, ΔT_{ac} , and the phase shift, Φ ($^\circ$), are [18]:

$$\Delta T_{ac} = \frac{\alpha S_h A P_0}{\omega C_p} \left(1 + \frac{1}{\omega^2 \tau_r^2} + \omega^2 \tau_c^2\right)^{-\frac{1}{2}} = \frac{\alpha S_h A P_0}{\omega C_p} f \quad (3.13)$$

and

$$\cos \Phi = \frac{\tau_c}{\omega} \left(\frac{1}{\tau_c \tau_r} - \omega^2\right) f \quad (3.14)$$

With f expressing a correction function, τ_r (s) signifying the external thermal relaxation time attributable to the radiative and conductive heat transfer in the ambient gas and τ_c (s) is the internal thermal relaxation time attributable to the conductive heat transfer in the sample. The relaxation times are defined as [16]:

$$\tau_r = \frac{C_p}{K_r} = \frac{C_p}{A(4\varepsilon\sigma T_0^3 + h_{conv})} \quad (3.15)$$

and

$$\tau_c = \frac{C_p}{K_c} = V_h(1 - V_h) \quad (3.16)$$

The term $\alpha S_h A p_0$ in Eq. (3.13) represents the laser input power absorbed by an object and it does not matter how it is evaluated in detail. In this work, it is assessed quantitatively using the products of the laser power and absorptivity at a laser wavelength

of the object. Assuming Kirchoff's law, the absorptivity, α , can be expressed as the emissivity, ε (compare sections 2.2 and 3.6). The distribution of the laser intensity is Gaussian with an e^{-2} radius of the laser beam being 2 mm for sample droplets of 4-6 mm radius. In this case, the effect of the sample curvature on the absorptivity was ignored [16, 19].

The condition $\omega^2\tau_r^2 \gg 1 \gg \omega^2\tau_c^2$, which satisfies $f \cong 1$, is achieved by a proper choice of the modulation frequency. The heat capacity can be determined from the temperature amplitude, ΔT_{ac} , from Eq. (3.13). Given this condition, the correction function, f , as a function of the modulation frequency exhibits a maximum value close to unity. Consequently, the term, $\omega\Delta T_{ac}$, displays a maximum value depending on the modulation frequency. For the corresponding modulation frequency, the phase difference equals 90° , as can be evolved from the condition that $\frac{\partial f}{\partial \omega} = 0$. Therefore, the heat capacity is determined experimentally from the temperature amplitude, with the satisfaction of the above mentioned requirements [16-19, 22].

The uncertainty of the molar heat capacity at constant pressure is discussed in detail in the *Appendix*. All heat capacity results with the corresponding experimental errors using the experimental methods described in this section are discussed in section 5.3.

3.8 Oscillating drop method

The oscillating drop method [84] in combination with EML can be applied to determine the surface tension. For the measurements at the Fukuyama lab, the method was also combined with a static magnetic field, as described in section 3.5. In this case, the static magnetic field was used in the initial levitation phase to stabilize the sample during the melting process and turned off afterwards. In the case of the DLR-MP, the surface tension was measured as a function of temperature as described in section 3.2.3, while at the Fukuyama lab time-dependent measurements at constant temperature were conducted. For the latter, the temperature was kept stable within experimental fluctuations, and the surface tension of Ti was obtained repeatedly during one measurement after certain time intervals, as presented in section 5.6.2.2. However, in both laboratories, the oscillating drop method was applied.

The oscillating drop method is based on the fact that the surface tension acts as a restoring force for surface oscillations of liquid drops. The time-dependent geometrical deformation of a liquid sample due to its surface oscillations can be described as normal modes by spherical harmonics $Y_{l,m}$ [38, 75]:

$$R_d(\theta, \varphi, t) = \sum_{l=0}^{\infty} \sum_{m=-l}^{+l} \alpha_{l,m}(t) Y_{l,m}(\theta, \varphi, t) \quad (3.17)$$

With R_d being the radius of the droplet depending on the time, t , the polar angle, θ , and azimuthal angle, φ . Here, $\alpha_{l,m}(t)$ denotes the time dependent deformation with $l \geq 0$ and $|m| \leq l$ being the integers of the spherical harmonics marking the oscillation modes [75, 83]. The sample oscillations are observed by means of a digital complementary metal oxide semiconductor (CMOS)-camera directed at the sample from above. Self-excited surface oscillations originate under gravitational conditions from turbulent flow in the sample while being exposed to an electromagnetic field. Under microgravity conditions, the surface oscillations are excited by induced pulses, e.g., heating pulses. The schematic setup for monitoring the surface oscillations can be seen in Figure 3.11 [38].

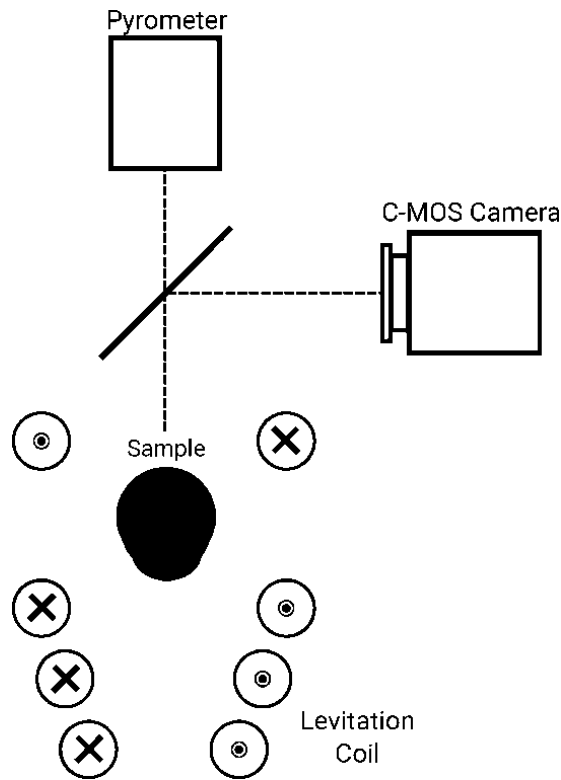


Figure 3.11: Schematic profile of the optical setup used to measure the surface tension by electromagnetic levitation. Based on Figure 3 by Brillo et al. [72].

The camera has a pixel resolution of 400x400 and operates at a frequency of 400 Hz. A series of $2^n = 4196$ frames is recorded for each surface tension measurement and investigated temperature. This gives a good compromise between the quality and operational constraints, as longer exposure times could lead to greater evaporation. Conversely, a higher sampling rate requires a reduction in the spatial resolution of the taken images, due to limited data rates between the camera and hard disk. The pictures are analyzed by means of digital

image processing, extracting the following parameters as a function of time, t : the center of mass with respect to the x - and y -direction as $x_0(t)$ and $y_0(t)$, respectively, the visible droplet area, $A(t)$, and two perpendicular radii, $r_x(t)$ and $r_y(t)$ [30]. By fast Fourier transform (FFT), those parameters are transformed yielding frequency dependent characteristic spectra (compare section 3.8.1) of the sample radii, R_d , comprising the intensities of the sample's oscillations and translations.

For the relation between the surface tension, γ , and the surface oscillations, $\omega_{l,m}$, Rayleigh proposed the following equation, pre-conditioning a spherical non-rotating sample of mass, m [75]:

$$\omega_{l,m} = l(l+2)(l-1) \frac{4\pi}{3m} \gamma \quad (3.18)$$

Premising spherical symmetry and incompressibility of the liquid, the frequencies in Eq. (2.27) do not depend on the index m and the mode $l=0$ does not appear. The mode $l=1$ corresponds to a translational oscillation of the entire droplet. Therefore, the fundamental oscillation mode is $l=2$, which is called Rayleigh-frequency, ω_R , with a five-fold degenerate $(-2, -1, 0, +1, +2)$ [73]:

$$\omega_{2,m} = \omega_2 = \omega_R \quad (3.19)$$

with

$$\omega_R^2 = \frac{32\pi}{3m} \gamma \quad (3.20)$$

For sample masses around 1 g, $\omega_R/2\pi$ is typically in the order of 40 Hz [73], [30]. Oscillation modes with $l > 2$ are well separated due to their distinctly higher frequencies and are often not visible, because of their strong damping. Opposed to the pre-conditions by Rayleigh [75], under terrestrial conditions the droplet has to be considered as non-spherical and slightly rotating, as relatively strong field gradients are acting to compensate the gravitation, acting on the sample with an additional magnetic pressure on the sample's surface. Cummings and Blackburn [75] have investigated this influence theoretically and shown that in this case the Rayleigh-frequency, ω_R , splits up into three frequencies, $\omega_{2,\pm 2}$, $\omega_{2,\pm 1}$ and $\omega_{2,0}$ [75]:

$$\omega_{2,0} = \omega_R^2 + \overline{\Omega_{\text{Tr}}^2} \left(3.832 - 0.1714 \left(\frac{g}{R_d} \right)^2 \right) \quad (3.21)$$

$$\omega_{2,\pm 1} = \omega_R^2 + \overline{\Omega_{Tr}^2} \left(3.775 - 0.5143 \left(\frac{g}{R_d} \right)^2 \right) \quad (3.22)$$

$$\omega_{2,\pm 2} = \omega_R^2 + \overline{\Omega_{Tr}^2} \left(-0.9297 - 2.571 \left(\frac{g}{R_d} \right)^2 \right) \quad (3.23)$$

Here, $\omega_{2,m}$ are the shifted surface oscillation frequencies for $l = 2$, g denotes the gravitational acceleration and R_d the radius of the sample, which is assumed to be spherical.

Additionally, the three translational frequencies, ω_x , ω_y , ω_z , can be identified from the motion of the droplet's centre in the three spatial directions, x , y , z , and thus, the mean quadratic translational frequency, $\overline{\Omega^2}$, can be calculated as [73, 75]:

$$\overline{\Omega^2} = \frac{1}{3} (\omega_x^2 + \omega_y^2 + \omega_z^2) \quad (3.24)$$

In practise, due to the sample rotation the pairwise degeneration of $\omega_{2,\pm 1}$ and $\omega_{2,\pm 2}$ is annulled and thus, five peaks at different frequencies can be distinguished in the spectrum under terrestrially gravitational conditions. From the five surface oscillations, the three translational frequencies while combining Eqs. (2.28)-(2.33) with a correction function for terrestrial conditions, the surface tension, γ , can be determined, using the sum formula by Cummings and Blackburn [75]:

$$\gamma = \frac{3m}{160\pi} \sum_{m=-2}^{+2} \omega_m^2 - 1.9\Omega^2 - 0.3 \left(\frac{g}{R_d} \right)^2 \Omega^{-2} \quad (3.25)$$

3.8.1 Oscillation modes

From the fast Fourier transform (FFT) analysis, as described in section 3.8, the frequency dependent spectra can be obtained of the translations and oscillations in the x - and y -direction, $\text{FFT}(x_0(t))$ and $\text{FFT}(y_0(t))$, of the area, $\text{FFT}(A_0(t))$, of the sum, $\text{FFT}(r_x(t) + r_y(t))$, and of the difference, $\text{FFT}(r_x(t) - r_y(t))$, of the two perpendicular radii, x_0 and y_0 . A typical spectrum of the translations is shown in Figure 3.13. The frequencies ω_x and ω_y appear as pronounced peaks at approximately 5-12 Hz. For a perfect coil, both frequencies would be identical, though, realistically, they show small deviations. The vertical movement along the z -axis is visible in the spectrum of the area $\text{FFT}(A_0(t))$, as the apparent size changes when the sample moves towards the camera. To identify ω_z which is not always pronounced relatively to the background noise, the relation $\omega_z \approx 2\omega_x \approx 2\omega_y$ can be used.

Figure 3.12 visualizes the different oscillation modes and the corresponding (x, y, z) -direction dependent expansions. The figure illustrates how an expansion in one direction can be distinguishable in one FFT-analysis while it vanishes in another.

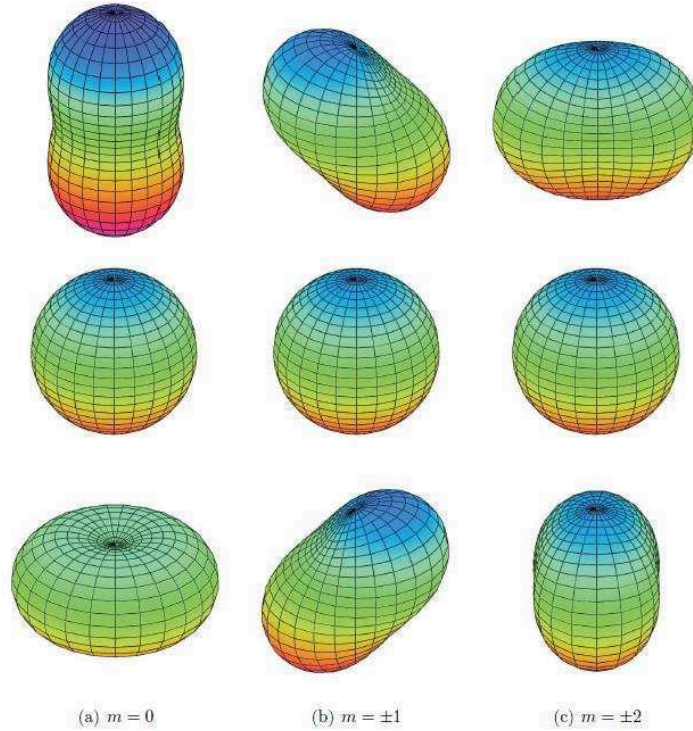


Figure 3.12: Geometry of oscillation mode $l = 1$, according to Eq. (2.26) illustrating the oscillations in different directions depending on the mode, m . The figure is taken from reference [38] by J. Schmitz.

This leads to selection rules [76] which make it possible to identify the characteristic frequencies, $\omega_{2,m}$, in the frequency dependent spectra with the oscillation modes. For example, for $\omega_{2,\pm 2}$ the peak is suppressed in the FFT of the sum, as the deviations of perpendicular radii from a circle eliminate each other. Consequently, for the $\omega_{2,\pm 2}$ oscillation mode, the sum of perpendicular radii, $r_x(t) + r_y(t)$, is a constant, which vanishes through a fast Fourier transform. Furthermore for $\omega_{2,0}$ the peak is suppressed in the FFT of the difference, $\text{FFT}(r_x(t) - r_y(t))$. Finally, the peaks appearing in both the sum and the difference spectra belong to $\omega_{2,\pm 1}$ [30, 76]. In Figure 3.13 an oscillation spectrum is shown comprising the five oscillation peaks of the sum and the difference of the FFT.

After the different oscillation and translational modes are identified, the Rayleigh-frequency, ω_R , can be determined using Eq. (3.25).

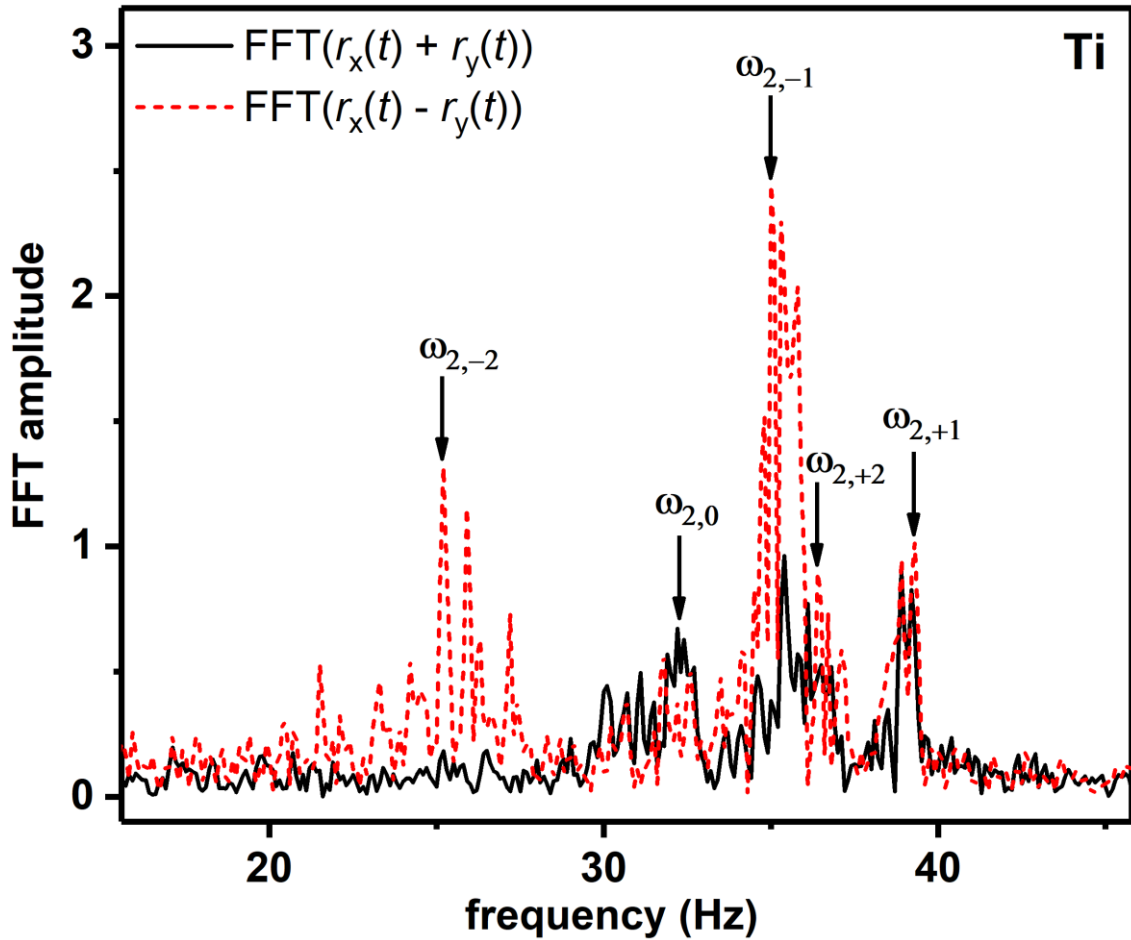


Figure 3.13: Frequency spectra of the sum (solid line) and difference (dashed line) signal of two perpendicular radii of the surface oscillations of a liquid Ti sample converted by fast Fourier transform (FFT).

In a conservative approach, the maximum error of the surface tension using this procedure allows a margin of $\Delta\gamma/\gamma \leq 5.0\%$ assuming numerical errors for the parameters in Eq. (3.25) [30]. The uncertainty for the frequency is estimated as 0.5 Hz, which has shown to be the upper limit. Other error sources are similar to the ones of the density measurement, counting evaporation, mass loss, strong sample rotation and uncertainties in temperature determination. Thus, analogously to the density measurements, the mass loss must be monitored, and the sample rotation controlled to preclude these potential error contributions. The purity of the sample and the environment can have a significant influence on the surface tension. Some materials are highly sensitive to surface active species, such as oxygen and sulfur. However, in many systems, the actual error of the surface tension in dependence of the concentration or temperature is much smaller than 5%, and thus a statistical error will be given in this work when possible [30].

The corresponding results for the surface tension measurements based on the experimental method as introduced in this chapter will be presented in section 5.5.

3.8.2 Oscillating drop method in microgravity (TEMPUS)

Surface tension measurements under microgravity conditions as described in detail in [89, 90] are conducted on parabolic flights performed in the TEMPUS facility, analogously to viscosity measurements as introduced in the following section 3.9. The TEMPUS facility is described in section 3.3 and, more detailed in various works, e.g. [31]. For the surface tension measurement in microgravity, the oscillating drop technique in combination with EML is used analogously to measurements under terrestrial conditions as described in this section 3.8. However, different to terrestrial measurement conditions, the spherical symmetry and incompressibility of the liquid can be premised. Consequently, the surface tension can be calculated from the Rayleigh-frequency, ω_R , based on Eq. (3.18) neglecting the correction function for terrestrial conditions.

3.9 Viscosity measurement

The oscillating drop technique (section 3.8) can also be used for the determination of viscosities by either using ESL or EML techniques under microgravity conditions (section 3.3) to ensure that no magnetic damping or fluid flow occur [26]. The latter has been performed, e.g., on the ISS or, as in the case of this work in the TEMPUS facility during parabolic flights.

The analysis of the viscosity is based on Lamb's formula which expresses the damping of the oscillations of a liquid viscous droplet [31, 76]. As under microgravity conditions, no self-excited oscillations occur, the oscillations are induced by pulses on the surface of the droplet, generated through the heating circuit of the TEMPUS facility during the free cooling phase. The pulses are superimposed to the vertical positioning field with a frequency close to the sample's eigenfrequency, which corresponds to the sample's mass with an amplitude of 0.4 - 2 kV. If the initial radius of a droplet, R_0 , undergoes small oscillations over time, $R_d(t)$, the oscillations can be described as following [31, 53]:

$$R_d(t) = R_0(1 + \hat{u} \sin(\omega t + \Phi) \exp(-\tau t)) \quad (3.26)$$

The damping constant, τ , can be calculated by fitting the amplitude, \hat{u} , the angular frequency, ω , and the phase shift, Φ to the radius data. With the damping constant, the viscosity of an axisymmetric ($n = 2$ and $m = 0$ mode) surface oscillation induced by a single excitation, can be calculated from its density [30, 31, 76].

$$\eta = \frac{\rho R_0^2 \tau}{5} \quad (3.27)$$

Viscosity measurements using EML in combination with the oscillating drop technique in microgravity are technically challenging and susceptible to error sources. Vibrations resulting from the aircraft during parabolic flights might cause additional forces on the levitated sample and disturb the free damping behavior. Additionally, multiple oscillations modes can occur, particularly at lower temperatures close to the liquidus temperature and for viscosities lower than 20 mPas, as in the case of Al-Ti [53]. These distributions cause uncertainty in the analysis of the damping constant.

From Eq. (3.27), the uncertainty of the viscosity can be calculated from the uncertainties of the density, the sample radius, and the damping constant by error propagation, as discussed in detail in the *Appendix*. Based on these experimental methods the viscosity has been measured with the corresponding results presented in section 5.4.

3.10 Oxygen control and monitoring

When measuring thermophysical properties of liquid metals, especially with regards to the surface tension, a consideration of the influence of oxygen partial pressure is crucial, as already introduced in section 2.6. To investigate this influence, means are needed to monitor or even control the oxygen partial pressure. By those means not only the results of the different properties can be related to the oxygen partial pressure, but also results can be obtained revealing insight into the processes on an atomic scale, as adsorption and oxide formation (compare section 2.6). In the following chapter, the means used in this work to investigate the oxygen partial pressure processes are presented.

3.10.1 Oxygen ion pump

The oxygen partial pressure can be monitored and controlled through an oxygen ion pump based on an ionic conductor. The ionic conductor needs to be operated in a temperature range high enough to establish O₂ transport through an electrolyte and low enough to suppress electronic conduction. For ionic conductivity, the oxygen flux, J_{O_2} , can be defined using the electric current, I , and the Faraday constant, F , (96485 C mol⁻¹) as [63, 91, 92]:

$$J_{O_2} = \frac{I}{4F} \quad (3.28)$$

Under the condition that the oxygen flow, J_{O_2} , is comparatively low with respect to the total gas flow, J_{tot} , the resulting oxygen partial pressure can be expressed in dependence of the latter and also taking the total pressure, P_{tot} , and the initial oxygen partial pressure, $P_{O_2}^0$, in the carrier gas into account [63, 92]:

$$P_{O_2} = P_{O_2}^0 + P_{\text{tot}} \frac{J_{O_2}}{J_{\text{tot}}} \quad (3.29)$$

Through the Nernst equation, given by

$$E_{\text{cell}} = \frac{RT}{4F} \ln \left(\frac{P_{O_2}}{P_{O_2}^{\text{ref}}} \right) \quad (3.30)$$

describing a relation between the electromotive force, E_{cell} , and the ratio of the oxygen partial pressure, P_{O_2} , to the oxygen partial pressure of a reference gas (ambient air), $P_{O_2}^{\text{ref}}$, with R being the universal gas constant and T the temperature. Thus, through Eq. (3.30) it is possible to monitor and actively set the oxygen partial pressure by measuring or applying a respective voltage [63, 92].

Figure 3.14 shows a schematic picture of an oxygen ion pump using YSZ (Yttrium-stabilized Zirconia) tubes. In the case of an oxygen partial pressure monitoring, the potential induced by a certain oxygen partial pressure can be measured, and in turn, the acting oxygen partial pressure can be evaluated. For an active oxygen partial pressure controlling, the carrier gas is delivered through the inlet into the active area, where an electric current, I , is applied. In dependence of the polarity, then the pump either enriches or depletes the oxygen concentration in the carrier gas. The system at the DLR-MP, controlling the oxygen partial pressure actively, normally comprises two ion pumps, whereas the large electrode is used to pump oxygen to achieve certain pressures, while the small electrode is used to monitor the resulting oxygen partial pressure [63, 91].

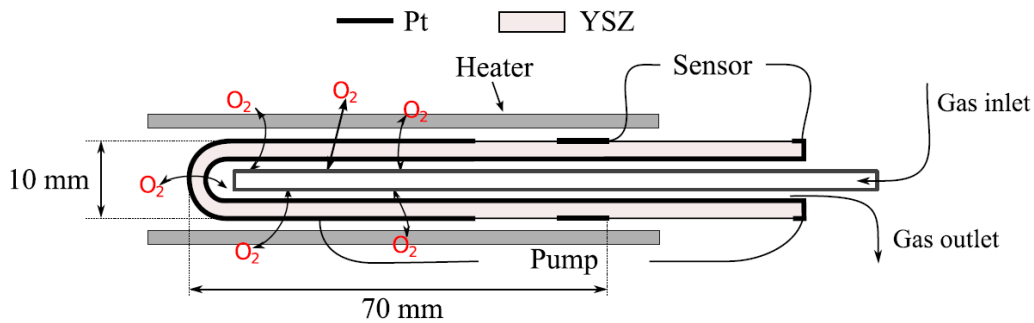


Figure 3.14: Schematic profile of a YSZ based oxygen ion pump. An electric current is applied at the inlet area, which enriches or depletes the oxygen concentration in the carrier gas depending on the polarity. The figure is taken from reference [63], Fig. 1 by Schulz et al. (Elsevier copyright license number 4265221154584).

3.10.2 Oxygen control system (OSC)

For the measurements carried out at the Fukuyama lab, an oxygen ion pump (ROX-530 Canon Machinery Inc.) is used to measure the oxygen partial pressure of the introduced

high purity gases and buffer gas mixtures (see section 3.10.4). This way a constant oxygen partial pressure, P_{O_2} , of about 10^{-21} Pa in the inlet gas throughout the measurements can be assured [23].

At the DLR-MP, the P_{O_2} is controlled using two YSZ tubes which are operated as an oxygen ion pump and sensor, respectively. The oxygen control system (OSC) is schematically shown in Figure 3.15.

The OSC is positioned at the top of the EML facility. Normally, the OSC would be implemented as close to the sample as possible to ensure that the actual oxygen partial pressure in the sample's vicinity is measured. However, this specific setup was chosen intentionally, as it serves as a prototype for the OSC addition to the μg -EML on the ISS with an equivalent setup as the one at the DLR-MP (section 3.3).

First, the inlet gas is passing through the ion pump, called the OLS pump. It is functioning as a pump but also includes an oxygen partial pressure sensor to improve the stability of the control algorithm and providing additional information about the system. Figure 3.15 illustrates the setup of the device with a large pumping area of about 125 cm^2 and a small inner sensor area of about 3 cm^2 , both coated with platinum [63].

Subsequently, the gas is introduced into the chamber and then, after leaving the chamber is monitored by an additional potentiometric system sensor (SS1), measuring the oxygen partial pressure in the outlet gas. The sensor consists of a platinum coated outer electrode of 3 cm^2 and an inner electrode with the general design similar oxygen pumps [63].

The oxygen pump has a high resolution of at least $10^{-3}\text{ mm}^3\text{min}^{-1}$ compared to conventional mass flow controllers which adjust the oxygen flow with an uncertainty of about $50\text{ mm}^3\text{min}^{-1}$. In combination with the oxygen sensor, it enables precise control of the oxygen partial pressure ranging from 10^{-7} to 10 Pa [63].

Both the oxygen ion pump and the sensor are operated at 873 K to enable high oxygen ion mobility and long-term stability of the system. The YSZ tubes are enclosed in large thermal insulation blocks to minimize the temperature gradients. The temperature is monitored close to the oxygen sensors used as input data for the calculations in Eq. (3.30) and expected to be uniform within these areas. To shield the OSC electronics from the potential electromagnetic noise of the EML-facility, the OSC consists of a robust, customized construction. Furthermore, resistive temperature sensors are used instead of commonly used thermocouples [63].

The pumping current, I , of up to 40 mA is set by pulse width modulation control, based on a PID algorithm. The algorithm and control device has been developed in cooperation with Michal Schulz and the Clausthal University of Technology [63]. Respective PID parameters are adjusted for different oxygen partial pressures due to the strong nonlinearity of $P_{O_2}(I)$. Additionally, the system features a cascade PID controller, which enables to adjust the PID parameters manually and independently for both sensors. The

controller provides an accuracy of about $1 \mu\text{A}$. The OSC can be operated using a manual operation device or a computer program. The program shows the trend of the oxygen partial pressure of the OLS and SS1 as a function of time, the manual device provides only the instantaneous values of the P_{O_2} [63].

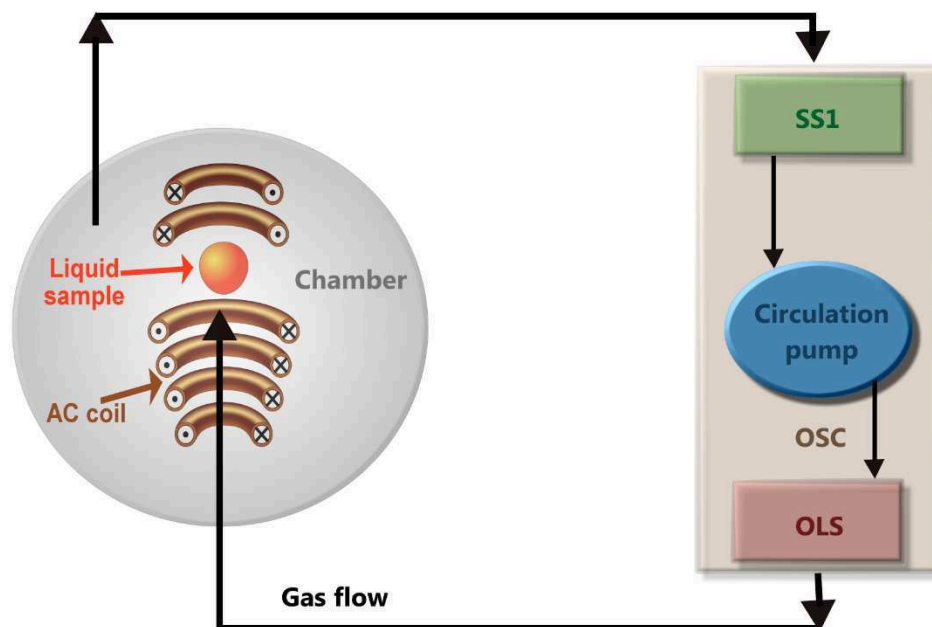


Figure 3.15: Schematic setup of the EML facility connected to the OSC (oxygen control system) and gas flow directions between the devices.

Prior to an experiment, the oxygen control system is started, and the temperature increased until it reaches its operative temperature of 873 K. Once the OLS and SS1 have reached the operative temperature, target values for the P_{O_2} either at the inlet (OLS) or outlet (SS1) system can be set. For an oxygen partial pressure dependent measurement, normally low initial values are set and increased during the measurement. To achieve even lower values at the beginning of the measurement, sublimation pumps can be used before and during the measurement, as explained in the next section 3.10.4. To establish a certain value, the OLS system starts pumping oxygen until the respective value is reached. Ideally, in the case of an equilibrium state, the oxygen partial pressure in the inlet would equal the one in the outlet after a sufficiently long pumping time to exchange the gas in the chamber completely. Deviations may indicate a leak in the experimental setup, oxygen sources or absorbers in the chamber including the sample itself [63].

In the case of Ti and Al, the surface tension measurements, $\gamma(P_{\text{O}_2})$, cover a P_{O_2} range of about 10^{-7} - 10 Pa. The P_{O_2} -range limitations depend on the quality of the vacuum, the gaseous atmospheric composition, the OSC capabilities and the sample itself as it might adsorb or emit oxygen. The accuracy of the P_{O_2} values and adjustable steps additionally depend on the PID parameter settings for at the respective P_{O_2} .

3.10.3 Sublimation pumps

An additional method to control and reduce the oxygen partial pressure is the use of sublimation pumps. Sublimation pumps contain filaments through which a high current of 20-40 A is passed. The current causes the filaments to reach the sublimation temperature of its respective material. The filaments typically consist of highly reactive components which react with the atmospheric gas, extract oxygen from the gas and, hence reduce the oxygen partial pressure. At the Fukuyama lab, a pump with magnesium filaments is used, and at the DLR-MP, a titanium sublimation pump is operated, shown in Figure 3.16.



Figure 3.16: Picture of the titanium sublimation pump used at the DLR-MP.

3.10.4 Oxygen equilibrium in buffer gas mixtures

To further reduce the oxygen partial pressure, buffer gases can be used, such as Ar-5% H₂ at the Fukuyama lab. Then, Eq. (3.30) describing the oxygen partial pressure based on the Nernst equation, has to be adjusted and the gas equilibrium taken into account. In hydrogen-containing atmospheres, water is formed in the presence of oxygen [63]:



With the equilibrium constant

$$K_{\text{H}_2\text{O}}(T) = \frac{P_{\text{H}_2\text{O}}}{P_{\text{H}_2} P_{\text{O}_2}^{1/2}} \quad (3.32)$$

In this equation, $P_{\text{H}_2\text{O}}$, P_{H_2} and P_{O_2} are the partial pressures of H₂O, H₂ and O₂, respectively. The equilibrium constant, $K_{\text{H}_2\text{O}}(T)$, is temperature dependent and can be evaluated from the Gibbs free energy of formation of H₂O.

The OSC sensor cannot measure the P_{O_2} of the gas corresponding to the droplet's temperature instead, it detects the P_{O_2} of an atmospheric gas introduced into the oxygen

sensor at its operative temperature. The P_{O_2} of the mixture gases was calculated as a function of temperature using the Gibbs free energy of formation of H_2O , assuming the ratio of P_{H_2O} and P_{H_2} to be constant with varying temperature [93].

The experimental results presented based on the method procedures related to an oxygen control and monitoring as presented in this section are discussed in section 5.6.

3.11 Summary

In this chapter, the experimental methods used for conventional techniques (section 3.1), electromagnetic levitation under gravitational (section 3.2) and microgravity conditions (section 3.3), optical dilatometry (section 3.4), static magnetic field (section 3.5), normal spectral emissivity (section 3.6), non-contact modulated laser calorimetry (section 3.7), oscillating drop method (section 3.8), viscosity measurement (section 3.9) and oxygen control and monitoring (section 3.10) were introduced. The corresponding sample preparation, procedures, and analysis will be explained in chapter 4.

4 Sample preparation, procedures, and analysis

As a first step of the sample preparation, the aimed sample mass and volume of the pure or alloy sample must be determined. Typically, the alloy samples have diameters of 3-10 mm and masses of approximately 0.5-1 g, depending on the levitation facility and coil, the density of the sample and the temperature range limitations like the melting point and evaporation at high temperatures, as described in section 3.2.3 [53]. The weight calculations in dependence of the molar ratios of the alloys, Al-Ti and Ti-O are described in section 4.1.1 and 4.1.2, respectively, including also a description of the material-specific sample preparations. After the corresponding amounts of the materials are obtained, the components are melted together by arc melting. Subsequently, an ultrasound bath in propanol is used for cleaning and the removal of scales. Large differences in the melting temperatures, especially in the case of Al (933 K) and Ti (1941 K) may present a challenge for the processing of the liquid alloys, due to partially intense evaporation of the component with the lower melting point. This may cause a shift in the sample's mass and its composition. These effects may limit the accuracy of the experimental results. Therefore, the mass loss of each sample is evaluated before and after each measurement and, if it exceeds 0.1 % of the initial sample mass, the results are dismissed.

4.1.1 Binary alloys Al-Ti

For the Al-Ti measurements, *Alfa Aesar* products, aluminum, and titanium, both of 99.999 % purity are used with liquidus temperatures at 933 K and 1941 K, respectively. Samples with different molar ratios of Al:Ti, are chosen over a brought composition range: Al, Al₈₀Ti₂₀, Al₇₀Ti₃₀, Al₆₀Ti₄₀, Al₅₀Ti₅₀, Al₄₀Ti₆₀, Al₃₀Ti₇₀, Al₂₅Ti₇₅, Al₂₀Ti₈₀ and Al₁₀Ti₉₀ and Ti. The Al-Ti phase diagram can be seen in Figure 4.1, and the corresponding liquidus temperatures are taken from reference [80].

To calculate the mass, m_i , of the components corresponding to the desired molar ratios, X_i , with i denoting the components Al and Ti, the following relation can be used:

$$m_i = m_{\text{tot}} \frac{M_i X_i}{\sum_i M_i X_i} \quad (4.1)$$

Here, m_{tot} stands for the desired total mass of the alloy's specimen and M_i the molar masses of Al and Ti, which are 26.982 gmol⁻¹ and 47.867 gmol⁻¹, respectively.

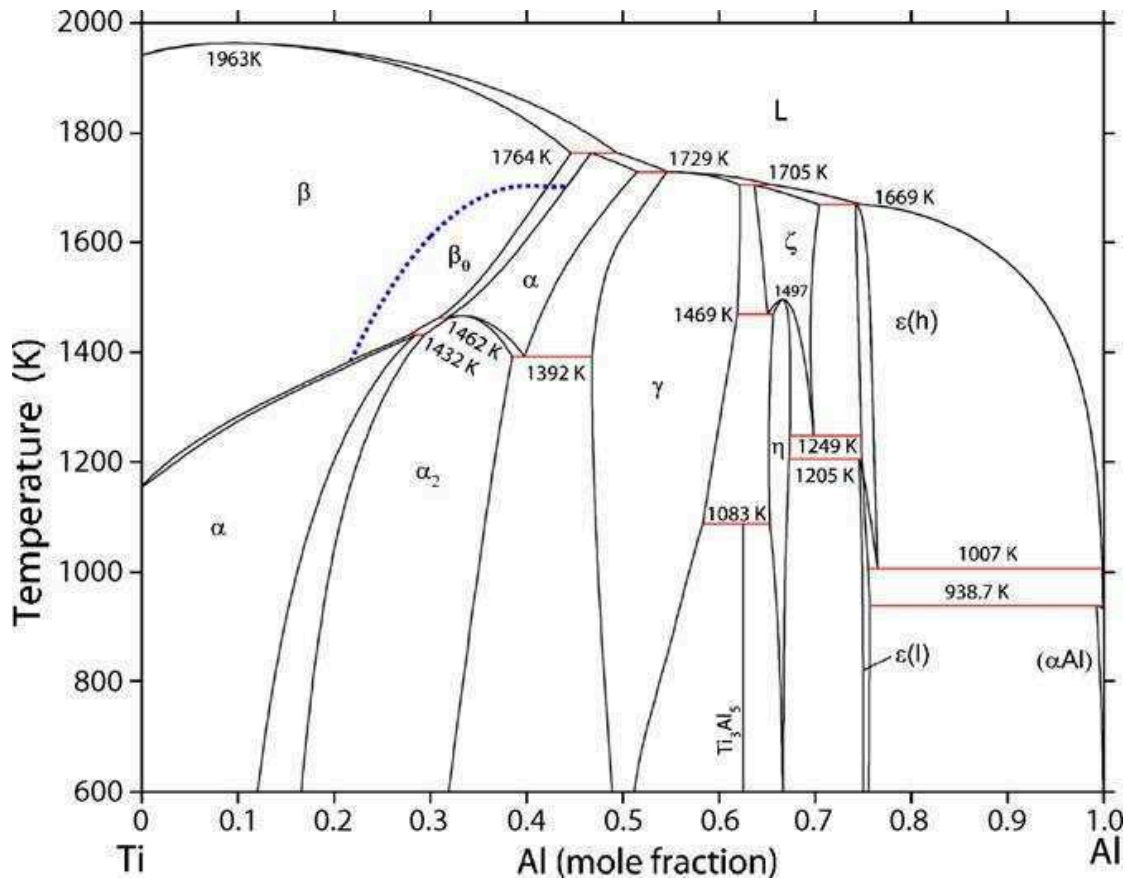


Figure 4.1: Phase diagram of the liquid Al-Ti system, taken from reference [80] (Elsevier copyright license number 4265230007269).

The titanium material is given in the form of a rod of 12.7 mm diameter which is cut into discs with a thickness according to the approximated desired weight. For the cutting of titanium, an ISOMET 1000 precision diamond saw is used, in combination with a lube solution (volume ratio of 1/20 lube and 19/20 water) to avoid heating due to friction. As aluminum is relatively easy to cut, the use of a wire cutter is sufficient to divide pieces into the approximate right size. Subsequently, all pieces are limed and polished using a polishing machine and SiC papers of medium grain size to remove possible oxide layers on the surface. To prepare a correct Al-Ti mass ratio, the mass of Al is further adjusted using finer-grained liming paper until accuracy of fourth-order decimal is achieved. The pieces are cleaned in an ultrasound bath in isopropanol to avoid contamination, e.g., through remaining SiC-particles. Afterwards the samples are treated further as described in section 4.2 and stored in isopropanol until the measurement to avoid oxidation. As a first step of the levitation experiment, all samples are briefly heated up to a temperature of at least T_L+100 K. This procedure allows further purification through evaporation of volatile Al-oxides.

4.1.2 Binary alloys Ti-TiO₂

For the preparation of Ti-O samples with defined amounts of oxygen, pure titanium and titanium oxide powder are used. The titanium used for these samples is the same as for the Al-Ti samples. The titanium (IV) oxide of the chemical formula TiO₂ (rutile) is a product of *Sigma-Aldrich* with a high purity of 99.995% and a molar mass, $M_{\text{ox}} = 78.87 \text{ gmol}^{-1}$. Samples with different molar ratios of Ti:O were used, counting Ti₉₉O₁, Ti₉₇O₃, Ti₉₄O₆, Ti₈₆O₁₄ and Ti₇₄O₁₆. The Ti-O phase diagram can be seen in Figure 4.2 and the corresponding liquidus temperatures are taken from reference [94].

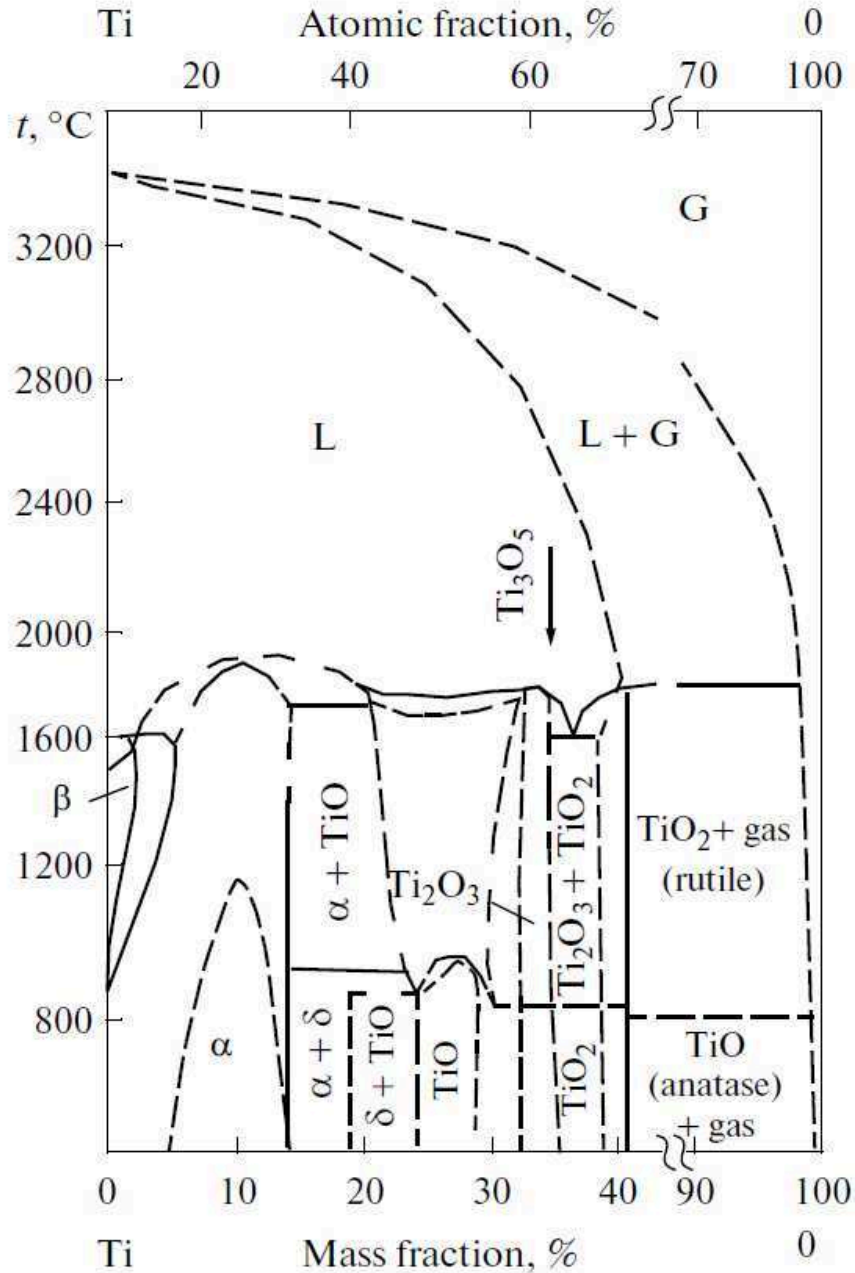


Figure 4.2: Phase diagram of the liquid Ti-O system, taken from reference [24] by Belyanchikov with the copyright license number 4265230759036 granted by Springer Nature.

To calculate the needed masses of pure Ti and TiO₂ to obtain samples with certain molar ratios of Ti:O, the following calculations have been made.

The weight ratio, w_i , of component i , is defined as $w_i = \frac{m_i}{m_{\text{tot}}}$ with $\sum_i w_i = 1$, thus, based on Eq. (4.1) the respective molar ratio, X_i can be denoted as:

$$X_i = \frac{\frac{w_i}{M_i}}{\sum_i \frac{w_i}{M_i}} \quad (4.2)$$

The formation of the dioxide, TiO₂, can be expressed by the following reaction:



If N'_i and N'_{tot} respectively define the number of atoms of component i and the total number of atoms involved in a reaction (4.3) before the reaction takes place and N_i and N_{tot} the corresponding numbers of atoms after TiO₂ is formed, then Eqs. (4.4) and (4.5) are valid:

$$N'_{\text{tot}} = N'_{\text{Ti}} + N'_0 \quad (4.4)$$

$$N_{\text{tot}} = N_{\text{Ti}} + N_{\text{O}} \quad (4.5)$$

The initial contributions of the oxide can then be written as their resulting contributions to the alloy components Ti and O, with $N_{\text{Ti}} = N'_{\text{Ti}} + N'_{\text{TiO}_2}$ and $N_{\text{O}} = 2N'_{\text{TiO}_2}$ and, subsequently, Eq. (4.5) can be evolved to

$$N_{\text{tot}} = N'_{\text{Ti}} + N'_{\text{TiO}_2} + 2N'_{\text{TiO}_2} = N'_{\text{Ti}} + 3N'_{\text{TiO}_2} \quad (4.6)$$

and the molar ratio, X_{Ti} and X_{O} , of Ti and O can thus, be defined by the initial ratios, X'_{Ti} and X'_{TiO_2} , of Ti and TiO₂ as:

$$X_{\text{Ti}} = \frac{X'_{\text{Ti}} + X'_{\text{TiO}_2}}{X'_{\text{Ti}} + 3X'_{\text{TiO}_2}} \quad (4.7)$$

And

$$X_O = \frac{2X'_{\text{TiO}_2}}{X'_{\text{Ti}} + 3X'_{\text{TiO}_2}} \quad (4.8)$$

The titanium used for the Ti-O samples is prepared in the same way, as described in section 4.1.1. As the TiO₂ is given in powder form, it can easily be weighted in desired quantities. The Ti pieces and TiO₂ powder are melted in the same procedure as the Al-Ti and pure samples, by arc-melting with special attention paid to mass loss during the melting process due to the loss of fine-grained TiO₂ particles.

4.2 Sample analysis

After the experiments, the solidified Ti-O samples were analysed according to standard metallographic procedures to provide additional insight into the properties and processes of the liquid samples.

4.2.1 Scanning electron microscope (SEM)

The solidification microstructures were investigated using a DLR-MP in-house scanning electron microscope (SEM) LEO 1530 VP. The device is equipped with an Oxford Instruments energy dispersive X-ray analysis (EDX) apparatus for the measurement of the relative composition variations of the different phases observed in the samples [95]. A corresponding computer program analyses the results and visualizes the overserved sample surface instantaneously. For the SEM investigations, the respective spherical samples need to be cut in half and embedded in *PolyFast* bedding material. Furthermore, the sample's flat surface at the cutting interface needs to be polished to ensure an even and uncontaminated plane.

4.2.2 Oxygen analysis

To investigate the oxygen content after the measurement, the Ti-O samples were analysed by an oxygen-nitrogen analysis. For the samples at the DLR-MP, the analyses were performed by the company *Umicore* with a Leco TC-600 device. Concerning the samples at the Fukuyama lab, the University's *Analytical Research Core for Advanced Materials* conducted the measurements using a Leco TC-436 device.

Approximately half of the samples' size is needed for the analysis. The investigated specimen is put in a closed tin capsule and placed in a Ni basket, positioned in a graphite crucible. Subsequently, the sample material is heated under He as a carrier gas. Under the heating process, the whole feed is melted, and the entire oxygen contained in the sample is set free from its binding elements. As a result, the oxygen reacts with the graphite from

the crucible and transforms into CO or CO₂ gas. These gases are analysed by an infrared measuring cell, and the observed signal is transferred into the total oxygen content.

4.3 Summary

Subsequent to the introduction of this work, the theoretical background and the experimental methods were introduced in chapter 2 and 3, respectively. Subsequently, in this chapter, the corresponding sample preparation and procedures for the binary systems Al-Ti (section 4.1.1) and Ti-TiO₂ (section 4.1.2) were established, as well as the sample analysis techniques (section 4.2). By this, the foundation has now been laid to proceed to the results and discussion in chapter 5.

5 Results and discussion

In this chapter, the results of the experimental methods introduced in chapter 3 are presented. The results and discussions for high temperature density (section 5.1), normal spectral emissivity (section 5.2), isobaric heat capacity (section 5.3), high temperature viscosity under reduced gravity (section 5.4), high temperature surface tension (section 5.5) and the influence of oxygen on the surface tension (section 5.6) are reported in the respective sections. Each section begins with a short outlook on the respective data and discussions and ends with a summary.

The dependencies of the properties, such as temperature, composition and oxygen partial pressure dependencies are displayed and compared to models, for example, the Butler model [43] in the case of the surface tension data. Furthermore, the accuracy of the data and the experimental and statistical uncertainties as reasoned in the respective sections of chapter 3 are addressed.

For the measurements, different devices have been used for the respective properties (see chapter 3) counting the DLR-MP EML-facility, the EML-facility of the Fukuyama lab and the μg -EML TEMPUS facility during parabolic flight.

5.1 High-temperature density

In this section, the results of the high-temperature density measurements at the DLR-MP EML-facility are presented and discussed concerning the temperature and composition dependencies in the Al-Ti system. Additionally, the calculated ideal molar volumes of the alloys and the evaluated real molar volumes are provided and discussed concerning excess properties. The data of this chapter have been published before in the publication *Density, Molar Volume, and Surface Tension of liquid Al-Ti* by Wessing and Brillo [7], and some parts of this chapter including graphics are based on evaluations and discussions of the publication above. The reuse of data, graphics, and content was granted by a Springer copyright license with the number 4127610503802. This section is based on the sections 2.1 and 3.4 of this work, where the respective theoretical background and the experimental methods have been introduced.

5.1.1 Results

As discussed in the *Appendix*, the uncertainties of the density and molar volume are assumed to be $\Delta\rho/\rho = \Delta V/V \leq \pm 1.0\%$.

Figure 5.1 shows measured density data of liquid Al-Ti samples in dependence of the temperature, $\rho(T)$. Each measurement was conducted over a broad temperature range, of 150-500 K. This range included up to 200 K undercooling below the respective liquidus temperature, limited by the nucleation of the solid phase at low temperatures and by mass loss due to evaporation at sufficiently large temperatures. The illustrated alloy compositions range with Al mole fractions, X_{Al} varies from 0 to 100 at.-%.

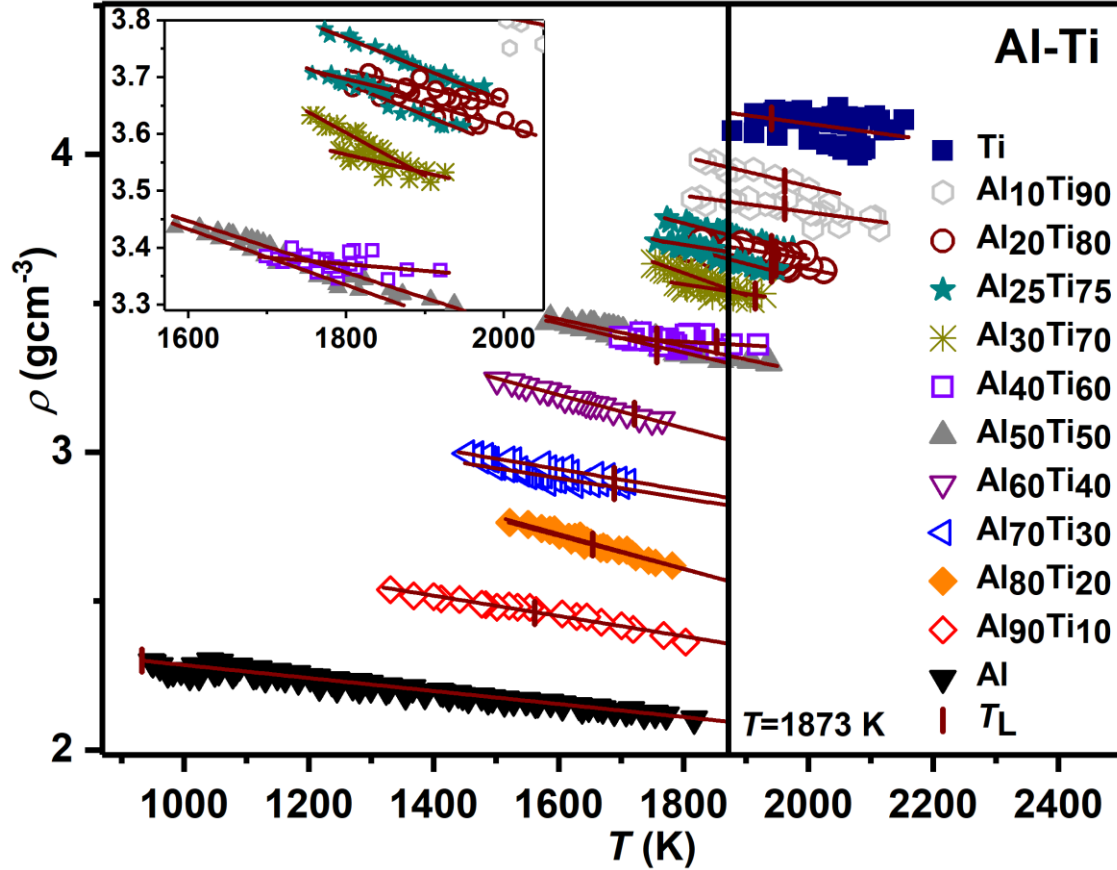


Figure 5.1: Measured density data, ρ , of liquid Al-Ti (symbols) and their linear fits (lines) versus temperature, T , in compliance with Eq. (2.11). The data fits of the pure elements relate to mean values over all measurements of Al and Ti. The inset shows a magnified portion of the figure for Al-mole fractions X_{Al} , ranging from 10 to 50 at.-%. Based on Fig. 2 by Wessing et al. from reference [7] with the Springer copyright license number 4127610503802.

For all compositions depicted in Figure 5.1, the density, ρ , decreases linearly with increasing temperature. Additionally, the density changes gradually with X_{Al} with pure Al exhibiting the lowest density, and Ti the largest, whereas the density values of the alloys lie within these two extremes [7]. The experimentally obtained values of $\rho(T)$ are fitted by Eq. (2.11) with the fits shown in Figure 5.1 by the solid lines, yielding values for ρ_L and ρ_T for each measurement. The resulting data, as well as the thermal expansion coefficient, β , calculated from these data via Eq. (2.13), are listed along with the

corresponding liquidus temperatures in Table 1, containing the data for Al and Ti and Table 3 for the binary alloys [7].

In Table 1 the mean value of ρ_L for liquid Ti amounts to $4.12 (\pm 0.04) \text{ gcm}^{-3}$, corresponding to a relative deviation of 1 %. The respective density temperature coefficient, ρ_T , scatters around $-2.85 (\pm 1.24) \cdot 10^{-4} \text{ gcm}^{-3}\text{K}^{-1}$. The thermal expansion coefficient, β , shows a mean value around $0.69 \cdot 10^{-4}\text{K}^{-1}$ within $0.30 \cdot 10^{-4}\text{K}^{-1}$, hence equal to a 43% relative uncertainty for both ρ_T and β [7].

Comp.	T_L (K)	ρ_L (gcm^{-3})	ρ_T ($10^{-4}\text{gcm}^{-3}\text{K}^{-1}$)	ρ ($T = 1873\text{K}$) (gcm^{-3})	β (10^{-4}K^{-1})
Ti	1941	4.14	-1.48	4.15	0.36
Ti	1941	4.15	-4.4	4.18	1.06
Ti	1941	4.06	-3.14	4.08	0.77
Ti	1941	4.13	-2.38	4.14	0.58
Ti	1941	4.12 ± 0.04	-2.85 ± 1.23	4.14 ± 0.04	0.69 ± 0.30
Al	933	2.32	-2.52	2.08	1.09
Al	933	2.28	-1.88	2.10	0.82
Al	933	2.29	-2.14	2.09	0.93
Al	933	2.30 ± 0.02	-2.18 ± 0.32	2.09 ± 0.01	0.95 ± 0.13

Table 1: Parameters T_L , ρ_L , ρ_T , β , the interpolated density ρ ($T = 1873 \text{ K}$) and their mean values in bold font of pure liquid Al and Ti. The table is based on Table 6 in reference [7].

In the case of Al, ρ_L deviates around a mean value of 2.30 gcm^{-3} , within $\pm 0.02 \text{ gcm}^{-3}$, corresponding to a relative uncertainty of $\pm 0.09 \%$. The respective values of ρ_T show a mean of $-2.18 \cdot 10^{-4} \text{ gcm}^{-3}\text{K}^{-1}$, within $\pm 0.32 \cdot 10^{-4} \text{ gcm}^{-3}\text{K}^{-1}$, according to $\pm 15 \%$ relative deviation. The corresponding values for β are distributed with 15 % relative uncertainty around $0.95 (\pm 0.13) \cdot 10^{-4}\text{K}^{-1}$ [7].

Comp.	ρ_L (gcm ⁻³)	ρ_T (10 ⁻⁴ gcm ⁻³ K ⁻¹)	Reference	Method
Al	2.37	-2.6	Brillo et al. [96]	A
Al	2.39	-3.9	Schmitz et al. [6]	BP
Al	2.37	-2.6	Kobatake et al. [25]	SD
Al	2.38	-3.3	Kobatake et al. [97]	SD
Al	2.37	-3.1	Butler et al. [43]	G
Al	2.38	-2.3	Kaptay et al. [44]	G
Al	2.38	-2.3	Tanaka et al. [45]	R
Al	2.37	-3.1	Tanaka et al. [98]	R
Al	2.36	-3.3	Gebhardt et al. [99]	EML
Al	2.36	-3.0	Gebhardt et al. [99]	EML
Al	2.29	-2.5	Gebhardt et al. [99]	EML
Al	2.36 ± 0.03	-2.91 ± 0.50		
Ti	4.17	-2.2	Kaptay et al. [46]	ESL
Ti	4.10	-9.9	Wynblatt et al. [47]	ESL
Ti	4.21	-5.1	Cummings et al. [75]	ESL
Ti	4.14	-2.25	Tanaka et al. [45]	R
Ti	4.29	-2.3	Antion et al. [48]	WE
Ti	4.1	-3.3	Gebhardt et al. [99]	EML
Ti	4.17 ± 0.07	-4.18 ± 3.02		

Table 2: Parameters ρ_T and ρ_L and its mean values in bold font for the density of pure Al and Ti selected from the literature. The references and methods are specified in the fourth and fifth column, and the method key can be found in *Method abbreviations*. The table is based on Table 3 in reference [7].

Table 2 contains data for ρ_L and ρ_T , and their mean values selected from the literature along with the references and used method. Figure 5.2 and Figure 5.3 show the corresponding dependencies $\rho(T)$ according to Eq. (2.11) of the literature data, the results of this work and the work of Wessing et al. [7] for Al and Ti, respectively.

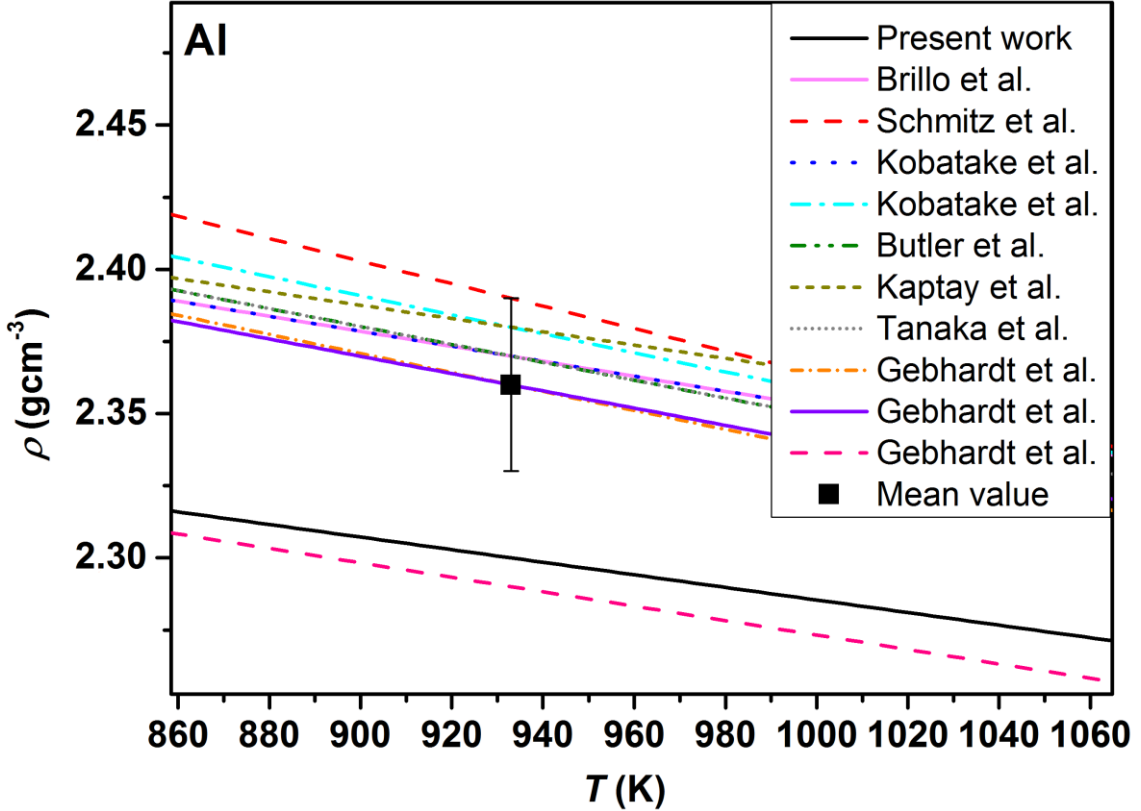


Figure 5.2: Temperature-dependent density, $\rho(T)$, of liquid Al by Eq. (2.11). The corresponding ρ_L and ρ_T data are taken from this work and [7] (solid line) as a mean value of all measurements, literature data (non-solid lines with references given in Table 2) and the corresponding mean value at the liquidus temperature (933 K), including error bars showing the statistical uncertainty.

In the case of pure Al (Table 2 and Figure 5.2) the mean value of the density-temperature coefficient, ρ_T , of the present work, $-2.18 (\pm 0.32) \cdot 10^{-4} \text{ gcm}^{-3}\text{K}^{-1}$, agrees well with the respective mean value of the selected literature data of $-2.91 (\pm 0.5) \cdot 10^{-4} \text{ gcm}^{-3}\text{K}^{-1}$ within the uncertainty. However, the ρ_L mean value for pure Al of the present work of $2.30 (\pm 0.02) \text{ gcm}^{-3}$, lies below the errors bars of the mean value, $2.36 (\pm 0.03) \text{ gcm}^{-3}$, given by literature [7].

In the case of Ti, the mean values of the literature data shown in Table 2 and Figure 5.3 amount to $4.17 (\pm 0.07) \text{ gcm}^{-3}$ for ρ_L and $-4.18 \cdot 10^{-4} (\pm 3.02) \cdot 10^{-4} \text{ gcm}^{-3}\text{K}^{-1}$ for ρ_T ,

respectively. Therefore, the data for both parameters ρ_L and ρ_T presented in the present work, [7] (Table 1) are in good agreement with the literature and lie within the error for the mean value of pure Ti [7].

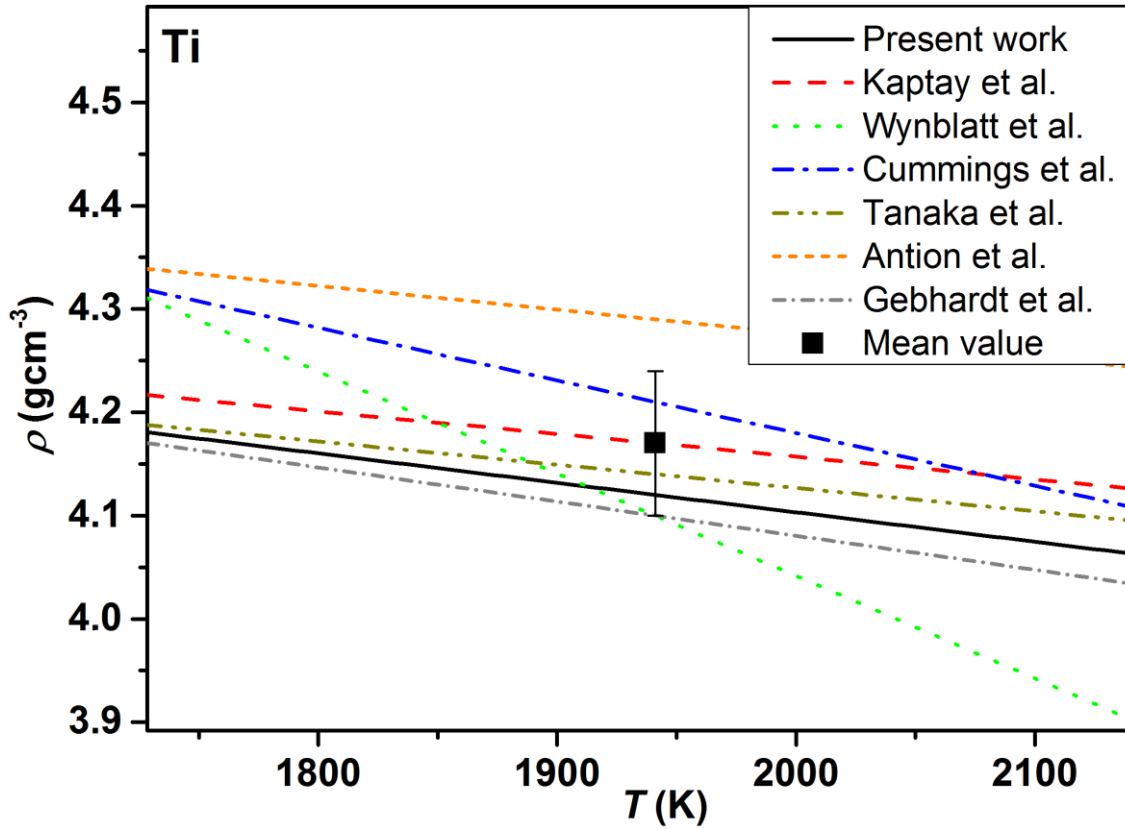


Figure 5.3: Temperature-dependent density, $\rho(T)$, of liquid Ti by Eq. (2.11) plotted with ρ_L and ρ_T data taken from this work, [7] (solid line) as a mean value of all measurements, literature data (non-solid lines with references given in Table 2), the corresponding mean value at the liquidus temperature (1941 K) with error bars showing the statistical uncertainty.

In the case of the binary alloys Al-Ti, the values of ρ_L and ρ_T , obtained by the data fit depicted in Figure 5.1, as well as the corresponding liquidus temperature, T_L , and the thermal expansion coefficient, β , are shown in Table 3. The values of ρ_L change gradually with increasing X_{Al} . Except for $Al_{40}Ti_{60}$, $Al_{60}Ti_{40}$, and $Al_{90}Ti_{10}$, all compositions were measured more than once, and, in these cases, the observed scattering in ρ_L , ρ_T and β was in the same order of magnitude as for the pure elements [7].

Generally, the precise determination of ρ_T and, consequently of β , is highly sensitive to the accuracy of the data points determined at the margins of the temperature intervals. These data points are most exposed to the impact of potential sources of error, such as evaporation at high temperatures, or possible oxide formation, inter alia, at lower temperatures. In the case of this work, this led to relatively large deviations in both values of up to 43 % (Table 1 and Table 3).

However, the magnitude of the variation among the different values for ρ_T and β over all compositions (Table 3), X_{Al} , lies within the deviations for one composition. Therefore, it is justified to claim that with respect to the experimental accuracy of the data, ρ_T is basically constant with a mean value of $-3.83 (\pm 1.6) \cdot 10^{-4} \text{ gcm}^{-3}$ [7].

This is in accordance with β , for which a mean value of $1.18 (\pm 0.5) \cdot 10^{-4} \text{ K}^{-1}$ is found over all compositions. This is illustrated in Figure 5.4 by the values of the thermal expansion coefficient, β , with a relative uncertainty of 43 % plotted against the mole fractions, X_{Al} , ranging from 0 to 100 at.-%. However, considering the β value of $0.35 \cdot 10^{-4} \text{ K}^{-1}$ for $X_{Al} = 40$ at.-% an outlier, one might interpret a trend that shows the lowest β values for the pure elements and relatively higher values for the binary alloys. Moreover, it has to be taken into account that the mean β values for the pure components amount to 0.69 and $0.95 \cdot 10^{-4} \text{ K}^{-1}$ for Ti and Al, respectively which indicates an additional progression of β over the composition range.

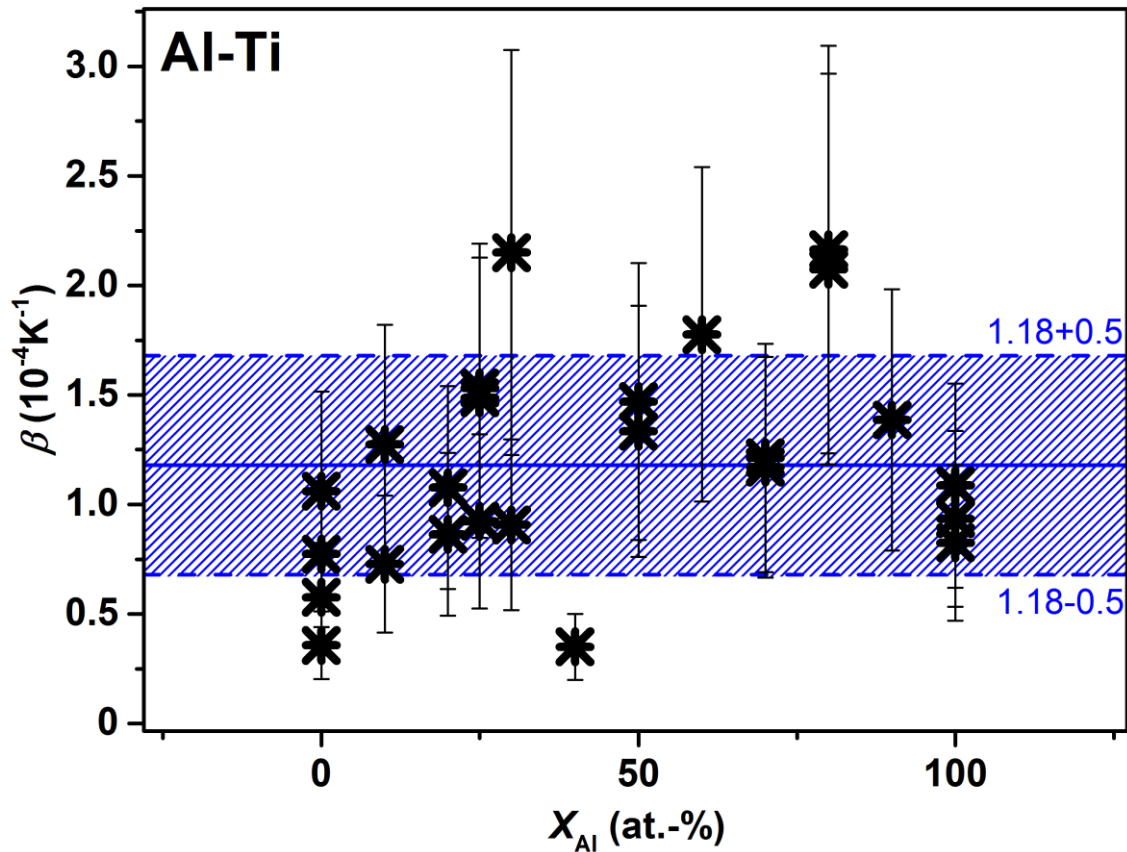


Figure 5.4: Thermal expansion coefficient, β , with a relative statistical uncertainty of 43 % against the corresponding mole fractions, X_{Al} , ranging from 0 to 100 at.-%.

Comp.	T_L (K)	ρ_L (gcm ⁻³)	ρ_T (10 ⁻⁴ gcm ⁻³ K ⁻¹)	ρ ($T = 1873$ K) (gcm ⁻³)	β (10 ⁻⁴ K ⁻¹)
Al ₁₀ Ti ₉₀	1962	3.91	-4.98	3.96	1.27
Al ₁₀ Ti ₉₀	1962	3.82	-2.78	3.84	0.73
Al ₂₀ Ti ₈₀	1948	3.63	-3.91	3.66	1.08
Al ₂₀ Ti ₈₀	1948	3.67	-3.17	3.69	0.86
Al ₂₅ Ti ₇₅	1941	3.69	-5.49	3.73	1.49
Al ₂₅ Ti ₇₅	1941	3.65	-3.37	3.67	0.92
Al ₂₅ Ti ₇₅	1941	3.61	-5.53	3.65	1.53
Al ₃₀ Ti ₇₀	1915	3.52	-7.57	3.55	2.15
Al ₃₀ Ti ₇₀	1915	3.53	-3.2	3.54	0.91
Al ₄₀ Ti ₆₀	1853	3.37	-1.18	3.36	0.35
Al ₅₀ Ti ₅₀	1757	3.34	-4.91	3.36	1.47
Al ₅₀ Ti ₅₀	1757	3.38	-4.51	3.32	1.33
Al ₆₀ Ti ₄₀	1721	3.13	-5.56	3.04	1.77
Al ₇₀ Ti ₃₀	1689	2.91	-3.53	2.85	1.21
Al ₇₀ Ti ₃₀	1689	2.88	-3.37	2.82	1.17
Al ₈₀ Ti ₂₀	1654	2.69	-5.82	2.57	2.16
Al ₈₀ Ti ₂₀	1654	2.69	-5.58	2.57	2.07
Al ₉₀ Ti ₁₀	1562	2.46	-3.41	2.36	1.39

Table 3: Parameters T_L , ρ_L , ρ_T , β and the extrapolated density ρ ($T = 1873$ K) of the investigated liquid alloys Al_xTi_{100-x}. The table is based on Table 5 in reference [7].

5.1.2 Discussion

In addition to the values above, Table 1 and Table 2 also display the isothermal density calculated from Eq. (2.11) at $T=1873$ K. This temperature was chosen as an intermediate temperature with respect to all temperature ranges covered by the experiments. From the Tables it can be seen that $\rho(T = 1873 \text{ K})$ decreases monotonically from $\rho_{\text{Ti}} = 4.14 (\pm 0.04) \text{ gcm}^{-3}$ to $\rho_{\text{Al}} = 2.09 (\pm 0.01) \text{ gcm}^{-3}$ upon increasing X_{Al} [7].

In section 2.1 the term isothermal molar volume, V , was introduced, which can be derived from the mass density by Eq. (2.9) with the molar masses, in the case of Al and Ti accounting to 26.98 gmol^{-1} and 47.87 gmol^{-1} , respectively. In contrast to the mass density, the molar volume is an additive quantity. If only the mass density is considered, effects originating from the packing and ordering of atoms could be obscured by the mass differences between the pure elements, Al and Ti. Therefore, to illustrate and understand how the density changes with composition, to consider the isothermal molar volume instead of the mass density is more insightful [7].

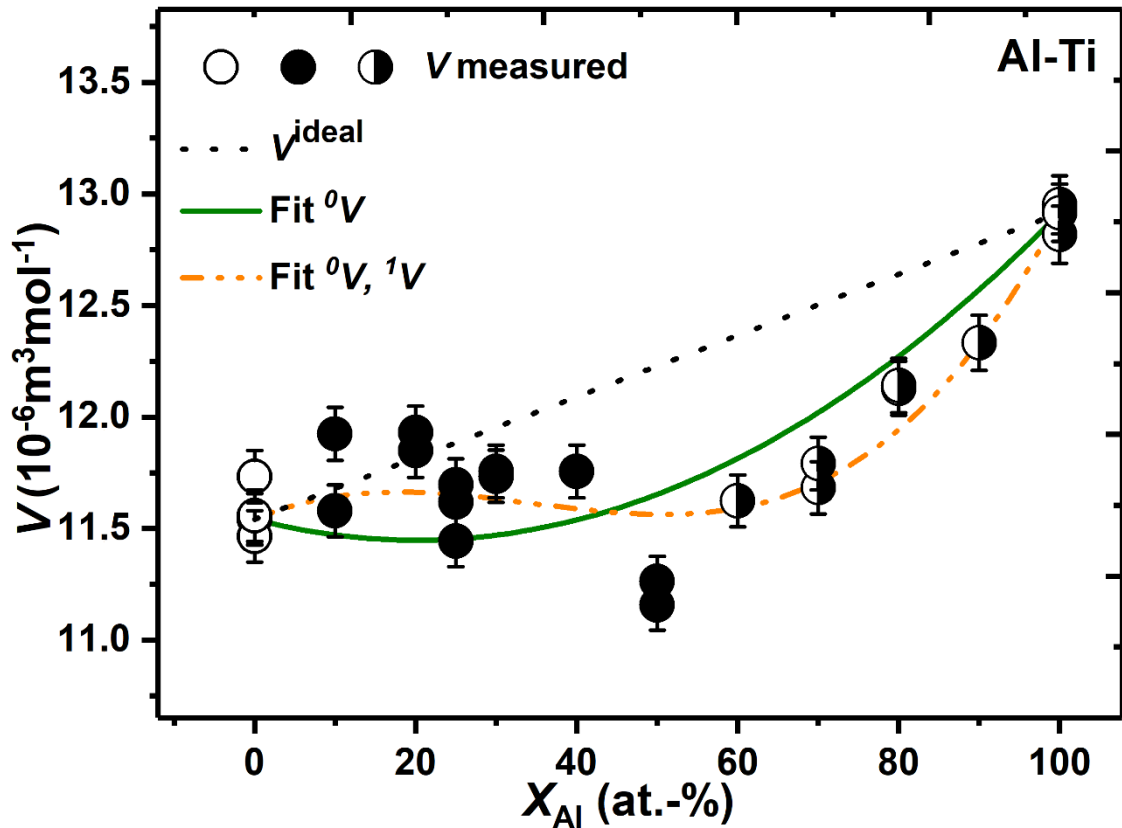


Figure 5.5: Molar volumes in dependence of the mole fraction, X_{Al} , at $T = 1873$ K (solid circles), molar volumes extrapolated to a temperature range below (hollow circles) and above (half-solid circles) measurement conditions. The lines show the ideal molar volumes (dotted line) and fitted molar volumes with one fit parameter, 0V , (solid line) and two fit parameters, 0V and 1V , (dashed-dotted-dotted line), following Eq. (4, 5). The Figure is taken from reference [7], Fig. 3.

In Figure 5.5, the molar volume at 1873 K is considered and plotted versus X_{Al} . Due to the aforementioned temperature range boundaries, for some alloys, 1873 K lies outside the actual measured temperature range, and the values were derived from an extrapolated density through Eq. (2.11). This is reasonable, as the precise location of the phase boundaries is not crucial in this context, but the properties of the stable (or metastable) melt are of primary interest. As can be seen from the figure, the measured molar volume, V , generally increases with an increasing mole fraction, X_{Al} , between the respective mean values of the pure elements Ti and Al from $11.54 \text{ cm}^3\text{mol}^{-1}$ to $12.92 \text{ cm}^3\text{mol}^{-1}$. Starting on the right side in Figure 5.5 at the molar volume of Al, V steeply decreases with increasing X_{Al} , for $X_{\text{Al}} > 30 \text{ at.-%}$. Whereas, for $X_{\text{Al}} \leq 30 \text{ at.-%}$, there seems to be the tendency that V only slightly increases. However, this tendency is beyond the scatter of the experimental data [7].

Figure 5.5 additionally shows the calculated ideal molar volume, V^{ideal} , at $T = 1873 \text{ K}$ as a function of Al concentration, X_{Al} . The ideal molar volume was calculated by Eq. (2.8) using the averaged density values of the pure components presented in this work, [7] at $T = 1873 \text{ K}$, as $\rho_{\text{Al}} = 2.09 \text{ gcm}^{-3}$ and $\rho_{\text{Ti}} = 4.14 \text{ gcm}^{-3}$ [7]. The deviation between the measured molar volume, V , and the ideal molar volume, V^{ideal} , is defined as the excess molar volume, V^{E} , in Eq. (2.5) and depicted in Figure 5.6. In Figure 5.5, $V(X_{\text{Al}})$, as well as the Redlich-Kister polynomial fits of zeroth ($N = 0$) and first ($N = 1$) order by Eq. (2.6) are displayed. The fitted, temperature-dependent excess parameters, 0V and 1V , are listed in Table 4 [7].

ν	${}^\nu V(T) (\text{m}^3\text{mol}^{-1})$
0	$0.00247 \cdot T - 6.55516$
1	$-0.001 \cdot T + 4.3711$

Table 4: Coefficients ${}^\nu V(T)$ of Redlich-Kister type polynomial fit, following Eq. (2.6) for fitted excess molar volumes, V^{E} . The table is based on Table 7 in reference [7].

With respect to V^{ideal} , the fitted V values exhibit a negative deviation, which corresponds to a negative excess molar volume apparent in Figure 5.5. In the case of a fitted excess molar volume with $N = 0$ in Eq. (2.6), a concave progression is exhibited, with the maximum negative excess molar volume of around $-0.37 \cdot 10^{-6} \text{ m}^3\text{mol}^{-1}$ for an Al concentration, $X_{\text{Al}} \approx 20 \text{ at.-%}$ (Figure 5.5).

In the case of an excess molar fit with $N = 1$ (Figure 5.5 and Figure 5.6), V steeply increases with increasing Al concentration with a maximum negative excess molar volume, $V^{\text{E}} \approx -0.8 \cdot 10^{-6} \text{ m}^3\text{mol}^{-1}$, for $X_{\text{Al}} = 67 \text{ at.-%}$. For $X_{\text{Al}} < 16 \text{ at.-%}$, V only slightly decreases and shows a minor local maximum at $X_{\text{Al}} = 16 \text{ at.-%}$. Then, for $16 \text{ at.-%} < X_{\text{Al}}$

< 60 at.-%, V slightly decreases. Finally, V slightly increases again with increasing Al concentration for $X_{\text{Al}} > 60$ at.-% until its final value is reached for pure Al [7].

Both non-ideal fits are in good agreement with the data, in contrast to the ideal molar volume V^{ideal} . Consequently, referring to the density and molar volume, it is justified to report that Al-Ti is a highly non-ideal system with distinct negative excess molar volumes. Among the fits of zeroth and first order, the fit of first-order reproduces the data, as well as the data trend more accurately. Therefore, two fit parameters, 0V and 1V , should be considered when describing the excess molar volume in the binary Al-Ti system [7].

When drawing a literature comparison, among other binary Ti-containing systems two fit parameters are generally used to fit molar volume data quantitatively and qualitatively well, as in the case of Cu-Ti [100, 101]. However, a positive excess volume has been found in the Cu-Ti system. Nonetheless, negative excess molar volumes have been found in other Al-containing systems such as Al-Ni [7, 12], Al-Fe [12], Al-Ag [84] and Al-Cu [102].

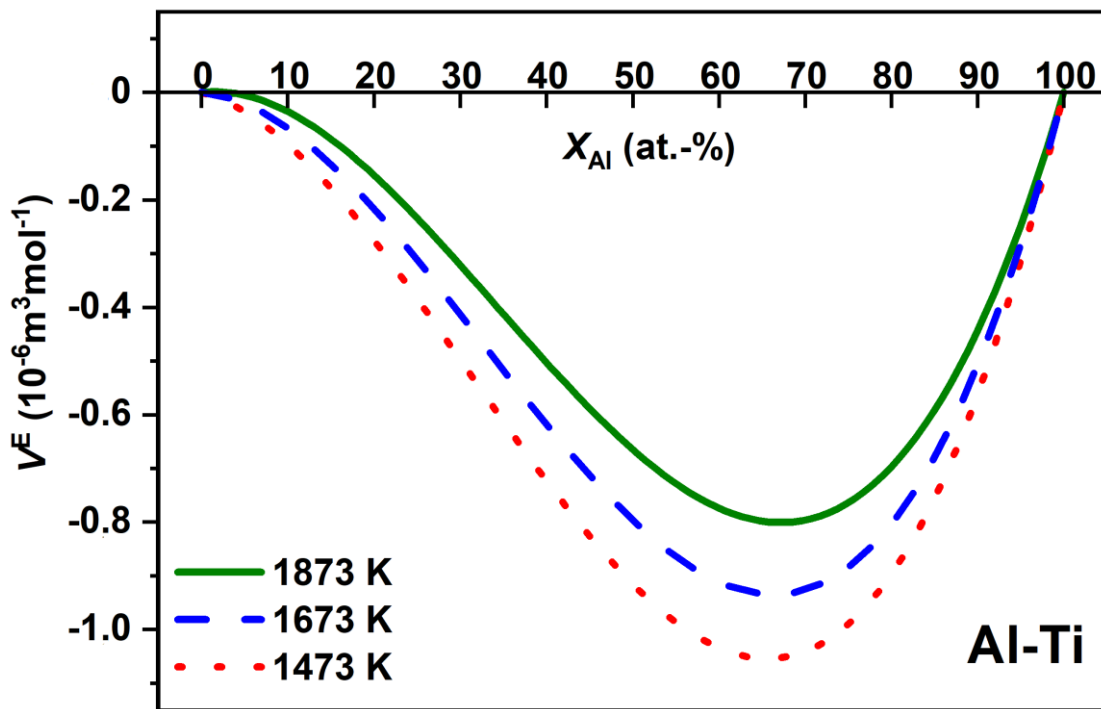


Figure 5.6: Fitted excess molar volumes, V^E (Eq. (2.6)), of first-order fits ($N = 1$) at $T = 1473$ K (dotted line), 1673 K (dashed line) and 1873 K (solid line).

Overall, the results of this work, [7] are in good agreement with literature data. This can also be consolidated by the investigations by Peng et al. for the Al-Au system [103]. According to Peng et al., non-ideal mixing behavior occurs due to apparent decreasing atomic radii of the Al atoms in the Al-Au system, leading to a shrunken close packing, especially of the Al-Al pairs [104]. Taking this into account, similar processes in the Al-

Ti system are likely. Further investigations, e.g., MD simulations, experiments with neutron and X-ray scattering could provide a wider insight to confirm these processes.

Figure 5.6 illustrates plotted and fitted isothermal excess molar volumes, V^E , as a function of the Al concentration, X_{Al} , for different temperatures, $T = 1473$ K, 1673 K, and 1873 K. Based on its definition, the excess molar volume for the pure elements Al and Ti equals zero in Figure 5.6 [7].

For all temperatures, the values show a concave shape with a maximum negative value of up to $V^E \approx -1.05 \cdot 10^{-6} \text{m}^3 \text{mol}^{-1}$ for $X_{Al} \approx 60\text{-}70$ at.-%. With increasing temperatures, the maximum negative excess molar volumes are shifted to higher Al concentrations while they are decreasing in their maximum value. This shift indicates that at lower temperatures relatively higher efficient packing and interactions take place. Whereas at higher temperatures, pronounced atomic mobility and dynamics suppress those interactions and entropy becomes the dominant factor [7].

In this section, the results for density and molar volume have been presented and discussed. It has been found that Al-Ti is a highly non-ideal system showing non-ideal density and molar volume in the composition dependence. Significantly highly negative values are found for the excess molar volume, which is in good agreement with other binary Ti-containing systems. A comparison with other properties and their composition dependence will be conducted in the next chapter 6, and finally, all results will be briefly summarized in chapter 7.

5.2 Normal spectral emissivity

The following section addresses the measurement results obtained at the EML-facility of the Fukuyama lab for normal spectral emissivity which are also taken as input data for the isobaric heat capacity evaluation presented in section 5.3. The temperature and composition dependencies are discussed and compared to literature results. This section is based on the sections 2.2 and 3.6 where the respective theoretical background and the experimental methods have been introduced.

5.2.1 Results

Figure 5.7 shows the relation between the spectral radiance estimated by Planck's law and the output count intensity of the spectrometer at 800 and 940 nm wavelengths. From the calibration of the linear dependence of the spectral radiance on the output count intensity, the respective sample radiance at a certain temperature and wavelength can be determined.

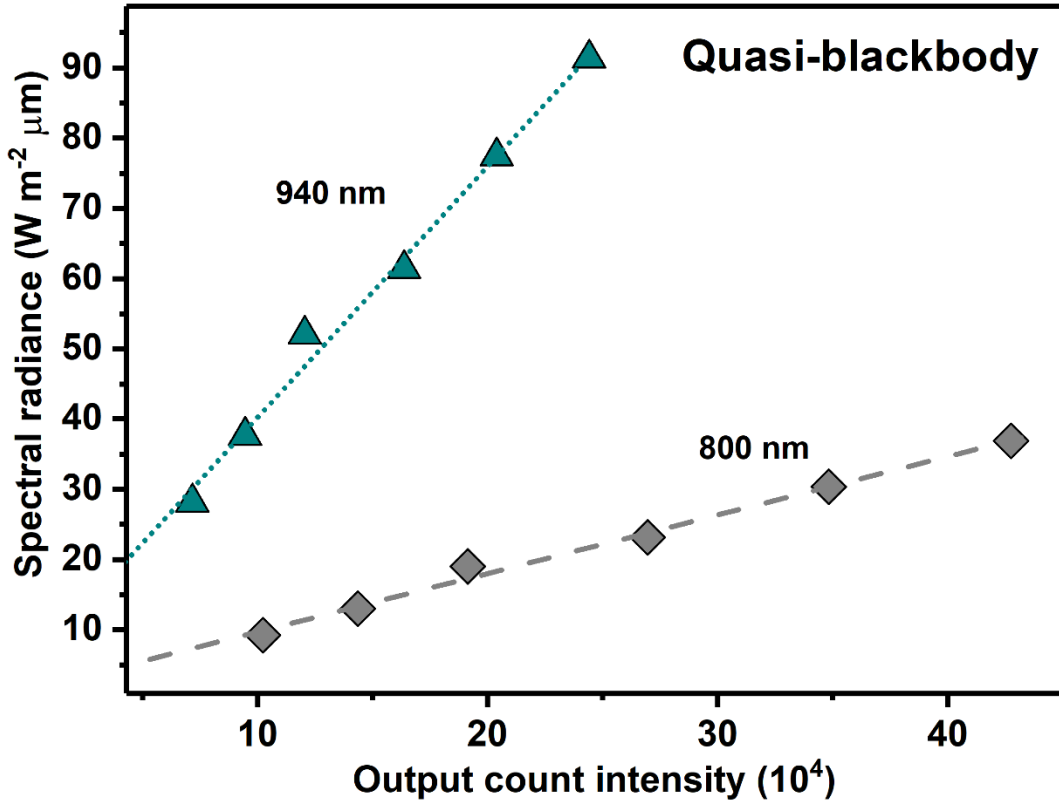


Figure 5.7: Relation between the spectral radiance and output count intensity of the spectrometer at 800 nm (diamonds) and 940 nm (triangles) wavelength.

Comp.	T_L (K)	$\varepsilon \phi$	T-range (K)
Al ₇₀ Ti ₃₀	1689	0.3026 ± 0.0063	1706 - 1815
Al ₅₀ Ti ₅₀	1757	0.3150 ± 0.0026	1734 - 1838
Al ₂₀ Ti ₈₀	1948	0.4006 ± 0.0061	1949 - 1987
Ti	1941	0.3675 ± 0.0053	1933 - 1970

Table 5: Composition, liquidus temperature and normal spectral emissivity as an average over the measured temperature range with the respective standard deviations of the Al-Ti melts at 940 nm wavelength.

Figure 5.8 shows the measured emissivity data of Ti, Al₂₀Ti₈₀, Al₅₀Ti₅₀, and Al₇₀Ti₃₀ in dependence of the wavelength. Each alloy was measured at different temperatures as indicated by the different continuous lines of data points for the respective alloys with the alloy specific temperature ranges displayed in the figure and listed in Table 5. As can be seen from Figure 5.8, in the case of Ti and Al₂₀Ti₈₀ the normal spectral emissivity, ε , decreases slightly with increasing wavelength, λ . For Al₅₀Ti₅₀ the normal spectral emissivity stays constant over the wavelength range while for Al₇₀Ti₃₀ an overall increase of the normal spectral emissivity can be observed with increasing wavelength. The latter

however, seems to show an almost constant wavelength dependence in the range above 800 nm.

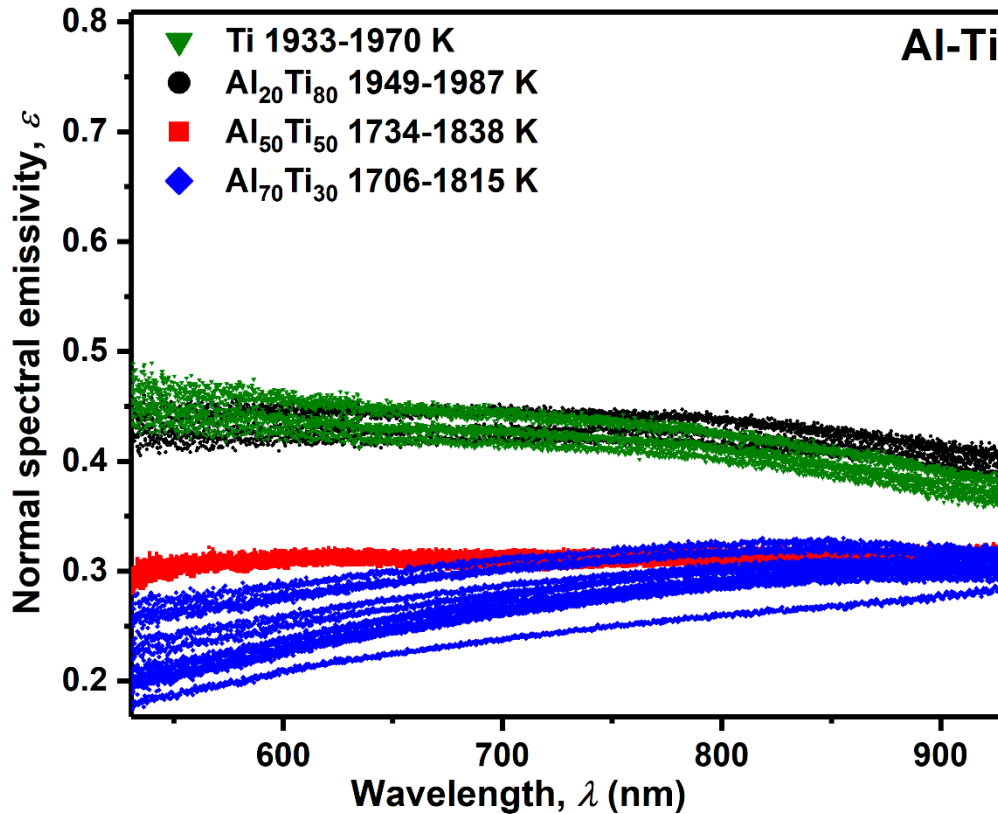


Figure 5.8: Normal spectral emissivity of Ti (green triangles), $\text{Al}_{20}\text{Ti}_{80}$ (black circles), $\text{Al}_{50}\text{Ti}_{50}$ (red squares) and $\text{Al}_{70}\text{Ti}_{30}$ (blue diamonds) in dependence of the wavelength.

Based on these results at a wavelength of 940 nm, Figure 5.9 shows the normal spectral emissivity of the Al-Ti melts along with the respective experimental error as a function of temperature, as discussed in section 3.6. The depicted experimental temperature range covers 1706-1987 K over all compositions and measurements with the alloy specific temperature ranges listed in Table 5.

For all alloys a negligible temperature dependence is exhibited and, therefore, a constant value over the investigated temperature range assumed. This validates the temperature measurement approach (section 3.2.3) using a single-color pyrometer calibrated at the liquidus temperature and assuming the wavelength to be constant over the investigated temperature range. However, it must be noted that for Ti, $\text{Al}_{20}\text{Ti}_{80}$ and $\text{Al}_{70}\text{Ti}_{30}$ one outlier from the constant mean value is visible within each alloy measurement, which will be discussed in the *Discussion* of this chapter. The corresponding results for the average emissivities are listed in Table 5, along with the experimental error, as described in the *Appendix*, the liquidus temperature, and the investigated temperature range. The same values serve as input data for the heat capacity evaluation as presented in section 5.5.

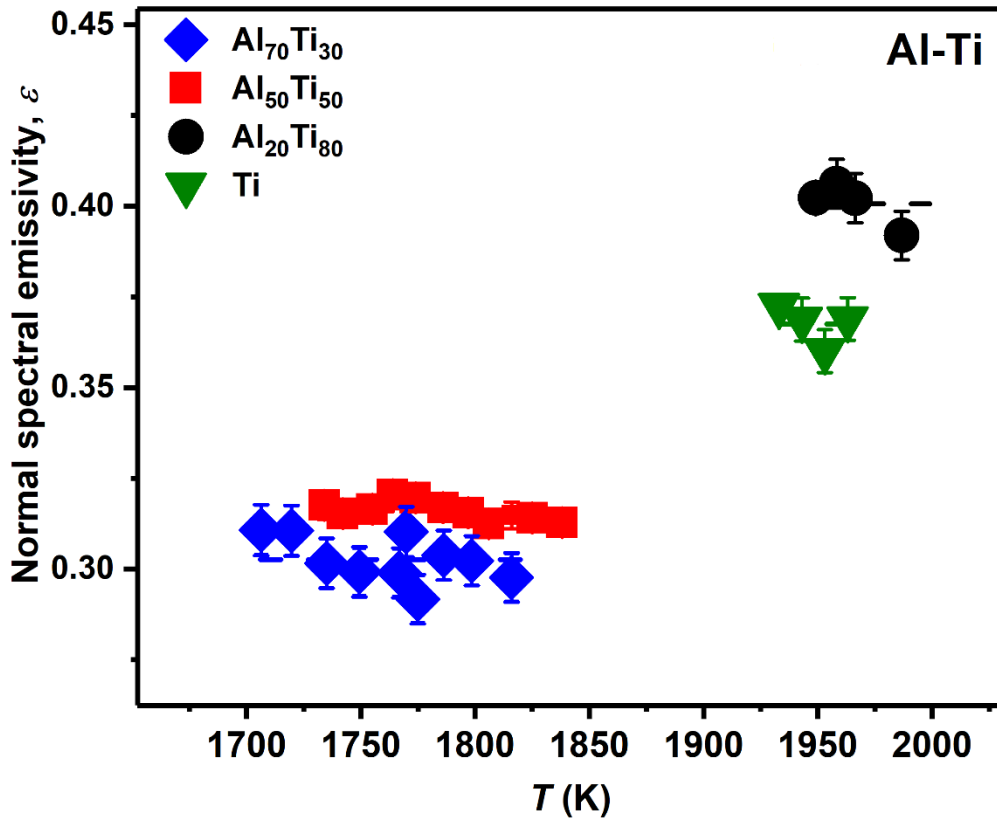


Figure 5.9: Experimental results (symbols) and average values (solid lines) of the normal spectral emissivity at 940 nm wavelength of Ti (green triangles), Al₂₀Ti₈₀ (black circles), Al₅₀Ti₅₀ (red squares) and Al₇₀Ti₃₀ (blue diamonds) in dependence of the temperature of Al-Ti melts. The error bars show the expanded uncertainty as discussed in the *Appendix*.

5.2.2 Discussion

The wavelength dependence of the normal spectral emissivity was introduced in the *Results* section of this chapter and depicted in Figure 5.8. As described in this section, different trends for the respective alloys can be observed. Generally, the emissivity of pure, uncontaminated metals has been reported to be almost constant but slightly decreasing with increasing wavelength except for the upper wavelength range above about 1 μm [105]. This has been found for example in the cases of Cu [28], Fe [36], Ag and Au [88]. Few data exist on the dependence of the emissivity on the wavelength of Al-Ti alloys. Only in the case of pure Ti, a corresponding study has been reported by Teodorescu et al. [105], which is, however, focused on the wavelength region of 1-16 μm . As discussed in the work by Watanabe et al. [88], an emissivity increase upon melting and a negative wavelength dependence can be theoretically derived from the work by Grass [106] which is an approximation based on the Drude model [15, 36, 88]. In the case of Ti and Al₂₀Ti₈₀ the negative wavelength dependence of the emissivity is, therefore, in good agreement with theory and literature. On the other hand, the trend observed for Al₅₀Ti₅₀ and Al₇₀Ti₃₀ with constant and overall positive wavelength dependence,

respectively is not consistent. In these cases, an error contribution in the calibration, measurement or due to contamination could be indicated, and it would be recommended to repeat the wavelength dependent measurements of the emissivity to neglect these factors. However, in this section, the emissivity at a constant wavelength of 940 nm will be discussed. In this wavelength range, both alloys show almost constant wavelength dependencies. Additionally, it will be found in this section that the measured data are in good agreement with other reported results. Overall it is therefore suggested, that the wavelength dependence of the emissivity of $\text{Al}_{50}\text{Ti}_{50}$ and $\text{Al}_{70}\text{Ti}_{30}$ might require further investigation. However, in this context, it is negligible concerning the emissivity at a wavelength of 940 nm which seems to be reasonable and accurate within the experimental error.

As mentioned in the *Results* section of this chapter and shown in Figure 5.9, for Ti, $\text{Al}_{20}\text{Ti}_{80}$, and $\text{Al}_{70}\text{Ti}_{30}$, one outlier beyond the experimental error from the constant mean emissivity over the investigated temperature range must be noted, respectively. The outliers show a deviation to smaller emissivities. As Watanabe et al. [88] investigated, the emissivities of liquid metals are generally larger than those of the respective solids. Therefore, the outliers might indicate the presence of oxide particles on the sample's surface that could reduce the emissivity, as the Al-Ti system is highly sensitive to oxygen (compare section 5.6). On the other hand, it could mean that the experimental error was evaluated as too low and higher temperature error contributions must be taken into account (see error propagation for emissivity in the *Appendix*).

Figure 5.10 displays the composition dependence of the emissivity of the Al-Ti melts taken as an average value over the investigated temperature range from Table 5. The largest emissivity is found for $\text{Al}_{20}\text{Ti}_{80}$ and the lowest for $\text{Al}_{70}\text{Ti}_{30}$ ranging from 0.4006 ± 0.0061 to 0.3026 ± 0.0063 . The data show good agreement with literature data for Ti by Qin et al. [107], Al-Ti alloys by Krishnan et al. [32] and the technical alloy Ti-6Al-4V [8] reported by Boivineau et al. which are listed in Table 6, along with the respective measurement method, temperature range and references.

The data and data trend of the emissivities for Al-Ti alloys measured by Krishnan et al. using electromagnetic levitation coincide well with the results of this work over the whole composition range. Nevertheless, on the Ti-rich side, the results of this work for Ti and $\text{Al}_{20}\text{Ti}_{80}$ show higher values than the value and trend given by Krishnan in the range of $0 \text{ at.-%} < X_{\text{Al}} < 40 \text{ at.-%}$. In the case of Ti, the value given by Krishnan of 0.309 is exceeded by the value of this work of 0.3675 by about 19 %. Lower emissivity values could imply the presence of oxide particles on the sample's surface in the study by Krishnan which can lead to lower emissivity values. The literature data result given by Qin et al. [107] for pure Ti of 0.303 agrees well within 7 % with the data of this work. Additionally, the

indicated data trend in this region by the result of Boivineau et al. seems to correspond to the results of this work for an Al ratio equal or smaller 6 at.-%. Nonetheless, one must keep in mind that even a comparatively small addition of V in the technical alloy Ti-6Al-4V might lead to significant deviations in the emissivity compared to the binary Al-Ti alloys.

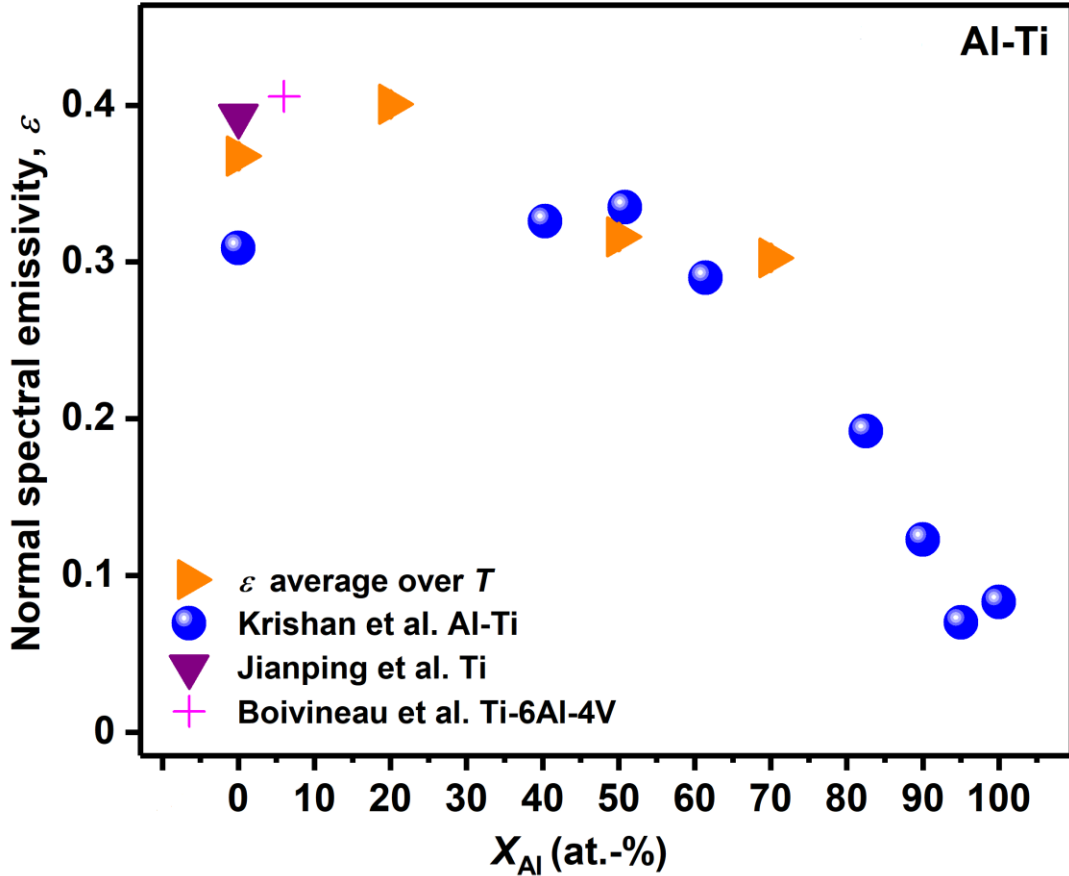


Figure 5.10: Composition dependence of the normal spectral emissivity of Al-Ti melts of experimentally obtained results of this work (right-pointing triangles) and literature data (Table 5 and Table 6).

Generally, the emissivity and its wavelengths dependence are dominated by two major mechanisms. In the longer wavelength range, intraband transitions of free electrons play the dominating role in the optical property while with decreasing wavelength the contributions of free carrier adsorption with interband transitions increase [28, 108]. Generally, the emissivity of metals increases with increasing interband transitions. The absorption edges due to the direct interband transition have been reported to lie in the ultraviolet (10 - 400 nm) and infrared (780 nm - 1 mm) for Al and Ti, respectively with the alloy system assumed to be in between these ranges [32]. Especially on the Al-rich site in the Al-Ti system, the emissivity measured at 940 nm might consequently lie in the intraband dominated range. To validate the weighting of the contributing mechanisms in future works, it is suggested to theoretically calculate the emissivity as a function of wavelength by applying the Drude model. The Drude model gives accurate predictions

in the longer wavelength region where intraband transitions are dominating. Experimental results complying with the Drude model consequently indicate that this mechanism plays the crucial role in the measured wavelength range.

Comp.	ϵ	T-range (K)	Reference	Method
Ti	0.309	1800	Krishnan et al. [32]	He-Ne laser ellipsometry at 632.8 nm
Al _{40.3} Ti _{59.7}	0.326			
Al _{50.8} Ti _{49.2}	0.335			
Al _{61.4} Ti _{38.6}	0.29			
Al _{82.5} Ti _{17.5}	0.192			
Al ₉₀ Ti ₁₀	0.123			
Al ₉₅ Ti ₅	0.07			
Al	0.083			
Ti-6Al-4V	$0.435 - 1.05 \cdot 10^{-5}T$	$T_L - 2920$	Boivineau et al. [8]	Pulse heating and fast laser polarimeter at 684.5 nm
Ti	0.393	1847 - 2430	Qin et al. [107]	EML and partial-radiation pyrometer operating at 650 nm

Table 6: Composition, normal spectral emissivity along with the respective temperature range, reference and method of literature results for unary, binary and multi-component Al-Ti melts.

In this section, the results for normal spectral emissivity have been presented and discussed. The results agree well with literature data [32] over the whole measured composition range. Emissivity is an important input parameter for the calculation of the isobaric heat capacity which is presented in the following section.

5.3 Isobaric heat capacity

In the following section measurement results obtained at the EML-facility of the Fukuyama lab for the isobaric heat capacity are presented. The temperature and composition dependencies are discussed and compared to literature results. Additionally, the composition dependence of the isobaric heat capacity is compared to the Neumann-

Kopp rule and its deviations related to isothermal excess heat capacity. This section is based on sections 2.3 and 3.7 where the respective theoretical background and the experimental methods have been introduced.

5.3.1 Results

A typical example of the temperature response during the isobaric heat capacity measurement in the ac steady state is presented in Figure 5.11 for pure Ti with the modulation frequency 0.3 Hz (1.88 rad s⁻¹). The temperature amplitude, ΔT_{ac} , and the phase shift, ϕ , are measured by changing the modulation angular frequency, ω , to obtain the corresponding relations $\omega-\phi$ and $\omega-\omega\Delta T_{ac}$.

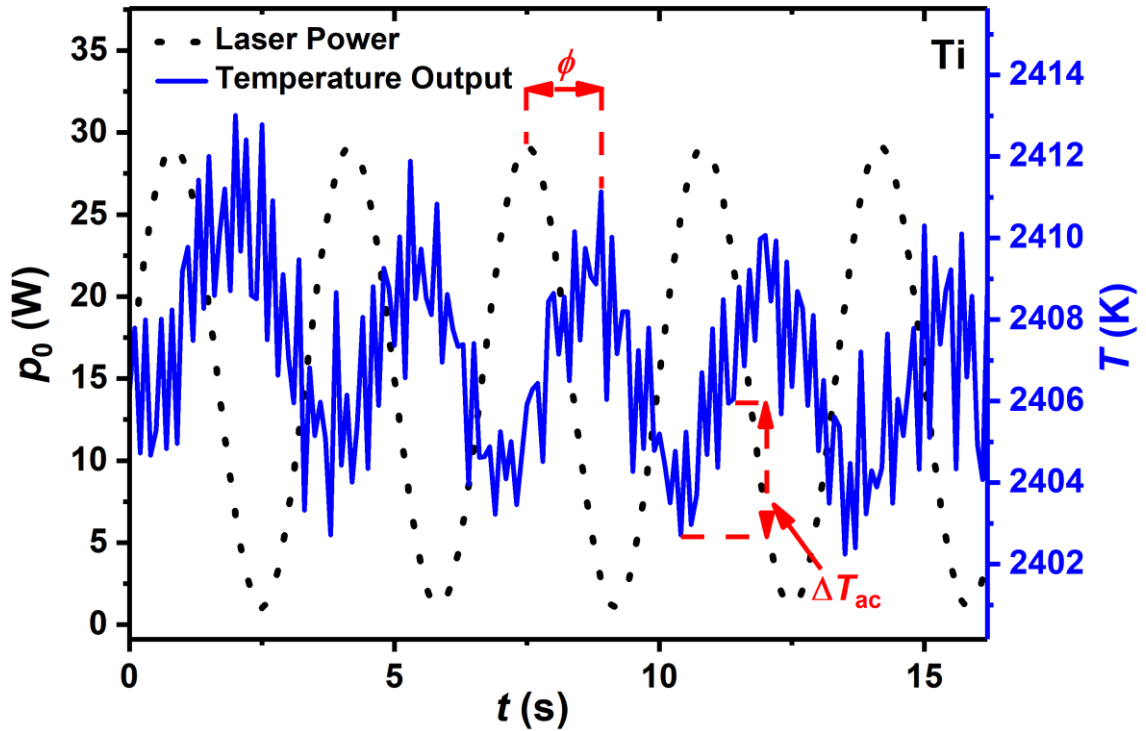


Figure 5.11: Modulated laser power, p_0 (dotted line), and temperature response, T_{ac} (solid line), at steady state in the non-contact modulated laser calorimetry with a modulation angular frequency of 0.1 Hz (0.75 rad s⁻¹).

For Ti at 2015 K, these relations and their fits are shown in Figure 5.12 in dependence of the modulation frequency. The value of $\omega\Delta T_{ac}$ exhibits a maximum value around $\omega = 0.1$ Hz (0.75 rad s⁻¹), where the phase satisfies the requirement of $\phi = 90^\circ$. The relaxation times τ_c and τ_r can be determined by fitting ϕ by Eq. (3.14), leading to values of 0.49 and 6.11, respectively. The correction function, f , can then be evaluated as a function of the modulation frequency corresponding to 0.93 at 0.1 Hz.

Consequently, substituting the correction function, f , and $\omega\Delta T_{ac}$ in Eq. (3.13) leads to the heat capacity, C_P as shown in Figure 5.13. The figure depicts the isobaric molar heat

capacity data of liquid $\text{Al}_{70}\text{Ti}_{30}$, $\text{Al}_{50}\text{Ti}_{50}$, $\text{Al}_{20}\text{Ti}_{80}$ and pure Ti along with the respective experimental errors, as discussed in the *Appendix*. For all compositions, the heat capacity shows negligible temperature dependence. The respective average values are given in Table 7 along with the respective standard deviations at constant pressure.

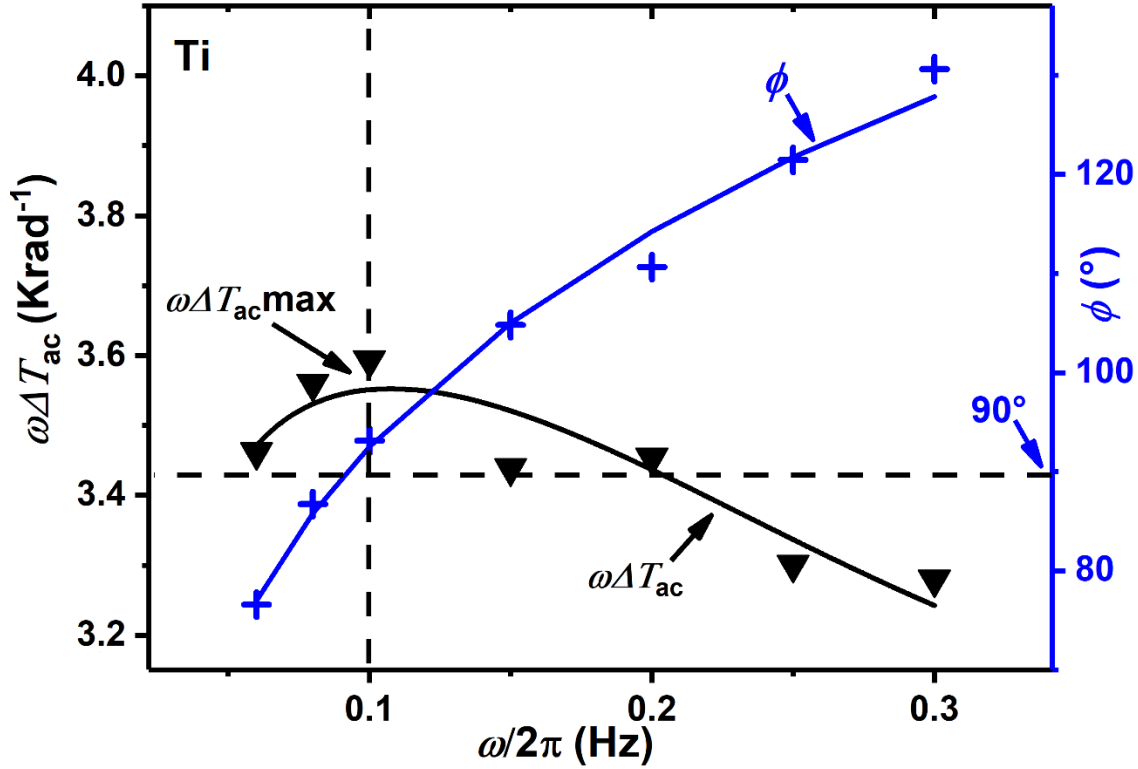


Figure 5.12: Phase shift, ϕ (black triangles), and angular average increase in temperature of the ac component, $\omega\Delta T_{ac}$ (blue crosses), of liquid Ti at 2015 K as a function of the modulation angular frequency. The solid lines represent the nonlinear least squares fitting to the experimental results.

Comp.	T_L (K)	$C_p\phi$ ($\text{JK}^{-1}\text{mol}^{-1}$)	Investig. T-range (K)
$\text{Al}_{70}\text{Ti}_{30}$	1689	57.59 ± 1.47	1665 - 1770
$\text{Al}_{50}\text{Ti}_{50}$	1757	46.20 ± 1.22	1765 - 1886
$\text{Al}_{20}\text{Ti}_{80}$	1948	54.61 ± 1.31	1930 - 2030
Ti	1941	48.50 ± 0.72	1930 - 2030

Table 7: Composition, liquidus temperature and average heat capacity over the measured temperature range along with the respective standard deviations of the Al-Ti melts at constant pressure.

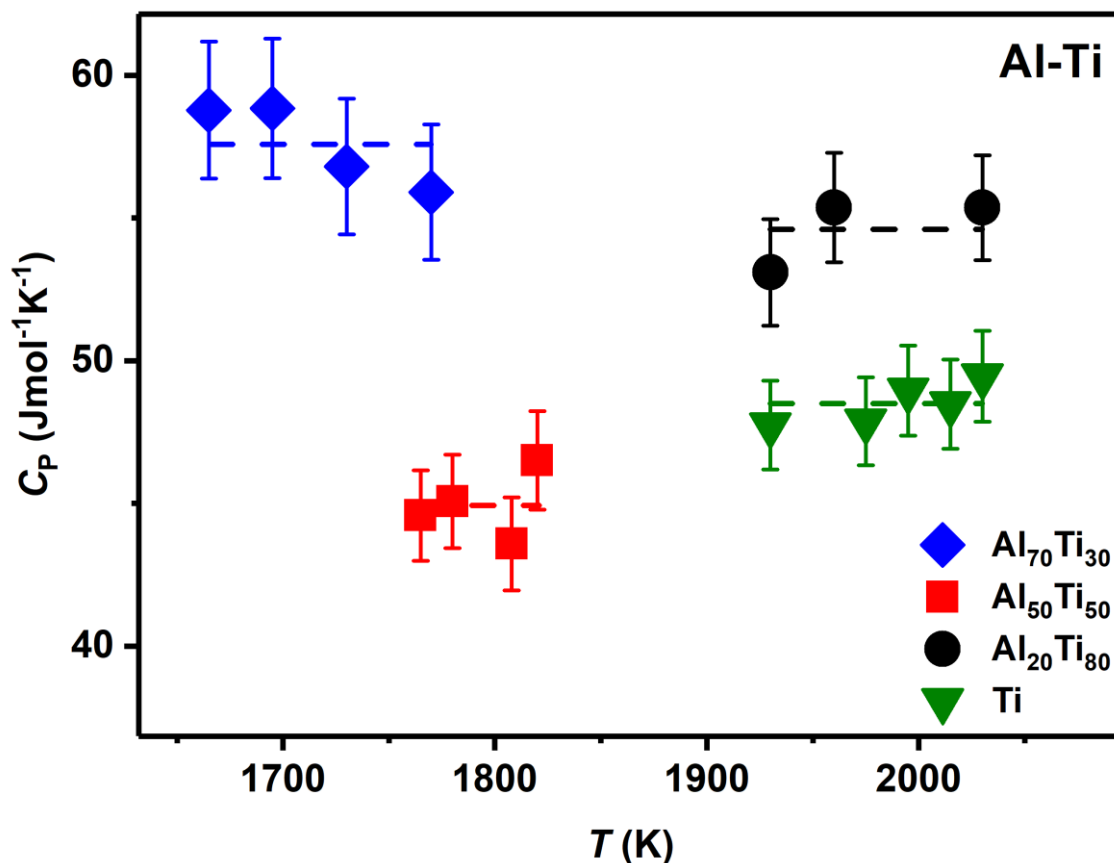


Figure 5.13: Experimental results (symbols) and linear fits (dashed lines) of the isobaric heat capacity of Ti (triangles), Al₂₀Ti₈₀ (circles), Al₅₀Ti₅₀ (squares) and Al₇₀Ti₃₀ (diamonds) in dependence of the temperature. The error bars show the expanded uncertainty as discussed in the *Appendix*.

5.3.2 Discussion

Figure 5.14 shows the composition dependence of the average heat capacity of the Al-Ti melts as given in Table 7. The largest values for the heat capacity are found for Al₇₀Ti₃₀ of about $57.59 \pm 1.47 \text{ Jmol}^{-1}\text{K}^{-1}$ and the lowest for pure Al₇₀Ti₃₀ of about $46.20 \pm 1.22 \text{ Jmol}^{-1}\text{K}^{-1}$. The error bars show the experimental uncertainty as discussed in the *Appendix*.

Also shown are literature data for Al, Ti and technical alloys Ti-6Al-4V and Ti-44Al-8Nb-1B which are listed in Table 8 along with the respective measurement methods, the temperature range, and references. For Ti, the result of this work is in good agreement with the literature data given by NIST-JANAF reference data [109] and Qin et al. [107]. Only the value given by Cagran et al. [9] lies significantly below the value given in this work and the other literature data by about 27 %.

For Al-Ti alloys the data on heat capacity are sparse, and thus, the data for the technical alloys is shown. The data on Ti-6Al-4V vary strongly from $35.5 \text{ Jmol}^{-1}\text{K}^{-1}$ by Reiter et al. [110] to $52.6 \text{ Jmol}^{-1}\text{K}^{-1}$ by Boivineau et al. [8]. Especially the data given by Kaschnitz et al. [111] and Boivineau seem to be in good agreement with the data and data trend of this

work. However, when comparing these data, it should not be disregarded that the addition of V in the technical alloy Ti-6Al-4V might lead to deviations in the heat capacity compared to the binary Al-Ti alloys.

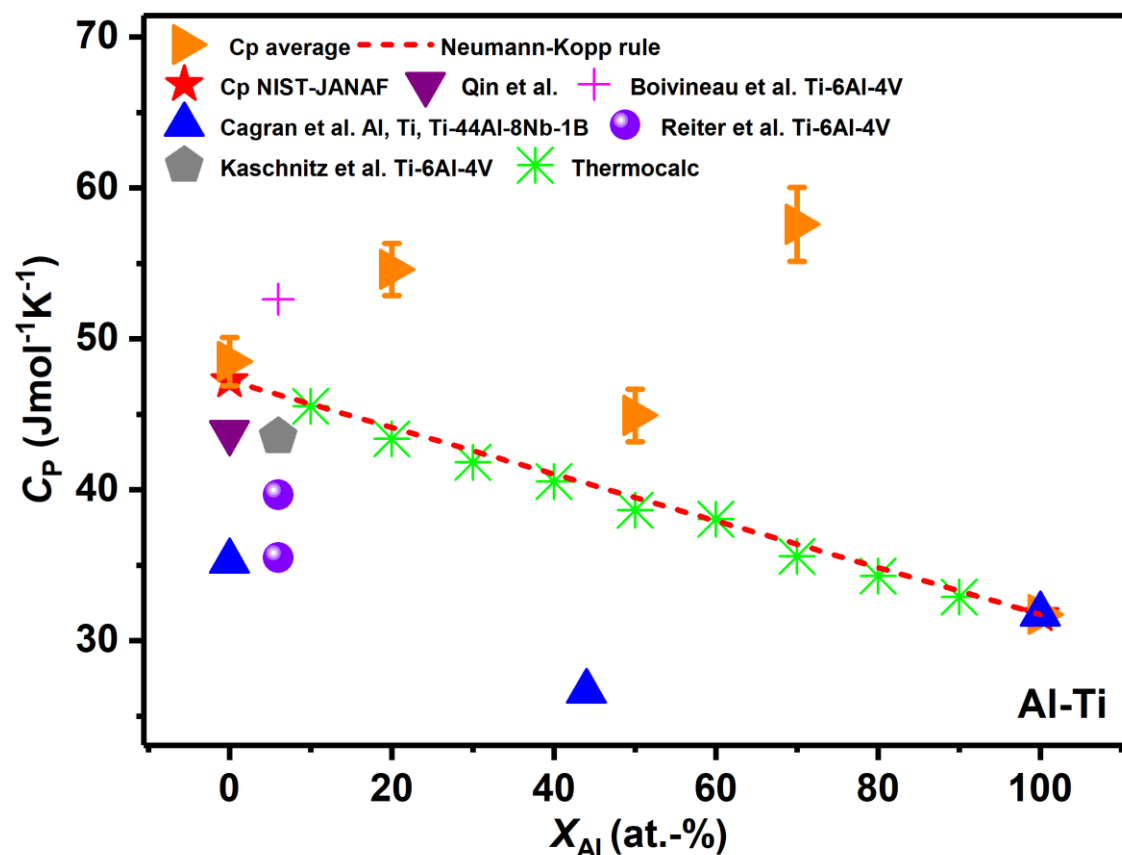


Figure 5.14: Composition dependence of the heat capacity at constant pressure of Al-Ti melts of experimentally obtained results of this work (right-pointing triangles), a linear composition dependence based on the Neumann-Kopp rule (dashed line) and literature results (Table 7 and Table 8).

The same applies to the heat capacity value for Ti-44Al-8Nb-1B by Cagan et al. which deviates significantly from the result of the heat capacity of $\text{Al}_{50}\text{Ti}_{50}$ given in this work by about $22 \text{ Jmol}^{-1}\text{K}^{-1}$. Nevertheless, besides the composition differences, it can be also taken into account that Cagan et al. underestimate the heat capacity value of Ti, with respect to other reference values and literature data. The dashed line in Figure 5.14 illustrates the ideal heat capacities of Al-Ti according to the Neumann-Kopp relation, calculated by Eq. (2.18), with $C_p^{\text{Al}} = 31,75 \text{ Jmol}^{-1}\text{K}^{-1}$ and $C_p^{\text{Ti}} = 47,24 \text{ Jmol}^{-1}\text{K}^{-1}$ taken from the NIST-JANAF reference data [109]. The data from the Thermocalc software [112] for the Al-Ti heat capacities for Al-Ti comply well with the Neumann-Kopp rule and seem to be determined from the same reference data derived from the enthalpies of mixing. All values for the heat capacity values of Al-Ti exceed the values for the ideal heat capacities with a maximum for $\text{Al}_{70}\text{Ti}_{30}$ amounting to a difference of $20.1 \text{ Jmol}^{-1}\text{K}^{-1}$.

Comp.	C_p ($\text{JK}^{-1}\text{mol}^{-1}$)	T -range (K)	Reference	Method
Ti	47.24	1939 - 3631	NIST-JANAF [109]	derived from enthalpy measurements in crucibles
Al	31.75	720 - 3000		
Ti-6Al-4V	52.63	T_L - 2920	Boivineau et al. [8]	differential scanning calorimeter (DSC)
Ti	43.79	1847 - 2430	Qin et al. [107]	derived from enthalpy measurements by levitation-drop calorimetry
Ti	35.28	1800	Cagran et al. [9]	pulse-heating
Ti-44Al-8Nb-1B	26.65			
Al	31.76			
Ti-6Al-4V	35.52	1650	Reiter [110]	ms pulse-heating
	39.68	1900		
Ti-6Al-4V	43.51 \emptyset over T -range	1400 - 2300	Kaschnitz et al. [111]	ms and μs pulse-heating

Table 8: Composition, isobaric heat capacity along with the respective temperature range, reference and method of literature results for unary, binary and multi-component Al-Ti melts.

The deviation between the ideal heat capacity and the measured heat capacity is called excess heat capacity, C_p^E , and defined by Eq. (2.19). Figure 5.15 depicts the excess heat capacity of Al-Ti with respect to an ideal heat capacity calculated by the Neumann-Kopp rule using the aforementioned NIST-JANAF reference data for Al and the Ti result of this work given in Table 7. The excess heat capacity is positive for all compositions. The dashed line in Figure 5.15 illustrates a fit of the excess heat capacity by a Redlich-Kister polynomial in accordance with Eq. (2.20) with the fit parameters, 0c , 1c and 2c , listed in Table 9.

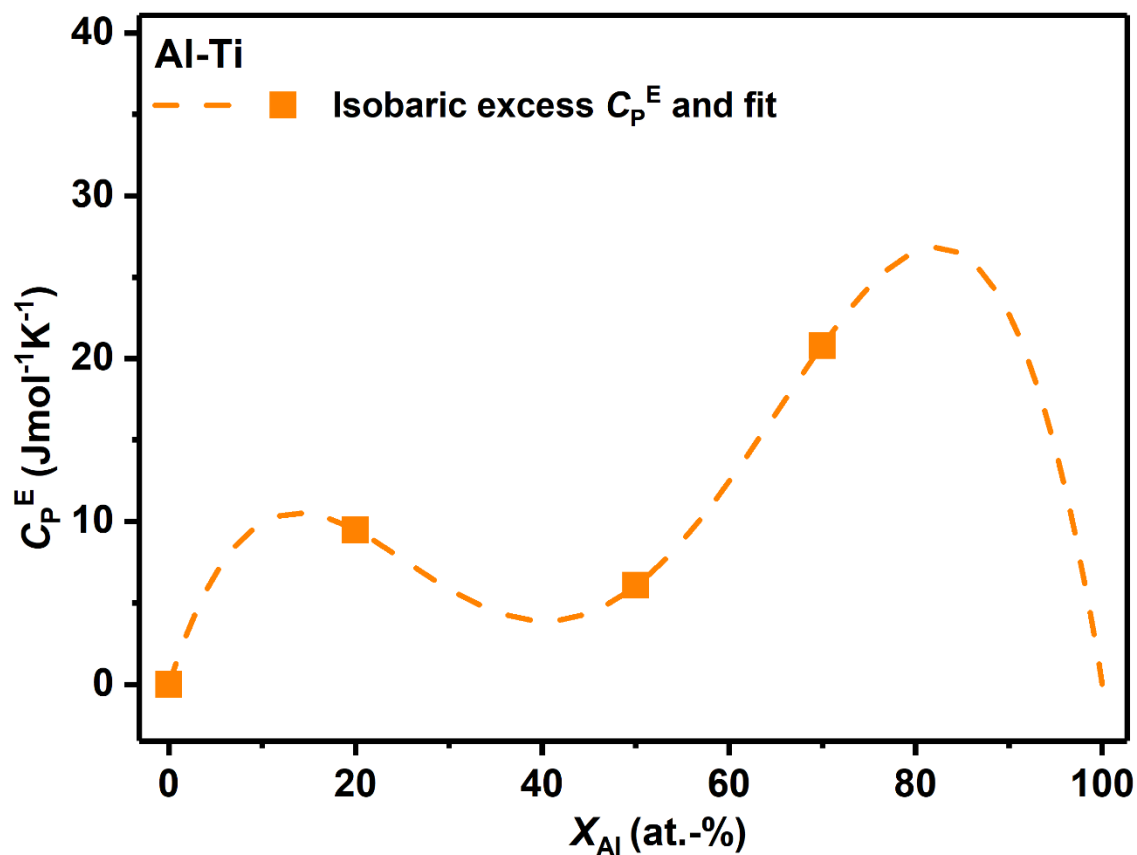


Figure 5.15: Composition dependence of the excess heat capacity at constant pressure of the Al-Ti melts. The squares symbolize fitted values of the linear temperature dependencies, and the dashed line shows a Redlich-Kister fit with fit parameters listed in Table 9.

ν	νc ($\text{m}^3\text{mol}^{-1}$)
0	24.30
1	89.01
2	245.09

Table 9: Redlich-Kister type fit parameter of ν -th order used for the excess heat capacity fit illustrated in Figure 5.15. As the heat capacity is assumed to be constant over temperature, consequently, the fit parameters are not dependent on temperature, either.

Considering all data, the result of positive excess heat capacity in the Al-Ti system is highly interesting and opposed to the literature results for multi-component industrially used Al-Ti based alloys. However, with regards to the lack of comparable data in the binary Al-Ti system, the sensitivity of Al-Ti alloys to contamination and the resulting influence on its properties, further validation in future works is required. For example, the presence of non-visible oxides on a sample during one measurement might significantly influence the molar heat capacity and in the following composition

dependent data trend. Therefore, it is suggested for future works to investigate the molar heat capacity of more compositions in the Al-Ti system to verify the trend of the composition dependent excess heat capacity fit. Nonetheless, as for all compositions, a unified positive excess molar volume has been found, it is justified to claim that the molar heat capacity of the binary Al-Ti system shows positive deviations from the Neumann-Kopp rule. This is in agreement with other metallic systems such as Fe-Ni where a positive deviation from the Neumann-Kopp rule over the entire composition range was found accordingly by Watanabe et al. [86].

In this section, the results for the isobaric heat capacity have been presented and discussed. It was found that generally high isobaric heat capacity results were obtained in this work with respect to literature data. Positive excess heat capacity is shown over the whole measured composition range. A comparison with other properties and their composition dependence will be conducted in chapter 6.

5.4 High-temperature viscosity under reduced gravity (μg)

High-temperature viscosity results of $\text{Al}_{50}\text{Ti}_{50}$ obtained under reduced gravity (μg) in the TEMPUS facility (compare section 3.3) during parabolic flight are thematised in this section. The temperature dependence of the data is fitted according to Arrhenius law and compared to literature data for the viscosity of Al and Ti. Different models, e.g., the Hirai model [55] are applied to illustrate possible composition dependencies in the Al-Ti system. This section is based on the sections 2.5 and 3.9 where the respective theoretical background and the experimental methods were introduced.

5.4.1 Results

Figure 5.16 shows measured viscosity data, η , of liquid $\text{Al}_{50}\text{Ti}_{50}$ obtained under reduced gravity conditions at three different temperatures. The data, ranging from 5.73 mPas to 6.88 mPas and the respective uncertainties are listed in Table 10 along with the corresponding temperatures. The uncertainties as discussed in the *Appendix*, vary up to about 10%, as depicted in Figure 5.16. The data are fitted by Arrhenius law (Eq. (2.42)), as introduced in section 2.5.1 with the fit parameters, η_{∞} and E_A , given in Table 10. It should be noted that the fit can only be validated within the measured temperature range. As a comparison and due to non-available data for the viscosities of the binary system Al-Ti, literature data for the pure elements Al, reported by Assael et al. with the corresponding Arrhenius fit [14] and data for Ti given by Agaev [113] and Paradis et al. [114] are shown. Except for the data given by Paradis et al. as a linear function over a

temperature range of 1750-2050 K, all literature values lie below the results presented in this work.

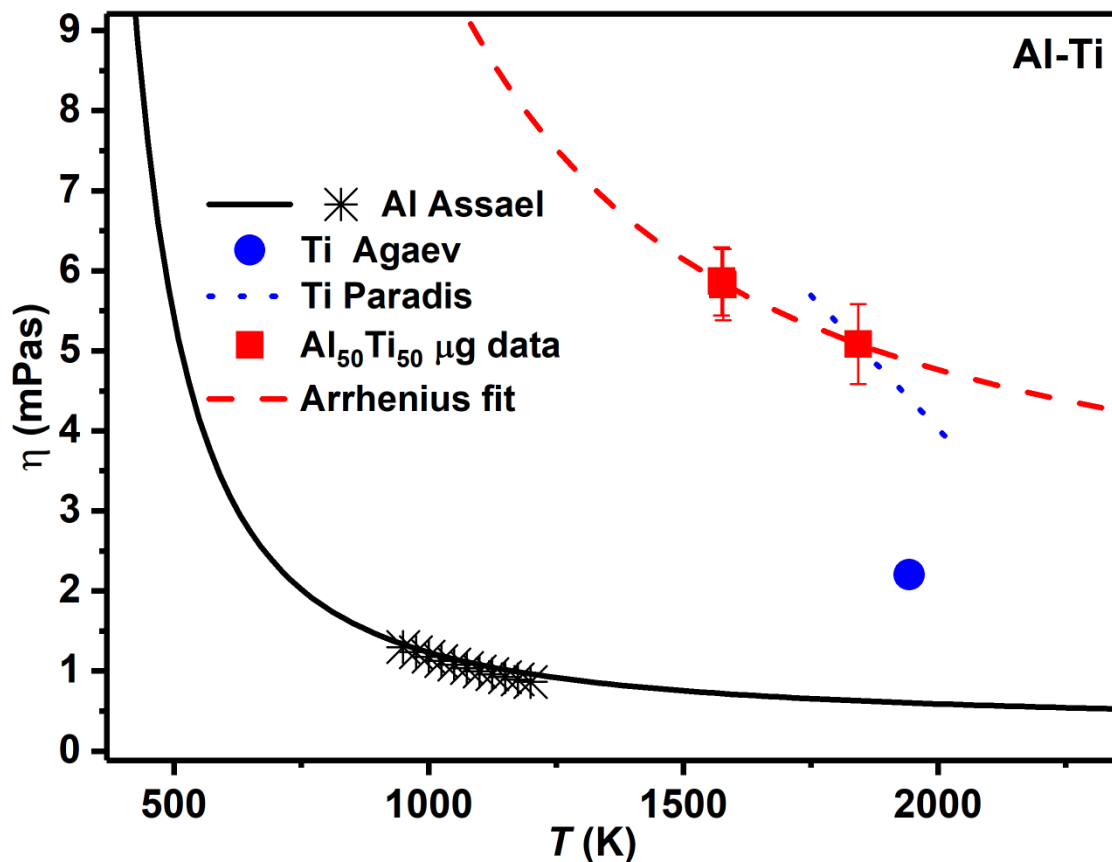


Figure 5.16: High-temperature viscosity data of liquid Al by Assael et al. (star symbols) and the corresponding Arrhenius fit (solid line) [14], Ti reported by Agaev (circles) [113] and Paradis et al. (dotted line, valid for 1750-2050 K) [114] and $\text{Al}_{50}\text{Ti}_{50} \mu\text{g}$ results and Arrhenius fit of the present work (squares and dashed line) valid for the measured temperature range 1574 – 1843 K.

T (K)	η (mPas)	$\Delta\eta$ (mPas)	η_{∞} (mPas)	E_A (10^4 Jmol^{-1})
1574	6.88	0.43	2.23	1.27
1578	6.82	0.44		
1843	5.73	0.50		

Table 10: $\text{Al}_{50}\text{Ti}_{50} \mu\text{g}$ viscosity data, η , and uncertainty, $\Delta\eta$, at the respective temperature, T , of the present work and corresponding η_{∞} and E_A Arrhenius fit parameters.

The data by Paradis et al. [114] intersect with the Arrhenius fit of the $\text{Al}_{50}\text{Ti}_{50}$ data at about 1843 K, showing lower viscosity values for Ti with respect to the alloy at higher temperatures and higher viscosities at temperatures below 1843 K. The viscosities for Ti

are given respectively as 4.4 mPas and 2.2 mPas at about 1943 K by Paradis and Agaev et al. Respectively, the data by Assael et al. [14] are presented as chemical reference data for the viscosity of liquid Al, taking values from 0.87 mPas to 1.30 mPas over the measured temperature range.

5.4.2 Discussion

In Figure 5.17 additional literature data for the isothermal viscosity of Al and Ti are depicted as a function of mole fraction, X_{Al} , including the results of this work for $Al_{50}Ti_{50}$. All data, except the one given by Agaev et al. [113] at 1943 K, have been calculated for 1750 K by Arrhenius law, according to Eq. (2.42) using the data reported for η_{∞} and E_A in the respective references. The calculated and reported values for the viscosity, along with the corresponding temperatures, methods and references are listed in Table 11.

The viscosity for Ti reported by Paradis et al. [114] is distinctively higher than the one given by Agaev et al. [113], varying about 54% (at different temperatures). In the case of Al, the viscosity is more uniform, scattering around a mean value of 0.6 (± 0.05) mPas, corresponding to a relative uncertainty of 8% among the reported literature data at 1750 K. The viscosity value for $Al_{50}Ti_{50}$ of this work of 5.31 mPas exceeds the mean values of the pure elements almost by a factor of 1.4 and 9 for Ti and Al, respectively. Moreover, the value is twice as large as the respective value calculated on the basis of linear dependence between the pure elements, indicating a positive excess behaviour of $Al_{50}Ti_{50}$. However, it is not possible to draw any other conclusions concerning excess or ideal behaviour and a general trend in the composition dependence of the viscosity, due to a lack of additional reference data of viscosities in the binary system Al-Ti.

Furthermore, Figure 5.17 illustrates various models for the composition dependence of the viscosity in the Al-Ti system, including an ideal, linear dependence between the viscosities of the pure elements of 0.65 mPas and 5.69 mPas for Al and Ti, respectively. The models, as introduced in section 2.5.2, have been calculated for 1750 K and as input parameter for the pure elements, the reference data by Assael et al. for Al [14] and the data given by Paradis et al. for Ti [114] of 0.65 mPas and 5.69 mPas, respectively, are used. The data by Dessai et al. [115] are employed for the enthalpy of mixing, ΔH_{mix} , as input parameter needed for the calculations of some viscosity models. The input data for the molar volume, V , taking an excess molar volume into account, are taken from this work, as presented in section 5.1. As can be seen from Figure 5.17, the models predict highly varying viscosity values and trends in the Al-Ti system. The reason for the strong differences among the models lies within the different weighting of the parameters, in particular with partially negative or positive pre-exponential factors of the parameters ΔH_{mix} , V and M .

The Hirai model [55] (Eq. (2.43)) and the Kaptay model [57] (Eq. (2.45)) depicted in Figure 5.17, fail to predict the experimental data of this work completely. For the corresponding composition $\text{Al}_{50}\text{Ti}_{50}$ both models show negative deviations with respect to a linear dependence between the viscosities of the pure elements and underestimate the experimental data by 48% and 73%, respectively. A general positive viscosity deviation from the linear composition dependence can be found for the Kozlov model [56] (Eq. (2.44)) which seems to depict the trend of the measured data approximately. However, for the corresponding composition $\text{Al}_{50}\text{Ti}_{50}$, the Kozlov model underestimates the data by 28% and lies, therefore, beyond the experimental uncertainty of 9%.

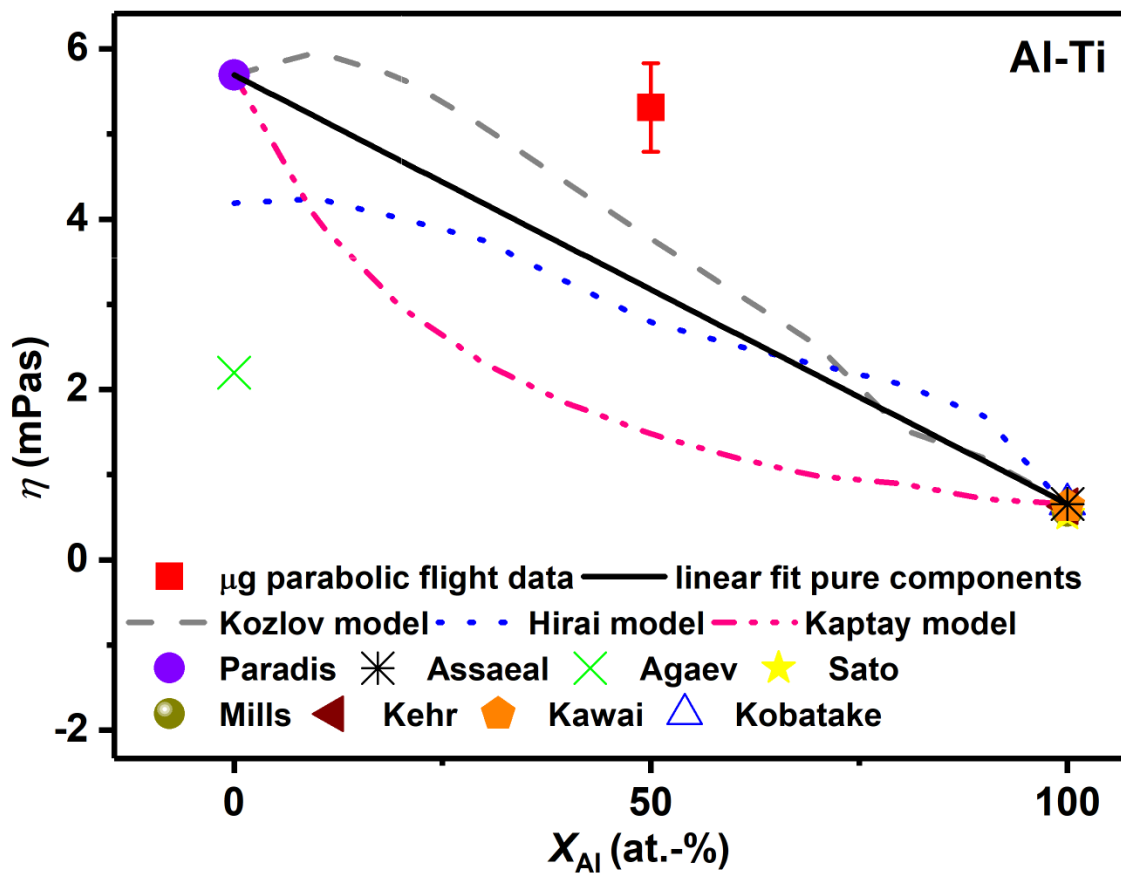


Figure 5.17: Literature data for the viscosity for Ti by Agaev et al. [113] and Paradis et al. [114], for Al reported by Assael et al. [14], Kobatake et al. [97], Mills et al. [116], Sato et al. [117], Kehr [118], Kawai et al. [119] and μg viscosity results of the present work for $\text{Al}_{50}\text{Ti}_{50}$. Additionally, composition dependence predictions are depicted, according to models by Hirai [55], Kozlov [56] and Kaptay [57]. All models and literature data besides the value by Assael et al. [14] at 1941 K were calculated for 1750 K (compare Table 11).

Overall, it can be observed that none of the models fits the experimental value for $\text{Al}_{50}\text{Ti}_{50}$ of 5.31 mPas within the experimental uncertainty of 9%. As described in the sections 3.3 and 3.9, electromagnetic levitation in combination with the oscillating drop technique in the TEMPUS facility under microgravity conditions was used to measure the viscosity of

liquid $\text{Al}_{50}\text{Ti}_{50}$. Viscosity measurements at constant temperature are not possible in the TEMPUS facility. To elucidate the influence of internal flow in the sample induced by heating pulses, viscosity measurements can only be determined upon free cooling in the TEMPUS facility. Therefore, the measurements are performed over a cooling phase of about 1 s with a temperature decrease of 30-40 K, which leads to increased uncertainty in the temperature determination [53]. Nonetheless, the residual fluid flow might also influence the accuracy of the viscosity. Additionally, the uncertainty of the viscosity is influenced by vibrations transferred from the airplane to the TEMPUS facility due to the unpredictable wind, weather and flight conditions. These vibrations can lead to position instabilities [53].

Comp.	T (K)	η (mPas)	Method	Reference
Ti	1943	2.2	C	AgaeV [113]
Ti	1750	5.69	OD	Paradis [114]
Al	1750	0.59	R	Assael [14]
Al	1750	0.65	OC	Kobatake [97]
Al	1750	0.57	OC	Mills [116]
Al	1750	0.53	OC	Sato [117]
Al	1750	0.63	OC	Kehr [118]
Al	1750	0.63	OC	Kawai [119]
$\text{Al}_{50}\text{Ti}_{50}$	1750	5.31	μg -OD	Present work

Table 11: Viscosity data of liquid Al, Ti reported in the literature and $\text{Al}_{50}\text{Ti}_{50}$ microgravity data of this work, along with the respective temperature, method, and references. The key to the method abbreviations in the fifth column can be found in section *Method abbreviations*.

Overall, microgravity measurements in the TEMPUS facility offer the great opportunity to conduct comparative and complementary viscosity measurements for ground-based experiments [53]. However, in cases like liquid Al-Ti alloys where ground-based results are rare or not existing, the large error in the microgravity measurement renders it necessary to repeat measurements for verification. Additionally, it is suggested to measure the

viscosity over the whole composition range of the binary Al-Ti alloy system to validate the composition dependent trend of the isothermal viscosity.

In this section, the results for high-temperature viscosity under reduced gravity have been presented and discussed. The viscosity of one composition, Al₅₀Ti₅₀ has been measured in the Al-Ti system. The results show higher values compared to literature results found for the pure components which would indicate a positive excess viscosity with regards to a linear viscosity dependence. Concerning model predictions, all models used failed to predict the data. The Kozlov model is the only model predicting the approximate viscosity trend in agreement with the measured result. However, it underestimates the value for Al₅₀Ti₅₀ by far by about 28%. It is suggested to repeat the measurement to verify the data and to measure over the whole Al-Ti composition range. A comparison with other properties and their composition dependence will be conducted in the next chapter 6, and finally, all results will be briefly summarized in chapter 7.

5.5 High-temperature surface tension

In this section, the results of the high-temperature surface tension measurements as a function of temperature at the DLR-MP EML-facility are shown and compared to literature data. Additionally, different models are applied such as the Chatain [47] and Butler [43] model, compared to the composition dependence in the Al-Ti system and related to non-ideal behaviour and interatomic processes. The data of this chapter were published before in the publication *Density, Molar Volume, and Surface Tension of liquid Al-Ti* by Wessing and Brillo [7] and some parts of this chapter including graphics are based on evaluations and discussions of the aforementioned publication. The reuse of data, graphics, and content was granted by a Springer copyright license with the number 4127610503802. This section is based on the sections 2.4 and 3.8, where the respective theoretical background and the experimental methods have been introduced.

5.5.1 Results

Figure 5.18 shows measured surface tension data, γ , plotted versus temperature of pure Ti and the binary liquid alloys Al-Ti, as already reported in the preceding work by Wessing and Brillo [7]. In order to visualize the complete composition range of the system, the figure also shows linear regression lines of the data of pure Al taken from the publications by Kobatake et al. [25, 96]. Therefore, the depicted Al-mole fraction, X_{Al} , in Figure 5.18 ranges from 0 to 100 at.-%.

Each measurement was carried out over a broad temperature range of 100-250 K, including up to 200 K undercooling below the respective liquidus temperature.

Corresponding to the measurements of other properties of the liquid phase, e.g., density, surface tension measurements are restricted by the same temperature range boundaries [7].

For all compositions, the surface tension decreases linearly with rising temperature. In addition, γ changes gradually with the composition, exhibiting an increase with decreasing X_{Al} with the lowest values observed for pure Al and the highest results for pure Ti [7]. Besides the data measured at the DLR-MP, surface tension values for $X_{\text{Al}} = 50$ at.-% obtained under microgravity conditions in the TEMPUS facility on board of a parabolic flight (as described in section 3.3) are illustrated in Figure 5.18. The data fits in accordance with Eq. (2.23) are represented in Figure 5.18 by the solid lines. The obtained values for γ_{L} and γ_{T} together with the corresponding liquidus temperatures T_{L} are listed in Table 12 and Table 13 for the pure elements and the alloy system, respectively. In the case of Al, the data, refer to the data of the work by Kobatake et al. [25, 96].

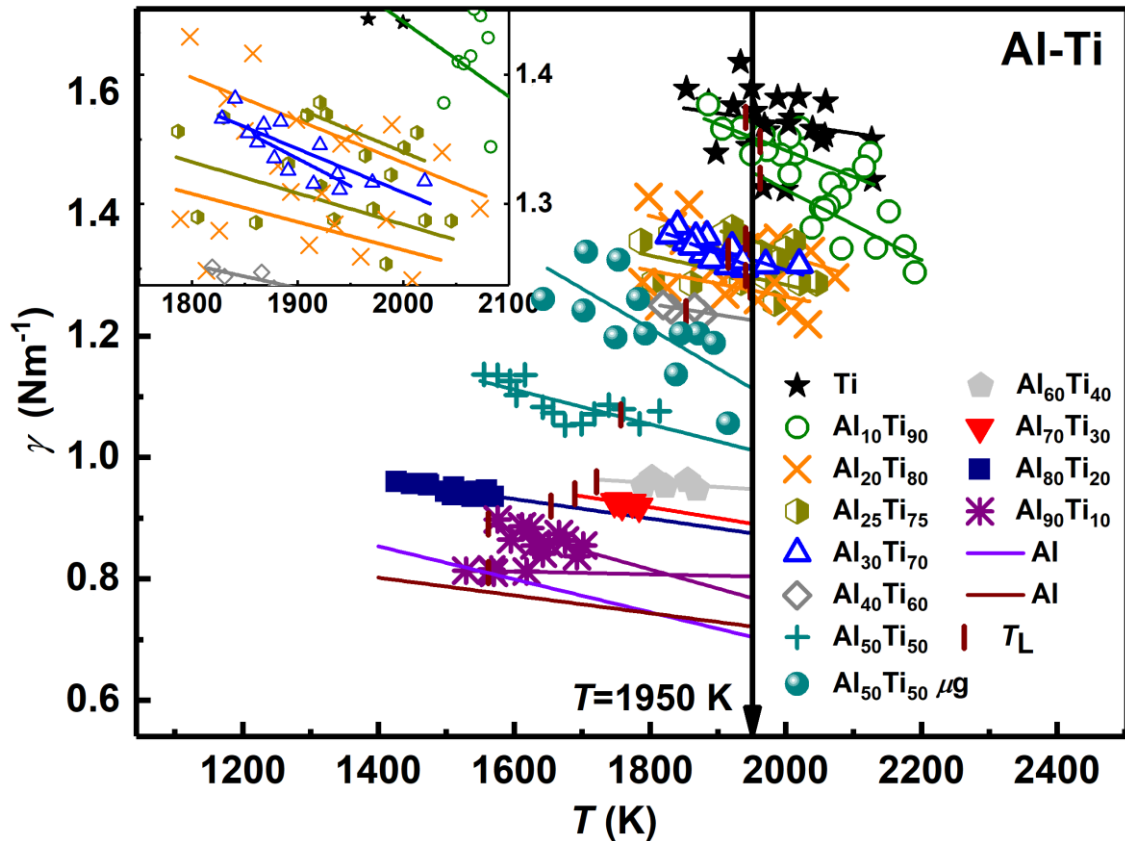


Figure 5.18: Literature surface tension data, γ , of liquid Al [30, 96] and measured surface tension results of liquid Ti, Al-Ti (symbols) and their linear fits (lines) in dependence of temperature, T , following Eq. (2.23). The spheres illustrate data measured in microgravity. The inset shows a magnified portion of the figure for Al-mole fractions X_{Al} ranging from 0 to 40 at.-%. Based on Fig. 6 by Wessing et al. [7].

As shown in Table 13, the values of γ_{L} change gradually with increasing mole fraction, X_{Al} . In the case of γ_{T} , the margin over all compositions is around 55 %, while the

magnitude of variation among the γ_T data of each composition is also around 20 - 60 %. Therefore, it is reasonable to conclude that γ_T is essentially constant, with a mean value of $(-2.51 (\pm 1.37)) \cdot 10^{-4} \text{Nm}^{-1} \text{K}^{-1}$ within the experimental accuracy [7].

Additionally, Table 12 and Table 13 show the isothermal surface tension calculated from Eq. (2.23) at $T = 1950 \text{ K}$, chosen from the middle of the total range of temperatures covered by the experiments. Correspondingly to the density data, some of the extrapolated values, $\gamma(T = 1950 \text{ K})$ outlying the measured temperature range for some alloys, which is not relevant in the context. As can be seen from the Tables, upon increasing X_{Al} , $\gamma(T = 1950 \text{ K})$ decreases from $\gamma_{\text{Ti}} = 1.56 (\pm 0.02) \text{ Nm}^{-1}$ to $\gamma_{\text{Al}} = 0.71 (\pm 0.01) \text{ Nm}^{-1}$ [7].

Comp.	T_L (K)	γ_L (Nm ⁻¹)	γ_T (10 ⁻⁴ Nm ⁻¹ K ⁻¹)	$\gamma(T = 1950 \text{ K})$ (Nm ⁻¹)	Reference
Ti	1941	1.56	-0.62	1.56	[7], present work
Ti	1941	1.58	-2.49	1.57	[7], present work
Ti	1941	1.54	-1.85	1.54	[7], present work
Ti	1941	1.56 ± 0.02	-1.65 ± 0.95	1.55 ± 0.02	Average value
Al	933	0.98	-2.71	0.70	[96]
Al	933	0.87	-1.46	0.72	[25]
Al	933	0.92 ± 0.08	-2.09 ± 0.88	0.71 ± 0.02	Average value

Table 12: Melt composition, references, parameters γ_L , γ_T , and the extrapolated isothermal surface tension $\gamma(T = 1950 \text{ K})$ with the mean values in bold font. The data relate to the results of this work, [7] and literature results in the case of Ti and Al, respectively.

Comp.	T_L (K)	γ_L (Nm ⁻¹)	γ_T (10 ⁻⁴ Nm ⁻¹ K ⁻¹)	$\gamma(T = 1950 \text{ K})$ (Nm ⁻¹)
Al ₁₀ Ti ₉₀	1962	1.52	-4.34	1.53
Al ₁₀ Ti ₉₀	1962	1.46	-5.81	1.47
Al ₂₀ Ti ₈₀	1948	1.35	-3.29	1.35
Al ₂₀ Ti ₈₀	1948	1.28	-2.18	1.28
Al ₂₅ Ti ₇₅	1941	1.30	-2.42	1.30
Al ₂₅ Ti ₇₅	1941	1.36	-3.38	1.36
Al ₃₀ Ti ₇₀	1915	1.34	-3.38	1.33
Al ₃₀ Ti ₇₀	1915	1.33	-4.24	1.31
Al ₄₀ Ti ₆₀	1853	1.24	-1.79	1.23
Al ₅₀ Ti ₅₀ (μg)	1757	1.24	-6.46	1.11
Al ₅₀ Ti ₅₀	1757	1.07	-2.86	1.01
Al ₆₀ Ti ₄₀	1721	0.96	-0.68	0.95
Al ₇₀ Ti ₃₀	1689	0.94	-1.80	0.89
Al ₈₀ Ti ₂₀	1654	0.92	-1.61	0.88
Al ₉₀ Ti ₁₀	1562	0.89	-3.14	0.77
Al ₉₀ Ti ₁₀	1562	0.81	-0.23	0.80

Table 13: Melt composition, parameters γ_L , γ_T , and the interpolated surface tension $\gamma(T = 1950 \text{ K})$ of the investigated liquid alloys Al_xTi_{100-x}.

In Figure 5.19 the isothermal surface tension data at $T = 1950$ K are plotted in dependence of X_{Al} . In the range of $X_{\text{Al}} < 20$ at.-% in Figure 5.19, $\gamma(T = 1950$ K) decreases with concentration. For $20 \text{ at.-%} \leq X_{\text{Al}} \leq 30 \text{ at.-%}$, there seems to be the tendency, that $\gamma(T = 1950$ K) is approximately constant, however, this tendency is beyond the scatter of the experimental data. Finally, for compositions, $X_{\text{Al}} > 30$ at.-%, $\gamma(T = 1950$ K) steeply decreases with X_{Al} , featuring a concave shape until its final value is approached at $X_{\text{Al}} = 100$ at.-% [7].

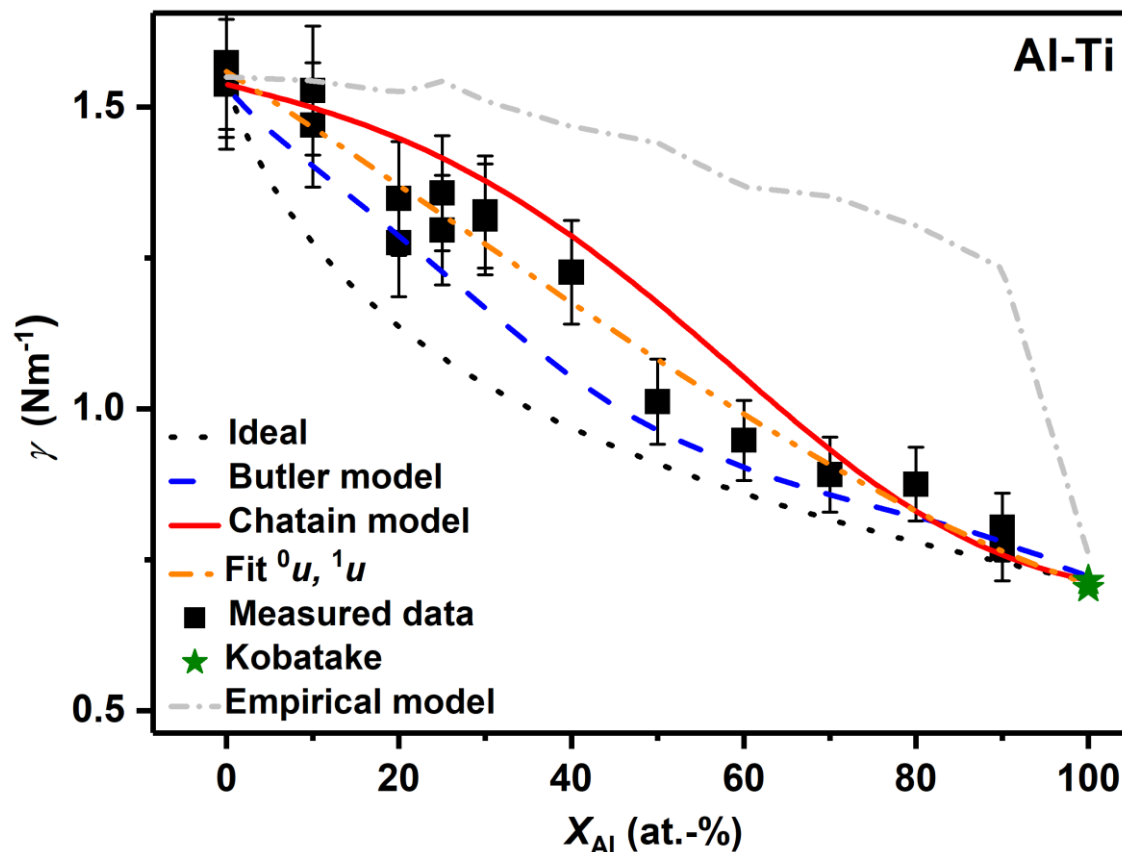


Figure 5.19: Measured isothermal surface tension, γ , of liquid Al-Ti alloys and Al literature data [25, 96], in dependence of the mole fraction, X_{Al} , at 1950 K. The squares show the extrapolated measured surface tension data, the lines represent the data fits with two fit parameters, 0u and 1u , (dashed-dotted-dotted line, Table 14). Additionally, surface tension values calculated with the Butler model [43] for subregular solutions with ideal (dotted line) and non-ideal mixing behaviour (dashed line) and the Chatain model [47, 48] for subregular solutions (solid line) are shown. Based on Fig. 7 by Wessing et al. [7].

5.5.2 Discussion

Moreover, Figure 5.19, illustrates a comparison of the experimental data to model calculations for the isothermal surface tension, $\gamma(T = 1950$ K). Analogously to the molar volume in chapter 5, the data are fitted by a Redlich-Kister type polynomial of first order ($N = 1$) based on Eq. (2.27) with the corresponding fit parameters, ${}^0u(T = 1950$ K) and ${}^1u(T = 1950)$, listed in Table 14. The fit is in good agreement with the data and the data

trend. However, for $10 \text{ at.-%} < X_{\text{Al}} < 30 \text{ at.-%}$ it does not reproduce the kink, and the surface tension is slightly overestimated [7].

As can be seen from Figure 5.20, the empirical model by Allen [50], introduced in section 2.4.5, is not in good agreement with the data and overestimates the surface tension almost over the entire composition range of the binary system Al-Ti. Only for $X_{\text{Al}} \leq 10 \text{ at.-%}$, the isothermal surface tension γ ($T = 1950 \text{ K}$) lies within the experimental error. Consequently, the model fails to describe the data correctly.

In the case of an ideal solution in accordance with Eq. (2.28), the model follows a concave form, with the highest values found for pure Ti and lowest values for pure Al. The model underestimates the surface tension for all alloys except for $\text{Al}_{90}\text{Ti}_{10}$. Analogously to other properties, for example, density and heat capacity, the Al-Ti system does consequently not show ideal solution behavior concerning surface tension [7].

A far better agreement is achieved by the calculations of the Butler model [43] and the Chatain model [47, 48] for subregular non-ideal solutions, introduced by Eq. (2.32) and Eq. (2.34), respectively, with the temperature dependent interaction parameters, ${}^{\nu}L_{\text{Al,Ti}}(T)$, listed in Table 14. Both models succeed to predict the data, and the data tendency, with positive excess values exhibited relative to the ideal solution [7]. The predictions by the Chatain model [47, 48], are generally in good agreement with the measured data and follow the kink for an Al concentration around 25-50 at.-%. However, for $40 \text{ at.-%} < X_{\text{Al}} < 70 \text{ at.-%}$ the model overvalues $\gamma(T = 1950 \text{ K})$ by 5-12 %. For Al concentrations greater than 70 at.-%, the Chatain model lies within the error bars, but the model shows a negative kink in this interval, while in contrast, the data follow a minor positive kink. Overall, the Butler model describes the data accurately, in particular in the composition range of $25 \text{ at.-%} \geq X_{\text{Al}} \geq 50 \text{ at.-%}$, following the data within all error bars. Nonetheless, for compositions $25 \text{ at.-%} < X_{\text{Al}} < 50 \text{ at.-%}$, the Butler model underestimates the data by 5-16 % and does not reproduce the kink, featured in this interval [7].

ν	${}^{\nu}L \text{ (Jmol}^{-1}\text{)}$	${}^{\nu}u(T) \text{ (Nm}^{-1}\text{mol}^{-1}\text{)}$
0	$41.972T - 118048$	$-2.18327 \cdot 10^{-4} T + 0.21604$
1	$19.704T - 23613$	$-0.00136 T + 2.8091$
2	$-13.844T + 34757$	

Table 14: Temperature-dependent parameters ${}^{\nu}L$ used for the calculations of the subregular solution models by Butler Eq. (2.32) and by Chatain Eq. (2.34) and coefficients ${}^{\nu}u(T)$ being temperature dependent material-specific interaction parameters for the excess surface tension of a Redlich-Kister type polynomial of the first order, fitted by Eq. (2.27).

In Figure 5.20, calculations based on the compound formation model, proposed by Egry, Eq. (2.37), for an ideal behaviour with no compound formation and potential compound formations with Al_2Ti , Al_3Ti and $\text{Al}_{11}\text{Ti}_5$ compositions are shown. The compound formation can be particularly evident in systems with intermetallic phases at the respective compositions, as both processes are triggered by the pronounced attraction between unlike atoms. In the Al-Ti phase diagram different intermetallic compounds, i.e., TiAl , TiAl_3 , TiAl_2 , $\text{Ti}_5\text{Al}_{11}$, Ti_3Al_5 , Ti_2Al_5 , and $\text{Ti}_9\text{Al}_{23}/\text{Ti}_8\text{Al}_{24}$ have been identified. However, their individual stability ranges in dependence on composition and temperature have not been clarified up to now [80, 120, 121].

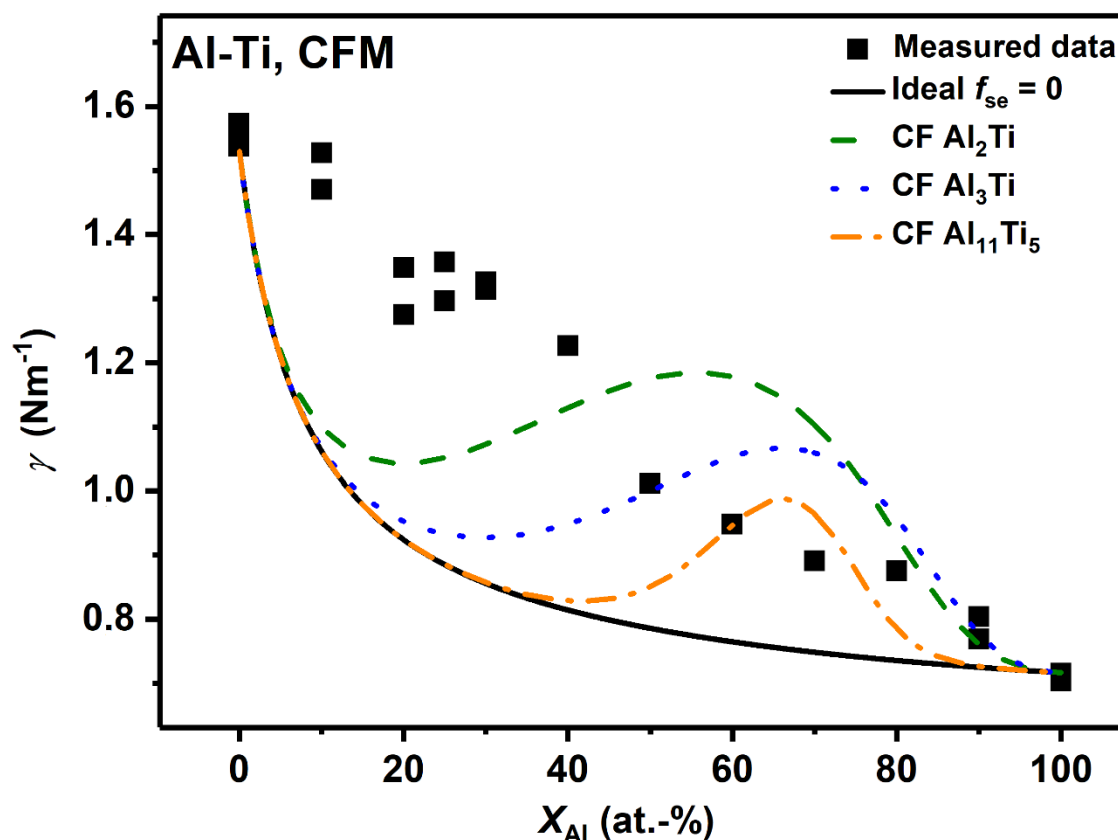


Figure 5.20: Isothermal measured surface tension, γ , of liquid Al-Ti and literature data for pure liquid Al [25, 96], in dependence of the mole fraction, X_{Al} , at 1950 K (black squares). The lines represent calculations based on the compound formation model by Egry [49], introduced in section 2.4.4 for an ideal behaviour with no compound formation (solid line) and non-ideal behaviour with compound formation present at different compositions Al_nTi_m .

Generally, the model by Egry (Figure 5.20) exhibits a concave shape, with a distinct underestimation up to 16% in the case of ideal behavior. For a predicted compound formation, the model shows a kink to higher γ ($T = 1950$ K) values at the respective compound formation composition Al_nTi_m , with X_{Al} (at.-%) = $100 \cdot n/(n + m)$. In the range of the compound formation composition, the model generally overestimates the data, in

particular for Al_2Ti and Al_3Ti . The model neither fits the value accurately nor does it reproduce the data's trend and, therefore, fails to describe the data completely.

Even though only the calculations for three potential compositions for compound formations are shown in the figure; the model has been evaluated for all possible compound formation compositions, as taken from the intermetallic phases in the system. For all compositions, the model fails to reproduce the data and data trend. Thus, it can be said, that no compound formation occurs in the liquid Al-Ti system that affects the surface tension in agreement with the Egry model. That is in agreement with other Al containing systems, e.g., Al-Au [96, 104] and Al-Cu [122].

After consideration of all evaluated models, the Butler model for non-ideal solutions predicts the data most accurately in the Al-Ti system. For many systems, ideal solution models do not comply with the experimental data, as those models neglect the excess Gibbs energy, $^E G$, (compare section 2.4.1 on Gibbs free energy). As a consequence, the models predict the data only based on the surface segregation of the surface-active component, e.g., Al in the case of Al-Ti. Here, the mechanism is described, that the component with the smaller surface tension becomes enriched in the surface layer in order to minimize the energy of the entire system. However, in the case of systems with $^E G \neq 0$ also inter-atomic effects must be taken into account. For non-ideal solutions, two cases can be distinguished, namely $^E G > 0$ with enhanced surface segregation and $^E G < 0$. The latter refers to systems where the surface segregation of the surface-active component is suppressed due to interatomic attractions, consequently leading to an increased surface tension with regards to the ideal system. This is the case for many Al-systems, such as Al-Cu, Al-Ni, Al-Fe, and Al-Au, as reported by Brillo et al. [30] and strengthened by the results of this work for Al-Ti [7].

As displayed in Figure 5.21, the Butler model [43] and the Chatain model [47], [48] also allow us to evaluate the Al-content in the respective layers of the surface, X_{Al}^{S} , versus the Al-content of the bulk, X_{Al}^{B} , and to draw a direct comparison with the respective ratio in the ideal solution. Inherently, in the case of the Butler model, a monolayer is considered and for the Chatain model, multiple layers are taken into account. For all models, including the ideal solution, a general Al segregation is shown in an enriched Al-content in the surface versus the bulk. However, for $X_{\text{Al}}^{\text{B}} \leq 60$ at.-%, it also becomes apparent that the concentration of the top layer is relatively depleted by Al, by up to 40 % for the Butler model and up to 60 % for the Chatain model with regards to the ideal solution, which signifies a suppressed segregation. For Al concentrations higher than 60 at.-% and 80 at.-% in the case of the Butler model and the Chatain model, respectively, no further depletion is identifiable, and the models are in agreement with the ideal behavior [7].

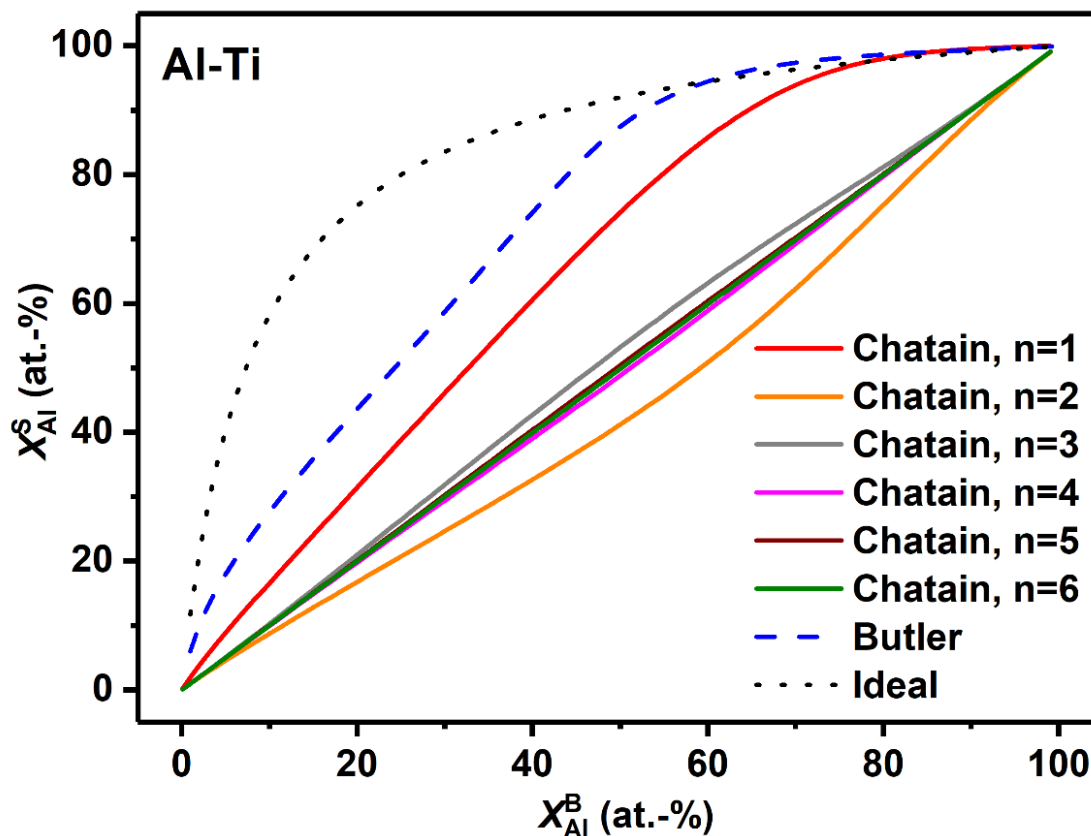


Figure 5.21: Calculated surface mole fraction, X_{Al}^S , as a function of the bulk mole fraction, X_{Al}^B , at $T = 1950$ K using the ideal (dotted line) and non-ideal (dashed line) subregular solution model by Butler [43] and by Chatain [47, 48] (solid lines) for different layers, where layer ‘1’ denotes the layer at the surface. The layer numbers increase with their distance to the surface. Based on Fig. 9 by Wessing et al. [7].

As depicted in Figure 5.21 and Figure 5.22, the Chatain model yields highly fluctuating values for Al enrichment and depletion in the surface layers, the so-called chemical layering. This is also apparent in Figure 5.22 illustrates the concentration, $X_{Al}^{(n)}$, of each layer plotted against the layer number, n , for $Al_{50}Ti_{50}$, at two different temperatures, $T = 1700$ K and $T = 1950$ K. As expected, the first layer exhibits an enrichment of Al of around 25 % relative to the bulk. However, the second layer shows a depletion of Al of about 10 %. This oscillating behavior continues for both temperatures in the figure over the different layers, until, in the layer, $n = 6$, the bulk composition is approached [7]. These oscillations can be explained by a mechanism where the segregation of one component to the surface leads to an excess of the other component in the following layer and in turn, due to the negative excess free energy, the other component is then favored in the second layer. At low temperatures atomic dynamics are less dominant with respect to higher temperatures and, thus, enhanced interactions between atoms occur, which is indicated by the pronounced chemical layering at $T = 1700$ K. Chemical layering has been observed in several systems with negative excess free energy [7], for example in the cases of Al-Ni [5], Al-Au [96] and Al-Cu [122].

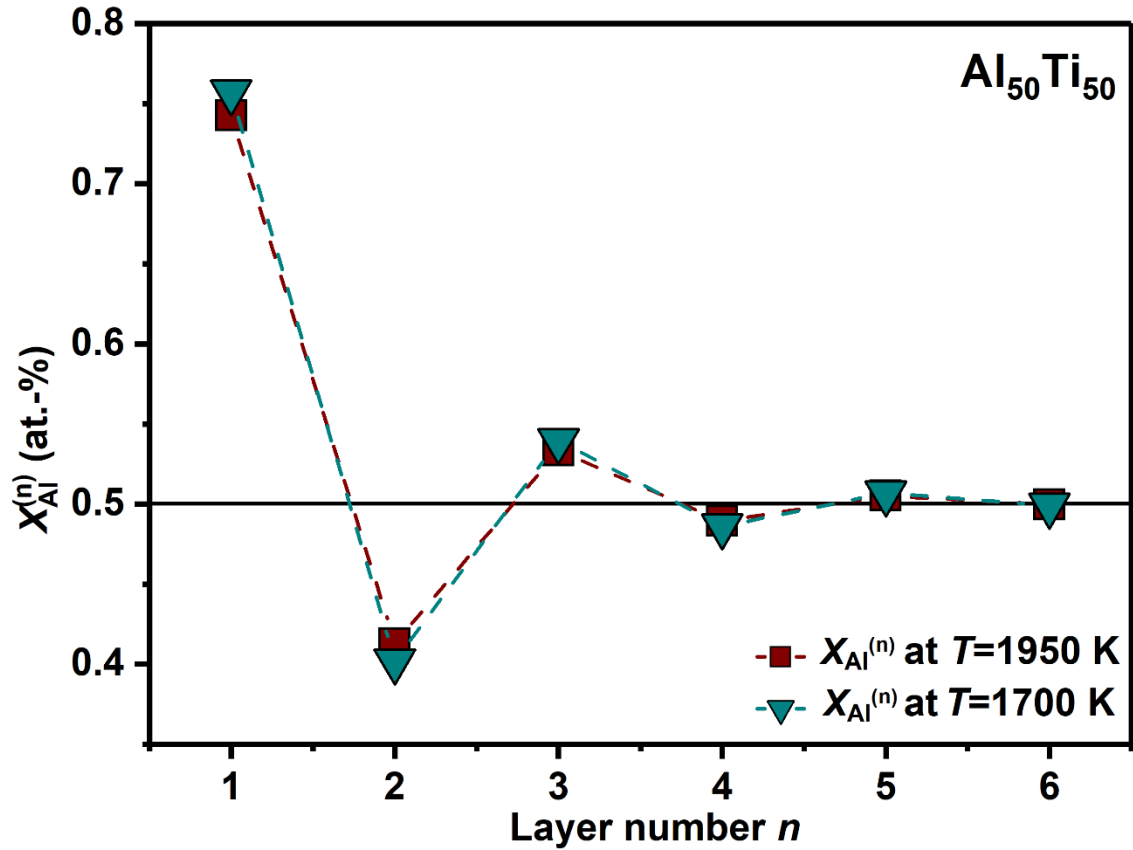


Figure 5.22: Calculated ratio of the surface mole fraction, $X_{Al}^{(n)}$, to the bulk mole fraction, X_{Al}^B , at $T = 1700$ K (triangles) and $T = 1950$ K (squares) in dependence of the layer number using the non-ideal subregular solution model by Chatain [47, 48]. Based on Fig. 10 by Wessing et al. [7].

The experimentally obtained values for the surface tension temperature coefficient, γ_T , and the values calculated by the Chatain and Butler model, are plotted in Figure 5.23 versus X_{Al} . In section 5.5.1, γ_T was assumed to be constant, with a mean value of $-2.51 (\pm 1.37) 10^{-4} \cdot \text{Nm}^{-1}\text{K}^{-1}$. Therefore, the temperature coefficient predicted by the Butler model, with a mean value of $-2.14 (\pm 0.89) 10^{-4} \cdot \text{Nm}^{-1}\text{K}^{-1}$, is in better agreement with the experimental data than the one of the Chatain model with a mean value of $-1.50 (\pm 0.21) 10^{-4} \cdot \text{Nm}^{-1}\text{K}^{-1}$. There appears to be the tendency that the experimental values for γ_T slightly decrease for $X_{Al} < 40$ at.-% and increase for higher Al concentrations with increasing Al concentration. Even though this trend corresponds well to the predictions of the Butler model, this tendency is beyond the scatter of the experimental data.

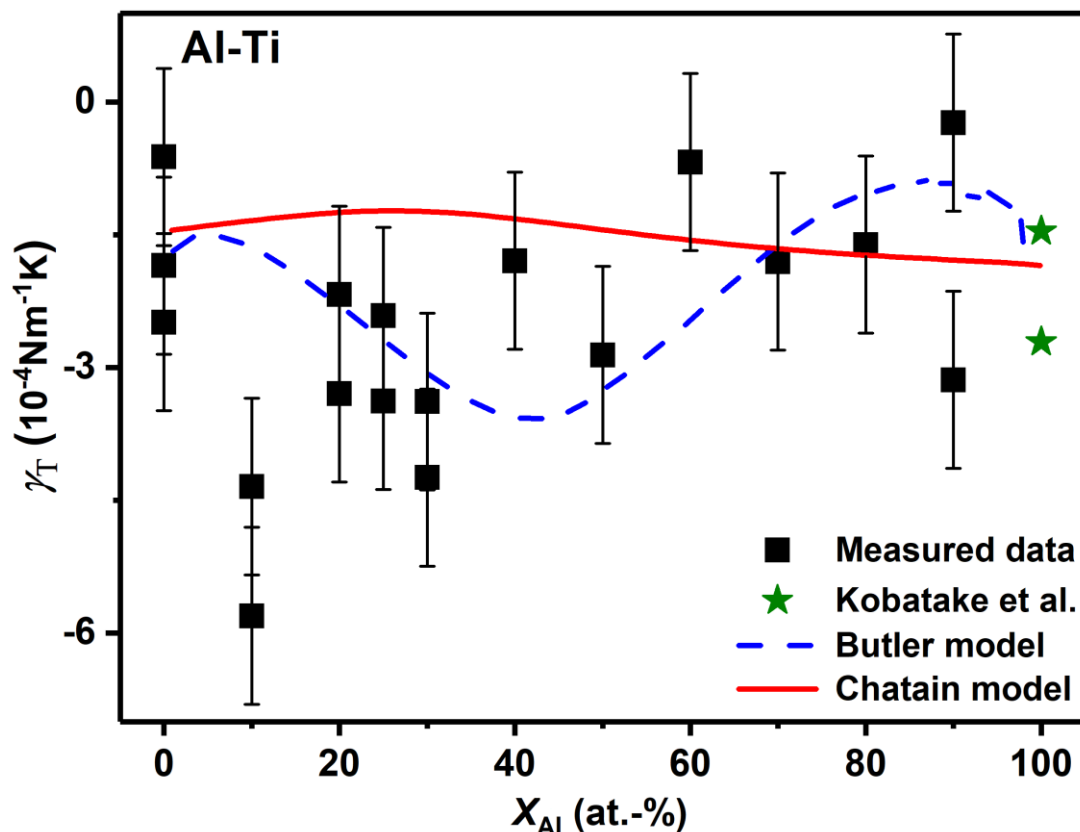


Figure 5.23: Surface tension temperature coefficient values, γ_T , (Eq. (2.23)) in dependence of the mole fraction, X_{Al} , of measured data at 1950 K (squares). The lines represent the calculated temperature coefficient values for the non-ideal subregular solution model by Butler [43] (dashed line) and by Chatain [47, 48] (solid line). In the case of Al, the data refer to the work by Kobatake et al. [25, 96]. Based on Fig. 11 by Wessing et al. [7].

Figure 5.24 shows the excess surface tension values, γ^E , versus X_{Al} at 1950 K for the measured values and the values calculated from the Chatain and Butler model. The data are evaluated using Eq. (2.26), and the necessary input values for γ^{ideal} are taken from the respective models. The highest excess surface tension is found for $X_{Al} \leq 40$ at.-%, which amounts to 0.28 Nm^{-1} . In the case of higher Al concentrations, the excess surface tension is significantly smaller, around 0.1 Nm^{-1} . Overall, both models are in good agreement with the experimental excess surface tension data, respectively. The Chatain model reproduces the data within the experimental uncertainty, except for $X_{Al} \approx 50\text{-}60$ at.-%, but overestimates the data, except for $X_{Al} > 80$ at.-%. On the other hand, the Butler model undervalues the data, especially for $X_{Al} \leq 40$ at.-% but lies within the error bars. In the range $X_{Al} \leq 40$ at.-%, the Chatain model appears to be more accurate while the Butler model follows the data trend more precisely for $X_{Al} > 40$ at.-%. Considering the data, the results shown in Figure 5.21 and the trend of the Butler model it could be assumed that a pronounced suppression of Al segregation only appears up to a certain Al concentration, of around 40 at.-% [7].

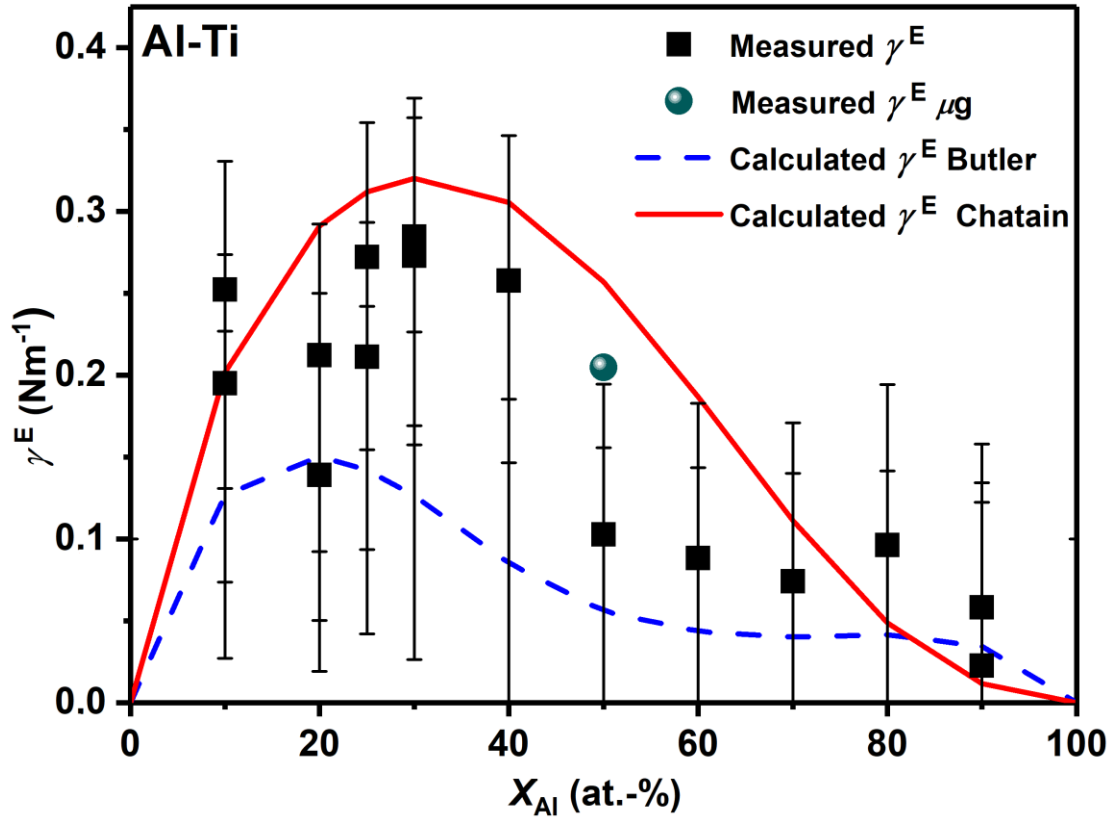


Figure 5.24: Isothermal excess surface tension, γ^E , of liquid Al-Ti as a function of the bulk fraction, X_{Al} , at $T = 1950$ K. The symbols show the extrapolated measured surface tension data subtracted by the calculated surface tension values of the Butler [43] (squares) and Chatain [47, 48] (triangles) models for ideal subregular solutions. The lines represent the excess surface tension, γ^E , (Eq. (2.26)), calculated as the difference between the Butler (dashed line) and Chatain (solid line) model for ideal and non-ideal subregular solution. In the case of Al, the data refer to the work by Kobatake et al. [25, 96]. Based on Fig. 1 by Wessing et al. [7].

In Figure 5.25 the isothermal surface tension data of the binary Al-Ti system measured at the DLR-MP EML facility and the isothermal surface tension data of $\text{Al}_{50}\text{Ti}_{50}$ obtained under microgravity conditions in the TEMPUS facility during parabolic flight (as described in section 3.3), both at $T = 1950$ K, are shown as functions of the Al concentration. The data are in good agreement. However, the data accessed under microgravity conditions lie about 10% higher than the respective ground data for $X_{\text{Al}} = 50$ at.-%. Additionally, literature surface tension data of pure Al and Ti and some industrially used, binary and multicomponent alloys at equivalent temperatures are displayed. As aforementioned in section 1.1, multicomponent alloys on the basis of Al-Ti are highly attractive industrially used materials, but only a few corresponding thermophysical data are reported in the literature. As can be seen in Figure 5.25, the surface tension data of the binary system and the multicomponent alloys correspond well with deviations up to 10%, in the case of $\text{Al}_6\text{Ti}_{90}\text{V}_4$, reported by Egry et al. [10]. Those deviations lie within the same range of order as the relative uncertainties over the depicted

literature data of the pure liquids, e.g., 8 % for Ti and binary components, e.g., 24 % for $\text{Al}_{80}\text{Ti}_{20}$, as reported by Novacovic et al. [121] and in the present work. In conclusion, the data presented in the present work and the preceded work [7], provide accurate thermophysical properties data for binary Al-Ti alloys, as well as build a foundation for investigations and industrial processing of Al-Ti based multi-component alloys [7].

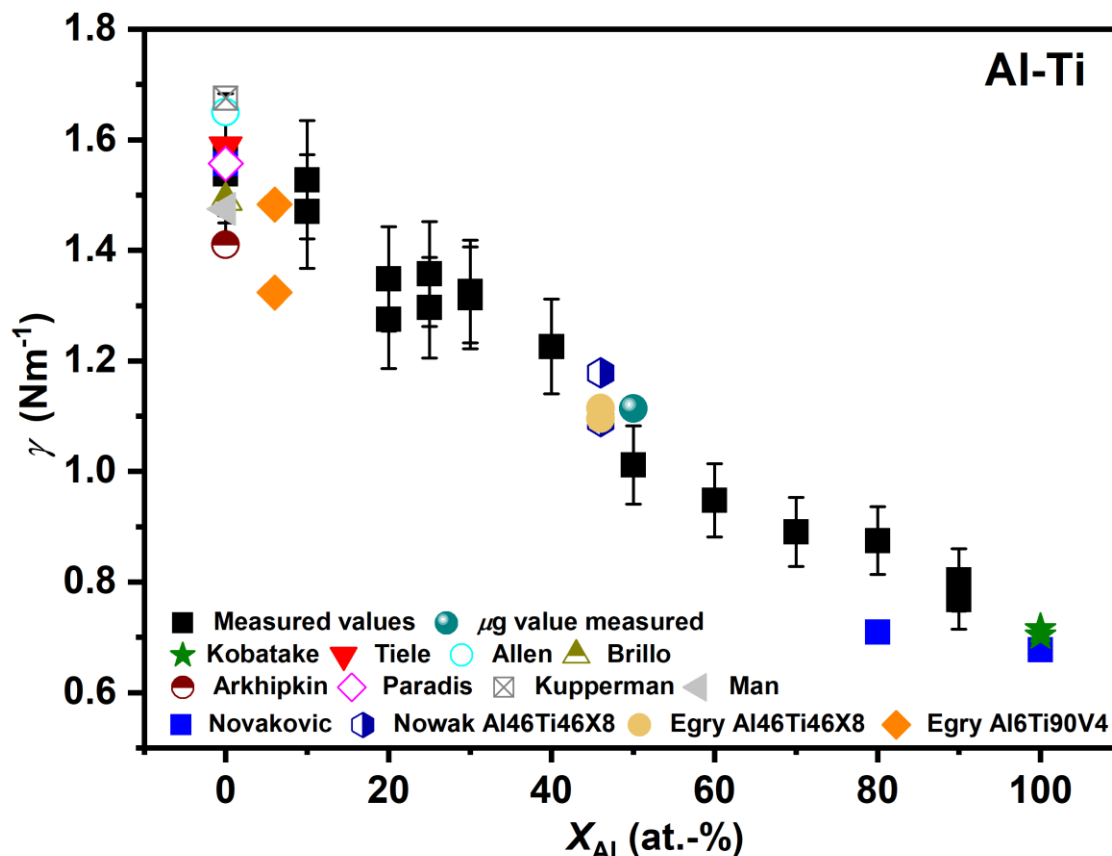


Figure 5.25: Surface tension data, γ , of liquid Al [25, 96], Ti, Al-Ti in dependence of the mole fraction, X_{Al} , of measured data at 1950 K and of industrially used Al-Ti based alloys at similar temperatures: Tiele = [102]=[102], Allen [123], Brillo [101], Arkhipkin [124], Paradis [125, 126], Kuppermann [127], Man [103], Nowak [11], Novakovic [121] and Egry [10]. The key to the method abbreviations can be found in section *Method abbreviations*. Based on Fig. 13 by Wessing et al. [7].

In this section, the results for high-temperature surface tension have been presented and discussed. It was found that all results are in good agreement with literature data and the predictions by the Butler and Chatain model. A highly non-ideal behavior was shown in the composition dependence showing a positive excess surface tension over the whole composition range with a suppressed surface segregation of the surface-active component Al. A comparison with other properties and their composition dependence will be conducted in the next chapter 6, and finally, all results will be briefly summarized in chapter 7.

5.6 Influence of oxygen on the surface tension

In the following section, the influence of the oxygen partial pressure on the surface tension is investigated. Oxygen adsorption on the surface of the sample can produce a reduction in the surface tension. Using electromagnetic levitation techniques, pollution from contact with a substrate or crucible is avoided. Hence, the level of impurities originating from processing is reduced to a minimum. However, it does not avoid contact with the gas phase; an oxygen-reduced sample surface can still be achieved as introduced in sections 2.6 and 3.10. However, due to the high affinity of oxygen to both elements, Al and Ti, the impact of potentially existing traces of oxygen on the surface tension needs to be discussed. Experimental surface tension results for Al and Ti in dependence of the oxygen partial pressure of the surrounding gas and chemical addition of oxygen to Ti in the form of Ti-O are presented. In the case of Ti-O, the results are fitted by the Belton/Szyszkowski adsorption equation introduced in section 2.6.1. Furthermore, calculations for the stability of Al-oxides in dependence of the oxygen partial pressure are presented along with a discussion for the surveyed oxygen partial pressure range. This section is based on sections 2.6 and 3.10, where the respective theoretical background and the experimental methods have been introduced.

5.6.1 Results

Before the results can be interpreted, the temperature dependent influence of buffer gas mixtures on the oxygen partial pressure in the sample surrounding atmosphere needs to be investigated, as introduced in section 3.10.4. This is necessary if the oxygen partial pressure is actively reduced as in the case of the Fukuyama lab with Ar-5% H₂ processing gas and when the temperature in the sample's vicinity differs from the operating temperature at the oxygen sensor. The oxygen partial pressure in the sample's surrounding, $P_{O_2}^S$, was evaluated using Eq. (3.31) with the Gibbs free energy of formation of H₂O, as $\Delta G = -246535 + 54.94 T$ Jmol⁻¹ to calculate the corresponding temperature dependant equilibrium constant, $K_{H_2O}(T)$. The oxygen partial pressure in the chamber at the position of the inlet gas during the measurement of $P_{O_2}^{Ch} = 10^{-22}$ Pa, was measured by the oxygen sensor at the Fukuyama lab (section 3.10.2) at 988 K operating temperature. Based on these initial values, Figure 5.26 shows the oxygen partial pressure in the sample's vicinity depending on the temperature. As can be seen from the figure, $P_{O_2}^S$ increases logarithmically with increasing temperature. In the sample's vicinity of the Al-Ti system, the temperature can vary from 1600 to 2100 K, which leads to $P_{O_2}^S$ values ranging from 10⁻¹² to 10⁻⁶ Pa at the Fukuyama lab.

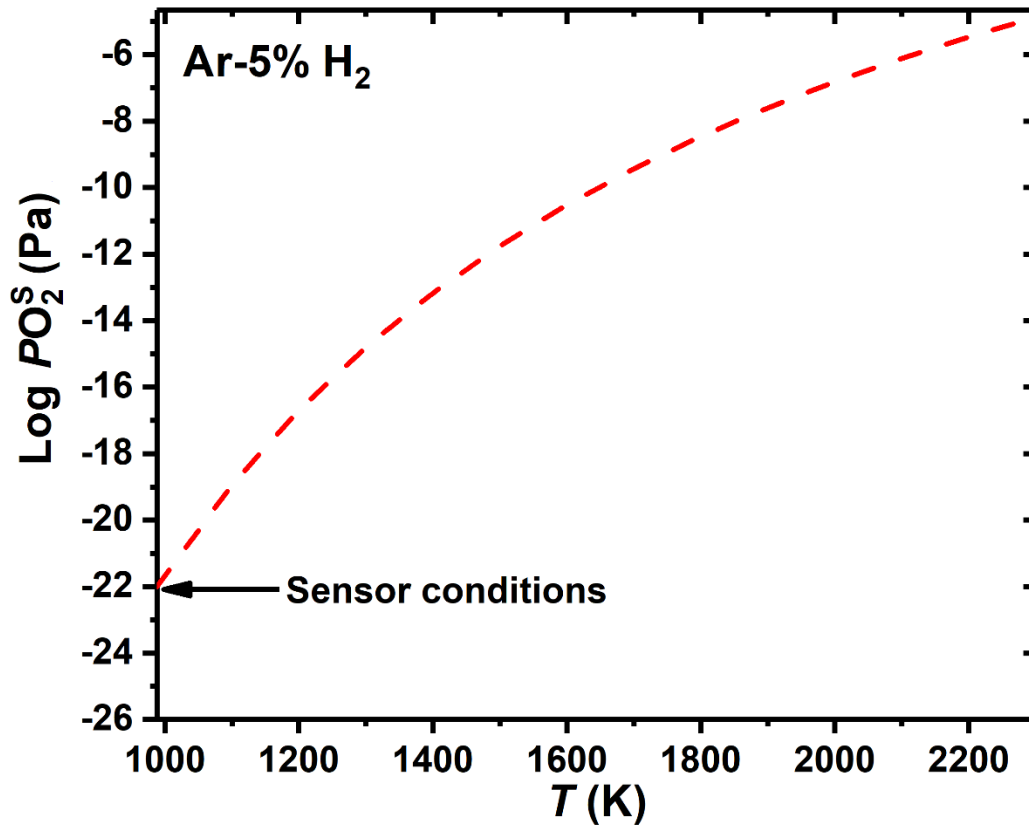


Figure 5.26: Temperature dependence of the sample oxygen partial pressure, $P_{O_2}^S$, of buffer gas mixtures Ar-5% H_2 used at the Fukuyama lab (solid line) estimated by Eq. (3.21).

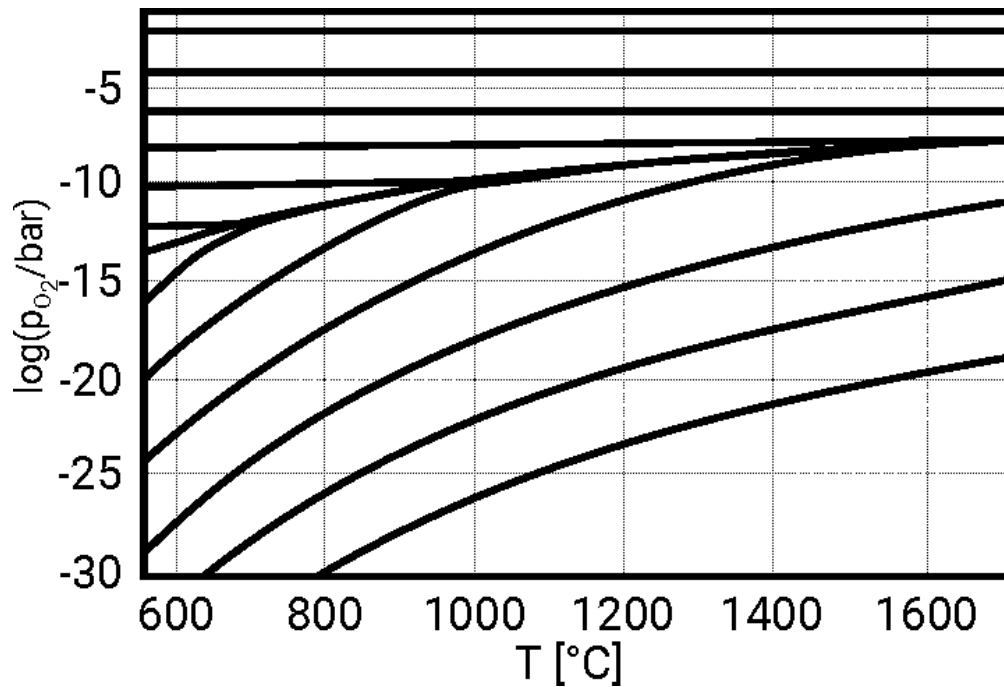


Figure 5.27: Oxygen partial pressure in the sample's vicinity depending on the temperature. The Figure is taken from the reference by Schulz et al. [63] with the DLR copyright license number 4215320209794.

At the DLR-MP, no buffer gases were used for the measurement. To neglect possible influences of H_2 impurities in the high purity processing gases, Schulz et al. [63] investigated the temperature dependence of the oxygen partial pressure of high purity gases, as illustrated in Figure 5.27. The study complies with the conditions of this work using high purity gases of 99.9999 vol.-% purity, with the total amount of hydrogen corresponding to $P_{O_2}^S < 10^{-7}$ bar. Schulz et al. [63] report that, if $P_{O_2}^{873\text{ K}} \geq 10^{-7}$ bar (10^{-2} Pa) measured at the sensor with an operating temperature of 873 K, temperature changes have a minor impact on the $P_{O_2}^S$. As can be seen from Figure 5.28 and Figure 5.29, the oxygen partial pressure ranges covered in this work, amount to 10^{-7} Pa $< P_{O_2}^{Ch} < 10$ Pa and, therefore, lie partially in a range where the temperature may affect the oxygen partial pressure. Taking the temperature dependence of the oxygen partial pressure into account, the measured lower boundary of $P_{O_2}^{873\text{ K}} = 10^{-11}$ bar (10^{-6} Pa) would correspond to an oxygen partial pressure in the sample's surrounding of $P_{O_2}^S = 10^{-8}$ bar (10^{-3} Pa) which reduces the measured oxygen partial pressure range to 10^{-3} Pa $< P_{O_2}^{Ch} < 10$ Pa.

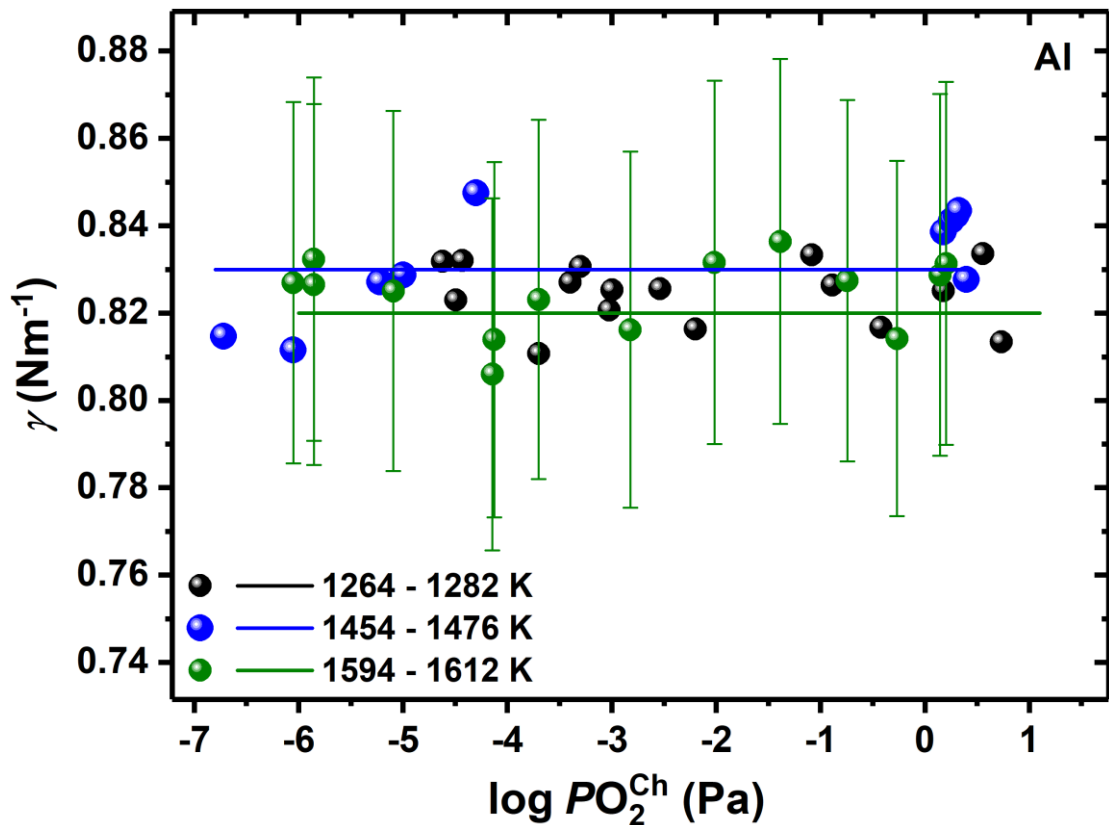


Figure 5.28: Surface tension measurements as a logarithmic function of the oxygen partial pressure in the chamber, $P_{O_2}^{Ch}$, of liquid Al at a constant temperature within 0.5 % scattering (Table 24 in the *Appendix*). Exemplarily, the experimental uncertainty as introduced in section 3.8, is depicted by the errors bars within 5 % uncertainty for one experiment. The oxygen partial pressure was measured by the potentiometric system sensor (SS1) at the outlet gas.

Figure 5.28 depicts surface tension data for Al as a logarithmic function of the oxygen partial pressure, $\log P_{O_2}$, covering 4 individual experiments. The oxygen partial pressure depicted was obtained by the potentiometric system sensor (SS1), measuring the oxygen partial pressure in the outlet gas of the oxygen control system (OSC), as introduced in section 3.10.2. All oxygen partial pressure values reported in this section refer to the values measured by the sensor. All measurements were conducted at constant temperatures within 0.5% scattering, as referred to in Table 24 in the *Appendix*. The oxygen partial pressure in Figure 5.28 is directly measured and not corrected according to Figure 5.27, covering a range of $10^{-7} \text{ Pa} < P_{O_2}^{\text{Ch}} < 10 \text{ Pa}$. However, in Table 24 the corrected upper boundary values are appended in brackets in the column of the measured $P_{O_2}^{\text{Ch}}$ boundaries. Taking the calculations by Schulz et al. into account the oxygen partial pressure range in the sample's surrounding and temperature should amount to $10^{-3} \text{ Pa} < P_{O_2}^{\text{S}} < 10 \text{ Pa}$, respectively. As can be seen from Figure 5.28 the surface tension is constant over all measurements and varying oxygen partial pressures within the 5% experimental uncertainty (compare section 3.8) amounting to $0.82 \pm 0.01 \text{ Nm}^{-1}$.

Figure 5.29 shows the surface tension data for pure Ti and Ti-O, listed in Table 16 and Table 25 in the *Appendix* as a logarithmic function of the oxygen partial pressure in the chamber, $\log P_{O_2}^{\text{Ch}}$. Analogously to the measurements of Al (Figure 5.28), the oxygen partial pressure was measured at the outlet gas (SS1) at the sensor temperature of 873 K covering $10^{-6} \text{ Pa} < P_{O_2}^{\text{Ch}} < 10 \text{ Pa}$. According to the calculations by Schulz et al. [63] and Figure 5.27, this corresponds to a sample oxygen partial pressure range of $10^{-3} \text{ Pa} < P_{O_2}^{\text{S}} < 10 \text{ Pa}$. In the case of Ti, ten experiments have been conducted at constant temperatures within 0.5% scattering (Table 25 in the *Appendix*). Over all measurements and the entire oxygen partial pressure range, the surface tension exhibits negligible oxygen partial pressure dependence with a constant value of $1.52 \pm 0.02 \text{ Nm}^{-1}$.

Concerning Ti-O, the samples have been prepared by addition of respective amounts of TiO_2 , as described in section 4.1.2. All compositions, $\text{Ti}_{74}\text{O}_{26}$, $\text{Ti}_{86}\text{O}_{14}$, Ti_{94}O_6 , Ti_{97}O_3 and Ti_{99}O_1 , show negligible oxygen partial pressure dependence and are therefore, basically constant over measured range. Generally, the surface tension values of the Ti-O melts (Table 16) lie below the ones of pure Ti, and with increasing O-ratio the surface tension gradually decreases, starting from $1.47 \pm 0.01 \text{ Nm}^{-1}$ in the case of Ti_{99}O_1 to the lowest value for $\text{Ti}_{74}\text{O}_{26}$ amounting to $0.97 \pm 0.01 \text{ Nm}^{-1}$. As can be seen in Figure 5.29 by the 5% relative uncertainty exemplarily illustrated for one measurement of Ti, this trend exceeds by far the experimental scattering, with up to 36% variation between the surface tension of Ti and the Ti-O melts.

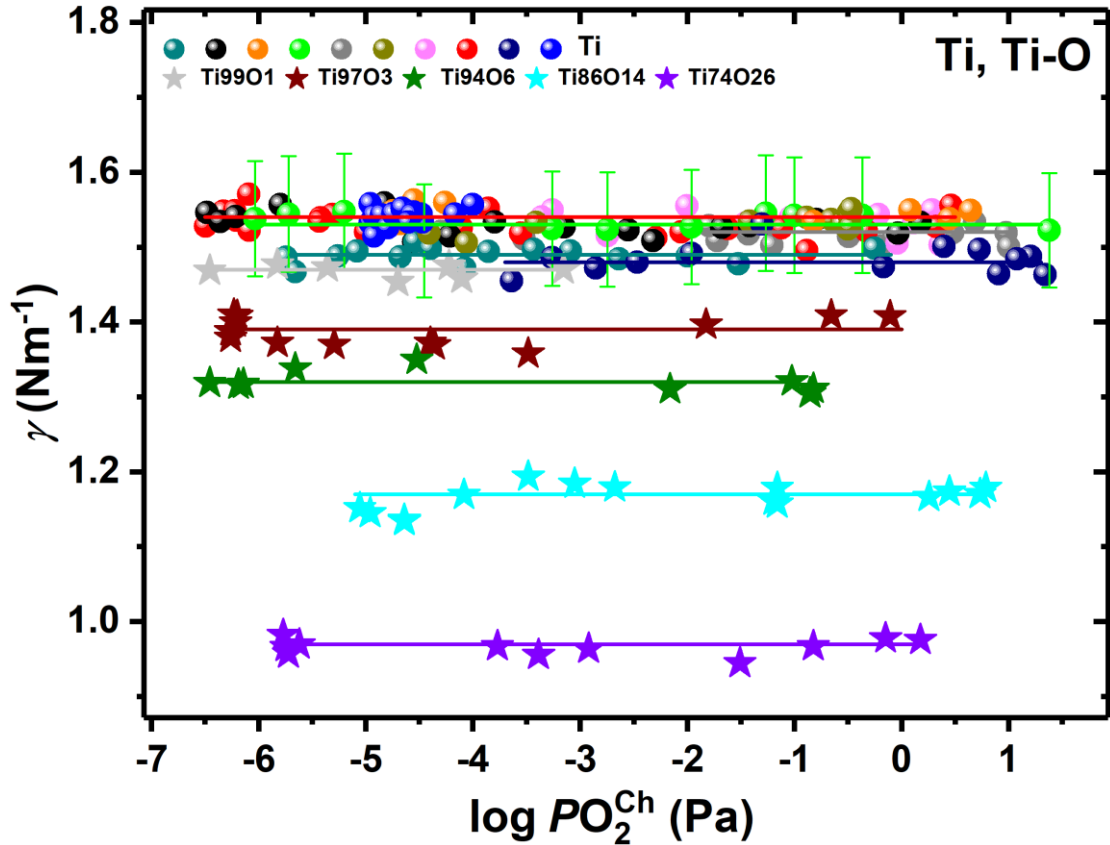


Figure 5.29: Surface tension measurements as a logarithmic function of the oxygen partial pressure in the chamber, $P_{O_2}^{Ch}$, of liquid Ti and Ti-O at a constant temperature within 0.5 % scattering (Table 16 and Table 25 in the *Appendix*). Analogously to Figure 5.28, the experimental uncertainty is shown by the errors bars within 5 % uncertainty for one experiment and the oxygen partial pressure was measured at the outlet gas at the sensor temperature of 873 K.

5.6.2 Discussion

In the following the results of section 5.6.1 will be discussed concerning the Al-O and Ti-O system.

5.6.2.1 Al-O system

When considering the Al-O system, the conditions and boundaries for surface oxidation should be defined and discussed. In this context, the temperature and the oxygen partial pressure are the crucial triggers for the equilibrium conditions for Al-oxide formation. Additionally, it is important to distinguish the conditions in the chamber and the conditions in the vicinity of the sample which have been discussed in previous studies, e.g., by Eustathopoulos [29, 128, 129] and Ricci [65, 130-132]. The studies show that the oxygen partial pressure in the sample's vicinity can be much smaller than the one in the surrounding gas in the chamber. Sophisticated models have been reported by the

aforementioned authors to explain the relation between the oxygen partial pressure on the sample's surface, $P_{O_2}^S$, to the oxygen partial pressure in the chamber, $P_{O_2}^{Ch}$ [25].

In particular, the studies by Kobatake et al. [25], Eustathopoulos et al. [128] and Molina et al. [133] are dedicated to the discussion of those models with regards to the Al-systems. In the following, the major processes leading to a reduced oxygen partial pressure in the sample's vicinity are explained, and the equilibrium oxygen partial pressure for Al-oxide formation is calculated for five different temperatures, 1200 K, 1300 K, 1400 K, 1500 K and 1600 K, as shown Figure 5.30.

One attributable reaction is the formation of Al-oxides on the pure liquid Al sample, also referred to as passive oxidation [61]:



The equilibrium constant of the reaction as introduced in section 2.6.2 can be calculated as the sum of the individual reactants involved in the reaction, according to Eq. (2.58). As the equilibrium constants of pure components can be approximated as one and, thus be neglected when calculating the equilibrium constant of the entire reaction, it can be formulated as following, only taking the equilibrium constant of the solid oxide Al_2O_3 into account:

$$\begin{aligned} \log K &= \log K_{\text{Al}_2\text{O}_3} - \frac{3}{2} \log K_{\text{O}_2} - 2 \log K_{\text{Al}} = \log K_{\text{Al}_2\text{O}_3} - 0 - 0 \\ &= \log K_{\text{Al}_2\text{O}_3} \end{aligned} \quad (5.2)$$

The data for the equilibrium constants have been taken from NIST-JANAF, thermochemical tables [109] and in the case of $\log K_{\text{Al}_2\text{O}_3}$ at 1400 K amounts to 45.896. By the *law of mass action*, the equilibrium constant of the reaction, K , can be defined by the respective the activities, α_i , as described in section 2.6.2. Here, the equilibrium constant of the reaction is connected to the respective activities, $\alpha_{\text{Al}_2\text{O}_3}$ and α_{Al} , and the oxygen partial pressure, P_{O_2} . As the activities of solid and pure liquid phases can be assumed as unity, 1, the following can be derived:

$$\log K = \log \left(\frac{\alpha_{\text{Al}_2\text{O}_3}}{P_{\text{O}_2}^{3/2} \cdot \alpha_{\text{Al}}} \right) = \log \left(\frac{1}{P_{\text{O}_2}^{3/2} \cdot 1} \right) = -\frac{3}{2} \log P_{\text{O}_2} \quad (5.3)$$

At 1400 K this leads to an oxygen partial pressure boundary for the oxide formation of $\text{Al}_2\text{O}_3 (s)$ of $\log P_{\text{O}_2} = -30.579 \text{ bar} = -25.579 \text{ Pa}$. Respective values for additional temperatures are listed in Table 15.

Another significant reaction contributing to a difference in the oxygen partial pressure in the sample's vicinity, $P_{O_2}^S$, and the oxygen partial pressure of the chamber, $P_{O_2}^{Ch}$, is the formation of Al-oxide gases from liquid Al and gaseous oxygen in the chamber.



This process describes active oxidation as referred to by Drevet et al. for silicon oxides, respectively [61], consisting of the direct transformation of incident oxygen to gaseous Al_2O . Analogously to the reactions (5.1) and (5.2), the equilibrium constant of the reaction, as an example at 1400 K can be calculated as

$$\log K = \log K_{\text{Al}_2\text{O}}^S - \frac{1}{2} \log K_{\text{O}_2}^S - 2 \log K_{\text{Al}} = \log K_{\text{Al}_2\text{O}}^S = 9.332 \quad (5.5)$$

Using the equilibrium constant, a relation between the partial pressure of oxygen to the one of Al_2O , $P_{\text{Al}_2\text{O}}^S$, in the sample's vicinity can be defined as

$$\log P_{\text{Al}_2\text{O}}^S = \log K + \frac{1}{2} \log P_{\text{O}_2}^S + 0 = 9.332 + \frac{1}{2} \log P_{\text{O}_2}^S \quad (5.6)$$

Finally, the last essential reaction describes the gas-liquid-solid phase equilibrium on the sample's surface which leads to deoxidation through the formation of gaseous Al-oxides.



Accordingly, the equilibrium constant of the reaction and consequently the Al_2O partial pressure can be derived exemplarily for 1400 K as

$$\log K = 3 \log K_{\text{Al}_2\text{O}} - \frac{1}{2} \log K_{\text{Al}_2\text{O}_3} - 4 \log K_{\text{Al}} = 3 \cdot 9.332 - 45.869 - 0 \quad (5.8)$$

and

$$\log K = \log \left(\frac{P_{\text{Al}_2\text{O}}^3}{\alpha_{\text{Al}_2\text{O}_3} \cdot \alpha_{\text{Al}}} \right) = 3 \log P_{\text{Al}_2\text{O}} \quad (5.9)$$

respectively.

Therefore, at 1400 K, $\log P_{\text{Al}_2\text{O}}$ amounts to $-5.958 \text{ bar} = -0.958 \text{ Pa}$, assuming the activity of the solid Al_2O_3 and the one of the pure Al equal one. This value defines the maximum Al_2O partial pressure for a 'clean' surface, due to deoxidation.

The oxygen partial pressure in the sample's vicinity is affected by the processes of oxidation, corresponding to Eq. (5.1) and deoxidation as described by Eq. (5.7). To quantitatively connect those counteracting processes and relate them to oxygen partial pressure boundaries, flow equations can be used. The oxygen flow onto the sample's surface, J_0^+ (Eq. (5.1)), and the oxygen flow leaving the surface J_0^- , (Eq. (5.7)), under the condition that $P_{O_2}^{Ch} \gg P_{O_2}^S$, can be determined as

$$J_0^+ = 2 \cdot \left(\frac{D_{O_2}}{RT} \right) \left(\frac{P_{O_2}^{Ch}}{\delta} \right) \quad (5.10)$$

$$J_0^- = 1 \cdot \left(\frac{D_{Al_2O}}{RT} \right) \left(\frac{P_{Al_2O}^S - 0}{\delta} \right) \quad (5.11)$$

Here, D_{O_2} and D_{Al_2O} define the diffusion coefficients of oxygen and Al-oxide respectively and δ is the thickness of the diffusion boundary layer in the gas. Assuming equilibrium, it is valid to claim that $J_0^+ = J_0^-$, therefore:

$$2 \left(\frac{D_{O_2}}{RT} \right) \left(\frac{P_{O_2}^{Ch}}{\delta} \right) = \left(\frac{D_{Al_2O}}{RT} \right) \left(\frac{P_{Al_2O}^S}{\delta} \right) \quad (5.12)$$

Resultantly, Eq. (5.12) yields the relation between the partial pressure of oxygen in the chamber and the one of Al-oxide on the sample's surface.

$$\log P_{O_2}^{Ch} = P_{Al_2O}^S - \log \left(\frac{2D_{O_2}}{D_{Al_2O}} \right) \quad (5.13)$$

The maximum value for the Al_2O partial pressure for a 'clean' surface as calculated in Eq. (5.9) can now be related to a respective oxygen partial pressure in the chamber, using the gas diffusion ratio of $D_{Al_2O}/D_{O_2} = 3.45$, as reported by Kobatake et al. [25]. As an example, at 1400 K, the critical oxygen partial pressure in the chamber, $\log P_{O_2}^{Ch}$, for a 'clean' surface amounts to - 5.721 bar = -0.721 Pa. Respective values for additional temperatures are listed in Table 15.

Finally, the combination of Eq. (5.13) with Eq. (5.6) provides a direct relation between the oxygen partial pressure on the surface in dependence of the oxygen partial pressure in the chamber as a result of the oxidation and deoxidation processes:

$$\log P_{O_2}^S = \log \left(\frac{2D_{O_2}}{D_{Al_2O}} \right) + 2 \log P_{O_2}^{Ch} - 2K_{Al_2O} \quad (5.14)$$

With Eq. (5.14), the critical oxygen partial pressure in the sample's vicinity, $\log P_{O_2}^S$, for a 'clean' surface can be calculated from the respective critical oxygen partial pressure in the chamber gas, $P_{O_2}^{Ch}$, calculated above by Eq. (5.13). At 1400 K, the critical value in the chamber, $\log P_{O_2}^{Ch} = -5.721$ bar corresponds to a significantly reduced oxygen partial pressure on the sample's surface, $\log P_{O_2}^S = -30.343$ bar = -25.343 Pa. The respective boundary values for Al_2O_3 formation on the sample's surface, the critical $\log P_{O_2}^S$ and $\log P_{O_2}^{Ch}$ values with regards to a 'clean surface' and the equilibrium constant K_{Al_2O} at 1200 K, 1300 K, 1400 K, 1500 K and 1600 K are listed in Table 15. With increasing temperature, the oxygen formation boundary shifts to higher oxygen partial pressures, in the case of $\log P_{O_2}^{Ch}$ from -3.08 to 1.21. Consequently, under measurement conditions, a 'clean' surface can either be achieved by an oxygen partial pressure decrease or by increasing the temperature.

T (K)		1200	1300	1400	1500	1600
Al_2O_3 formation $\log PO_2$ (Pa)		-32.59	-28.81	-25.58	-22.78	-20.33
'clean' surface	$\log P_{O_2}^{Ch}$ (Pa)	-3.08	-1.81	-0.76	0.22	1.21
	$\log P_{O_2}^S$ (Pa)	-32.35	-28.58	-25.34	-22.54	-20.10
$\log K_{Al_2O}$		10.47	9.86	9.33	8.87	8.46

Table 15: Boundary values for Al_2O_3 formation on the sample's surface with critical $\log P_{O_2}^S$ and $\log P_{O_2}^{Ch}$ values with regards to a 'clean' surface and the equilibrium constant K_{Al_2O} at 1200 K, 1300 K, 1400 K, 1500 K and 1600 K.

The oxygen partial pressure in the sample's vicinity, $\log P_{O_2}^S$, as a linear function (Eq. (5.14)) of the one in the chamber, $\log P_{O_2}^{Ch}$, exemplarily at 1200 K, 1400 K and 1600 K is depicted in Figure 5.30. Additionally, the boundaries for Al_2O_3 formation, calculated from Eq. (5.1) for 'clean' conditions based on Eqs. (5.4), (5.9), (5.13) and (5.14) are shown for 1400 K. As can be seen from the picture and the calculations, the Al_2O_3 formation is starting to occur at $\log P_{O_2} = -25.58$. Nonetheless, for maximum values of up to $\log P_{O_2}^{Ch} = -25.34$ and $\log P_{O_2}^S = -0.76$, indicated by the dotted lines in Figure 5.30, a 'clean' surface prevails. Above those values for the oxygen partial pressure, stable oxide formation is dominant at 1400 K. When comparing the $\log P_{O_2}^S$ ($\log P_{O_2}^{Ch}$) relations for different temperatures, it can be seen, that at a given $\log P_{O_2}^{Ch}$ the oxygen partial pressure reduction in $\log P_{O_2}^S$ is less dominant with increasing temperature.

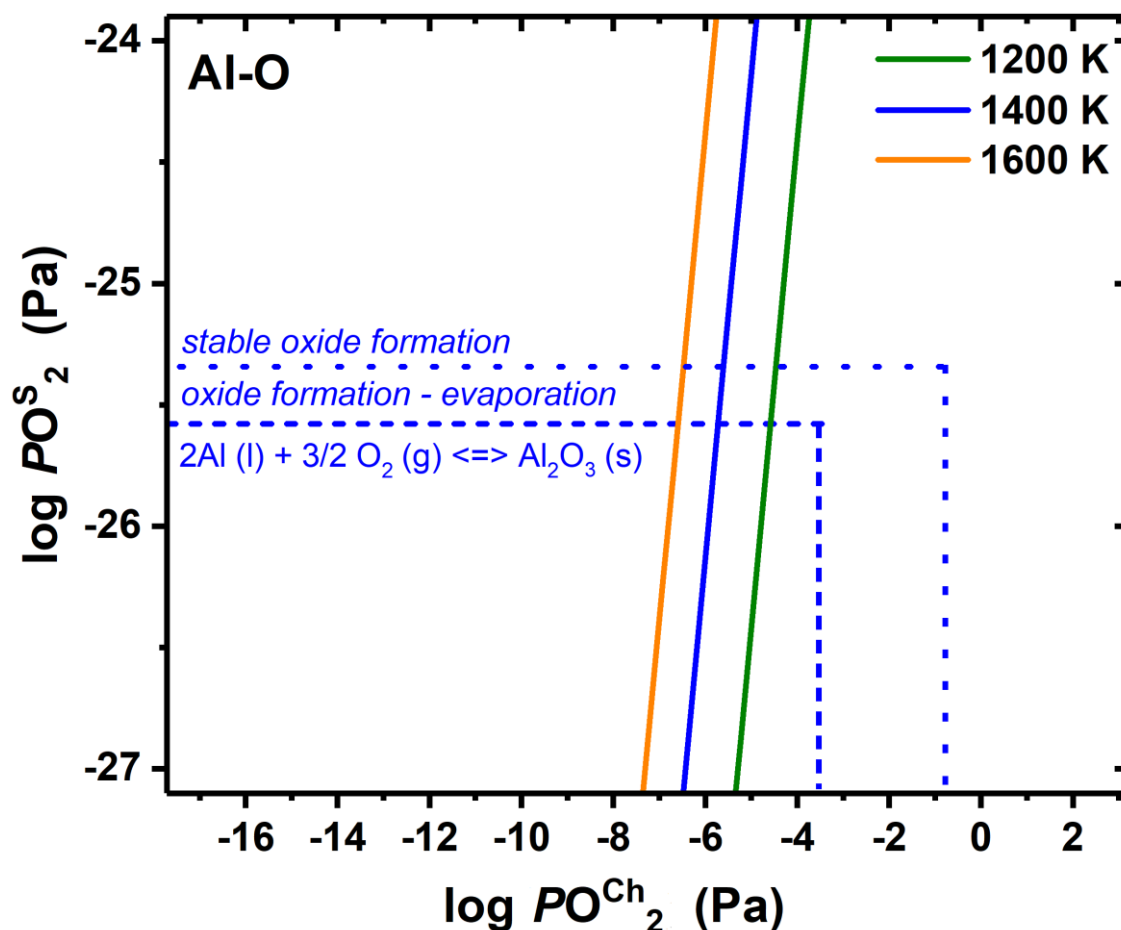


Figure 5.30: The oxygen partial pressure in the sample's vicinity, $\log P_{O_2}^S$, as a linear function (Eq. (2.58)) of the one in the chamber, $\log P_{O_2}^{Ch}$, exemplarily at 1200 K, 1400 K and 1600 K. Additionally, the boundaries for Al_2O_3 formation, calculated from Eq. (5.1) for 'clean' conditions are shown for 1400 K.

As presented in section 5.6.1, the surface tension data for liquid Al in dependence of the oxygen partial pressure in the chamber, are listed in Table 24 in the Appendix. The last column of Table 24 contains an evaluation of the surface condition of the respective measurements. For the evaluation, of the corrected oxygen partial pressure range, as discussed in section 5.6.1, and the calculations of this section as presented in Table 15 are taken into account. As can be seen from Table 24, the measurements conducted at 1601 K and 1463 K can, therefore, be considered 'clean', while the measurement at 1271 K was performed under partly oxidising conditions.

All literature data in Table 22 and Figure 5.31 for the surface tension at the liquidus temperature scatter around a mean value of $\gamma_L = 0.89 \pm 0.10 \text{ Nm}^{-1}$ corresponding to a relative uncertainty of 11%, depicted by the red star in Figure 5.31. The statistical uncertainty of 11% lies far above the experimental uncertainty of up to 5% due to the large scattering of the data and data obtained at different measurement conditions. The corresponding mean surface tension temperature coefficient, γ_T , amounts to $1.66 \cdot 10^{-4} \text{ N}$

$\text{m}^{-1}\text{K}^{-1}$, within $\pm 0.60 \cdot 10^{-4}\text{Nm}^{-1}\text{K}^{-1}$. Most data lie within the standard deviation for the mean value of the surface tension at liquidus temperature.

Figure 5.31 also shows a comparison of selected Al surface tension results as a function of temperature presented in this work and data reported by literature. The depicted values for $\gamma(T)$, γ_L and γ_T (according to Eq. (2.23)) are given in Table 22 in the *Appendix* along with the respective methods and references. Additionally, the tables contain literature data which is not displayed in the figure to not overload it.

The data by Ayushina [134] and Levin [135] underestimate the surface tension of Al by far with regards to the mean literature value, in the case of Levin up to 31%. Nonetheless, another result for Al is reported by Levin [135], $\gamma_L = 0.866 \text{ Nm}^{-1}$, which agrees well with the mean literature value. On the other hand, the data given by for example Goumiri et al. [136], Cordovilla et al. [137] and Pamies et al. [138] and Kanian et al. [139] overestimate the mean literature data in the range of 25%. Molina et al. have discussed these values extensively in [133].

In the case of Goumiri et al. [136], an approximate 20% increase in the oxygen partial pressure was found if during the measurement the oxygen cover of the sample was removed to a nearly ‘clean’ surface. Molina et al. [133] argue that even though a general increase in the surface tension accompanying the cleaning process is likely, the value presented by Goumiri et al. [136] might be overestimated by approximately 10-15%. Molina et al. [133] suggest an overestimation of results by Goumiri et al. [136] due to the measurement configurations of the used Auger chamber.

Cordovilla and Pamies et al. [137, 138] report a value of $\gamma = 1.09 \text{ Nm}^{-1}$ at 1073 K for an oxide-free surface and a reduced oxygen partial pressure, and a value of $\gamma = 0.87 \text{ Nm}^{-1}$ at the same temperature in the case of a sample with an adsorbed oxygen layer covering the surface. However, in a later study [140] the authors stated that the high value could have been a consequence of the wetting of the capillary used to bubble argon into the liquid metal [133].

Kanian et al. suggested a value of $\gamma = 1.05 \text{ Nm}^{-1}$ at $T_L = 933 \text{ K}$ [139]. The authors used the oscillating drop method at high temperatures in the range of 1770–2170 K to remove Al-oxides on the surface. Due to likely evaporation at these temperatures, the accuracy of measurement might be affected. Additionally, the extrapolation of the measured values to the significantly smaller liquidus temperature may lead to a large error in γ_L [133].

Almost exclusively, the data in Figure 5.31 stand for measurement conditions where no particular attention was paid to the oxygen partial pressure. Only the data reported by Kobatake et al. [58] and Molina et al. [133] designated as ‘clean’ conditions and the data by Molina et al. [133] measured for an oxygen saturated liquid surface represent

exceptions. In accordance with the calculations of this work, these data refer to results obtained in some cases under conditions below or above the equilibrium oxygen partial pressure for Al-oxide formation. The measurements by Kobatake et al. [58] were conducted with the same EML-device and oxygen control system (OSC) as the measurements of this work and the data of Kobatake [37] yield values of $\gamma_L = 0.98 \text{ Nm}^{-1}$ and $\gamma_T = -2.71 \cdot 10^{-4} \text{ Nm}^{-1} \text{ K}^{-1}$. The oxygen partial pressure in the chamber, $\log P_{\text{O}_2}^{\text{Ch}}$, was controlled at -1 Pa. Using the same models for the formation of oxides as presented in this chapter, Kobatake et al. argue that the value for $\log P_{\text{O}_2}^{\text{Ch}}$ is below the equilibrium boundary for stable oxide formation on the sample's surface and thus, the results were obtained under 'clean' conditions [58].

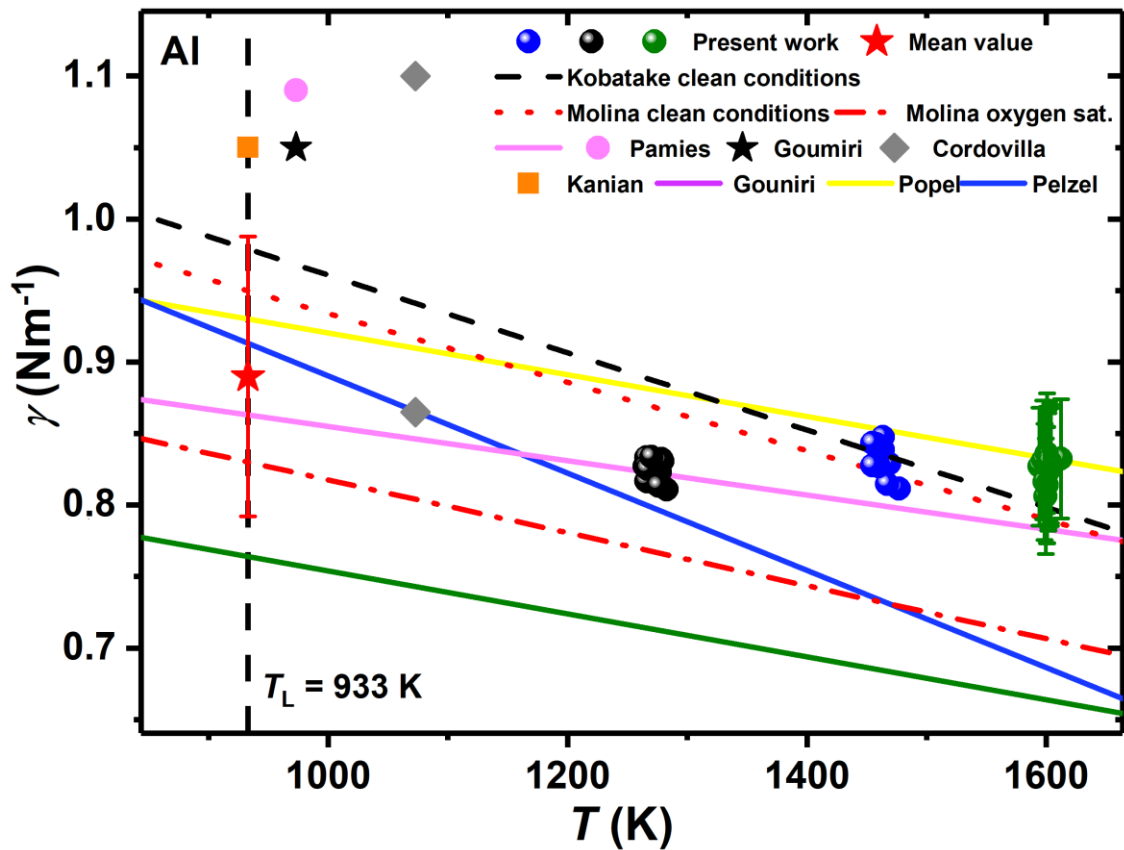


Figure 5.31: Al surface tension data in dependence of the temperature as a comparison between results of this work (circles) and selected literature data (lines) by Gouniri [141], Popel [142], Cordovilla [137], Pelzel [143], Pamies [138], Molina [133], Kanian [139] and Kobatake [58]. The used values for $\gamma(T)$, γ_L and γ_T (according to Eq. (2.23)) are given in Table 22 and Table 24 in the *Appendix* with additional literature data. The star symbol corresponds to the mean literature value at $T_L = 933 \text{ K}$.

The data by Kobatake et al. are in good agreement with the results by Molina of $\gamma_L = 0.95 \text{ Nm}^{-1}$ and $\gamma_T = -2.4 \cdot 10^{-4} \text{ Nm}^{-1} \text{ K}^{-1}$, also representing Al surface tension data for an oxygen-free surface [133]. In the case of Molina et al., the oxygen partial pressure was not actively measured, but the oxidized and 'clean' state of the sample was achieved due to high

vacuum conditions and measurements at high and low temperatures. Molina et al. [133] used the same calculations for boundary definitions of Al-oxide formation as presented in this work to attribute different temperatures to oxidation and de-oxidation state under the measurement conditions used. According to Molina et al. [133], the aforementioned value of $\gamma_L = 0.95 \text{ Nm}^{-1}$ obtained at high temperatures relates to a ‘clean’ surface and values of $\gamma_L = 0.83 \text{ Nm}^{-1}$ and $\gamma_T = -1.85 \cdot 10^{-4} \text{ Nm}^{-1} \text{ K}^{-1}$ obtained at lower temperatures are associated with an oxidized state [133].

Given a 10% reduction of the surface tension value by Goumiri et al. of 1.05 Nm^{-1} , the result is in good agreement with other data for reportedly measured under ‘clean’ conditions as presented in this study and by Molina et al. [133] and Kobatake et al. [58].

The data of this work presented in Table 24 for the surface tension of liquid Al at 1601 K and 1463 K obtained under ‘clean’ conditions, are in really good agreement with the data by Molina et al. [133] and Kobatake et al. [58] in a deoxidized state, respectively. Especially, the data by Kobatake et al. yield almost the exact values at the respective temperatures, within 0% and 2% deviation. In comparison with Molina et al., the data given in this work exceed the data slightly, by 1% and 3%, which lies within the general experimental uncertainty of 5%. All data associated with a deoxidized state overestimate the mean literature value by about 11%, thus lie outside the experimental uncertainty. However, it has to be taken into account that this value is subject to great data scattering and the above mentioned extreme and disputable values for much higher and lower surface tension are likewise contributing to the mean value.

The data reported by Molina et al. [133] related to an oxygen saturated condition lie approximately 14% below the data reported by the same group for a de-oxidized state. This works’ data obtained at 1271 K partly under oxidising conditions lie in between these two values by Molina and vary from both values about 7%. It agrees well with the majority of the literature results where no particular attention was paid to the oxygen partial pressure.

As described in section 2.6.1, there are main states in the process of oxide formation on the surface of a material. On the one hand, there is the complete oxidation of the surface with a continuous oxide film of a thickness in the nanometer scale. The surface tension values measured in this condition may vary with the respective thickness of the oxide film. In an intermediate state, the continuity of oxide film is disturbed, and the surface contains some oxide compounds as well as some chemisorbed oxygen (section 2.6.1, [133]). The surface tension in this state may be affected by the number of formed oxides and chemisorbed oxygen on the surface.

At last, a ‘clean’ or de-oxidized condition describes the complete lack of oxide particles on the surface. In this case, all oxygen is ideally removed from the surface, but realistically the surface still contains some minor pollution of adsorbed oxygen [133]. Considering these different states and variations within each state, it is understandable why the scattering in the reported surface tension results for liquid Al is so large. Most literature results are assumedly associated with disrupted oxidation and chemisorbed oxygen on the surface, assumedly varying with the respective amount or with the thickness of covering oxide films. The same applies for the result of this work at 1271 K; the surface condition might be associated with the intermediate state with disrupted oxides on the surface or with a continuous oxide film of a certain thickness.

In this section, the results on the influence of oxygen on the surface tension of liquid Al have been presented and discussed. All surface tension measurements of liquid Al as a function of the oxygen partial pressure have been found to be constant over the measurement range. The results of this work presented in this section and the one of Molina et al. [133] and Kobatake et al. [58] for ‘clean’ conditions, respectively are all in very good agreement and it seems reasonable to say that these measurements relate to oxide-free surfaces with either zero or minor adsorbed oxygen particles. This is in good agreement with the calculated oxide formation boundaries as calculated in this section. In chapter 7, all results will be summarized.

5.6.2.2 Ti-O system

In the Ti-O system, different mechanisms are prevailing than in the Al-O system. Numerous studies on the Ti-O system have been conducted, such as by Cancarevic et al. [144], Kornilov et al. [145], Murray et al. [94] and, among the most recent ones by Belyanchikov [24]. The latter author has performed a detailed thermodynamic analysis on oxygen in liquid and solid Ti showing that the removal of oxygen as free oxygen or volatile monoxides cannot be achieved under realistic measurement conditions as it requires very low residual pressures (e.g. $P_{O_2} = 10^{-13}$ Pa at 2023 K) [24]. Therefore, de-oxidation processes as in the Al-O system, leading to a reduced oxygen partial pressure in the sample’s vicinity can be neglected.

Ti surface tension results of this work and literature as a function of the temperature, T , are depicted in Figure 5.32. The corresponding data of this work measured at constant temperature (within experimental scattering) have been shown before in dependence of the oxygen partial pressure, $P_{O_2}^{Ch}$, in Figure 5.29 and are listed in Table 25 in the *Appendix*. Additionally, the temperature dependent results of Ti measured without consideration of the oxygen partial pressure, as presented in this work in section 5.5 are illustrated [7]. Moreover, Ti surface tension results obtained at the Fukuyama lab (Table 16) as a

function of time at constant temperature are included in Figure 5.32, as well as comparable literature data listed in Table 23 in the *Appendix*. The literature results by Brillo et al. [101] were obtained at the same EML facility as used in this work. For the surface tension of pure Ti, no comparable results for measurements under oxygen reduced atmosphere are published at this point.

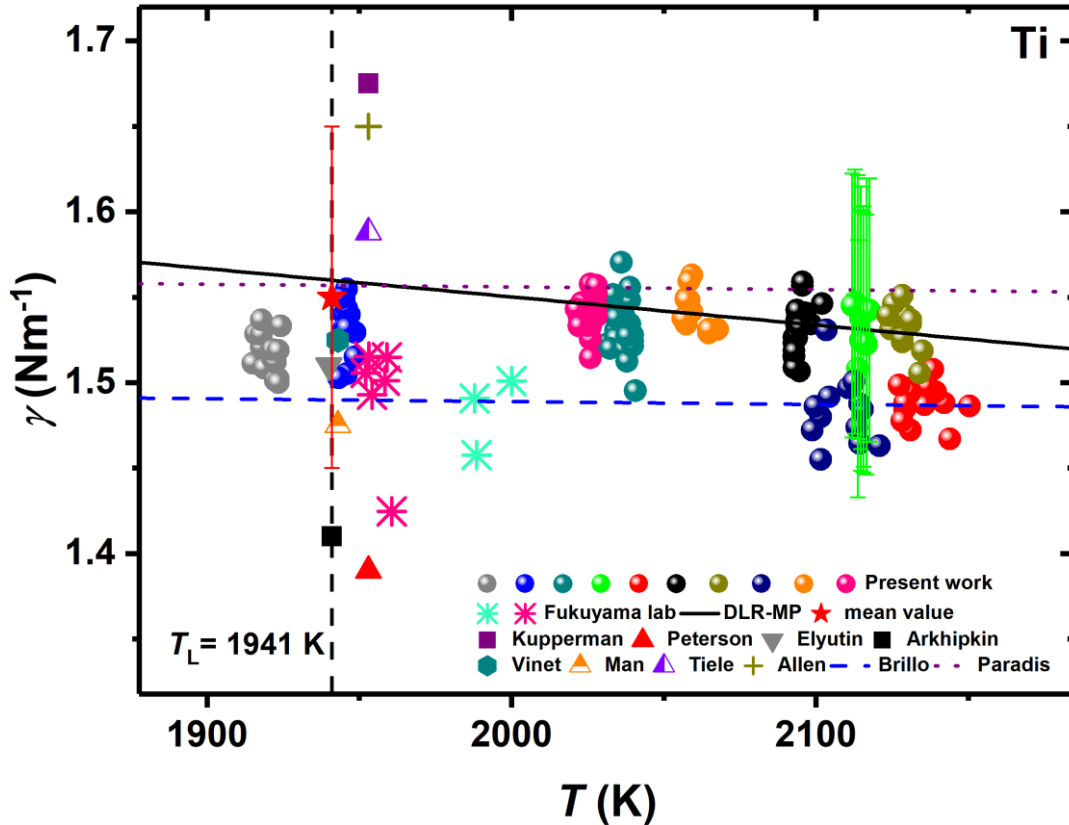


Figure 5.32: Liquid Ti surface tension values as a function of temperature of this work from the Fukuyama lab and DLR-MP and literature data by Brillo et al. [101], Kuppermann [127], Peterson et al. [146], Elyutin et al. [147], Arkhipkin et al. [124], Vinet et al. [148], Man et al. [103], Tiele et al. [102], Allen et al. [123], Paradis et al. [125], according to Eq. (2.23), Table 16, Table 23 and Table 25 in the *Appendix*. The star symbol corresponds to the mean literature value at $T_L = 1941$ K.

All literature data scatter around a mean value of $1.55 (\pm 0.1) \text{ Nm}^{-1}$ (red star in Figure 5.32), corresponding to 6.5 % relative standard deviation, which exceeds the general experimental uncertainty of 5 %. The data by Allen et al. [123] and Kuppermann [127] overestimate the surface tension of Ti with respect to the mean literature value by up to 8 %, while the data by Arkhipkin et al. [124] and Peterson et al. [146] underestimate the value by up to 10%. Among the results obtained at the Fukuyama lab, two respective values stand out, exhibiting smaller values than the other results within the same measurement. All measurements which were measured as a function of the oxygen partial pressure, $P_{\text{O}_2}^{\text{Ch}}$, scatter around a mean surface tension value of $1.52 (\pm 0.02) \text{ Nm}^{-1}$ (within 2057.21 ± 74.88 K) which corresponds to 1.3 % relative standard deviation and therefore,

are basically constant (Table 23 in the *Appendix*). The data agree well with literature results, especially with the data by Paradis et al. [125] and Brillo et al. [101].

Additionally, the data comply perfectly with the results obtained at the Fukuyama lab under reduced oxygen partial pressure (compare section 3.10.4) and the ones presented in section 5.6.1. As described before in section 3.2.2, for each measurement the experimental chamber was initially evacuated and backfilled with high-purity inert gases to avoid (oxygen) impurities. Nonetheless, in the case of the data presented in section 3.2.2 for $\gamma(T)$ of Ti, no particular attention was paid to the oxygen partial pressure, corresponding to most literature data. Thus, based on studies that oxygen may lead to a reduction of the surface tension [65], the result is surprising. Paradis et al. argued [125] that the reported results on pure and oxygen-free liquid Ti should be correct because the pronounced evaporation of liquid Ti might induce a self-purification process of the sample. However, this argument is subject to question [24].

The Ti-O phase diagram is presented in section 4.1.2 revealing that oxygen has a large solubility in solid titanium, of up to 32 at.-% in α -titanium [145]. However, the oxygen solubility in liquid titanium in contact with Ti-oxides is significantly lower, as stated by Belyanchikov [24]. Among the oxides, the highest solubility is found for TiO₂, which amounts to 1.7 wt.-% = 4.9 at.-% at 1943 K in the case of solid TiO₂ and 1.4 wt.-% = 4.1 at.-% at 2193 K in the case of liquid TiO₂ [24]. The solubility limits are already reached at very low oxygen partial pressures, e.g. $P_{O_2} = 10^{-13}$ Pa at 2023 K, the melting temperature of TiO₂ [24]. Additionally, Belyanchikov reports that, Ti can practically not be reduced by any of the strongest deoxidizers known, i.e., Ba, Be, Ca, Ce, Hf, La, Mg, Sr, Zr, and Fe [7, 24]. Therefore, according to Belyanchikov [24], the oxygen concentration in liquid Ti should be maximum under realistic measurement conditions.

To further investigate the oxygen concentration, some samples were analysed by the company *Umicore* with a Leco TC-600 device (section 4.2.2). The results are shown in Table 16 in the third row. All oxygen concentrations lie below the maximum value for the oxygen solubility of about 1.4 wt.-% = 4.1 at.-% as reported by Belyanchikov [24]. Especially the unprocessed samples (description in the second row of Table 16) feature very low oxygen concentrations of about 0.1% and are, thus, smaller than the maximum value by a factor of 10 to 20. In general, the processed samples show slightly higher oxygen partial pressure values than unprocessed samples which means that the samples accumulate oxygen during the measurement. This is in good agreement with the assumption by Belyanchikov [24] that under real measurement conditions the oxygen partial pressure of Ti cannot be reduced. However, as it is not maximum even after 90 min processing, it could mean that the process of oxygen adsorption on the liquid surface takes longer time under measurement conditions, e.g., low oxygen partial pressures.

Alternatively, it could mean that the calculations by Belyanchikov [24] could not be accurate for realistic conditions.

Lab	Comment	O-analysis (at.-%)	Measured time (min)	γ (Nm ⁻¹)
DLR-MP	no processing	0.12495	0	
DLR-MP	measurement	0.46081	≈ 60	1.52
Fukuyama lab	arc melting	0.07909	0	
Fukuyama lab	measurement	0.14795	15	1.50
Fukuyama lab	measurement	0.31646	45	1.45
Fukuyama lab	measurement	0.1678	60	1.48
Fukuyama lab	measurement	0.23046	90	1.50

Table 16: Surface tension data of liquid Ti measured at the Fukuyama lab and the DLR-MP with the corresponding measurement times and oxygen concentrations of the analysed samples after the measurement. For ‘0 min’ measurement time it relates to samples that were analysed before a measurement, either after the sample preparation but prior to arc melting (DLR-MP) or after the sample preparation and arc melting (Fukuyama lab).

To further investigate if time-dependent oxygen adsorption influences the surface tension, respective measurements at the Fukuyama lab and sample analysis of measurements at the DLR-MP and the Fukuyama lab were performed, accordingly. At the DLR-MP two samples were analysed with respect to their oxygen concentration, one processed Ti sample after a standard measurement time of about 60 min and Ti material after the sample preparation but prior to arc melting (0 min), as described in the second row of Table 16. An equivalent analysis was performed at the Fukuyama lab for one sample after arc melting but before the measurement (0 min) and for four samples after a processing time of about 15 min, 45 min, 60 min and 90 min, respectively.

The oxygen concentration is plotted against time in Figure 5.33 on the right y-axis. During the 45 min and 90 min measurements, the surface tension was measured every 15 min and the respective surface tension data (last row in Table 16) as a function of time is shown on the left y-axis. In the case of the 15 min and 60 min processing time, the corresponding surface tension values in the last row in Table 16 relate to the average

values of the 45 min and 90 min measurements at the respective time. For one surface tension measurement after 75 min, the experimental error of 5 % (section 3.8) is exemplarily shown.

Considering the surface tension data obtained at the Fukuyama lab, in Figure 5.33 there seems to be a decrease from an initially high value of 1.50 Nm^{-1} after 15 min measurement to 1.45 Nm^{-1} after 45 min processing time. In the time interval from 45 min to 90 min, the surface tension increases again up to 1.50 Nm^{-1} . This trend which is supported by both measurements of 45 min and 90 min time with up to 6.4 % decrease, lies, however within the experimental error of 5 % for each measurement. The value measured at the DLR-MP seems to support this trend but lies about 1.3 % higher than the results from the Fukuyama lab with a value of 1.52 Nm^{-1} . However, as can be seen from Figure 5.32, the results from the DLR-MP systematically lie about 1-2 % higher than the respective ones at the Fukuyama lab, which lies far below the experimental error of 5 %.

At the same time, the oxygen concentration undergoes the inverse trend to the surface tension from 0 min to 45 min with a maximum exhibited after 45 min of 0.3 at.-% oxygen concentration, corresponding to an increase of 113 %. From 45 to 90 min measurement time the oxygen concentration seems to stay constant at $0.24 (\pm 0.07)$ at.-%. Taking the data from the DLR-MP into account, a constant increase in the oxygen concentration from 0 min to about 60 min measurement time could be indicated. However, considering that the results for the oxygen concentration of the DLR-MP samples only consist of two data points, the data trend might not be constant in between 0 min and 60 min after all.

Nevertheless, the results suggest that there is an increase in the oxygen concentration over the measurement time. This increase might either stagnate after a certain measurement time, as indicated by the data from the Fukuyama lab, e.g., due to evaporation processes [125]. As another option, there might be a constant increase in the oxygen concentration until the maximum oxygen solubility is reached at $1.4 \text{ wt.-%} = 4.1 \text{ at.-%}$. However, if oxygen is adsorbed constantly, this process must take longer than 90 min for completion, as the maximum oxygen concentrations detected after the measurements only amount to 0.23 at.-% to 0.46 at.-%, thus below the theoretical maximum value.

It has been reported in the literature [62, 65] that the surface tension generally decreases with increasing amount of adsorbed oxygen. This process seems to be applicable within the first 45 min in Figure 5.33. However, that the surface tension rises again after 45 min while the oxygen concentration increases or stays constant, seems to be counter-intuitive. This might indicate some interactions between the species in the bulk phase and the surface of the sample. A similar mechanism was reported by Iida et al. [149]. In the beginning, the solute is adsorbed on the surface with minimal or no exchange with the bulk causing a decrease in the surface free energy over time. Eventually, the oxygen from

the surface could migrate to the bulk, in turn leading to an increase in the surface tension again and a relative depletion of oxygen on the surface, while the overall oxygen concentration may continuously rise or stagnate. However, as mentioned before, the surface tension does not decrease sufficiently beyond the boundaries of the experimental error to provide a definite time-dependent progression.

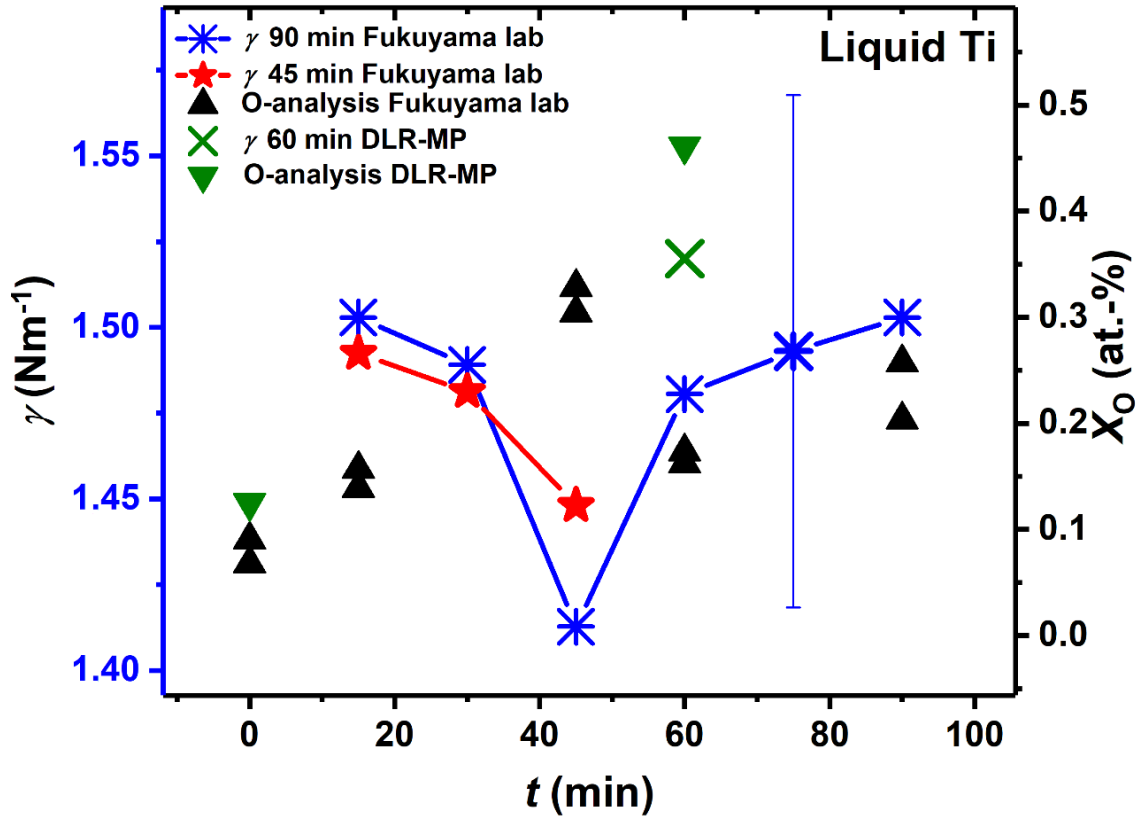


Figure 5.33: Surface tension (left y-axis) and oxygen concentration (right y-axis) of liquid Ti as a function of measurement time at the Fukuyama lab and the DLR-MP.

Generally, the question remains if and how the oxygen concentration affects the surface tension and in what range of oxygen concentration. As could be shown in this study, the surface tension stays constant over the oxygen partial pressure ranging from 10^{-12} to 10^{-6} Pa at the Fukuyama lab and from 10^{-6} to 10 Pa at the DLR-MP and oxygen concentrations between 0.08 at.-% (initial value after preparation) and 0.46 at.-% (after the measurement) with the maximum oxygen solubility only reached at 1.4 wt.-% = 4.1 at.-%. Up to now, there are no comparable literature results published relating the oxygen concentration to the surface tension of liquid Ti. Nonetheless, for other systems, e.g., Si [64], Fe [150], Ag [151] it has been reported that the saturated equilibrium oxygen partial pressure, $\log P_{O_2}^{\text{sat}}$ (Pa), amounts to -14, -1, 7 with oxygen solubilities of 0.0018 wt.-%, 0.35 wt.-%, 2 wt.-%, respectively. It is interesting, that among those materials the oxygen solubilities increase with increasing saturated equilibrium oxygen partial pressure. However, according to Belyanchikov [24], Ti does not really fit to these data with

saturated equilibrium oxygen partial pressure, of 10^{-13} Pa, close to the one of Si and on the other hand a high oxygen solubility of 1.4 wt.-%, similar to the one of Fe.

Based on the comparison and the results of this work, the assumption can be made that there are three possibilities for the process of oxygen adsorption on liquid Ti and its boundaries.

- a) The reduction of the surface tension of liquid Ti occurs at lower oxygen concentrations than 0.12 at.-% and oxygen partial pressure, 10^{-12} Pa as covered by this work. This would mean that all measurements presented in this work were conducted in conditions above the threshold value for a saturated oxygen surface coverage (compare section 2.6.1), where the surface tension stays constant with increasing oxygen partial pressure and oxygen concentration in the bulk phase. This possibility is supported by the study of Belyanchikov [24] stating that the solubility limits should already be reached at very low oxygen partial pressures of 10^{-13} Pa at 2023 K. All, or most literature data and industrial used Ti materials would, therefore, exhibit constant surface tensions values under the influence of oxygen on the surface. It is possible that the studies by Allen et al. [123] and Kuppermann [127] represent exceptions, as the respective surface tension results lie above the mean literature value (Figure 5.32). However, it seems unlikely to achieve realistic measurement conditions with oxygen concentrations smaller than 0.12 at.-% and oxygen partial pressures lower than 10^{-12} Pa [24]. Additionally, a counter-argument for this possibility is, that Belyanchikov [24] stated that already at 10^{-13} Pa at 2023 K the maximum solubility of oxygen in liquid Ti should be reached with 1.4 wt.-% = 4.1 at.-%, but only lower oxygen concentrations by a factor of 4 and more could be found for even higher oxygen partial pressures up to 10 Pa.
- b) The dissolved oxygen in liquid Ti does not significantly influence the oxygen partial pressure or only within the experimental error. Thus, such influence cannot be detected with the commonly used methods, and a much more sensitive method would be needed. In this case, the deviations in literature to lower (e.g., Arkhipkin et al. [124]) and higher (e.g., Allen et al. [123]) values might be coincidental and not related to the oxygen coverage on the surface or might indicate small variations in the amount of adsorbed oxygen.
- c) The reduction of the surface tension of liquid Ti occurs at higher oxygen concentrations than 0.46 at.-% and oxygen partial pressure of 10 Pa as covered by this work. This would be in good agreement with Fe where a comparable oxygen solubility of 2 wt.-% (in the case of Ti 1.4 wt.-%), goes along with a high saturated equilibrium oxygen partial pressure, $\log P_{\text{O}_2}^{\text{sat}}(\text{Pa}) = 7$. This would contradict

however Belyanchikov [24], reporting a much lower value for Ti of $\log P_{O_2}^{\text{sat}}$ (Pa) = -13. On the other hand, the process of maximum oxygen dissolution in the sample during the measurement could just take longer than most measurements, e.g., 90 min as in the case of this work and only after a certain threshold a significant surface tension reduction would be shown. This could be the case at least for measurement conditions with high purity Ti and low oxygen partial pressure atmospheres (e.g., through inert gas backfilling after chamber evacuation), as provided in most oxygen partial pressure studies. In this case, underestimated surface tension values with respect to the mean literature value for Ti, as e.g., reported Peterson et al. [146] and Arkhipkin et al. [124], might relate to a reduced surface tension after all, as possibly obtained under higher oxygen conditions.

To further investigate the influence of higher oxygen concentrations, TiO_2 was added actively to the Ti material during the sample preparation, as described in section 4.1.2. From the amount added, the oxygen concentration, X_O (at.-%), was calculated, based on Eq. (4.8). The compositions as $Ti_{1-x}O_x$, the mean measurement temperature values, the respective surface tension, the measured and real (in brackets, compare section 5.6.1) $\log P_{O_2}$ ranges, along with the oxygen concentration analysis values, (compare section 4.2.2) are shown in Table 17. All measurements have been conducted above the liquidus temperatures of Ti (1941 K) and TiO_2 (2023 K), respectively.

Comp.	$T \text{ } \emptyset$ (K)	γ (Nm ⁻¹)	T_L (K) [24]	$\log P_{O_2}$ SS1 (Pa) min	$\log P_{O_2}$ SS1 (Pa) max	O analysis (at.-%) /SEM
$Ti_{74}O_{26}$	2192.79 ± 3.64	0.97 ± 0.01	1680	-6 (-3)	0	SEM
$Ti_{86}O_{14}$	2289.56 ± 2.93	1.17 ± 0.02	1690	-5 (-3)	1	14.83
$Ti_{94}O_6$	2119.94 ± 6.85	1.32 ± 0.01	1710	-6 (-3)	1	6.85
$Ti_{97}O_3$	2101.04 ± 3.61	1.39 ± 0.02	1745	-6 (-3)	0	3.63
$Ti_{99}O_1$	2212.31 ± 5.10	1.47 ± 0.01	1880	-6 (-3)	-3	no analysis

Table 17: Compositions, mean measured temperature values, the respective surface tension values, the measured and real (in brackets, compare section 5.6.1) $\log P_{O_2}$ range, along with the oxygen concentration analysis values (if analysed, compare section 4.2.2) of liquid $Ti_{1-x}O_x$ alloys.

Figure 5.34 shows the surface tension values of the Ti- TiO_2 mixtures as functions of the logarithmic oxygen concentration, $\log X_O$ (at.-%), added (black squares) and analysed (red stars). Additionally, the table contains surface tension data from the Fukuyama lab (blue

triangles) and the DLR-MP lab (green circle) of pure Ti samples as a function of their analysed oxygen concentration, as listed in Table 16. The grey lines in Figure 5.34 illustrate the oxygen concentration of the unprocessed samples. Interestingly, the analysed oxygen concentrations in the samples, $\text{Ti}_{86}\text{O}_{14}$, Ti_{94}O_6 and Ti_{97}O_3 agree well with the added values but exceed them in the range of 4% - 9%. This increase could be coincidental uniformly over the three measurements and lie within the analysis error or caused by the sample preparation or LECO analysis standards, but it seems that oxygen is dissolved in the $\text{Ti}_{1-x}\text{O}_x$ samples during the measurements.

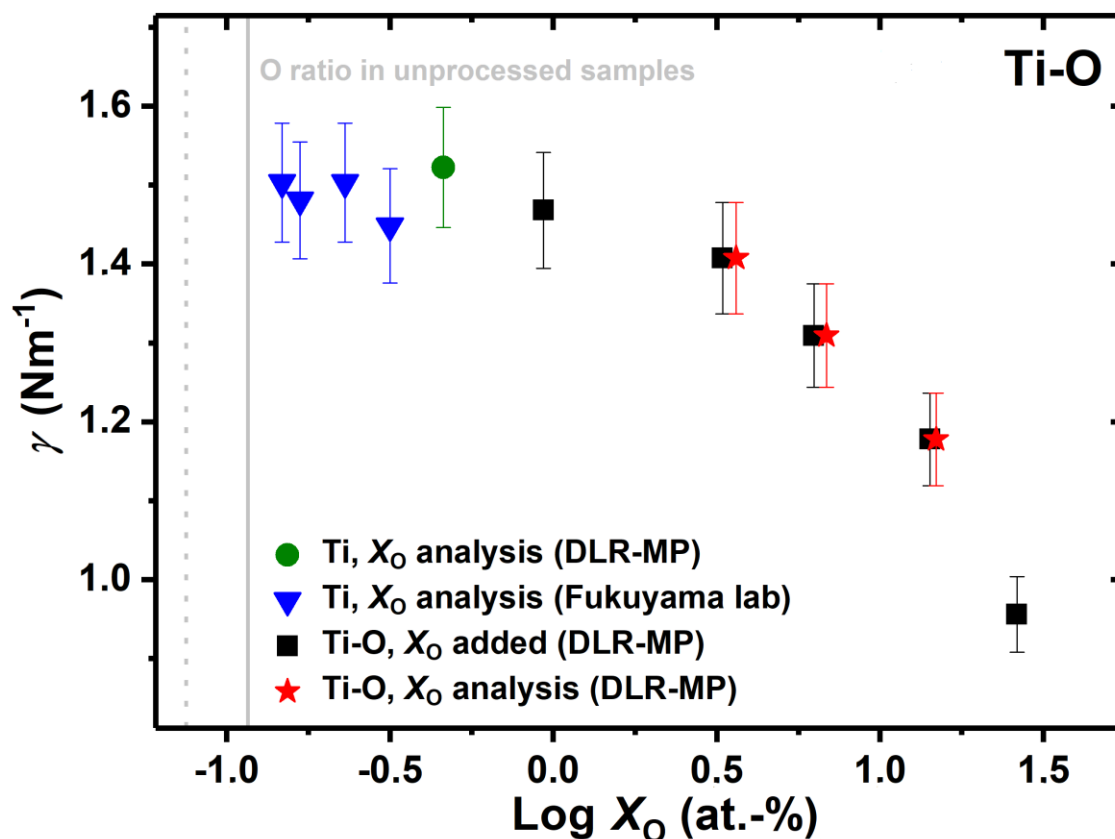


Figure 5.34: Surface tension values of Ti-TiO₂ mixtures as a function of the logarithmic oxygen concentration, $\log X_O$ (at.-%), added (black squares) and analysed (red stars). Additionally, the table contains surface tension data from the Fukuyama lab and the DLR-MP for pure liquid Ti samples as a function of their analysed oxygen concentration as listed in Table 16. The grey lines signify the oxygen concentrations of the unprocessed samples.

According to Belyanchikov [24], only the compositions Ti, Ti_{97}O_3 and Ti_{99}O_1 lie within the oxygen solubility boundary for liquid Ti in contact with liquid TiO₂ of 1.4 wt.-% = 4.1 at.-%. Neglecting the Ti data from the Fukuyama lab after 45 min where different processes might be apparent as discussed before, there seems to be a clear tendency of a decrease in the surface tension value with increasing oxygen concentration, from 1.48-1.52 Nm^{-2} for pure Ti, followed by 1.48 Nm^{-2} in the case of Ti_{99}O_1 to a value of 1.39 Nm^{-2} for Ti_{97}O_3 . This supports strongly the assumption c) that the reduction of the surface

tension of liquid Ti occurs at higher oxygen concentrations than covered by this work and generally assumed.

Concerning $\text{Ti}_{74}\text{O}_{26}$, $\text{Ti}_{86}\text{O}_{14}$ and Ti_{94}O_6 , all compositions are in the range of the oxygen solubility in solid Ti (compare phase diagram Figure 4.2) but according to Belyanchikov et al. [24] exceed the maximum oxygen solubility in liquid Ti. Thus, as defined by Belyanchikov the mixtures should not be considered as liquid Ti with the respective amounts of dissolved oxygen but rather as liquid Ti in equilibrium with liquid TiO_2 . However, it should be noted, that the study refers to vacuum conditions and no comparison values are available for the inert gas atmosphere at approximately 1 bar.

Nonetheless, in Figure 5.35, all data points of Figure 5.34 were considered as part of the binary Ti-O system. In Figure 5.35, the surface tension decreases logarithmically with increasing oxygen concentration, $\log X_{\text{O}}$ (at.-%), from about 1.52 Nm^{-2} to 0.97 Nm^{-2} . Moreover, the data were fitted by the Belton/Szyszkowski equation as defined in Eq. (2.51) [63]. Commonly, the Belton/Szyszkowski equation is used to describe the surface tension of a liquid metal adsorbent under the influence of oxygen adsorption, and thus as a function of the oxygen activity or oxygen partial pressure. Therefore, it is important to clarify that the data fit presented in Figure 5.35 and fit parameters listed in Table 18 as a function of the oxygen concentration, $\log X_{\text{O}}$ (at.-%), cannot be directly compared to the respective fits in dependent of the oxygen partial pressure or activity. Nonetheless, a similar mechanism seems to take place, and the Belton/Szyszkowski fit describes the data accurately.

However, it must be emphasized again, that $\log X_{\text{O}}$ (at.-%), does not necessarily describe the oxygen dissolution on the sample's surface but represents a mean value for the oxygen concentration in the bulk and the surface. Additionally, as reported by Belyanchikov et al. [24] above a value of $1.4 \text{ wt.-%} = 4.1 \text{ at.-%}$ the liquid system Ti- TiO_2 and not Ti-O should be regarded. Even though the boundary value might be discussable, the depicted Ti-O and possibly Ti- TiO_2 system in Figure 5.35 differs to a liquid sample under a certain oxygen partial pressure, where the surface and the bulk eventually reach natural boundary values for saturated oxygen. The shown system will only exhibit a final surface tension value in the case of pure TiO_2 , undergoing maybe several phases of surface tension values, actually describing two or more different liquid phases, Ti and Ti-oxides, in equilibrium.

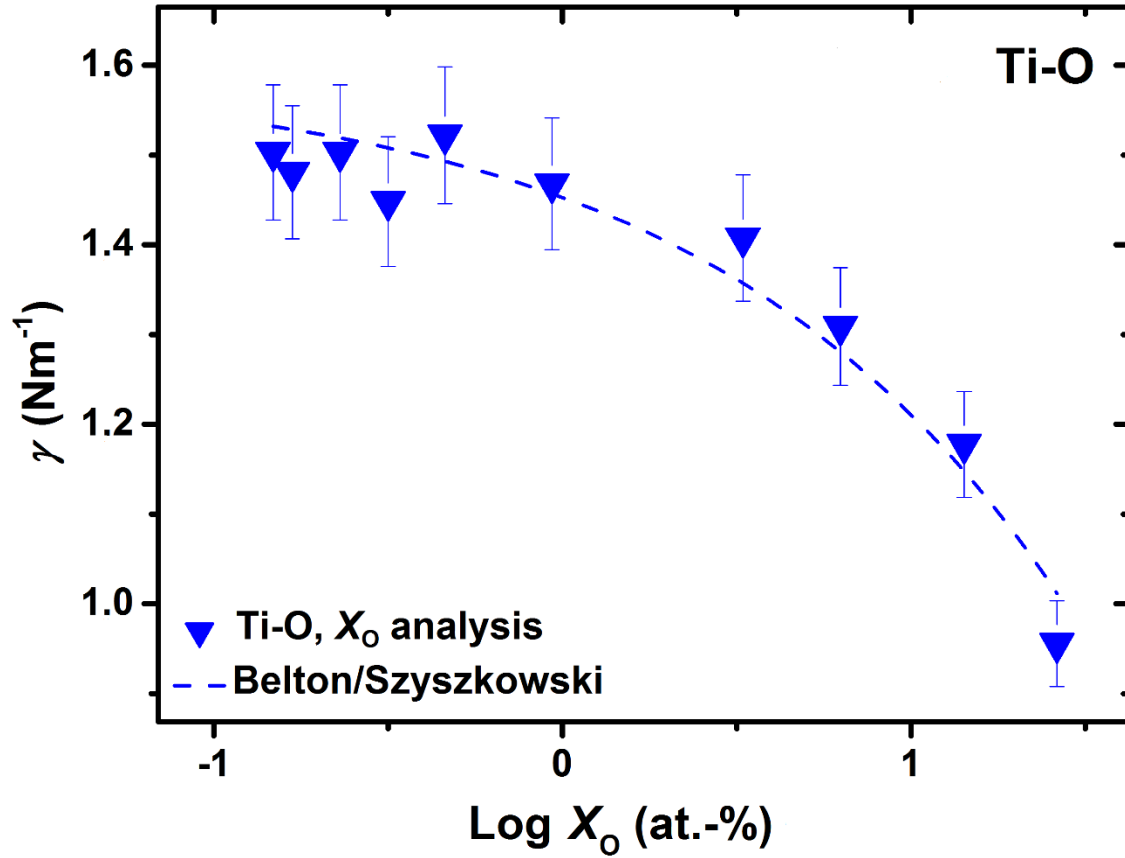


Figure 5.35: Surface tension data of liquid Ti-TiO₂ mixtures as a function of the logarithmic oxygen concentration, $\log X_O$ (at.-%) fitted by the Belton/Szyszkowski equation (Eq. (2.51)).

$T \varnothing$ (K)	γ^{pure} (Nm^{-1})	Γ_i^0	K_{ad} (10^{-6})
2047.17	1.59	1.30	6.35

Table 18: Fit parameters of surface tension data in dependence of the oxygen concentration, $\log X_O$ (at.-%), of liquid Ti-TiO₂ mixtures (Figure 5.35) fitted by the Belton/Szyszkowski equation (Eq. (2.51)).

The fit parameters in Table 18, Γ_i^0 , normally defining the saturated surface excess concentration of the surface-active component for full coverage adsorption and the equilibrium constant of the oxygen adsorption generally denoted by K_{ad} (Eq. (2.51)) are not comparable with values of other system related to the oxygen partial pressure. However, the fit parameter for pure Ti, γ^{pure} , provides a quantitatively comparable value. The value amounts to 1.59 Nm^{-1} , which is slightly above the mean value for the surface tension of liquid Ti of 1.52 Nm^{-1} as reported in this work and slightly below the values by Kuppermann [127] of 1.68 Nm^{-1} .

To provide an insight into the structure of the solid samples, one Ti sample and one sample with the composition Ti₇₄O₂₆ was additionally analysed after the measurement. The samples were analysed by a Scanning Electron Microscope (SEM), as described in section 4.2.1, showing the microstructure of polished samples' surfaces. The results are

depicted in Figure 5.36, with the Ti sample on the left side and the $\text{Ti}_{74}\text{O}_{26}$ sample on the right side. On the surface of the Ti sample one phase, A, is recognizable, the $\text{Ti}_{74}\text{O}_{26}$ sample shows three apparent phases, A, B and C. The phases were additionally analysed with regards to their content (Table 19), and both samples are featuring different ratios of Ti and O in each phase. The SEM-analysis does not provide quantitative information about the concentration of the phases but may allow the comparison of the ratios between phases.

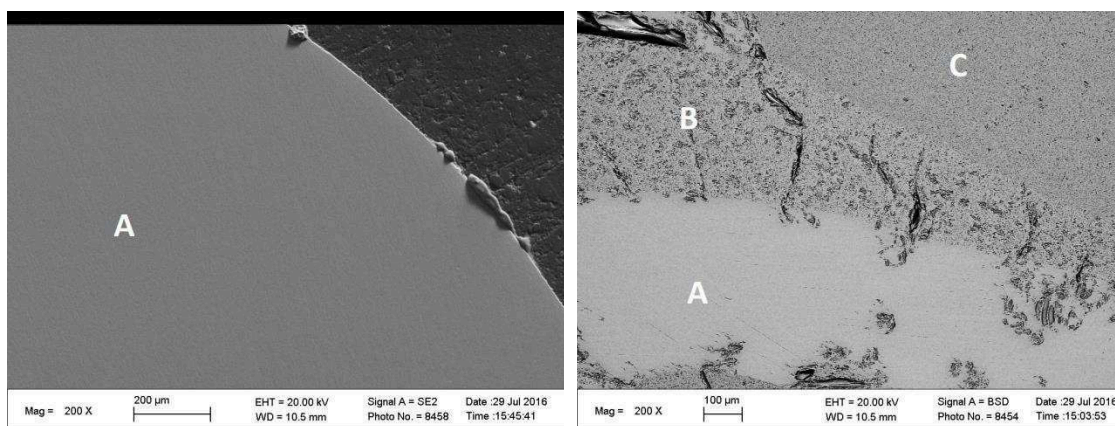


Figure 5.36: SEM analysis of a Ti (left side) and $\text{Ti}_{74}\text{O}_{26}$ (right side) sample, showing the microstructure of the polished surfaces. In the Ti sample one phase, A, is recognizable, in the $\text{Ti}_{74}\text{O}_{26}$ three phases, A, B, and C, referring to different compositions as listed in Table 19.

In the case of the pure Ti sample, it is likely that phase A relates to α -Ti, as it is the low-temperature Ti phase in the corresponding composition range (compare phase diagram in section 4.1.2). Even though in the liquid state of Ti, the highest oxygen solubility only amounts to about 4.9 at.-% according to Belyanchikov [24], the conditions are very different for solid Ti at high temperatures with up to 33 at.-% oxygen solubility. In the composition range of $\text{Ti}_{74}\text{O}_{26}$, α -Ti is the metastable phase at higher temperatures, while at lower temperatures α -Ti, TiO_2 and Ti_3O may be formed. This is in good agreement with the three phases observed in the $\text{Ti}_{74}\text{O}_{26}$ sample with different Ti-O ratios.

Area	$\text{Ti}_{74}\text{O}_{26}$		Ti	
	Ti	O	Ti	O
A	72	27	85	14
B	67	32		
C	66	33		

Table 19: Different phases A, B, C recognized in the samples Ti and $\text{Ti}_{74}\text{O}_{26}$ as shown in Figure 5.36 by SEM analysis with respective relative ratios between the phases.

In this section, the results for the influence of oxygen on the surface tension of liquid Ti have been presented and discussed. All measurements of the surface tension of liquid Ti as a function of the oxygen partial pressure have been found to be constant over the measurement range. Therefore, it is suggested in this work that the reduction of the surface tension of liquid Ti occurs at higher oxygen concentrations than covered ($P_{O_2} > 10$ Pa). and generally assumed. Additionally, the surface tension of liquid Ti-TiO₂ mixtures have been measured, exhibiting logarithmic functions in dependence of the oxygen concentrations which were fitted by the Belton/Szyszkowski equation. In chapter 7, all data will be summarized.

5.7 Summary

In this chapter 5, the results concerning high temperature density (section 5.1), normal spectral emissivity (section 5.2), isobaric heat capacity (section 5.3), high temperature viscosity under reduced gravity (section 5.4), high temperature surface tension (section 5.5) and the influence of oxygen on the surface tension (section 5.6) were presented and discussed. In the following chapter, the different properties and their composition dependencies will be compared with special regards to the relations of the excess properties.

6 Inter-property relations

In this work numerous thermophysical properties in the Al-Ti system have been investigated and discussed, such as density and molar volume (section 5.1), normal spectral emissivity (section 5.2), isobaric heat capacity (section 5.3), high temperature surface tension (section 5.5) and high temperature viscosity under reduced gravity (section 5.4). Some of these properties can be related directly, such as normal spectral emissivity is an input parameter for the calculation of the heat capacity and density is used for the evaluation of the isobaric heat capacity, the viscosity and the surface tension, respectively. Some inter-property relations might not be as apparent but based on similar mechanisms. In the following, the correlations between the properties will be discussed in more detail. Conclusively, an overall comparison between the composition dependencies of the excess and mixing properties will be presented.

Thermophysical properties of liquid compounds can be influenced among others by the enthalpy of mixing, ΔH_{mix} , and the Gibbs free energy of formation, ΔG , (section 2.1) and, therefore be correlated by those parameters. In these cases, overarching composition dependence tendencies might be exhibited and especially pronounced with regards to excess behavior. As a result, models using the enthalpy of mixing and the Gibbs free energy of formation or other thermophysical properties as input parameters can provide accurate predictions for the behavior of a material and its properties.

For instance, in the case of the viscosity, the enthalpy of mixing and the Gibbs free energy of formation (e.g., Kozlov model Eq. (2.44), the density and molar volume (e.g., Hirai model Eq. (2.43)) are used as input data for the composition dependence modeling. Correspondingly, to predict the surface tension of solutions the commonly used models by Butler (Eq. (2.32)) and by Chatain (Eq. (2.34)) employ the Gibbs free energy of formation and the empirical model by Hirai (Eq. (2.39)) the molar volume, respectively. In another model by Kaptay (Eq. (2.40)) the heat capacity is correlated with the surface tension.

To provide some more insights, it is interesting to look at the enthalpy of mixing and the Gibbs free energy of formation of liquid Al-Ti directly. Both parameters are temperature dependent and correlated by the entropy of formation, ΔS , as introduced in section 2.1. The enthalpy of mixing can be measured but is generally reported in the literature for certain temperatures only, as in the case of liquid Al-Ti by Desai et al. [115] for $T = 2000$ K. However, the enthalpy of mixing as a function of temperature can be related to heat

capacity. Neglecting a temperature dependence of the excess heat capacity, C_p^E , the enthalpy of mixing, ΔH_{mix} , can be determined as a function of C_p^E , the temperature, T , and originating from the given enthalpy of mixing at a certain temperature.

Using Eqs. (2.17) and (2.19) and literature data reported by Desai et al. [115] for liquid Al-Ti at $T = 2000$ K, the temperature dependent enthalpy can be derived as follows:

$$\begin{aligned}\Delta H_{\text{mix}}(T) &= \int_{2000\text{K}}^T C_p^E dT + \Delta H_{\text{mix}}(2000\text{K}) \\ &= C_p^E(T - 2000\text{K}) + \Delta H_{\text{mix}}(2000\text{K})\end{aligned}\quad (6.1)$$

Figure 6.1 shows literature data by Desai et al. [115] for $\Delta H_{\text{mix}}(2000\text{K})$ and the enthalpy of mixing calculated at 1800 K, 2100 K and 2200 K using Eq. (6.1). As can be seen in Figure 6.1, the enthalpy of mixing exhibits negative values over the whole Al-Ti composition range with a maximum around $X_{\text{Al}} \approx 50\text{-}70$ at.-% with decreasing temperature shifting to higher Al ratios. For systems with a positive excess heat capacity, as for Al-Ti, the enthalpy of mixing increases with increasing temperature, as can be seen in Figure 6.1. This shift indicates that at higher temperatures, pronounced atomic mobility and dynamics suppress interactions between atoms while the entropy and enthalpy of mixing increase, respectively.

The relation between the excess molar volume and thermodynamic properties, such as the enthalpy of mixing, ΔH_{mix} , the Gibbs free energy of formation, ΔG , and the entropy of formation, ΔS , have been investigated in previous studies, which has been summarized in detail by Watanabe et al. [152]. Scatchard suggested in his work [153] that a volume change upon mixing does not much effect the Gibbs free energy of formation but has a significant influence on the entropy of formation and enthalpy of mixing. In the following Kleppa [154] introduced expressions for the volume contributions to changes in the thermodynamic properties in relation to the thermal expansion coefficient, β , and the isothermal compressibility, α [152].

$$\Delta S \approx \left(\frac{\beta}{\alpha}\right) V^E \quad (6.2)$$

$$\Delta H_{\text{mix}} \approx T \left(\frac{\beta}{\alpha}\right) V^E \quad (6.3)$$

$$\Delta G = \Delta H_{\text{mix}} - T\Delta S \approx 0 \quad (6.4)$$

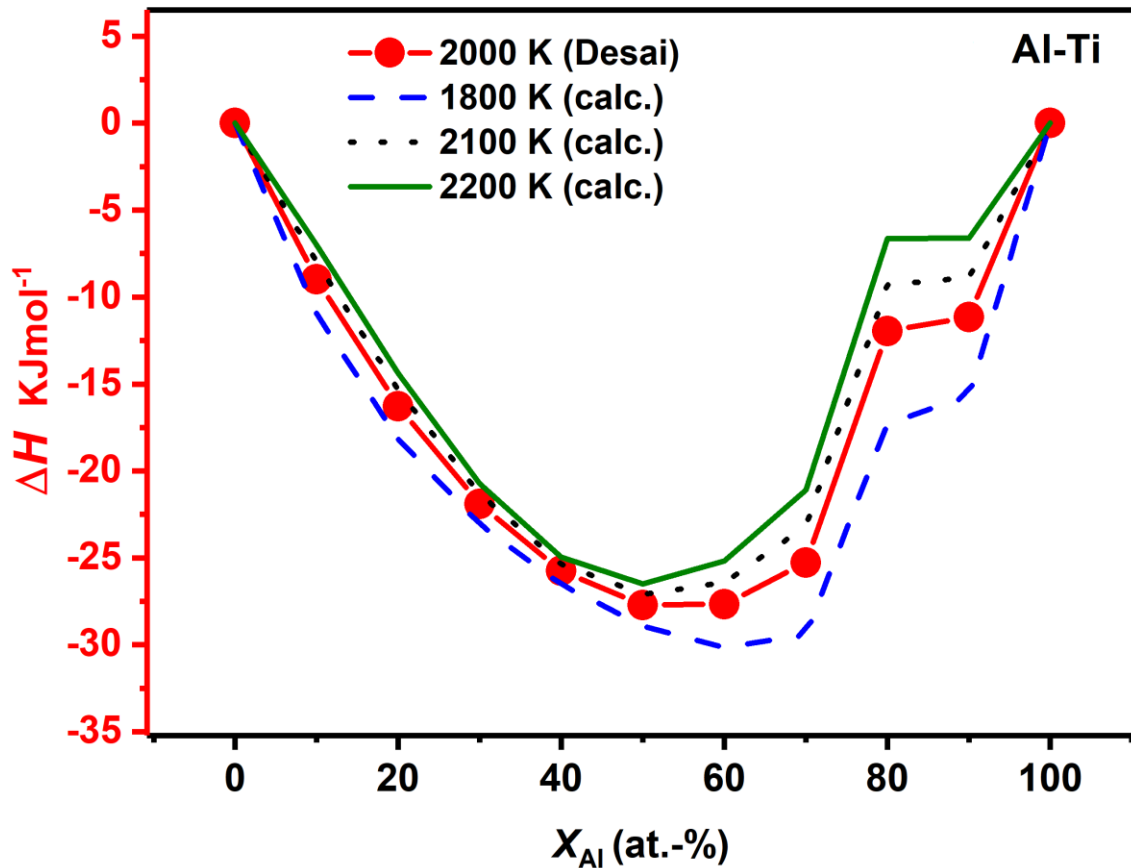


Figure 6.1: Literature data by Desai et al. [115] at 2000 K (symbol-solid line) and calculated values of the composition dependence of enthalpy of mixing at 1800 K (dashed line), 2100 K (dotted line) and 2200 K (solid line).

Various researchers have later criticized this as not being accurate for the processes in many systems [155, 156]. Kubaschewski and Alcock [157] and Iida and Guthrie [158] differentiated in their studies that compound forming systems are expected to exhibit negative values for ΔH_{mix} , ΔS , ΔG and V^E and system with a miscibility gap generally display positive values for these parameters. Corresponding to the work by Watanabe et al. [152] covering over 16 binary systems, Figure 6.2 a) and b) show the correlations between V^E , ΔH_{mix} , as well as V^E and ΔG for various binary alloys at 0.5 mole fraction, respectively. The values are taken from literature (see references below the picture) at various temperatures around the liquidus temperature range [152] and values for the Al-Ti system have been added, accordingly.

The excess free energy, ${}^E G$, can be calculated by Eq. (2.4) as a function of concentration and temperature dependent material-specific interaction parameters listed in Table 14 at 1873 K. The value for $\text{Al}_{50}\text{Ti}_{50}$ amounts to $-9,86 \text{ KJmol}^{-1}$ as displayed in Figure 6.2 a).

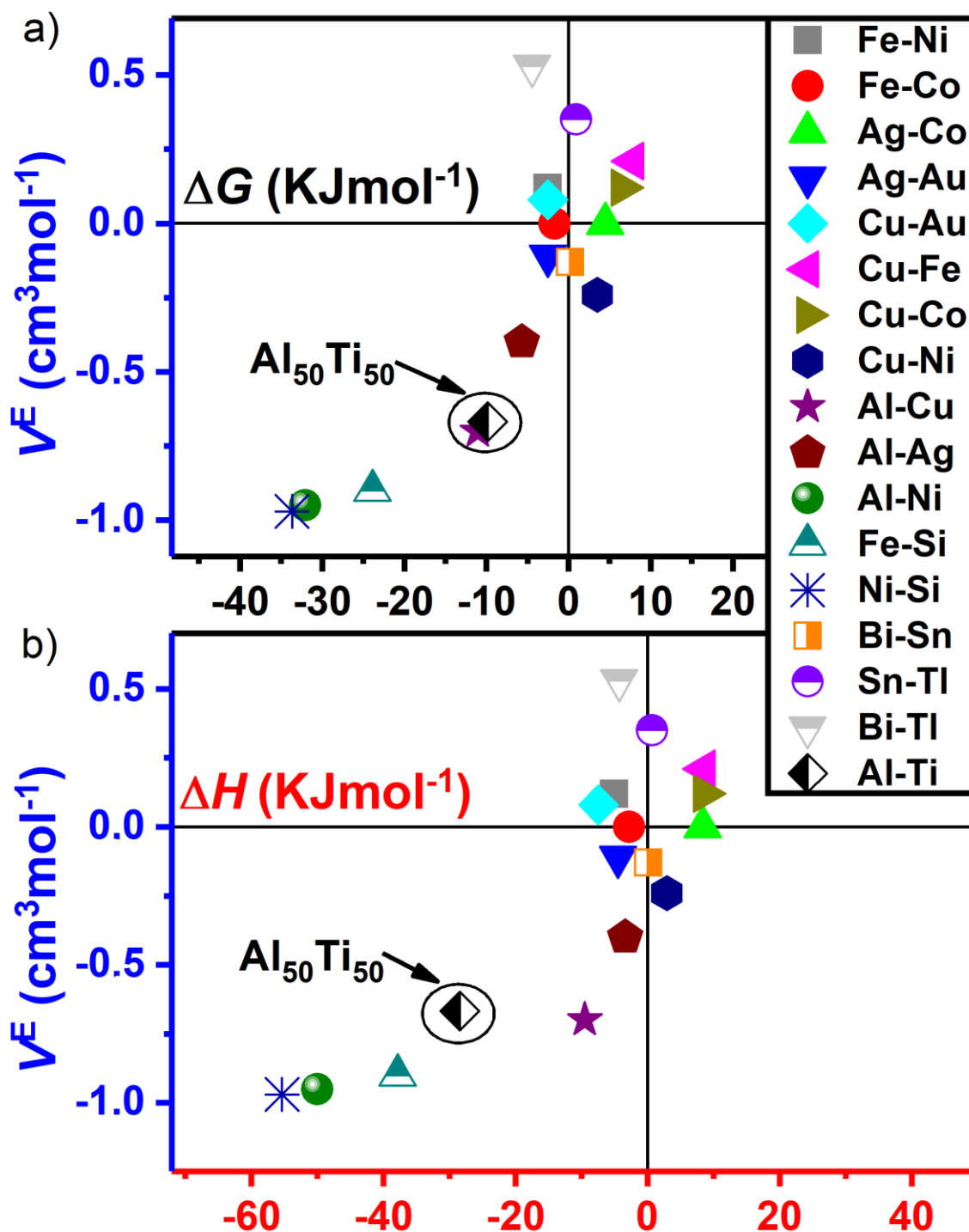


Figure 6.2: Correlations between the excess molar volume and a) the Gibbs energy of formation and b) the enthalpy of mixing at 1873 K, based on an extensive literature review by Watanabe et al. [152] for binary liquids at 0.5 mol fraction for Fe-Ni [152, 159, 160], Fe-Co [152, 161-163], Ag-Co [163, 164], Ag-Au [152, 163], Cu-Au [163, 165], Cu-Fe [166, 167], Cu-Co [163, 165], Cu-Ni [166, 168], Al-Cu [84, 169, 170], Al-Ag [84, 171], Al-Ni [84, 115], Fe-Si [152, 172], Ni-Si [152, 172], Bi-Sn [155], Sn-Tl [155] and Bi-Tl [155].

The depicted value for ΔH_{mix} in Figure 6.2 b) for the binary alloy $\text{Al}_{50}\text{Ti}_{50}$ is taken from reference [115] by Desai and recalculated for 1873 K by Eq. (6.1) as $-28.07 \text{ KJmol}^{-1}$. The corresponding value for V^{E} amounts to $-0,67 \text{ cm}^3\text{mol}^{-1}$ (compare section 5.1.2).

As can be seen from the figures, ΔH_{mix} and ΔG generally increase with increasing V^{E} . Additionally, most systems, including Al-Ti, agree with the observations by Iida and Guthrie [158] correlating negative values for V^{E} with negative values for ΔH_{mix} and ΔG and on the other hand positive values for all parameters. However, there are exceptional cases, including Fe-Ni reported by Watanabe et al. [152], where negative V^{E} are combined with positive ΔH_{mix} and ΔG , as well as inversely. According to Watanabe et al. this can be attributed to local liquid structures. The relation $V^{\text{E}} - \Delta G$ exhibits a narrower band-widths than the one of $V^{\text{E}} - \Delta H_{\text{mix}}$ and it seems reasonable to say that this contradicts the assumptions by Kleppa [154] (Eq. (2.58)) that a volume change upon mixing does not significantly influence the Gibbs free energy of formation. Therefore, the $V^{\text{E}} - \Delta G$ relation is an interesting indicator reflecting on equilibrium atomic arrangement, i.e., interatomic distance and atomic coordination [152]. The values for Al-Ti are in good agreement with the literature data, enqueueing well in the bands of $V^{\text{E}} - \Delta G$ and $V^{\text{E}} - \Delta H_{\text{mix}}$ correlations. The system Al-Ti shows relatively intermediate to high negative values for all parameters, V^{E} , ΔH_{mix} and ΔG , respectively, indicating strong differences in the interaction energies and non-ideal mixing behavior.

In Figure 6.3 a comparison between the excess properties, enthalpy of mixing, ΔH_{mix} , Gibbs energy of formation, ΔG , excess molar volume, V^{E} , excess heat capacity, C_{p}^{E} , excess surface tension, γ^{E} , and excess viscosity, η^{E} , of the liquid Al-Ti system at 1950 K is displayed. The enthalpy of mixing, ΔH_{mix} , was derived from the values by Desai et al. [115] and calculated for the respective temperature by Eq. (6.1). The excess free energy, ${}^{\text{E}}G$, was calculated by Eq. (2.4) with the temperature dependent parameters ${}^{\text{v}}L$ listed in Table 14.

The values for V^{E} , C_{p}^{E} , γ^{E} and η^{E} designate the deviation from the ideal behaviour as discussed in the chapters 5.1.2, 5.3.2, 5.5.2 and 5.4.2, respectively. In the case of V^{E} the excess values relate to the fitted excess molar volumes by Eq. (2.6), of a Redlich-Kister type polynomial fit of first order with fit parameters ${}^{\text{v}}V(\text{T})$ listed in Table 4. Accordingly, the values for C_{p}^{E} were fitted by Eq. (2.19) with the fit parameters listed in Table 9. In the case of the surface tension, the depicted excess results describe the deviation between the ideal and non-ideal subregular solution by Butler (2.32) with temperature dependent parameters ${}^{\text{v}}L$ listed in Table 14.

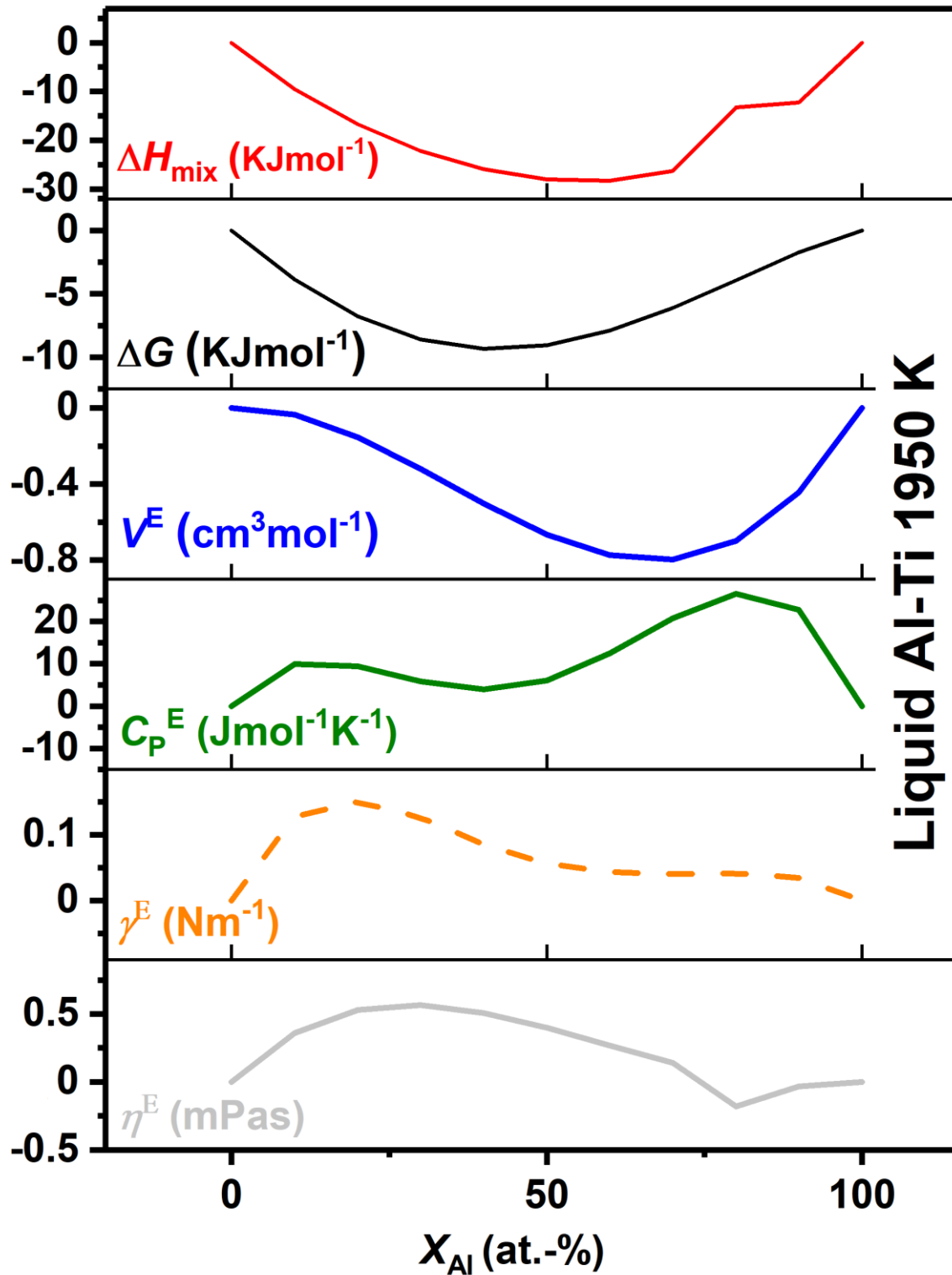


Figure 6.3: Enthalpy of mixing, ΔH_{mix} , Gibbs energy of formation, ΔG , excess molar volume, V^E , excess heat capacity, C_p^E , excess surface tension, γ^E , and excess viscosity, η^E , as a function of composition in the liquid binary Al-Ti system at 1950 K.

As for η^E , the displayed excess behaviour relates to the deviation between the Kozlov model Eq. (2.44) and a linear dependence between the viscosities of the pure elements as

0.59 mPas reported by Assael et al. for Al [14] and 4.03 mPas measured by Paradis et al. for Ti [114], respectively.

Comparing all data with respect to their composition dependencies in Figure 6.3, no direct overall tendency is distinguishable, except that all properties feature highly non-ideal behaviour. In the case of ΔH_{mix} , ΔG and V^E negative excess properties are exhibited, while C_p^E , γ^E and η^E show positive deviations from the ideal behaviour. ΔH_{mix} , ΔG , V^E and η^E have in common that only a single maximum or minimum is formed over the composition range. However, the position of the extrema seems to be on the Al-rich site in the case of ΔH_{mix} and V^E , on the Ti-rich site for ΔG and at a composition around Al₅₀Ti₅₀ for η^E , respectively.

On the other hand, C_p^E and γ^E display a ‘m-shaped’ progression with two maxima which is conditioned by the use of two fit parameter for the excess property fits as described in the respective chapters. These two properties show good agreement concerning the position of their local minima, which can be observed in the range of Al₅₀Ti₅₀ similar to η^E , and their maxima which are formed at $X_{\text{Al}} \approx 25$ at.-% and $X_{\text{Al}} \approx 75$ at.-%.

As can be seen from Figure 6.3 and described at the beginning of this section, similar processes, such as atomic interactions and energy minimisation, influence all thermophysical properties investigated in this work. Additionally, the properties can be directly or indirectly (e.g., via modeling) related to the thermodynamic properties ΔH_{mix} and ΔG . However, the range of processes that contribute to the formation of the respective properties and their composition dependencies is too wide-ranging and additionally interacting to comprehend a unified trend over all properties. Nonetheless, as shown in this section and the respective sections about V^E (5.1), C_p^E (5.3), γ^E (5.5) and η^E (5.4), it can be concluded that systems such as Al-Ti which exhibit highly non-ideal behaviour in one area, generally tend to feature non-ideal behaviour over all interacting thermophysical properties.

In this section, a comparison between the thermophysical properties presented in this work and their respective composition dependence has been discussed. It can be summed up that Al-Ti generally exhibits highly non-ideal behaviour over all investigated thermophysical and thermodynamic properties. Most of these properties are directly or indirectly interacting. However, no unified trend over all properties can be observed as the range of processes contributing is too wide-ranging. In the following chapter 7, all data will be summarized.

7 Summary

The central objective of this work was to study thermophysical properties of Al, Ti and to provide data for the creation and completion of materials databases with systematically varied compositions in the binary Al-Ti system [30]. In addition, it has been found that thermophysical property data on the binary Al-Ti system are also a good starting point for investigations on multicomponent alloys and industrially used compounds, as well as their need for thermophysical data for materials processing. Among the properties investigated, accurate data on density, molar volume, surface tension, viscosity, emissivity, and heat capacity measurements have been presented. Moreover, the influence of oxygen with regards to the surface tension has been discussed. Conclusively, an overall comparison between the composition dependencies of the excess and mixing properties has been presented with regards to the enthalpy of mixing and the Gibbs free energy of formation.

The overall method used for the measurements of this work was electromagnetic levitation. As Al-Ti alloys are highly reactive and generally show high evaporation at elevated temperatures, conventional container-based techniques render vast difficulties. Therefore, contact-free electromagnetic levitation methods offer many advantages, enable to minimize error sources and measure with high accuracy.

High-temperature density, ρ , measurements as a function of temperature were performed at the DLR-MP over the whole Al-Ti composition range. The data were analyzed concerning the density at liquidus temperature, ρ_L , the density temperature coefficients, ρ_T , the thermal volume expansion coefficient, β , the molar volume, V , and the excess molar volume, V^E . For all Al-Ti compositions, the density, ρ , decreases linearly with increasing temperature. Additionally, the density changes gradually with Al mole fraction, X_{Al} , with pure Al exhibiting the lowest density of 2.30 gcm^{-3} , and Ti the largest of 4.12 gcm^{-3} , at the respective liquidus temperatures. The density values of the alloys lie within these two extremes. It was found that Al-Ti exhibits significantly highly non-ideal behavior with large negative values for the excess molar volume with a maximum negative value of $V^E \approx -1.05 \cdot 10^{-6} \text{ m}^3 \text{ mol}^{-1}$ for $X_{Al} \approx 60\text{-}70 \text{ at.}\%$. This is in good agreement with other systems, such as the Al-Au system [104]. It is suggested that shrunk Al radii upon mixing contribute to that mechanism.

The normal spectral emissivity, ε , of four compositions in the Al-Ti system in dependence of the wavelength and temperature, covering a temperature range of 1706-1987 K was measured at the Fukuyama lab. It was found that all compositions show negligible

temperature dependence at the investigated wavelength of 940 nm. The results validate the temperature measurement approach using a single-color pyrometer calibrated at the liquidus temperature and assuming the wavelength to be constant over the investigated temperature range. The emissivity results amount to 0.30, 0.32, 0.40 and 0.37 for Al₇₀Ti₃₀, Al₅₀Ti₅₀, Al₂₀Ti₈₀ and Ti, respectively. With respect to literature data of binary and multi-component Al-Ti based alloys, the composition dependence of the emissivity results is in very good agreement, especially with the data by Qin et al. [107]. The obtained values were used as input data for the isobaric heat capacity measurements of this work.

Analogously to the normal spectral emissivity, isobaric heat capacity, C_p , measurements were conducted at the Fukuyama lab of the same four compositions of liquid Al-Ti melts as a function of temperature covering 1665-2030 K over all compositions. For all compositions, the heat capacity shows negligible temperature dependence with average values of 57.59, 46.20, 54.61 and 48.50 JK⁻¹mol⁻¹ for Al₇₀Ti₃₀, Al₅₀Ti₅₀, Al₂₀Ti₈₀ and Ti, respectively. The composition dependence of the isobaric heat capacity results at constant pressure was compared to results by the Neumann-Kopp rule and literature. The results of this work were found to be significantly higher than the available literature data on multi-component Al-Ti based alloys. The deviation between the measured values and the linear dependence, the excess heat capacity, C_p^E , was evaluated, exhibiting positive values for all compositions with a maximum deviation for Al₇₀Ti₃₀ of about 21 JK⁻¹mol⁻¹.

High-temperature viscosity, η , of liquid Al₅₀Ti₅₀ was measured under reduced gravity conditions at three different temperatures during parabolic flight measured in the DLR μ g-EML facility, TEMPUS. The data vary from 5.73 mPas to 6.88 mPas in the temperature range of 1574-1843 K. The results were fitted by an Arrhenius fit with 2.23 mPas and $1.27 \cdot 10^4$ Jmol⁻¹ corresponding to the respective Arrhenius fit parameters, η_∞ and E_A . The isothermal viscosity at 1750 K was compared to available Al and Ti literature data by Assael et al. [14] and Paradis et al. [114] of 0.65 mPas and 5.69 mPas, respectively. With respect to the result of this work, a positive viscosity deviation of about 2.2 mPas from the linear composition dependence of the pure elements was found. Moreover, the Hirai model [55], the Kaptay model [57] and the Kozlov model [56] were calculated to predict the composition dependence of the viscosity in the Al-Ti system. All models underestimate the experimental result of liquid Al₅₀Ti₅₀ by far. The closest agreement was found with the Kozlov model, predicting a value around 28% lower than the experimental result.

The surface tension, γ , of ten compositions in the Al-Ti system was measured at the DLR-MP as a function of temperature. The data include surface tension results on liquid Al₅₀Ti₅₀ obtained under microgravity conditions in the DLR TEMPUS facility. The respective data are in very good agreement with the results accessed under terrestrial

conditions. For all compositions the surface tension decreases linearly with rising temperature yielding linear fit parameters; the surface tension at the respective liquidus temperature, γ_L , and the surface tension temperature coefficient, γ_T . In addition, within the measured composition range, the surface tension changes gradually with the composition, exhibiting an increase with decreasing X_{Al} with the lowest values observed for $Al_{10}Ti_{90}$ of 1.49 Nm^{-1} and the highest results for pure Ti of 1.56 Nm^{-1} at the respective liquidus temperatures. The isothermal surface tension as a function of composition was calculated at $T = 1950 \text{ K}$ and compared to model predictions. A good agreement with the experimental results was achieved by the calculations according to the Butler model [43] and the Chatain model [47, 48] for subregular non-ideal solutions. A positive excess surface tension, γ^E , over the whole composition range was found with a maximum for $X_{Al} \approx 20\text{-}30 \text{ at.}\%$ amounting to about 0.29 Nm^{-1} at 1950 K . Relative to an ideal behavior a suppressed surface segregation of the surface-active component Al could be observed due to interatomic attractions.

Additionally, the influence of oxygen on liquid Al and Ti melts was investigated with regards to the surface tension. Surface tension measurements were conducted at the DLR-MP as a function of the oxygen partial pressure in the surrounding gas and chemical addition of oxygen to Ti in the form of TiO_2 . The oxygen partial pressure in the chamber was measured using an oxygen control system (OSC) and the measured range covered $10^{-7} \text{ Pa} < P_{O_2}^{Ch} < 10 \text{ Pa}$. For all compositions, the surface tension results showed a negligible dependence on the oxygen partial pressure over the measured range. However, with increasing chemical addition of oxygen to Ti in form of TiO_2 , the surface tension decreased gradually. Additionally, Ti surface tension measurements were performed at the Fukuyama lab as a function of time, exhibiting a decrease in the surface tension after 45 min. Oxygen partial pressures values of 10^{-22} Pa were achieved at the Fukuyama lab with buffer gas mixtures of Ar-5% H_2 , which were corrected according to the temperature dependent influence of buffer gas mixtures. All results for Ti-O were fitted by the Belton/Szyszkowski adsorption equation. Overall it was suggested, that in the case of liquid Ti the surface tension reduction occurs at higher oxygen concentrations, than covered ($P_{O_2} > 10 \text{ Pa}$) and generally assumed. Concerning Al, the temperature dependent oxygen partial pressure boundaries for surface oxidation were calculated to define the maximum oxygen partial pressure in the chamber and the sample's vicinity for a 'clean' surface. The Al surface tension results of this work obtained under 'clean' conditions' are in very good agreement with corresponding literature results by Molina et al. [133] and Kobatake et al. [58]. It was suggested that these measurements relate to oxide free surfaces with either zero or minor adsorbed oxygen particles.

Finally, all thermophysical properties investigated in this work were compared with special regards to excess properties and the relations to the enthalpy of mixing, ΔH_{mix} , and the Gibbs free energy of formation, ΔG . The enthalpy of mixing was calculated as a function of temperature based on the isothermal enthalpy of mixing by Desai et al. [115] at $T = 2000$ K and heat capacity results of this work. Overall it was shown that liquid Al-Ti alloys generally exhibit highly non-ideal behaviour for all investigated thermophysical and thermodynamic properties. Most of the properties are directly or indirectly interacting, however, no unified trend over all properties could be observed as the range of processes contributing are too wide-ranging.

Appendix

In this section, additional calculations and tables are provided accompanying the respective chapters of the main part of this work.

A.1 Uncertainty of high-temperature density and molar volume

This section A.1 is an addition to the sections 2.1, 3.4 and 5.1 on high-temperature density and molar volume. Based on the before discussed density error contributions in the described procedures and provided that the error contributions mentioned in section 3.4 are avoided, the obtained density results are accurate within $\Delta\rho/\rho \leq \pm 1.0\%$ [7, 30, 83]. This value corresponds to the uncertainty of the calibration [84]. Assuming this value, the uncertainty of the molar volume

$$V = \frac{m}{\rho} \quad (0.1)$$

can be determined according to a Gaussian error propagation:

$$\Delta V^2 = \left(\frac{\partial V}{\partial \rho} \Delta \rho\right)^2 = \left(\frac{m}{-\rho^2} \Delta \rho\right)^2 = \left(-V \frac{\Delta \rho}{\rho}\right)^2 \quad (0.2)$$

Which leads to the uncertainty of the molar volume, $\Delta V/V \leq \pm 1.0\%$, equal to the one of the density.

$$\left(\frac{\Delta V}{V}\right)^2 = \left(\frac{\Delta \rho}{\rho}\right)^2 \quad (0.3)$$

A.2 Uncertainty analysis of the normal spectral emissivity

This section A.2 follows the section 2.2, 3.6 and 5.2 on normal spectral emissivity. In the following, the error propagation of the normal spectral emissivity measurements is provided which were used for the respective error calculations. The uncertainty of the normal spectral emissivity, $\Delta\varepsilon$, is mainly caused by the uncertainty of the radiance, R_S , the wavelengths, λ , the spectrometer and the uncertainty of the temperature measurement combining temperature fluctuations, $T_{\text{Fluctuation}}$, and the uncertainty attributed to the emissivity uncertainty of the pyrometer, $T_{\text{Pyrometer}}$.

From Eqs. (2.14) and (2.15) the normal spectral emissivity can be expressed as:

$$\varepsilon(\lambda, T) = \lambda^5 \frac{R_S(\lambda, T) \cdot \left(e^{\left(\frac{C_2}{\lambda T}\right)} - 1 \right)}{C_1} \quad (0.4)$$

The combined standard uncertainty in normal spectral emissivity, $\Delta\varepsilon$, given in the following equation is based on the *Guide to the Expression of Uncertainty in Measurement* [173] with ΔR_S , $\Delta\lambda$, $\Delta T_{\text{Fluctuation}}$ and $\Delta T_{\text{Pyrometer}}$ expressing the standard deviations of the radiance intensity, the wavelengths, the fluctuation of the temperature measurement of the sample and the accuracy of the pyrometer, respectively:

$$\begin{aligned} \Delta\varepsilon(\lambda, T)^2 = & \left(\frac{\partial\varepsilon}{\partial R_S} \Delta R_S \right)^2 + \left(\frac{\partial\varepsilon}{\partial\lambda} \Delta\lambda \right)^2 + \left(\frac{\partial\varepsilon}{\partial T} \Delta T_{\text{Fluctuation}} \right)^2 \\ & + \left(\frac{\partial\varepsilon}{\partial T} \Delta T_{\text{Pyrometer}} \right)^2 \end{aligned} \quad (0.5)$$

The respective partial derivatives of the radiance, R_S , the temperature, T , and the wavelengths, λ , can be derived as following:

$$\frac{\partial\varepsilon}{\partial R_S(\lambda, T)} = \lambda^5 \cdot \frac{e^{\left(\frac{C_2}{\lambda T}\right)} - 1}{C_1} = \varepsilon(\lambda, T) \frac{1}{R_S(\lambda, T)} \quad (0.6)$$

$$\frac{\partial\varepsilon}{\partial\lambda} = 5\lambda^4 \cdot \frac{R_S(\lambda, T) \cdot \left(e^{\left(\frac{C_2}{\lambda T}\right)} - 1 \right)}{C_1} - \frac{C_2}{\lambda^2 T} \lambda^5 \cdot \frac{R_S(\lambda, T) \cdot \left(e^{\left(\frac{C_2}{\lambda T}\right)} \right)}{C_1}$$

$$= \varepsilon(\lambda, T) \frac{5}{\lambda} - \frac{C_2}{\lambda^2 T} \left(\lambda^5 \cdot \frac{R_S(\lambda, T) \cdot \left(e^{\left(\frac{C_2}{\lambda T}\right)} - 1 + 1 \right)}{C_1} \right)$$

$$= \varepsilon(\lambda, T) \frac{5}{\lambda} - \varepsilon(\lambda, T) \frac{C_2}{\lambda^2 T} - \frac{C_2}{\lambda^2 T} \left(\lambda^5 \cdot \frac{R_S(\lambda, T)}{C_1} \right)$$

$$= \varepsilon(\lambda, T) \frac{5}{\lambda} - \varepsilon(\lambda, T) \frac{C_2}{\lambda^2 T} - \varepsilon(\lambda, T) \frac{C_2}{\lambda^2 T} \left(\frac{1}{\left(e^{\left(\frac{C_2}{\lambda T}\right)} - 1 \right)} \right)$$

$$\frac{\partial \varepsilon}{\partial T} = -\frac{C_2}{\lambda T^2} \lambda^5 \cdot \frac{R_S(\lambda, T) \cdot \left(e^{\left(\frac{C_2}{\lambda T}\right)} - 1 \right)}{C_1} = -\varepsilon(\lambda, T) \frac{C_2}{\lambda T^2} \quad (0.7)$$

Eqs. (0.6) - (0.7) lead to

$$\begin{aligned} \left(\frac{\Delta \varepsilon(\lambda, T)}{\varepsilon(\lambda, T)} \right)^2 &= \left(\frac{\Delta R_S}{R_S(\lambda, T)} \right)^2 \\ &+ \left(\frac{\Delta \lambda}{\lambda} \right)^2 \cdot \left(5 - \frac{C_2}{\lambda T} \cdot \left(1 - \frac{1}{e^{\left(\frac{C_2}{\lambda T}\right)} - 1} \right) \right)^2 \\ &+ \left(\left(\frac{\Delta T_{\text{Fluctuation}}}{T} \right)^2 + \left(\frac{\Delta T_{\text{Pyrometer}}}{T} \right)^2 \right) \cdot \left(\frac{C_2}{\lambda T^2} \right)^2 \end{aligned} \quad (0.8)$$

The uncertainties, Δu , of the respective contribution, u , in the normal spectral emissivity of Ti at 940 nm are listed as an example in Table 20. The uncertainty in the sample radiance, ΔR_S , is derived from the product of the radiance-output count slope and the standard deviation of the output count intensity (Figure 5.7). The temperature uncertainty attributed to the fluctuation of the temperature, $\Delta T_{\text{Fluctuation}}$, has been evaluated from the temperature profile during the measurement and estimated as 2.11 K for liquid Ti. For the temperature uncertainty contribution due to the pyrometer uncertainty, $\Delta T_{\text{Pyrometer}}$, it was assumed that the emissivity used for the pyrometer has the same uncertainty as for the one evaluated at 940 nm, which implies an uncertainty of 2.78 K. The spectrometer has a resolution of 4 nm leading to an uncertainty of $\Delta \lambda = 2$ nm in the obtained wavelength value. The corresponding error is shown in Table 20.

Cause of uncertainty in	Standard uncertainty Δu	Contribution u	Contribution term to $\Delta \varepsilon / \varepsilon$
Sample radiance: ΔR_S	21.40 Wm ⁻² μm	245902.84 Wm ⁻² μm	$7.57418 \cdot 10^{-9}$
Wavelengths: λ	2 nm	940 nm	$4.8209 \cdot 10^{-5}$
Temperature fluctuations: $T_{\text{Fluctuation}}$	2.11 K	1970 K	$1.79174 \cdot 10^{-11}$
Pyrometer signal: $T_{\text{Pyrometer}}$	2.78 K	1970 K	$3.09361 \cdot 10^{-11}$

Absolute combined standard uncertainty, $\Delta\varepsilon$	0.0027
Expanded uncertainty, $U = 2\Delta\varepsilon$	0.0054

Table 20: normal spectral emissivity uncertainty evaluation, exemplarily for liquid Ti at 1970 K.

A.3 Uncertainty analysis of the isobaric heat capacity

This section A.3 follows the sections 2.3, 3.6 and 5.3 on isobaric heat capacity. The error propagation of the isobaric heat capacity which was used for the respective error calculations will be presented in the following. The uncertainty of the molar heat capacity at constant pressure ΔC_p was evaluated based on the following equations derived from Eq. (3.13):

$$\begin{aligned}
\Delta C_p^2 &= \left(\frac{\partial C_p}{\partial \varepsilon} \Delta \varepsilon \right)^2 + \left(\frac{\partial C_p}{\partial p_0} \Delta p_0 \right)^2 + \left(\frac{\partial C_p}{\partial \Delta T_{ac}} \Delta \Delta T_{ac} \right)^2 + \left(\frac{\partial C_p}{\partial m} \Delta m \right)^2 \\
&\quad + \left(\frac{\partial C_p}{\partial \omega} \Delta \omega \right)^2 \tag{0.9} \\
&= \left(\frac{p_0 M}{\omega \Delta T_{ac} m} f \Delta \varepsilon \right)^2 + \left(\frac{\varepsilon M}{\omega \Delta T_{ac} m} f \Delta p_0 \right)^2 + \left(\frac{-1}{\Delta T_{ac}} \cdot \right. \\
&\quad \left. \frac{p_0 \varepsilon M}{\omega \Delta T_{ac} m} f \Delta \Delta T_{ac} \right)^2 + \left(\frac{-1}{m} \cdot \frac{p_0 \varepsilon M}{\omega \Delta T_{ac} m} f \Delta m \right)^2 + \left(\left(\frac{p_0 \varepsilon M}{\omega \Delta T_{ac} m} \cdot \right. \right. \\
&\quad \left. \left. \left(-\frac{1}{2} \right) \cdot f^{-1} \left(\frac{-2}{\omega^3 \tau_f^2} + 2\omega \tau_c^2 \right) + \frac{p_0 \varepsilon M}{\omega \Delta T_{ac} m} f \cdot \left(-\frac{1}{\omega} \right) \right) \cdot \Delta \omega \right)^2 \\
&= \left(C_p \frac{\Delta \varepsilon}{\varepsilon} \right)^2 + \left(C_p \frac{\Delta p_0}{p_0} \right)^2 + \left(C_p \frac{-\Delta \Delta T_{ac}}{\Delta T_{ac}} \right)^2 + \left(C_p \frac{-\Delta m}{m} \right)^2 + \\
&\quad \left(C_p \left(f^{-1} \left(\frac{-2}{\omega^2 \tau_f^2} + 2\omega^2 \tau_c^2 \right) - 1 \right) \frac{\Delta \omega}{\omega} \right)^2 \\
&= \left(C_p \frac{\Delta \varepsilon}{\varepsilon} \right)^2 + \left(C_p \frac{\Delta p_0}{p_0} \right)^2 + \left(C_p \frac{-\Delta \Delta T_{ac}}{\Delta T_{ac}} \right)^2 + \left(C_p \frac{-\Delta m}{m} \right)^2 \\
&\quad + \left(C_p \left(f^{-1} \left(\frac{-2}{\omega^2 \tau_f^2} + 2\omega^2 \tau_c^2 \right) - 1 \right) \frac{\Delta \omega}{\omega} \right)^2
\end{aligned}$$

$$\left(\frac{\Delta C_p}{C_p}\right)^2 = \left(\frac{\Delta \varepsilon}{\varepsilon}\right)^2 + \left(\frac{\Delta p_0}{p_0}\right)^2 + \left(\frac{\Delta \Delta T_{ac}}{\Delta T_{ac}}\right)^2 + \left(\frac{\Delta m}{m}\right)^2 + \left(\left(f^{-1} \left(\frac{-2}{\omega^2 \tau_f^2} + 2\omega^2 \tau_c^2\right) - 1\right) \frac{\Delta \omega}{\omega}\right)^2$$

In Eq. (0.9), ΔC_p denotes the combined standard uncertainty of the heat capacity. The contributions $\Delta \varepsilon$, Δp_0 , $\Delta \Delta T_{ac}$, $\Delta \omega$ and Δm are the uncertainties of the uncertainty contributions of the spectral emissivity, the laser power, the modulation frequency, the temperature amplitude and the sample mass, respectively. Analogously to the emissivity, the uncertainty contributions, Δu , of the respective contributions, u , of the heat capacity for liquid Ti is given as an example in Table 21. The evaluation of the uncertainty of the emissivity, $\Delta \varepsilon$, is explained in section A.2. The uncertainties in the laser power, Δp_0 , the modulation frequency, $\Delta \omega$, and temperature amplitude, $\Delta \Delta T_{ac}$, are taken from reference [86] and assumed to be 0.03 W, $\frac{0.0005}{\sqrt{3}}$ rad s⁻¹ and 0.15 K, respectively. Concerning the uncertainty of mass, measurements exceeding a mass loss of 1% of the initial mass were not considered in this work, in order to reduce the error arising from the uncertainty in the mass, as well as to ensure a uniform sample composition of the alloys. Typical mass losses of up to 0.5% occurred; hence the uncertainty $\Delta m/m$ is estimated to be $\leq 0.5\%$.

Cause of uncertainty in	Standard uncertainty Δu	Contribution u	Contribution term to $\Delta C_p/C_p$
Normal spectral emissivity: ε	0.00268	0.36636	$5.3427 \cdot 10^{-5}$
Laser power: p_0	0.03 W	14 W	$4.59184 \cdot 10^{-6}$
Temperature amplitude: ΔT_{ac}	0.15 K	6.2897 K	$5.68751 \cdot 10^{-4}$
Mass: m	0.00158 g	1.31542 g	$1.44273 \cdot 10^{-6}$
Modulation frequency: ω	$\frac{0.0005}{\sqrt{3}}$ rad s ⁻¹	0.58774 rad · s ⁻¹	$3.41888 \cdot 10^{-7}$
Absolute combined standard uncertainty, ΔC_p			1.1933
Expanded uncertainty, $U = 2\Delta C_p$			2.3866

Table 21: Heat capacity uncertainty evaluation at constant pressure, exemplarily for liquid Ti at 1930 K.

A.4 Uncertainty analysis of high-temperature viscosity

This section A.4 offers an addition to the sections 2.5, 3.9 and 5.4 on high-temperature viscosity. Based on Eq. (3.27), the uncertainty of the viscosity, $\Delta\eta$, can be calculated from the uncertainties of the parameters density, ρ , the sample radius, R_d , and the damping constant, τ , by error propagation, as following.

$$\begin{aligned}
 \Delta\eta^2 &= \left(\frac{\partial\eta}{\partial\rho}\Delta\rho\right)^2 + \left(\frac{\partial\eta}{\partial R_d}\Delta R_d\right)^2 + \left(\frac{\partial\eta}{\partial\tau}\Delta\tau\right)^2 & (0.10) \\
 &= \left(\frac{R_d^2\tau}{5}\Delta\rho\right)^2 + \left(\frac{2\rho R_d\tau}{5}\Delta R_d\right)^2 + \left(\frac{\rho R_d^2}{5}\Delta\tau\right)^2 \\
 &= \left(\frac{\rho R_d^2\tau}{5}\frac{\Delta\rho}{\rho}\right)^2 + \left(\frac{2\rho R_d^2\tau}{5}\frac{\Delta R_d}{R_d}\right)^2 + \left(\frac{\rho R_d^2\tau}{5}\frac{\Delta\tau}{\tau}\right)^2 \\
 &= \left(\eta\frac{\Delta\rho}{\rho}\right)^2 + \left(2\eta\frac{\Delta R_d}{R_d}\right)^2 + \left(\eta\frac{\Delta\tau}{\tau}\right)^2 \\
 \left(\frac{\Delta\eta}{\eta}\right)^2 &= \left(\frac{\Delta\rho}{\rho}\right)^2 + \left(\frac{\Delta R_d}{R_d}\right)^2 + \left(\frac{\Delta\tau}{\tau}\right)^2
 \end{aligned}$$

As described in section A.1, the error in density can be assumed as $\Delta\rho \leq 1\%$. The mass of the sample was checked before and after the measurement to ensure that measurements with mass losses greater than 1% were precluded. As the mass is proportional to the third power of the radius, the uncertainty of the radius can be considered as $\Delta R_d \leq \frac{1}{3}\%$. This leads to negligibly small contributions of $\frac{\Delta\rho}{\rho} \leq \frac{1}{100}$ and $\frac{2\Delta R_d}{R_d} \leq \frac{1}{150}$ for the density and the radius, respectively. Thus, the uncertainty of damping constant yields the dominating term for the uncertainty of the viscosity. Here, $\Delta\tau$ ist the fit uncertainty of τ , which is found to vary up to about 10% [53].

A.5 Literature data and experimental results on the influence of oxygen on the surface tension

In this section A.5 additional tables with the experimental results obtained in this work and literature on the influence of oxygen on the high-temperature surface tension are presented, following the sections 2.6, 3.10 and 5.6 on the corresponding topic.

μ (Nm ⁻¹)	γ_T (10 ⁻⁴ Nm ⁻¹ K ⁻¹)	Method	Reference
0.87	-1.2	SD	Gouniri [141]
1.05	At 973 K	SD	Goumiri [136]
0.87	-1.5	SD	Levin [135]
0.61	-1.5	SD	Levin [174]
0.87	-1.5	SD	Kolland [96]
0.93	-1.46	SD	Popel [142]
0.88	-1.4	SD	Paramonov [175]
0.76	-1.5	SD	Ayushina [134]
0.83	-1.6	SD	Bykova [176]
0.87	-1.6	SD	Yatsenko [177]
0.87	-1.95	SD	Eustathopolous [178]
0.87	-1.5	SD	Vatolin [179]
0.83	-0.5	MBP	Davies [180]
1.1	At 1073 K	MBP	Cordovilla [137]
0.87	At 1073 K		
0.87	-1.5	MBP	Laty [181]
0.91	-3.4	MBP	Pelzel [143]
0.87	-1.52	MBP	Lang [182]
1.09	At 973 K	MBP	Pamies [138]
0.86	-1.2		
0.85	-1.5	MBP	Saravanan [140]
0.95	-2.4	LD ('clean' cond.)	Molina [133]
0.83	-1.85	LD (oxygen sat.)	
1.05	At 933 K	GJ	Kanian [139]
0.98	-2.71	OD ('clean' cond.)	Kobatake [25]
0.89 ± 0.10	-1.66 ± 0.60		

Table 22: Literature data of the surface tension, γ_L , and surface tension temperature coefficient, γ_T , of liquid Al, as depicted in Figure 5.31 according to Eq. (2.23) along with the used methods and references.

γ_L (Nm ⁻¹)	γ_T (10 ⁻⁴ Nm ⁻¹ K ⁻¹)	Method	Reference
1.51	At 1940 K	CR	Elyutin [147]
1.41	At 1941 K	DC	Arkhipkin [124]
1.557	-0.156	ESL	Paradis [125]
1.525	At 1943 K	DW/PW	Vinet [148]
1.48	At 1943 K	PD	Man [103]
1.49	-0.17	EML-OD	Brillo [101]
1.59	At 1953 K	DW	Tiele [102]
1.65	At 1953 K	PD	Allen [123]
1.39	At 1953 K	PD	Peterson [146]
1.68	At 1953 K	Levitation	Kupperman [127]
1.56	-1.65	EML-OD	Wessing [7]
1.55 ± 0.10	-0.65 ± 0.85		

Table 23: Literature data of the surface tension, γ_L , and surface tension temperature coefficient, γ_T , of liquid Ti, as depicted in Figure 5.32 according to Eq. (2.23) along with the used methods and references.

$T \text{ } \emptyset$ (K)	γ (Nm ⁻¹)	LogPO ₂ SS1 (Pa) min	LogPO ₂ SS1 (Pa) max	Surface condition
1601.33 ± 4.03	0.82 ± 0.01	-6 (-3)	0	'clean'
1462.67 ± 6.86	0.83 ± 0.01	-7 (-3)	0	'clean'
1270.77 ± 6.25	0.82 ± 0.01	-5 (-3)	1	Oxidation
1440.68 ± 153.79	0.82 ± 0.01			

Table 24: Surface tension results for liquid Al with the respective average of the measured temperature range, measured oxygen partial pressure boundaries and the evaluated surface condition, as discussed in section 5.6.2.

$T \text{ } \bar{\text{O}} \text{ (K)}$	$\gamma \text{ (Nm}^{-1}\text{)}$	Log PO_2 SS1 (Pa) min	Log PO_2 SS1 (Pa) max
2114.84 ± 1.73	1.53 ± 0.01	-6	-1
1945.83 ± 1.62	1.53 ± 0.02	-3	0
2134.68 ± 6.63	1.49 ± 0.01	-6	0
1922.67 ± 10.47	1.52 ± 0.01	-4	1
2129.04 ± 3.51	1.53 ± 0.01	-5	0
2108.52 ± 7.20	1.48 ± 0.02	-4	1
2060.02 ± 3.84	1.54 ± 0.01	-5	1
2036.80 ± 2.62	1.53 ± 0.02	-6	0
2094.54 ± 2.41	1.53 ± 0.01	-6	0
2025.17 ± 2.43	1.54 ± 0.01	-5	-4
2057.21 ± 74.88	1.52 ± 0.02		

Table 25: Surface tension results for liquid Ti with the respective average of the measured temperature range and measured oxygen partial pressure boundaries as discussed in section 5.6.2.

Bibliography

- [1] C Gregory. New technologies for reading: The lexicon and the digital library. *The Classical World*, 91 (6): 471–501, 1998.
- [2] W Gale and T Totemeier. *Smithells metals reference book*. Butterworth-Heinemann, 2003.
- [3] S Deevil, P Maziasz, V Sikka, and R Cahn. International Symposium on Nickel and Iron Aluminides: Processing, Properties, and Applications. *Materials Technology*, 12 (5-6): 165–170, 1997.
- [4] G Curran. Mmcs: the future. *Materials world*, 6 (1): 20–21, 1998.
- [5] I Egry, J Brillo, D Holland-Moritz, and Y Plevachuk. The surface tension of liquid Aluminium-based alloys. *Materials Science and Engineering: A*, 495 (1): 14–18, 2008.
- [6] J Schmitz, B Hallstedt, J Brillo, I Egry, and M Schick. Density and thermal expansion of liquid Al–Si alloys. *Journal of Materials Science*, 47 (8): 3706–3712, 2012.
- [7] J Wessing and J Brillo. Density, molar volume, and surface tension of liquid Al-Ti. *Metallurgical and Materials Transactions A*, 48 (2): 868–882, 2017.
- [8] M Boivineau, C Cagran, D Doytier, V Eyraud, M Nadal, B Wilthan, and G Pottlacher. Thermophysical properties of solid and liquid Ti-6Al-4V (TA6V) alloy. *International journal of thermophysics*, 27 (2): 507–529, 2006.
- [9] C Cagran, B Wilthan, G Pottlacher, B Roebuck, M Wickins, and R Harding. Thermophysical properties of a Ti-44% Al-8% Nb-1% B alloy in the solid and molten states. *Intermetallics*, 11 (11): 1327–1334, 2003.
- [10] I Egry, E Brooks, D Holland-Moritz, R Novakovic, T Matsushita, E Ricci, S Seetharaman, Wunderlich R, and Jarvis D. Thermophysical properties of γ -Titanium aluminide: the european impress project. *International Journal of Thermophysics*, 28 (3): 1026–1036, 2007.
- [11] R Nowak, T Lanata, N Sobczak, E Ricci, D Giuranno, R Novakovic, D Holland-Moritz, and I Egry. Surface tension of γ -TiAl-based alloys. *Journal of materials science*, 45 (8): 1993–2001, 2010.

- [12] Y Plevachuk, I Egry, J Brillo, D Holland-Moritz, and I Kaban. Density and atomic volume in liquid Al-Fe and Al-Ni binary alloys. *International journal of materials research*, 98 (2): 107–111, 2007.
- [13] P Nasch and S Steinemann. Density and thermal expansion of molten Manganese, Iron, Nickel, Copper, Aluminum and Tin by means of the gamma-ray attenuation technique. *Physics and Chemistry of Liquids*, 29 (1): 43–58, 1995.
- [14] M Assael, J Kakosimos, K Konstantinos, R Banish, R Michael, J Brillo, I Egry, R Brooks, P Queded, K Mills, A Nagashima, Y Sato, et al. Reference data for the density and viscosity of liquid Aluminum and liquid Iron. *Journal of physical and chemical reference data*, 35 (1): 285–300, 2006.
- [15] H Kobatake, H Khosroabadi, and H Fukuyama. Normal spectral emissivity of stable and undercooled liquid Silicon using electromagnetic levitation in a dc magnetic field. *Meas. Sci. Technol.*, 22: 015102, 2011.
- [16] H Fukuyama, H Kobatake, K Takahashi, I Minato, T Tsukada, and S Awaji. Development of modulated laser calorimetry using a solid Platinum sphere as a reference. *Measurement Science and Technology*, 18 (7): 2059, 2007.
- [17] H Kobatake, H Fukuyama, I Minato, T Tsukada, Takao, and S Awaji. Noncontact modulated laser calorimetry of liquid Silicon in a static magnetic field. *Journal of Applied Physics*, 104 (5): 054901, 2008.
- [18] H Fukuyama, K Takahashi, S Sakashita, H Kobatake, T Tsukada, and S Awaji. Noncontact modulated laser calorimetry for liquid austenitic stainless steel in dc magnetic field. *ISIJ international*, 49 (9): 1436–1442, 2009.
- [19] H Kobatake, H Fukuyama, T Tsukada, and S Awaji. Noncontact modulated laser calorimetry in a dc magnetic field for stable and supercooled liquid Silicon. *Measurement Science and Technology*, 21 (2): 025901, 2009.
- [20] J Naidich. The wettability of solids by liquid metals. *Progress in surface and membrane science*, 14: 353–484, 1981.
- [21] J Garandet, B Vinet, and P Gros. Considerations on the pendant drop method: a new look at Tate’s law and Harkins’ correction factor. *Journal of colloid and interface science*, 165 (2): 351–354, 1994.
- [22] H Fukuyama and Y Waseda. *High-temperature measurements of materials*, volume 11. Springer Science & Business Media, 2008.

- [23] S Ozawa, K Morohoshi, T Hibiya, and H Fukuyama. Influence of oxygen partial pressure on surface tension of molten silver. *Journal of Applied Physics*, 107 (1): 014910, 2010.
- [24] L Belyanchikov. Thermodynamics of Titanium-based melts: II. Oxygen in liquid titanium. *Russian Metallurgy (Metally)*, 2010 (12): 1156–1163, 2010.
- [25] H Kobatake, J Brillo, J Schmitz, and P Pichon. Surface tension of binary Al-Si liquid alloys. *Journal of Materials Science*, 50 (9): 3351–3360, 2015.
- [26] S Schneider. *Viskositäten unterkühlter Metallschmelzen*. PhD thesis, Bibliothek der RWTH Aachen, 2002.
- [27] M Kehr, W Hoyer, and I Egry. A new high-temperature oscillating cup viscometer. *International Journal of Thermophysics*, 28 (3): 1017–1025, 2007.
- [28] R Kurosawa, T Inoue, Y Baba, K Sugioka, M Kubo, T Tsukada, and H Fukuyama. Normal spectral emissivity measurement of molten Copper using an electromagnetic levitator superimposed with a static magnetic field. *Measurement Science and Technology*, 24 (1): 015603, 2012.
- [29] N Eustathopoulos and B Drevet. Surface tension of liquid Silicon: High or low value? *Journal of Crystal Growth*, 371: 77–83, 2013.
- [30] J Brillo. *Thermophysical properties of multicomponent liquid alloys*. Walter de Gruyter GmbH & Co KG, 2016.
- [31] I Egry, G Lohoefer, I Seyhan, S Schneider, and B Feuerbacher. Viscosity of eutectic Pd₇₈Cu₆Si₁₆ measured by the oscillating drop technique in microgravity. *Applied physics letters*, 73 (4): 462–463, 1998.
- [32] S Krishnan, C Anderson, J K Weber, P Nordine, W Hofmeister, and R Bayuzick. Optical properties and spectral emissivities at 632.8 nm in the Titanium-Aluminum system. *Metallurgical and Materials Transactions A*, 24 (1): 67–72, 1993.
- [33] D Luedecke and C Luedecke. *Thermodynamik: Physikalisch-chemische Grundlagen der thermischen Verfahrenstechnik*. Springer-Verlag, 2013.
- [34] R Schmid-Fetzer and J Groebner. *Adv. Eng. Mat.*, 3 (947), 2001.
- [35] L Vegard. Die Konstitution der Mischkristalle und die Raumfüllung der Atome. *Zeitschrift für Physik*, 5 (1): 17–26, 1921.
- [36] H Kobatake, H Khosroabadi, and H Fukuyama. Normal spectral emissivity measurement of liquid Iron and Nickel using electromagnetic levitation in direct current magnetic field. *Metallurgical and Materials Transactions A*, 43 (7): 2466–2472, 2012.

- [37] N Eustathopoulos, M Nicholas, and B Drevet. *Wettability at high temperatures*, volume 3. Elsevier, 1999.
- [38] J Schmitz. *Untersuchung der Anisotropie im Benetzungsverhalten flüssiger Al-Cu Legierungen auf einkristallinen orientierten Al₂O₃-Substraten*. PhD thesis, RWTH Aachen, 2011.
- [39] J Gibbs. *Scientific Papers: Thermodynamics*, volume 1. Dover Publications, 1961.
- [40] J Brillo, D Chatain, and I Egry. Surface tension of liquid binary alloys—theory versus experiment. *International Journal of Materials Research*, 100 (1): 53–58, 2009.
- [41] H Dörfler. *Grenzflächen und kolloid-disperse Systeme: Physik und Chemie*. Springer, 2002.
- [42] I Egry and J Brillo. The excess surface tension of regular binary liquid alloys. *High Temperatures-High Pressures*, 42: 59–68, 2013.
- [43] J Butler. The thermodynamics of the surfaces of solutions. *Proc R Soc*, A135: 348–374, 1932.
- [44] G Kaptay. A calphad-compatible method to calculate liquid/liquid interfacial energies in immiscible metallic systems. *Calphad*, 32 (2): 338–352, 2008.
- [45] T Tanaka and T Iida. Application of a thermodynamic database to calculation of surface tension for iron base liquid alloys. *Steel Res*, 65: 21–28, 1994.
- [46] G Kaptay. Partial surface tension of components of a solution. *Langmuir*, 31 (21): 5796–5804, 2015.
- [47] P Wynblatt, A Saul, and D Chatain. The effects of prewetting and wetting transitions on the surface energy of liquid binary alloys. *Acta Mater*, 46: 2337–2347, 1998.
- [48] C Antion and D Chatain. Liquid surface and liquid/liquid interface energies of binary subregular alloys and wetting transitions. *Surface science*, 601 (10): 2232–2244, 2007.
- [49] I Egry. Surface tension of compound forming liquid binary alloys: A simple model. *Journal of materials science*, 39 (20): 6365–6366, 2004.
- [50] B Allen. *Liquid metals, chemistry and physics*, edited by s. Beer (New York: Marcel Dekker), page 186, 1972.
- [51] G Kaptay. A unified model for the cohesive enthalpy, critical temperature, surface tension and volume thermal expansion coefficient of liquid metals of bcc, fcc and hcp crystals. *Materials Science and Engineering: A*, 495 (1): 19–26, 2008.

- [52] P Heintzmann. Untersuchungen der Zusammenhänge von atomarer Struktur, Selbstdiffusion, Interdiffusion und Viskosität in flüssigen Zr-Ni Legierungen. 2016.
- [53] I Jonas. 2016. PhD thesis, Universität des Saarlandes, Institute of Materials Physics in Space, German Aerospace Center (DLR), 2016.
- [54] J Brillo, R Brooks, I Egry, P Quested, M Wenderoth, S Vorberg, B Fischer, R Völkl, U Glatzel, G Vassilev, et al. Sa polyakov, I.-s. chang, ej mittemeijer. *Int. J. Mat. Res. (formerly Z. Metallkd.)*, 98 (6): 449, 2007.
- [55] M Hirai. Estimation of viscosities of liquid alloys. *ISIJ international*, 33 (2): 251–258, 1993.
- [56] L Kozlov, L Romanov, and N Petrov. Izv. vysch. uch. zav. *Chernaya Metallurgiya*, 3 (7), 1983.
- [57] I Budai, M Benkő, and G Kaptay. Analysis of literature models on viscosity of binary liquid metallic alloys on the example of the Cu-Ag system. In *Materials Science Forum*, volume 473, pages 309–314. Trans Tech Publ, 2005.
- [58] M Schick, J Brillo, I Egry, and B Hallstedt. Viscosity of al–cu liquid alloys: measurement and thermodynamic description. *Journal of Materials Science*, 47 (23): 8145–8152, 2012.
- [59] S Seetharaman and D Sichen. Estimation of the viscosities of binary metallic melts using Gibbs energies of mixing. *Metallurgical and Materials Transactions B*, 25 (4): 589–595, 1994.
- [60] R Gasser and G Ehrlich. An introduction to chemisorption and catalysis by metals, 1987.
- [61] B Drevet and N Eustathopoulos. Wetting of ceramics by molten silicon and Silicon alloys: a review. *Journal of Materials Science*, 47 (24): 8247–8260, 2012.
- [62] G Belton. Langmuir adsorption, the gibbs adsorption isotherm, and interracial kinetics in liquid metal systems. *Metallurgical Transactions B*, 7 (1): 35–42, 1976.
- [63] M Schulz, J Brillo, C Stenzel, and H Fritze. Oxygen partial pressure control for microgravity experiments. *Solid State Ionics*, 225: 332–336, 2012.
- [64] K Mukai, Z Yuan, K Nogi, and T Hibiya. Effect of the oxygen partial pressure on the surface tension of molten Silicon and its temperature coefficient. *Isij International*, 40 (Suppl): S148–S152, 2000.
- [65] E Ricci, E Arato, A Passerone, and P Costa. Oxygen tensioactivity on liquid-metal drops. *Advances in colloid and interface science*, 117 (1): 15–32, 2005.

- [66] M Willert-Porada. Hochtemperaturkorrosion von Werkstoffen. Praktikumsskript H4B, Stoffklassenübergreifende Bauteilfertigung (Werkstoffverarbeitung B), Lehrstuhl für Werkstoffverarbeitung, Universität Bayreuth, WS 2013/2014. URL http://www.lswv.uni-bayreuth.de/de/download/documents/Hochtemp-Korrosion_WiSe2014-15.pdf.
- [67] H Ellingham. Reducibility of oxides and sulfides in metallurgical processes. *J Soc Chem Ind*, 63: 125–133, 1944.
- [68] H Ellingham. Transactions and communications. *J. Soc. Chem. Ind.(London)*, 63 (5): 125, 1944.
- [69] M Hasegawa. Ellingham diagram. In *Treatise on Process Metallurgy: Process Fundamentals*, pages 507–516. Elsevier, 2014.
- [70] C Karrasch. *Solidification kinetics in undercooled pure iron and iron-boron alloys under different fluid flow conditions*. PhD thesis, Ruhr-Universität Bochum, 2016.
- [71] Westinghouse. Magnetic levitation and heating of conductive materials. Us patent 2686864, Electric Corp, 08/07 1954.
- [72] J Brillo, G Lohoefer, F Schmidt-Hohagen, D Schneider, and I Egry. Thermophysical property measurements of liquid metals by electromagnetic levitation. *International Journal of Materials and Product Technology*, 26 (3-4): 247–273, 2006.
- [73] P Paradis, T Ishikawa, G Lee, D Holland-Moritz, J Brillo, W Rhim, and J Okada. Materials properties measurements and particle beam interactions studies using electrostatic levitation. *Materials Science and Engineering: R: Reports*, 76: 1–53, 2014.
- [74] P Sahm, I Egry, and T Volkmann. *Schmelze, Erstarrung, Grenzflächen: Eine Einführung in die Physik und Technologie flüssiger und fester Metalle*. Springer-Verlag, 2013.
- [75] D Cummings and D Blackburn. Oscillations of magnetically levitated aspherical droplets. *Journal of Fluid Mechanics*, 224: 395–416, 1991.
- [76] I Egry and S Sauerland. Containerless processing of undercooled melts: measurements of surface tension and viscosity. *Materials Science and Engineering: A*, 178 (1): 73–76, 1994.
- [77] A Sneyd and H Moffatt. Fluid dynamical aspects of the levitation-melting process. *Journal of Fluid Mechanics*, 117: 45–70, 1982.
- [78] W Wien. On the division of energy in the emission-spectrum of a black body. *Philos. Magaz.*, 5 (43): 214–220, 1897.

- [79] G Kirshnan, H Hansen, R Hauge, and J Margrave. Spectral emissivities and optical properties of electromagnetically levitated liquid metals as functions of temperature and wavelength. *High temperature science*, 29 (1): 17–52, 1990.
- [80] V Witusiewicz, A Bondar, U Hecht, S Rex, and T Velikanova. The Al-B-Nb-Ti system: Iii. thermodynamic re-evaluation of the constituent binary system Al-Ti. *Journal of alloys and compounds*, 465 (1): 64–77, 2008.
- [81] J Lee, D Matson, S Binder, M Kolbe, D Herlach, and R Hyers. Magneto-hydrodynamic modeling and experimental validation of convection inside electromagnetically levitated Co–Cu droplets. *Metallurgical and Materials Transactions B*, 45 (3): 1018–1023, 2014.
- [82] A Gerst. Alexander gerst with the electromagnetic levitator, 11 2014. URL http://www.dlr.de/dlr/en/desktopdefault.aspx/tabid-10081/151_read-12057/year-all/#/gallery/-17105.
- [83] J Brillo and I Egry. Density determination of liquid Copper, Nickel, and their alloys. *International Journal of Thermophysics*, 24 (4): 1155–1170, 2003.
- [84] J Brillo, I Egry, and J Westphal. Density and thermal expansion of liquid binary Al-Ag and Al-Cu alloys. *International Journal of Materials Research*, 99 (2): 162–167, 2008.
- [85] T Tsukada, H Fukuyama, and H Kobatake. Determination of thermal conductivity and emissivity of electromagnetically levitated high-temperature droplet based on the periodic laser-heating method: Theory. *International journal of heat and mass transfer*, 50 (15): 3054–3061, 2007.
- [86] M Watanabe, M Adachi, and H Fukuyama. Normal spectral emissivity and heat capacity at constant pressure of Fe-Ni melts. *Journal of Materials Science*, 52 (16): 9850–9858, 2017.
- [87] R Wunderlich and H Fecht. Modulated electromagnetic induction calorimetry of reactive metallic liquids. *Measurement Science and Technology*, 16 (2): 402, 2005.
- [88] H Watanabe, M Susa, H Fukuyama, and K Nagata. Near-infrared spectral emissivity of Cu, Ag, and Au in the liquid and solid states at their melting points. *International journal of thermophysics*, 24 (4): 1105–1120, 2003.
- [89] I Egry, G Lohoefer, P Neuhaus, and S Sauerland. Surface tension measurements of liquid metals using levitation, microgravity, and image processing. *International journal of thermophysics*, 13 (1): 65–74, 1992.

- [90] I Egry, G Lohoefer, and G Jacobs. Surface tension of liquid metals: results from measurements on ground and in space. *Physical review letters*, 75 (22): 4043, 1995.
- [91] E Siebert, J Fouletier, and S Vilminot. Electrochemical system for measuring the partial oxygen pressure in a gaseous or liquid atmosphere, October 30 1984. US Patent 4,479,867.
- [92] J Fouletier, E Mantel, and M Kleitz. Performance characteristics of conventional oxygen gauges. *Solid State Ionics*, 6 (1): 1–13, 1982.
- [93] O Shumpei, M Keisuke, and H Taketoshi. Influence of oxygen partial pressure on surface tension of molten type 304 and 316 stainless steels measured by oscillating drop-let method using electromagnetic levitation. *ISIJ International*, 54 (9): 2097–2103, 2014. doi: [10.2355/isijinternational.54.2097](https://doi.org/10.2355/isijinternational.54.2097).
- [94] J Murray and H Wriedt. The O- Ti (Oxygen-Titanium) system. *Journal of Phase Equilibria*, 8 (2): 148–165, 1987.
- [95] X Lu, C Cao, M Kolbe, B Wei, and D Herlach. Microstructure analysis of Co-Cu alloys undercooled prior to solidification. *Materials Science and Engineering: A*, 375: 1101–1104, 2004.
- [96] J Brillo and G Kolland. Surface tension of liquid Al-Au binary alloys. *Journal of Materials Science*, 51 (10): 4888–4901, 2016.
- [97] H Kobatake, J Schmitz, and J Brillo. Density and viscosity of ternary Al-Cu-Si liquid alloys. *Journal of Materials Science*, 49 (9): 3541–3549, 2014.
- [98] K Tanaka, K Hack, T Iida T, and S Hara. Application of thermodynamic databases to the evaluation of surface tensions of molten alloys, salt mixtures and oxide mixtures. *Z. Metallkd*, 87: 380 ff, 1996.
- [99] E Gebhardt, M Becker, and S Dorner. Aluminium. *Fachzeitschrift der deutschen Aluminiumindustrie*, 31: 315–321, 1955.
- [100] S Amore, S Delsante, H Kobatake, and J Brillo. Excess volume and heat of mixing in Cu-Ti liquid mixture. *The Journal of chemical physics*, 139 (6): 064504, 2013.
- [101] S Amore, J Brillo, I Egry, and R Novakovic. Surface tension of liquid Cu-Ti binary alloys measured by electromagnetic levitation and thermodynamic modelling. *Applied Surface Science*, 257 (17): 7739–7745, 2011.
- [102] Tiele J and Kelly J. The surface tension of liquid Titanium. *Brit. J. Appl. Phys.*, 14: 717–719, 1963.
- [103] K Man. Surface tension measurements of liquid metals by the quasi-containerless pendant drop method. *International journal of thermophysics*, 21 (3): 793–804, 2000.

- [104] E Peng, T Voigtmann, G Kolland, H Kobatake, and J Brillo. Structural and dynamical properties of liquid Al-Au alloys. *Physical Review B*, 92 (18): 184201, 2015.
- [105] G Teodorescu, P Jones, R Overfelt, and B Guo. High temperature emissivity of high purity Titanium and Zirconium. In *Proceedings of the Sixteenth symposium on thermophysical properties*, 2006.
- [106] G Grass. Zur Anwendung der Drudeschen Theorie der freien Elektronen auf das optische Verhalten der Metalle im Sichtbaren und Ultraviolett. *Zeitschrift für Physik A Hadrons and Nuclei*, 139 (3): 358–364, 1954.
- [107] J Qin, M Rösner-Kuhn, K Drewes, U Thiedemann, Gr Kuppermann, B Camin, R Blume, and M Frohberg. Spectral emissivities at wavelengths in the range 500-653 nm, enthalpies, and heat capacities of the liquid phases of Cobalt, Titanium, and Zirconium. *High temperature and materials science*, 37 (3): 129–141, 1997.
- [108] N Ravindra, B Sopori, O Gokce, S Cheng, A Shenoy, L Jin, S Abedrabbo, W Chen, and Y Zhang. Emissivity measurements and modeling of silicon-related materials: an overview. *International journal of thermophysics*, 22 (5): 1593–1611, 2001.
- [109] NIST-JANAF. *THERMOCHEMICAL TABLES*, volume Monograph 9 (Part I and Part II). M. W. Chase, Jr., fourth edition (1998) edition, 1963.
- [110] P. Reiter. *Construction and operational characteristics of a millisecond pulse-heating system for the measurement of thermophysical properties of metals*. PhD thesis, Technische Universitat Graz, Austria, 2001.
- [111] E Kaschnitz, P Reiter, and J McClure. Thermophysical Properties of Solid and Liquid 90Ti-6Al-4V in the Temperature Range from 1400 to 2300 K Measured by Millisecond and Microsecond Pulse-Heating Techniques. *International Journal of Thermophysics*, 23 (1): 267–275, Jan 2002. ISSN 1572-9567. doi: [10.1023/A:1013925715428](https://doi.org/10.1023/A:1013925715428). URL <https://doi.org/10.1023/A:1013925715428>.
- [112] ThermoCalc Users Guide and Q Version. Thermocalc software ab. *Stockholm, Schweden*, 2004.
- [113] A Agaev, V Kostikov, and V Bobkovskii. Viscosity of refractory metal melts. *Izv. Akad. Nauk SSSR, Met.*, (3): 43–45, 1980.
- [114] P Paradis, T Ishikawa, and S Yoda. Non-contact measurements of surface tension and viscosity of Niobium, Zirconium, and Titanium using an electrostatic levitation furnace. *International journal of thermophysics*, 23 (3): 825–842, 2002.
- [115] P Desai. Thermodynamic properties of selected binary Aluminum alloy systems. *Journal of physical and chemical reference data*, 16 (1): 109–124, 1987.

- [116] K Mills. *Recommended values of thermophysical properties for selected commercial alloys*. Woodhead Publishing, 2002.
- [117] Y Sato. Research and development of innovative casting simulation. Technical report, supported by New Energy and Industrial Technology Development Organization NEDO, through the Japan Space Utilization Promotion Center- Report to the Ministry of Economy, Trade, 2004.
- [118] M Kehr. Aufbau eines Hochtemperaturviskosimeters und Messung der Viskosität von Schmelzen des Systems Aluminium-Nickel. 2009.
- [119] Y Kawai and Y Shiraishi. *Handbook of physico-chemical properties at high temperatures*. Iron and Steel Institute of Japan, 1988.
- [120] M Palm, L Zhang, F Stein, and G Sauthoff. Phases and phase equilibria in the Al-rich part of the Al-Ti system above 900 c. *Intermetallics*, 10 (6): 523–540, 2002.
- [121] R Novakovic, D Giuranno, E Ricci, A Tuissi, R Wunderlich, H Fecht, and I Egry. Surface, dynamic and structural properties of liquid Al-Ti alloys. *Applied Surface Science*, 258 (7): 3269–3275, 2012.
- [122] J Schmitz, J Brillo, I Egry, and R Schmid-Fetzer. Surface tension of liquid Al - Cu binary alloys. *International Journal of Materials Research*, 100 (11): 1529–1535, 2009.
- [123] B Allen. The surface tension of liquid transition metals at their melting points. *Trans. AIME*, 227, 1963.
- [124] V Arkhipkin, A Agaev, G Grigorev, and V Kostikov. Installation for measuring the surface tension of liquid refractory metals. *Ind. Lab.*, 39: 1340 ff, 1973.
- [125] T Ishikawa, P Paradis, T Itami, and S Yoda. Thermophysical properties of liquid refractory metals: Comparison between hard sphere model calculation and electrostatic levitation measurements. *J. Chem. Phys.*, 118: 7912, 2003.
- [126] T Ishikawa and P Paradis. Thermophysical properties of molten refractory metals measured by an electrostatic levitator. *Journal of electronic materials*, 34 (12): 1526–1532, 2005.
- [127] G Kuppermann. *The determination of the surface tension with the help of the levitated reciprocating drop under terrestrial conditions and in space*. PhD thesis, Technology University of Berlin, 2000.
- [128] V Laurent, D Chatain, C Chatillon, and N Eustathopoulos. Wettability of monocrystalline alumina by aluminium between its melting point and 1273 k. *Acta Metallurgica*, 36 (7): 1797–1803, 1988.

- [129] O Mailliart, F Hodaj, V Chaumat, and N Eustathopoulos. Influence of oxygen partial pressure on the wetting of SiC by a Co-Si alloy. *Materials Science and Engineering: A*, 495 (1): 174–180, 2008.
- [130] L Fiori, E Ricci, and E Arato. Dynamic surface tension measurements on molten metal-oxygen systems: model validation on molten Tin. *Acta materialia*, 51 (10): 2873–2890, 2003.
- [131] M Ratto, E Ricci, and E Arato. Mechanism of oxidation/deoxidation of liquid Silicon: theoretical analysis and interpretation of experimental surface tension data. *Journal of crystal growth*, 217 (3): 233–249, 2000.
- [132] E Ricci, D Giuranno, E Arato, and P Costa. Validation of an effective oxidation pressure model for liquid binary alloys. *Materials Science and Engineering: A*, 495 (1): 27–31, 2008.
- [133] J Molina, R Voytovych, E Louis, and N Eustathopoulos. The surface tension of liquid Aluminium in high vacuum: the role of surface condition. *International journal of adhesion and adhesives*, 27 (5): 394–401, 2007.
- [134] G Ayushima, E Levin, and P Geld. Effect of temperature and composition on the densities and surface tensions of Iron-Aluminum alloys. *Russ J Phys Chem*, 43: 1548–1551, 1969.
- [135] E Levin, G Ayushina, and P Geld. Density and surface-energy polytherms of liquid (molten) Aluminum. *High Temp.*, 6: 416–18, 1968.
- [136] L Goumiri and J Joud. Auger electron spectroscopy study of Aluminium-Tin liquid system. *Acta metallurgica*, 30 (7): 1397–1405, 1982.
- [137] C Garcia-Cordovilla, E Louis, and A Pamies. The surface tension of liquid pure Aluminium and Aluminium-Magnesium alloy. *Journal of Materials Science*, 21 (8): 2787–2792, Aug 1986. ISSN 1573-4803. doi: [10.1007/BF00551490](https://doi.org/10.1007/BF00551490). URL <https://doi.org/10.1007/BF00551490>.
- [138] A Pamies, C Garcia-Cordovilla, and E Louis. The measurement of surface tension of liquid Aluminium by means of the maximum bubble pressure method: the effect of surface oxidation. *Scripta metallurgica*, 18 (9): 869–872, 1984.
- [139] V Sarou-Kanian, F Millot, and J Rifflet. Surface tension and density of oxygen-free liquid Aluminum at high temperature. *International journal of Thermophysics*, 24 (1): 277–286, 2003.

- [140] R Saravanan, J Molina, J Narciso, C Garcia-Cordovilla, and E Louis. Effects of nitrogen on the surface tension of pure Aluminium at high temperatures. *Scripta Materialia*, 44 (6): 965–970, 2001.
- [141] L Gouniri, J Joud, P Resre, and J Michter J. Sensions superficielles dalliages liquides binaires presentant un caractere d immiscibilite: Al-Pb, Al-Bi, Al-Se et Yn-Bi. *Sur Sci*, 83: 471–486, 1979.
- [142] S Popel, V Kozhurkov, and A Zhukov. Density, surface tension and adhesion to Iron of Pb-Sn melts. *Prot Met, Izv Akad Nauk SSSR Met 5: 69 (in Russian)*. Cited in Popel SI, Zakharova TV, Kozhevnikova VA (1976), 12: 423–425, 1975.
- [143] Pelzel E. Surface tension of liquid metals and alloys, i-ii. *Berg Huttenmann Monatsh*, 93: 247–254, 1948.
- [144] M Cancarevic, M Zinkevich, and F Aldinger. Thermodynamic description of the Ti–O system using the associate model for the liquid phase. *Calphad*, 31 (3): 330–342, 2007.
- [145] I Kornilov. Effect of oxygen on Titanium and its alloys. *Metal Science and Heat Treatment*, 15 (10): 826–829, 1973.
- [146] A Peterson, H Kedesdy, P Keck, and E Scharz. Surface Tension of Titanium, Zirconium, and Hafnium. *J. Appl. Phys.*, 28: 213, 1958.
- [147] V Elyutin and M Maurakh. *Izv. A.N., O.T.N. (USSR)*, 6: 129–131, 1955.
- [148] B Vinet, L Magnusson, H Fredriksson, and P Desré. Correlations between surface and interface energies with respect to crystal nucleation. *Journal of colloid and interface science*, 255 (2): 363–374, 2002.
- [149] T Iida and R Guthrie. *The Thermophysical Properties of Metallic Liquids: Fundamentals*, volume 1. Oxford University Press, USA, 2015.
- [150] N Takiuchi, T Taniguchi, Y Tanaka, N Shinozaki, and K Mukai. (in japanese). *J Jpn Inst Met*, 55 (180), 1981.
- [151] G Bernard and C Lupis. The surface tension of liquid Silver alloys: Part ii. Ag- O alloys. *Metallurgical and Materials Transactions B*, 2 (11): 2991–2998, 1971.
- [152] M Watanabe, M Adachi, and H Fukuyama. Densities of Fe–Ni melts and thermodynamic correlations. *Journal of Materials Science*, 51 (7): 3303–3310, Apr 2016. ISSN 1573-4803. doi: [10.1007/s10853-015-9644-2](https://doi.org/10.1007/s10853-015-9644-2). URL <http://dx.doi.org/10.1007/s10853-015-9644-2>.
- [153] G Scatchard. Change of volume on mixing and the equations for non-electrolyte mixtures. *Transactions of the Faraday Society*, 33: 160–166, 1937.

- [154] O Kleppa. The volume change on mixing in liquid metallic solutions. i. alloys of cadmium with Indium, Tin, Thallium, Lead and Bismuth. *The Journal of Physical Chemistry*, 64 (10): 1542–1546, 1960.
- [155] B Predel and A Emam. Überschlußvolumina flüssiger Legierungen der Systeme Bi- Sn, Sn- Tl, Pb- Sn, Bi- Tl, Hg- In, Hg- Tl und Pb- Tl. *Materials Science and Engineering*, 4 (5): 287–296, 1969.
- [156] A Crawley. Densities of liquid metals and alloys. *International Metallurgical Reviews*, 19 (1): 32–48, 1974.
- [157] O Kubaschewski and C Alcock. Metallurgical thermochemistry 5th ed.(1979). Oxford, Pergamon Press.
- [158] T Iida and R Guthrie. The physical properties of liquid metals. Clarendon Press, Walton Street, Oxford OX 2 6 DP, UK, 1988.
- [159] G Zellars, S Payne, J Morris, and R Kipp. The activities of Iron and Nickel in liquid Fe–Ni alloys. *Trans Metall Soc AIME*, 215: 181–185, 1959.
- [160] W Rammensee and D Fraser. Activities in solid and liquid Fe- Ni and Fe- Co Alloys Determined by Knudsen Cell Mass Spectrometry. *Berichte der Bunsengesellschaft für physikalische Chemie*, 85 (7): 588–592, 1981.
- [161] N Maruyama and S Ban-Ya. Measurement of activities in liquid Fe-Ni, Fe-Co and Ni-Co Alloys by a Transportation Method. *Journal of the Japan Institute of Metals*, 42 (10): 992–999, 1978.
- [162] B Predel and R Mohs. Thermodynamic investigations of the Iron-Nickel and Iron-Cobalt systems. *ARCH EISENHUTTENWESEN*, 41 (2): 143–149, 1970.
- [163] J Brillo, I Egry, and I Ho. Density and thermal expansion of liquid Ag–Cu and Ag–Au alloys. *International journal of thermophysics*, 27 (2): 494–506, 2006.
- [164] R Edwards and J Downing. The thermodynamics of the liquid solutions in the triad Cu–Ag–Au. I. The Cu–Ag system. *The Journal of Physical Chemistry*, 60 (1): 108–111, 1956.
- [165] L Timberg, J Toguri, and T Azakami. A thermodynamic study of Copper-Iron and Copper-Cobalt liquid alloys by mass spectrometry. *Metallurgical and Materials Transactions B*, 12 (2): 275–279, 1981.
- [166] J Brillo and I Egry. Density and excess volume of liquid Copper, Nickel, Iron, and their binary alloys. *Zeitschrift für Metallkunde*, 95 (8): 691–697, 2004.

- [167] N Maruyama and S Ban-Ya. Measurement of the activities in molten Fe–Cu, Fe–Cr, and Fe–Sn alloys by a transportation method. *Journal of the Japan Institute of Metals*, 44 (12): 1422–1431, 1980.
- [168] J Tomiska and A Neckel. Knudsen cell-mass spectrometry for the determination of the thermodynamic properties of liquid Copper - Nickel alloys. *International Journal of Mass Spectrometry and Ion Physics*, 47: 223–226, 1983.
- [169] V Witusiewicz, U Stolz, I Arpshofen, and F Sommer. Thermodynamics of liquid Al-Cu-Zr alloys. *Zeitschrift für Metallkunde*, 89 (10): 704–713, 1998.
- [170] K Itagaki and A Yazawa. Heats of mixing in liquid Copper or Gold binary alloys. *Transactions of the Japan Institute of Metals*, 16 (11): 679–686, 1975.
- [171] T Wilder and J Elliott. Thermodynamic Properties of the Aluminum-Silver System. *Journal of the electrochemical society*, 107 (7): 628–635, 1960.
- [172] A Mizuno, H Kawauchi, M Tanno, K Murai, H Kobatake, H Fukuyama, T Tsukada, and M Watanabe. Concentration dependence of molar volume of binary Si alloys in liquid state. *ISIJ International*, 54 (9): 2120–2124, 2014.
- [173] L Kirkup and B Robert. *An introduction to uncertainty in measurement: using the GUM (guide to the expression of uncertainty in measurement)*. Cambridge University Press, 2006.
- [174] Naukova dumka (in russian). *Eremenko VN (ed) Fiz. Khim. Poverkh Yavleni*, 20: 153–156, 1971. Cited in Keene BJ (1993) Review of data for the surfacetension of pure metals. *Int Mater Rev* 38:157-192.
- [175] V Paramonov, E Karamydhev, and V Ukhov. Colloq. on physics and chemistry of surface melts. *Fiz. Khim. Poverkh Rasp. Tbilisi, Metsniyerba*, 155: 157–192, 1977.
- [176] N Bykova and V Schevchenko. Density and surface tension of Copper Aluminum, Gallium, Indium and Tin, physicochemical investigations of liquid metals and alloys. *Severdlovsk*, 29 (42), 1974.
- [177] A Yatsenko, V Kononenko, and A Sukhman. Experimental studies of the temperature dependence of the surface tension and density of Tin, Indium, Aluminum, and Gallium. *High Temp.*, 10 (55), 1972.
- [178] N Eustathopoulos, J Joud, P Desre, and J Hicter. The wetting of carbon by Aluminium and Aluminium alloys. *Journal of Materials Science*, 9 (8): 1233–1242, Aug 1974. ISSN 1573-4803. doi: [10.1007/BF00551836](https://doi.org/10.1007/BF00551836). URL <https://doi.org/10.1007/BF00551836>.

- [179] SV Lukin, VI Zhuchkov, and NA Vatolin. The surface tension, density and oxidation kinetics of Fe-Si-B alloys. *Journal of the Less Common Metals*, 67 (2): 399–405, 1979.
- [180] V Davies and J West. Influence of small additions of Sodium on surface tension of Aluminium+Aluminium-Silicon alloys, 1964.
- [181] P Lamy, J Joud, P Desre, and G Lang. Tension superficielle d'alliages liquides Aluminium-cuivre. *Surface Science*, 69 (2): 508–520, 1977.
- [182] Lang G. The influence of alloying elements to the surface tension of liquid super purity Aluminium. *Aluminium*, 50: 731–734, 1974.

Abbreviations

σ	Stefan–Boltzmann constant ($\text{Wm}^{-2}\text{K}^{-4}$)
ρ_e	electrical resistivity (Ωm)
\vec{F}_L	Lorentz force (N)
$\hat{\rho}_i^B$	constant number density in the bulk (mol^{-1})
$\hat{\rho}_i^G$	constant number density in the gas phase (mol^{-1})
ΔG^{ideal}	mixing free energy of the ideal solution (kJmol^{-1})
$\nabla_y v_x$	velocity gradient in direction y perpendicular to direction x
${}^{\text{drop}}V$	real droplet volume (cm^3)
${}^E G_i^B$	partial excess free energy of component i in the bulk (kJmol^{-1})
${}^E G_i^S$	partial excess free energy of component i in the surface (kJmol^{-1})
${}^E G$	excess free energy (kJmol^{-1})
h_{conv}	forced convection heat transfer coefficient of a gas surrounding the sample droplet ($\text{Wm}^{-2}\text{K}^{-1}$)
O_{ad}	adsorbed oxygen in the melt
${}^\nu C$	Redlich-Kister volume parameter of ν -th order ($\text{cm}^3\text{mol}^{-1}$) at 0 K
${}^\nu D$	linear temperature coefficient of Redlich-Kister volume parameter of ν -th order ($10^{-4}\text{cm}^3\text{mol}^{-1}\text{K}^{-1}$)
${}^\nu L$	Redlich-Kister coefficient of ν -th order for the free energy (Jmol^{-1})
${}^\nu V$	Redlich-Kister volume parameter of ν -th order ($\text{cm}^3\text{mol}^{-1}$)
${}^\nu c$	Redlich-Kister fit parameter of ν -th for the excess heat capacity
${}^\nu u$	Redlich-Kister fit parameter of ν -th for the excess surface tension ($\text{Nm}^{-1}\text{mol}^{-1}$)

$A_{S,i}$	partial molar surface area of pure liquid i ($\text{m}^2\text{mol}^{-1}$)
A_S	molar surface area ($\text{m}^2\text{mol}^{-1}$)
\vec{B}	magnetic field (T)
C_1	first radiation constant according to Planck's law of radiation ($3.742 \cdot 10^{16}$ (Wm^2))
C_2	second radiation constant according to Planck's law of radiation ($1.439 \cdot 10^2$ (mK))
C_p	heat capacity ($\text{Jmol}^{-1}\text{K}^{-1}$)
C_p^E	excess heat capacity ($\text{Jmol}^{-1}\text{K}^{-1}$)
C_p^i	heat capacity of component i ($\text{Jmol}^{-1}\text{K}^{-1}$)
$E_{A,i}$	activation energy of component i in a mixture (Jmol^{-1})
E_A	activation energy (Jmol^{-1})
E_{cell}	electromotive force (V)
F_x	shear force (N)
G_i^*	Gibbs energy of activation (Jmol^{-1})
G_i^0	Gibbs free energy of the pure component I (Jmol^{-1})
J_{O_2}	oxygen flux (m^3s^{-1})
J_{tot}	total gas flow (m^3s^{-1})
K_{ad}	equilibrium constant of the oxygen adsorption
K_c	thermal conductance for conductive heat transfer from the laser irradiated part to the nonirradiated part (WK^{-1})
K_r	thermal conductance for radiative heat transfer from the sample's surface to the heat reservoir in vacuum (WK^{-1})
M_i	molar mass of component i (gmol^{-1})
N'_i	number of atoms of component i involved in a reaction before the reaction takes place

N'_{tot}	total number of atoms involved in a reaction before the reaction takes place
N_{Av}	Avogadro constant ($6.023 \cdot 10^{23} \text{ mol}^{-1}$)
$N_{i,j}$	upper bound of summation
N_i	number of atoms of component i involved in a reaction after the reaction takes place
N_{tot}	total number of atoms involved in a reaction after the reaction takes place
P_{H_2}	partial pressure of H_2 (Pa)
$P_{\text{H}_2\text{O}}$	partial pressure of H_2O (Pa)
$P_{\text{O}_2,\text{sat}}$	saturated oxygen partial pressure (Pa)
P_{O_2}	oxygen partial pressure (Pa)
$P_{\text{O}_2}^0$	initial oxygen partial pressure in the OSC (Pa)
$P_{\text{O}_2}^{\text{Ch}}$	oxygen partial pressure in the chamber (Pa)
$P_{\text{O}_2}^{\text{ref}}$	oxygen partial pressure of a reference gas (ambient air)
$P_{\text{O}_2}^{\text{S}}$	oxygen partial pressure in the vicinity of the surface (Pa)
P_0	laser power (Wm^{-2})
P_{H}	heating power (J)
P_l	l -th Legendre polynomial
P_{tot}	total pressure in the chamber (Pa)
R_0	radius of the sample with spherical shape (m)
R_{B}	theoretical black-body radiance from Planck's law ($\text{Wm}^{-2}\mu\text{m}$)
R_{S}	normal spectral radiance emitted from a sample ($\text{Wm}^{-2}\mu\text{m}$)
R_d	sample radius (m)
S_{h}	fraction of the laser irradiated surface area during modulated laser calorimetry

S^S	molar entropy (JK^{-1})
S_e	segregation factor
T_0	initial sample temperature prior to heating (K)
T_h	temperature of the laser irradiated part during modulated laser calorimetry (K)
T_L	liquidus temperature (K)
T_l	temperature of the laser non-irradiated part during modulated laser calorimetry (K)
T_p	pyrometer signal (K)
V^B	volume of the bulk (cm^3)
V^E	excess molar volume ($\text{cm}^3\text{mol}^{-1}$)
V^G	volume of the gas phase (cm^3)
V_h	volume fraction corresponding to the laser irradiated surface area during modulated laser calorimetry
V_i	molar volume of component i ($\text{cm}^3\text{mol}^{-1}$)
V^{ideal}	molar volume of an ideal solution ($\text{gcm}^{-3}\text{mol}^{-1}$)
V_p	droplet volume in pixel units (pixel^3)
$X_i^{(n)}$	mole fraction of component i in the n -th surface layer (at.-%)
X_i	mole fraction of component i in a mixture (at.-%)
X_i	molar ratio of component i involved in a reaction after the reaction takes place (at.-%)
X'_i	molar ratio of component i involved in a reaction before the reaction takes place (at.-%)
X_i^B	mole fraction of component i in the bulk (at.-%)
X_i^S	mole fraction of component i in the surface (at.-%)
f_{geo}	geometrical factor

f_i	activity coefficient of oxygen in the liquid component i
f_{se}	adjustable fit parameter used for the Egry model for compound formation in alloy systems
k_B	Boltzmann constant ($1.38064852 \cdot 10^{-23} \text{ JK}^{-1}$)
\vec{m}	magnetic dipole moment (NmT^{-1})
m_i	mass of component i (g)
m_{tot}	total mass of a mixture (g)
n_i	number of moles of component i in a mixture
n_i^B	number of moles in the bulk
n_i^G	number of moles in gas phase
v_x	shear velocity in direction x (ms^{-1})
w_i	weight ratio of component i with respect to the total mass of a mixture
z_l	lateral coordination number
z_y	vertical coordination number
Γ_i	adsorption of component i
Γ_i^0	the saturated surface excess concentration of the surface-active component i
$\Phi_{i,j}$	single bond energy for a bond between atoms i and j (Jmol^{-1})
α_i	activity of component i
α_K	parameter of the empirical model by Allen (41 ± 10)
α_l	l -th edge curve coefficient
β_K	parameter of the empirical model by Allen ($(3,3 \pm 0.7) \cdot 10^{-3}$)
γ^E	excess surface tension (Nm^{-1})
γ_i	surface tension of component i (Nm^{-1})
γ^{ideal}	surface tension of an ideal solution (Nm^{-1})

γ_L	surface tension at liquidus temperature (Nm^{-1})
γ^{pure}	pure surface tension with no adsorbed impurities (Nm^{-1})
γ_T	temperature coefficient of surface tension ($10^{-4} \text{Nm}^{-1}\text{K}^{-1}$)
η_∞	pre-exponential factor for the temperature dependent viscosity by Arrhenius law (mPas)
θ_i	fractional coverage of the adsorbate i (m^{-2})
μ_0	magnetic permeability (NA^{-2})
μ_i	chemical potential of component i in the mixture
μ_i^0	the chemical potential of the standard (bulk) state
ρ_i	mass density of component i (gcm^{-3})
ρ_L	mass density at liquidus temperature ($\text{gcm}^{-3}\text{K}^{-1}$)
ρ_T	density temperature coefficient ($10^{-4}\text{gcm}^{-3}\text{K}^{-1}$)
$\sigma_{x,y}$	shear stress (Pa)
$\tau_c(\text{s})$	internal thermal relaxation time attributable to the conductive heat transfer in the sample
$\tau_r(\text{s})$	external thermal relaxation time attributable to the radiative and conductive heat transfer in the ambient gas
$\omega_{2,m} = \omega_2 = \omega_R$	Rayleigh-frequency (s^{-1}) with mode $m = -2, -1, 0, +1, +2$
$\omega_{l,m}$	surface oscillation frequency of mode m and l (s^{-1})
ω_x	translational frequency in x-direction (s^{-1})
ω_y	translational frequency in y-direction (s^{-1})
ω_z	translational frequency in z-direction (s^{-1})
ΔH_{mix}	enthalpy of mixing (kJmol^{-1})
ΔT_{ac}	average increase in temperature of the ac component due to laser heating (K)

ΔT_{dc}	average increase in temperature of the dc component due to laser heating (K)
ΔG	Gibbs free energy of formation (kJmol^{-1})
ΔS	entropy of mixing (JK^{-1})
$\Delta \delta$	gradual transition zone between the gas phase and bulk of a liquid
${}^E G$	excess Gibbs energy (Jmol^{-1})
$\text{FFT}(\mathbf{A}_0(t))$	fast Fourier transform (FFT) of the translations and oscillations of the area
$\text{FFT}(\mathbf{r}_x(t) - \mathbf{r}_y(t))$	fast Fourier transform (FFT) of the translations and oscillations of the difference
$\text{FFT}(\mathbf{r}_x(t) + \mathbf{r}_y(t))$	fast Fourier transform (FFT) of the translations and oscillations of the sum
$\text{FFT}(\mathbf{x}_0(t))$	fast Fourier transform (FFT) of the translations and oscillations in the x-direction
$\text{FFT}(\mathbf{y}_0(t))$	fast Fourier transform (FFT) of the translations and oscillations in the y-direction
h	Planck constant ($6.626 \cdot 10^{34}$ Js)
A	(surface) area (m^2)
F	Faraday constant (96485 C mol^{-1})
G	Gibbs free energy (kJmol^{-1})
H	enthalpy (kJmol^{-1})
$H(q)$	efficiency ratio of the absorption of heating power
I	electric current (A)
K	equilibrium constant
Q	power input from the levitation coil (W)

$Q(q)$	efficiency ratio
R	universal gas constant ($8.314 \text{ JK}^{-1}\text{mol}^{-1}$)
S	Entropy (JK^{-1})
T	temperature (K)
V	molar volume (cm^3)
b	semi-empirical parameter used for the Kaptay model of the composition dependence of the viscosity (0.155)
f	correction function of the modulated laser calorimetry
g	gravitational acceleration (9.81 m s^{-1})
i, j	chemical species (e.g., Al, Ti)
k	number of surface layers in the Chatain model
l	index
n	index of the surface layer in the Chatain model
P	pressure (Pa) or (bar)
q	scaling factor ($\text{cm}^3\text{pixel}^{-3}$)
t	time (s)
w	regular solution constant (Jmol^{-1})
z	coordination number
Φ	phase shift
Ω	mean translational frequency (s^{-1})
α	isothermal compressibility (Pa^{-1})
β	thermal volume expansion coefficient (10^{-4}K^{-1})
γ	surface tension (Nm^{-1})
δ	skin depth of a magnetic field (μm)
ε	normal spectral emissivity

η	shear viscosity (mPas)
λ	wavelength (nm)
μg	Microgravity (Nm^{-2})
ξ	factor accounting for a reduced coordination number in the surface
ρ	mass density (gcm^{-3})
τ	damping constant used for the determination of the viscosity (s^{-1})
φ	azimuthal angle ($^{\circ}$)
ω	frequency (s^{-1}), angular frequency (rad s^{-1})

Method abbreviations

A	Archimedian methods
BP	maximum bubble pressure
C	capillary technique
CR	rise method
DC	draining crucible
DW	drop weight
EML	electro magnetic levitation
ESL	electrostatic levitation
EW	exploding wire technique
G	γ -absorption dilatometry
GJ	gas jet technique
LD	large drop technique
OC	oscillating cup viscometer
OD	oscillating drop technique
PD	pendant drop technique
PW	pedant wire
R	recommended data from a literature review
SD	sessile drop method

Acknowledgements

First and foremost, I want to thank my Ph.D. supervisor Priv.-Doz. Dr. Jürgen Brillo for his continuous support and patience. His experience and our discussions have been very valuable and encouraging. I am very grateful to him for giving me the chance to work on this interesting topic, present at international conferences, participate in two parabolic flight campaigns and for my unforgettable experiences during my research project in Japan that he helped to organise.

I am grateful to Prof. Dr. Andreas Bührig-Polaczek for being the second referee and for his ongoing interest in my work and support.

I would like to thank Prof. Dr. Andreas Meyer for his support and for the extraordinary opportunity to work at the Institute of Materials Physics in Space at the German Aerospace Center in Cologne.

I would like to express my highest appreciation to Prof. Dr. Hiroyuki Fukuyama for the exceptional time in his laboratory, his expertise, and support. I couldn't be more thankful to all my former colleagues at Fukuyama lab. for being so incredibly welcoming and supportive in all matters during my time in Japan, professionally, as well as personally and for introducing me to the Japanese culture. Special thanks to Assistant Prof. Dr. Masayoshi Adachi, Hideo Higashi, Miwa Sasaki and Sonoko Hamaya. As well as special thanks to Dr. Hidekazu Kobatake who's knowledge, support and patience have guided me through my whole Ph.D. in Germany and Japan. Further, I would like to thank Prof. Dr. Yuzuru Sato for the enormous support and organisation of my research project in Japan.

I am very grateful to:

Prof. Dr. Dieter Herlach and Dr. Georg Lohöfer for their critical review of my work and valuable suggestions. Prof. Dr. Matthias Sperl for being my mentor. Dr. Matthias Kolbe for taking SEM images and the fruitful scientific discussions. Prof. Dr. Rainer Schmid-Fetzer for calculating the respective liquidus temperatures of the binary Al-Ti-system. Dr. Michal Schulz who has been a great support with the OSC. Prof. Dr. Florian Kargl for his advice, as well as scientific and administrative support. The TEMPUS parabolic flight team for their amazing support before, during and after the campaigns; Dr. Dirk Bräuer, Dr. Julianna Schmitz, Dr. David Heuskin, Dr. Marc Engelhardt and Dr. Stephan Schneider. Additionally, Sarah Zimmermann and Dr. Isabell Jonas for their support with the evaluation of the μg -data. DLR and the Institute of Materials Physics in Space for making my Ph.D. possible. All colleagues who have made these years such a great experience with the backbones of the institute in the workshop and with our secretaries Kim Prochnow and Ingeborg Parpart.

All my colleagues at DLR who have become dear friends over the years and supported me with motivation, knowledge, comfort in times of struggle and help with my work. Amongst many more, I would like to express thanks to Heliana Cardenas, Carolina Kreischer, Sebastian Pitikaris, Maïke Becker, Christian Karrasch, Jan Haeberle and Alexander Liliashvili. All my friends from all over the world who have supported me over the years with motivation, reviews, and their friendship. Thanks to my DM family Stuart Roberts and Kevin Burkett.

James Harpur for his endless patience, support and making every day better with his positive mindset.

My whole family, I couldn't have done it without them. I wouldn't be where and who I am today without the endless support of all my parents in all matters possible, among much more motivational, life advice, incredible patience, telling me to get it together if necessary, financially and simply food when I didn't have the time to cook. Special thanks to the best of all brothers for everything. Special thanks to my aunts, uncles, and cousins each one contributing to this thesis in one way or another. I would like to thank my grandfathers for always believing in me 100% and being there for me no matter what. Likewise, a great thanks to my three late grandmas for their support over the years, each one incredibly strong in her way, I would be honoured to claim that I inherited just a glimpse of it.

Curriculum Vitae

Johanna Jeanette Wessing, born 1st of January 1987 in Bergisch Gladbach, Germany

Contact: jowessing@googlemail.com

- 05/2014 – 06/2018 Ph. D. of Science with great honours (magna cum laude) at the Institute of Materials Physics in Space, German Aerospace Center (DLR), Cologne and Materials Science & Engineering (MatSE), RWTH Aachen University
- 12/2016 Publication: J Wessing and J Brillo. *Density, molar volume, and surface tension of liquid Al-Ti*. Metallurgical and Materials Transactions A, 48 (2): 868–882, 2017
- 09 – 12/2016 Scholarship by the Graduate School of Engineering, Tohoku University at Fukuyama lab, Sendai, Japan
- 04 – 12/2016 Among the last 86 candidates for the first female German astronaut
- 01/2013 – 04/2016 PADI scuba Divemaster training and work in Germany, Indonesia, and Australia
- 04 – 09/2012 Master thesis at the Institute of Engineering Thermodynamics, DLR, Stuttgart, Topic: *Modifikation von feinkörnigen Pulvern mit Hilfe von Nanopartikeln*
- 10/2010 – 09/2012 M. Sc. Geo Sciences with major subjects in *Geochemistry* and *Natural and synthetic materials* at the University of Cologne, Germany
- 11/2009 – 05/2010 Student research assistant at the University of Cologne, Institute for Geology and Mineralogy
- 10/2007 – 09/2010 B. Sc. Geo Sciences with major subjects in *Applied Geology*, *Geochemistry* and *Materials sciences* at University of Cologne, Germany
- 08/1996 – 09/2007 Courses in Spanish at an advanced level and tutoring in mathematics and English
- 08/1997 – 06/2006 Annette-von-Droste-Hülshoff-Gymnasium, Düsseldorf